

Power Systems

Hansjoachim Bluhm
Pulsed Power Systems

Hansjoachim Bluhm

Pulsed Power Systems

Principles and Applications

With 220 Figures

 Springer

Professor Dr. Hansjoachim Bluhm
Forschungszentrum Karlsruhe
Institut für Hochleistungsimpuls-
und Mikrowellentechnik
Postfach 36 40
76021 Karlsruhe
Germany
hansjoachim.bluhm@ihm.fzk.de

Library of Congress Control Number: 2005929279

ISBN-10 3-540-26137-0 Springer Berlin Heidelberg New York
ISBN-13 978-3-540-26137-7 Springer Berlin Heidelberg New York

This work is subject to copyright. All rights are reserved, whether the whole or part of the material is concerned, specifically the rights of translation, reprinting, reuse of illustrations, recitation, broadcasting, reproduction on microfilm or in other ways, and storage in data banks. Duplication of this publication or parts thereof is permitted only under the provisions of the German Copyright Law of September 9, 1965, in its current version, and permission for use must always be obtained from Springer. Violations are liable to prosecution under German Copyright Law.

Springer is a part of Springer Science+Business Media
springer.com

© Springer-Verlag Berlin Heidelberg 2006
Printed in Germany

The use of general descriptive names, registered names, trademarks, etc. in this publication does not imply, even in the absence of a specific statement, that such names are exempt from the relevant protective laws and regulations and therefore free for general use.

Typesetting: www.ptp-berlin.com
Final processing: www.ptp-berlin.com
Cover-Design: deblik, Berlin
Printed on acid-free paper 57/3141/Yu – 5 4 3 2 1 0

Preface

This book on pulsed power systems is the result of a course that I have been teaching for ten years at the Technical University of Karlsruhe. Initially planned as a course for German students, it became part of the courses offered to foreign students from all over the world in the International Department of the University in 1998. The book should provide students beginning in this field with the necessary background to explore the more advanced literature. In a similar way, it should also serve to help engineers and scientists from other fields to become familiar with the basic ideas and methods of pulsed power and to achieve a sound judgement of its potential usefulness for solving their problems. The main characteristic of pulsed power is the very high peak-to-average power ratio. Therefore it can exploit threshold and nonlinear effects. Another set of benefits can result from the short pulse duration, which allows one to exploit the time domain (e.g. in radar and flash X-ray radiography) or to avoid competing processes (e.g. electric breakdown or heat losses). Pulsed-power methods have fertilised many disciplines in electrical engineering, experimental physics, biotechnology, food technology and material science.

When I started the course on pulsed power in 1995, I realised the lack of an introductory textbook. Although a collection of unpublished technical papers emanating from the work of J.C. Martin at Aldermaston in the 1960s and 1970s on nanosecond intense flash X-ray sources for radiography was in common use at many pulsed-power laboratories, this was not an adequate substitute for a textbook. This situation did not change when, in 1996, T. Martin, A. Guenther, and M. Kristiansen published J.C. Martin's papers in a book entitled *J.C. Martin, On Pulsed Power*. Nevertheless, many of the empirical formulae derived by J.C. Martin are still very useful in designing pulsed-power systems and have been reproduced in the present book, generally keeping the original practical units.

The ideal textbook will never be completed. New and exciting developments appear continuously, and the reader is referred to the digests of technical papers of the biannual series of the IEEE International Pulsed Power Conferences, the records of the Power Modulator Symposia, and the proceedings of the International Conferences on High-Power Particle Beams for the latest advancements.

For many years, the majority of new developments in pulsed power appeared in the USA, and the IEEE International Pulsed Power Conferences, held since 1976 exclusively in the USA, underline this statement. Also, I took my first steps in this field during a stay at Cornell University, New York State, in 1980, where at that time the new discipline of collective pulsed ion beams was coming into existence. After the fall of the Iron Curtain, however, it became apparent that an equally large advancement in pulsed power had been made in the former Soviet Union. Although many of the objectives were purely military, some very fruitful innovations for civil applications became disclosed too, triggering a number of successful civil programmes, especially in Japan and Europe, but also at several universities in the US. Recently, the new discipline of bioelectrics, whose subject is the study of the interaction between strong pulsed electric fields and biological cells, has grown rapidly in the USA (Old Dominion University, Norfolk, Virginia), Japan (Kumamoto University, Kyushu Island), Germany (Forschungszentrum Karlsruhe), and other countries. It is fair to say that the selection of the topics of the chapters of this book on applications leans mainly towards my own interests and those of my research group in the Institute for Pulsed Power and Microwave Technology at Forschungszentrum Karlsruhe.

Although the largest part of this book was worked on during weekends and evenings, a six-month stay as a visiting professor at Kumamoto University in 2003 accelerated its completion. Therefore, I am very grateful to H. Akiyama for his kind invitation. Pulsed-power science at Forschungszentrum Karlsruhe would never have been possible without the initiative of G. Kessler in 1979 to begin an intense light-ion-beam programme for inertial fusion energy at the Institute of Neutron Physics and Reactor Technology. Soon after his retirement in 1999, it was decided to stop the light-ion-beam programme in Karlsruhe. As frequently happens in scientific research, a crisis brings with it the chance of a new beginning, and I am thankful to M. Thumm that he constantly supported our new approaches towards industrial applications of pulsed power in the newly founded Institute for Pulsed Power and Microwave Technology. The book comes with a CD containing the very useful transmission line code LEITER, written by my former colleague D. Rusch, whom I would like to thank for his agreement to include the program in the book. Also, I would like to thank my colleagues W. An, K. Baumung, W. Frey, H. Giese, P. Hoppé, G. Müller, M. Sack, C. Schultheiß and A. Weisenburger, whose expertise in pulsed power entered into this book.

My wife Ursula certainly suffered a lot during the finalisation of this book, which often prevented joint activities at weekends, and I am very grateful for her patience. Now it's done.

Contents

Symbols and Abbreviations	XI
1 The Essence of Pulsed Power	1
2 Static and Dynamic Breakdown Strength of Dielectric Materials	7
2.1 Introduction	7
2.2 Gases	8
2.2.1 Static Breakdown	8
2.2.2 Pulsed Breakdown	17
2.2.3 Spark Formation	23
2.3 Liquids	27
2.3.1 Basic Electrical Processes	27
2.3.2 Streamer Breakdown	34
2.3.3 Practical Considerations	38
2.4 Solids	41
2.4.1 General Observations	41
2.4.2 Charge Transport, Injection, and Breakdown	45
2.5 Statistical Interpretation of Breakdown Strength Measurements	50
3 Energy Storage	55
3.1 Pulse Discharge Capacitors	55
3.2 Marx Generators	63
3.2.1 Classical Marx Generators	63
3.2.2 <i>LC</i> Marx Generator	69
3.2.3 Basic Pulsed-Power Energy Transfer Stage	70
3.3 Inductive Energy Storage	73
3.3.1 Power and Voltage Multiplication	74
3.4 Rotors and Homopolar Generators	76
4 Switches	83
4.1 Closing Switches	83
4.1.1 Gas Switches	83
4.1.2 Semiconductor Closing Switches	104

4.1.3	Magnetic Switches	116
4.1.4	Summary	119
4.2	Opening Switches	119
4.2.1	Fuses	120
4.2.2	Mechanical Interrupters	121
4.2.3	Superconducting Opening Switches	123
4.2.4	Plasma Opening Switches	123
4.2.5	Plasma Flow Switches	127
4.2.6	Semiconductor Opening Switches (SOSs)	127
5	Pulse-Forming Networks	135
5.1	Transmission Lines	135
5.1.1	Terminations and Junctions	138
5.1.2	Transmission Lines with Losses	140
5.1.3	The Finite Transmission Line as a Circuit Element ...	142
5.1.4	Production of Pulses with Lossless Transmission Lines	144
5.2	<i>RLC</i> Networks	145
5.3	Circuit Simulation with LEITER	152
6	Pulse Transmission and Transformation	157
6.1	Self-Magnetic Insulation in Vacuum Lines	157
6.1.1	Vacuum Breakdown on Metallic Surfaces	159
6.1.2	Qualitative Description of Self-Magnetic Insulation ...	161
6.1.3	Quantitative Description of Self-Magnetic Insulation	163
6.2	Pulse Transformers	179
6.3	High-Voltage Power Supplies	184
6.3.1	Capacitor-Charging Techniques	184
6.3.2	Cascade Circuits	188
6.4	Transformation Lines	188
7	Power and Voltage Adding	193
7.1	Adding of Power	193
7.2	Voltage Adding	193
7.2.1	Voltage Adding by Transit-Time Isolation	193
7.2.2	Voltage Adding by Inductive Isolation	195
7.2.3	Blumlein Generators	197
7.2.4	Cumulative Pulse Lines	198
8	Examples of Pulsed-Power Generators	203
8.1	Single-Pulse Generators	203
8.1.1	KALIF	203
8.1.2	PBFA 2 and the Z-Machine	204
8.1.3	HERMES III	207

8.2	Repetitive Generators	208
8.2.1	RHEPP	208
8.2.2	Generators with Opening Switches	209
9	Diagnosics	211
9.1	Electromagnetic-Field Sensors	211
9.1.1	Capacitive Sensors	212
9.1.2	Inductive Sensors	214
9.2	Current-Viewing Resistors (CVRs)	218
9.3	Current Measurements Based on the Faraday Effect	220
9.4	Electric-Field Measurements Based on Electro-Optic Effects ..	222
9.5	Magnetic Ion Energy Analysers	223
9.6	Vacuum Voltage Monitors.....	224
10	Applications of Pulsed Electromagnetic Fields	227
10.1	Pulsed Electric Fields	227
10.1.1	Introduction	227
10.1.2	Pulse Generation	232
10.1.3	Treatment of Plant Cells.....	232
10.1.4	Bacterial Decontamination	236
10.1.5	Further Applications of PEF Treatment	237
10.2	Pulsed Magnetic Fields	238
10.2.1	Introduction	238
10.2.2	Field Limitations for Non-Destructive Coil Operation	240
10.2.3	Field Limitations for Destructive (Coil) Operation: Single-Turn Solenoid	246
10.2.4	Flux Compression	248
11	Intense Radiation Sources	257
11.1	High-Power Pulsed Electron Beams	257
11.1.1	Beam-Generated Forces and Transport Limits	257
11.1.2	High-Current Electron Sources	258
11.1.3	Pulsed Electron Diodes	259
11.1.4	Surface Modification of Materials	260
11.1.5	High-Power KrF Lasers.....	265
11.1.6	Flash X-Ray Radiography	267
11.2	High-Power Ion Beams	270
11.2.1	Accelerator Physics	271
11.2.2	Beam Transport	277
12	Pulsed Discharges Through Solid and Liquid Dielectrics... ..	279
12.1	Extracorporeal Shock Wave Lithotripsy	279
12.2	Electroimpulse Destruction of Solid Dielectric Materials	281
12.2.1	General Phenomena and Energy Balance	281
12.2.2	Selectivity of Destruction	286

12.2.3	The Fragmentation Device	288
12.3	Industrial Applications	292
12.3.1	Recycling of Building Materials	292
12.3.2	Treatment of Incineration Ash	295
12.3.3	Removal of Surface Layers and Drilling	297
12.3.4	Recycling of Other Products	299
12.3.5	Recycling of Elastoplastic Materials	301
12.3.6	Scaling and Economic Considerations in Relation to Recycling	304
References		307
Index		323

Symbols and Abbreviations

Symbols

\vec{A}	vector potential; vectorial element of area
A	area
\vec{B}	magnetic induction
C	capacitance; 0.577 (Eulerian constant)
c	velocity of light
c_v	specific heat per unit mass
\vec{D}	displacement
d	distance
\vec{E}	electric field
e	elementary charge
\vec{F}	force
$F(E, t)$	probability of failure at time t and field stress E
$F(W)$	Fermi–Dirac function at energy W
G	conductance; shear modulus
$G(p)$	transfer function
$G_{n,p}$	generation rates of electrons and holes
g	geometric factor
\vec{H}, H	magnetic field strength
H	Hamiltonian function
$H(t)$	Heaviside function
h	Planck’s constant; thickness
I	current
I_0	total current in vacuum line
I_α	Alfvén current
I_{cr}	critical current
I_w	wall current
i	imaginary unit $\sqrt{-1}$

XII Symbols and Abbreviations

$i(p)$	Laplace- or Fourier-transformed current
$i(t)$	small-signal current
J	current density integral
j	current density
K	Kerr constant
k	Boltzmann constant; mobility
k_{\pm}	constants
L	inductance
L_d	diffusion length
ℓ	length
M	macroscopic mass
m	particle mass
m_0	particle rest mass
N	total number of particles
n	number of atoms per unit volume
\vec{P}	canonical momentum
P	polarisation
P_{al}	matched-load power
P_{ab}	transition probability from state a to b
p	gas pressure; Laplace operator
Q	heat energy; specific energy density; electron charge per unit length of vacuum line
q	surface charge density
R	resistance
$R_{n,p}$	recombination rates of electrons and holes
r	radius
\vec{S}	Poynting vector
S	general stress parameter
s	channel length; path length
T	period; transit time; transmission coefficient; temperature
t	time
U	voltage
u	velocity
$u(p)$	Laplace-transformed voltage
$u(t)$	small-signal voltage
$\langle u \rangle$	mean swarm velocity
V	volume; Verdet constant
W_+, W_-	energy levels

W_{kin}	kinetic energy
w_{kin}	kinetic-energy density
x	spatial coordinate
Y	Young's modulus
Z	impedance
$Z(W)$	number of allowed states per unit energy interval at W
α	ionisation coefficient
α_n, α_p	ionisation coefficients for electrons and holes in a semiconductor
β	$u/c =$ particle velocity relative to the velocity of light; field enhancement factor
Γ	gamma function
γ	ω/α ; relativistic factor
δ	maximum stress/mean stress; detachment coefficient
δ_Φ	magnetic-flux skin depth
$\text{tg } \delta$	loss factor
ε	relative dielectric constant
ε_0	permittivity of free space
ζ	surface energy
η	efficiency; electron attachment coefficient
Θ	moment of inertia
Λ_{ab}	reconfiguration energy
λ	mean free path between collisions; thermal conductivity
μ	relative permeability; mobility
μ_0	permeability of free space
μ_n, μ_p	electron and hole mobilities in a semiconductor
ν	frequency
ν_{ei}	electron-ion collision frequency
$\xi(S)$	relative expected failure rate at stress S
Π	Paschen function
ρ	reflection coefficient
Σ	macroscopic cross-section
Σ_y	yield strength
σ	tensile strength; microscopic cross-section; conductivity; variance
σ_a	standard deviation
τ	time constant; time between collisions
Φ	magnetic flux
φ	potential; work function

XIV Symbols and Abbreviations

χ	ratio of specific heats
$\psi(S)$	survival probability at stress S
ω	angular frequency; secondary-electron emission coefficient

Abbreviations

ADP	ammonium dihydrogen phosphate
ADS	accelerator-driven reactor system
CVR	current-viewing resistor
DIN	Deutsche Industrienorm (German Industry Standard)
DSRD	drift step recovery diode
EMHD	electron magnetohydrodynamics
FRANKA	Fragmentierungsanlage Karlsruhe (Fragmentation Device, Karlsruhe)
FWHM	full width at half maximum
GESA	gepulste Elektronenstrahlenanlage (Pulsed-Electron-Beam Facility)
GTO	gate turn-off thyristor
GW	gigawatt
Gy	Gray, unit of radiation dose
HELIA	high-energy linear induction accelerator
IFE	inertial-fusion energy
IGBT	insulated-gate bipolar transistor
IHL	inner Helmholtz layer
KALIF	Karlsruhe light-ion facility
KDP	potassium dideuterium phosphate
KEA	Karlsruher Elektroporations Anlage (Karlsruhe Electroporation Facility)
MS	magnetic switch
OHL	outer Helmholtz layer
PBFA	particle beam fusion accelerator
PEF	pulsed electric field
PFL	pulse-forming line
PIC	particle in cell
POS	plasma opening switch
RHEPP	repetitive high-energy pulsed power
RLD	region of low density
SCR	silicon-controlled rectifier
SOS	semiconductor opening switch

SPT	self-pinched transport
SRD	step recovery diode
TBC	thermal barrier coating
TE	transverse electric (H-mode)
TGO	thermally grown oxide scale
TM	transverse magnetic (E-mode)
TVG	triggered vacuum gap
TW	terawatt
YSZO	yttria-stabilised zirconia

1 The Essence of Pulsed Power

Pulsed power is a scheme where stored energy is discharged as electrical energy into a load in a single short pulse or as short pulses with a controllable repetition rate. It is the aim of this book to describe the physical and technical foundations of the production and application of high-voltage pulses of very high power and high energy content. Pulsed power is pertinent to applications where the load must be pulsed or performs better if pulsed.

We shall speak of pulsed power if the electrical power of the pulses is around one gigawatt (10^9 W) and if their energy content is of the order of one kilojoule or greater. The highest energy and power that have been achieved in a single pulse are at present of the order of 100 MJ and a few hundred terawatts respectively. The corresponding voltage and current amplitudes are between 10 kV and 50 MV and between 1 kA and 10 MA, respectively.

In addition to its power and energy, a pulse is characterised by its shape, i.e., by its rise and fall times and by the duration and flatness of its plateau region. Typically, the overall duration of the high-power pulses considered here lies between a few nanoseconds and a few microseconds. Some important pulse shape parameters are shown in Fig. 1.1.

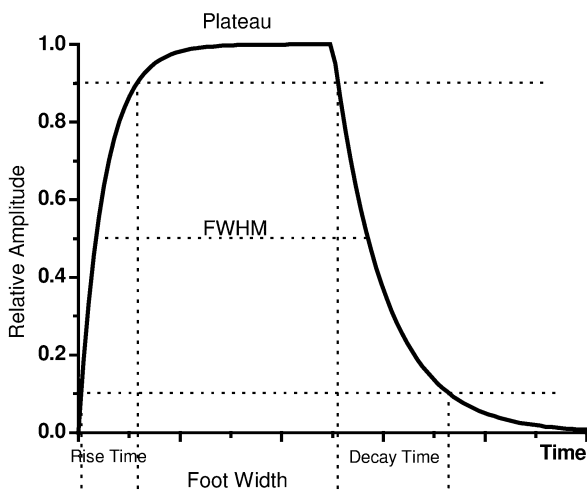


Fig. 1.1. Pulse shape parameters

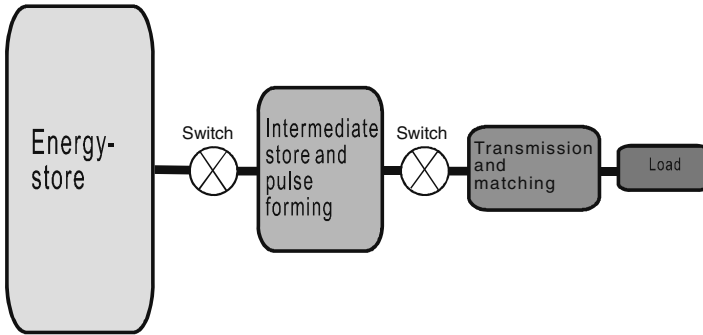


Fig. 1.2. General scheme of a pulsed-power generator

The pulse rise time is defined as the time it takes the voltage to rise from 10% to 90%. We can define the fall, or decay, time in a similar way. Both the fall and the rise time of a pulse depend on the evolution of the load impedance, which in most cases varies with time. There is no unique definition of the pulse duration in the literature. Sometimes it is understood as the full width at half maximum (FWHM) of the pulse. However, for some applications, it is better to define it as the duration at 90% of the peak amplitude. Flatness of the plateau region is an important requirement for driving some loads, for example Pockels cells.

A generator scheme for the production of high-power electrical pulses is always based on an energy store that is charged slowly at a relatively low charging power and, by activating a switch, is discharged rapidly. By this procedure, a large power multiplication can always be obtained. To achieve the desired power multiplication factor, this process can be repeated several times if necessary.

In addition to power multiplication, this scheme can simultaneously be applied to shape the pulse, i.e., to create the desired rise time and pulse duration. To optimise the energy transfer to a load, an impedance transformation may also become necessary. The components of a high-power pulse generator are sketched schematically in Fig. 1.2.

The energy can be stored either chemically, mechanically, or electrically. In some devices, chemical explosives are used to compress a pre-established magnetic flux and thus increase the power at which the stored magnetic energy can be released. Chemical energy storage will be discussed in Chap. 10 of this book.

Mechanical energy can be stored, for example, as the kinetic energy of a rotor. Here the energy stored equals $W_{\text{kin}} = (1/2) \Theta \omega^2$, where Θ is the moment of inertia and ω is the angular frequency of rotation. For a massive cylinder, we have $\Theta = (1/2) M r^2$, where M and r are the mass and the radius of the cylinder, respectively. Therefore the stored energy density is $w_{\text{kin}} = (1/4) r^2 \omega^2$. The ultimate energy density is limited by the tensile strength of

the material used to construct the rotor. The relationship between the tensile strength Σ and the maximum rotation frequency ω_{\max} can be described by $\Sigma = \rho \omega_{\max}^2 r^2/2$. For a stainless steel cylinder of radius 1 m, we obtain $\omega_{\max} = 400/\text{s}$. Compared with electrical storage, rather high energy densities are achievable. For a steel cylinder of radius 1 m, rotating at $\omega = 400/\text{s}$, we obtain $w_{\text{kin}} = 4 \times 10^4 \text{ J/kg} = 3.1 \times 10^8 \text{ J/m}^3$. The problem with mechanical storage is to release the energy in a sufficiently short time. Therefore, in general, several electrical compression stages are needed in combination with the mechanical storage to achieve the desired power level.

Electrical energy can be stored either capacitively in an electric field or inductively in a magnetic field. In the first case we have $w_e = \varepsilon \varepsilon_0 E^2/2$, which for a dielectric with $\varepsilon = 6$ and a breakdown strength of $E = 0.78 \times 10^8 \text{ V/m}$ (oilimpregnated paper), leads to a maximum energy density, of $w_e = 161 \text{ kJ/m}^3$. Because of the finite packing density, this must be multiplied by 0.5, i.e., $w_e = 80 \text{ kJ/m}^3$.

In the second case we have $w_B = B^2/2\mu\mu_0$. Here, the maximum energy density is limited by the onset of melting at the conductor surface or by the mechanical strength of the storage inductor. Joule heating at the conductor surface results from eddy currents generated during the diffusion of the magnetic field into the conductor. For a conducting half-space, the surface temperature can be expressed in the general form [Knoepfel 1970]

$$c_v \rho T(0, t) = \frac{1}{2\mu_0} B^2(0, t) \vartheta(t), \quad (1.1)$$

where c_v is the heat capacity per unit mass, ρ is the mass density, $T(0, t)$ is the surface temperature, $B(0, t)$ is the boundary field, and $\vartheta(t)$ is a factor of order unity depending on the form of the pulse. Using data for Cu, we find a value between 50 and 100 T for the maximum B -field, depending on the pulse shape. To estimate the limitations resulting from mechanical forces, we evaluate the criterion for static containment, which is valid if the charging time (and therefore the duration of the pressure pulse) is larger than the period of oscillation of the containment [Knoepfel 1970]:

$$\frac{B^2}{2\mu_0} < \Sigma_y \frac{r_o^2 - r_i^2}{r_o^2 + r_i^2}, \quad (1.2)$$

where Σ_y is the yield strength of the containment material, r_o is the outer radius of the cylindrical containment, and r_i is the inner radius. For the case of a thick ($r_o = 2r_i$) copper–beryllium ($\Sigma_y = 1000 \text{ N/mm}^2$) cylinder, we calculate $B < 38 \text{ T}$. In this case the average energy density in the containment, i.e., within the radius r_o amounts to $w_B = 39\,000 \text{ kJ/m}^3$. We see that, even if one considers technological conditions, i.e., one takes into account support structures, insulation, etc., the energy density stored in a magnetic field can be about two orders of magnitude higher than that storable in an electric field.

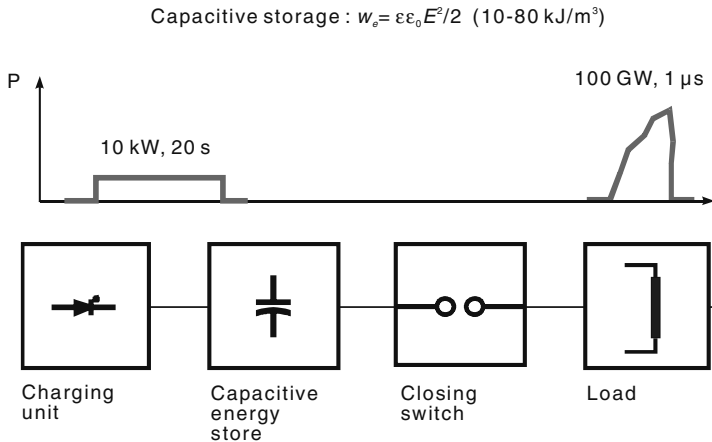


Fig. 1.3. Generator with capacitive energy storage and a closing switch. The numbers given in the upper part of the figure are typical for a single-pulse high-power generator. They assume that about 50% of the stored electrical energy reaches the load

The main components of a generator with *capacitive storage* are shown in Fig. 1.3. This generator requires one or more closing switches which remain open during charging and hold the charging voltage. When the switches are closed, this generator achieves its power multiplication by *current amplification*.

The generator with *inductive storage* shown in Fig. 1.4 requires an opening switch, which is closed during charge-up, carrying a large current at this stage. After completion of the charging process, the switch should open instantaneously and be capable of insulating the high voltage that is created. An inductive generator achieves power multiplication by *voltage amplification*. To keep the losses during charge-up small an inductive generator needs a high-current power supply. Since it is more difficult to build suitable opening switches, most high-power generators use capacitive storage despite the fact that their energy density is much smaller.

It is obvious that pulsed-power techniques can be successful in those fields of application where they can perform much better than existing methods or where they can carry out a unique task not possible with other methods. What are the unique advantages of pulsed power? Its main characteristic is the very high peak-to-average power ratio. Therefore it can exploit threshold and nonlinear effects. For example, strong pulsed electric fields can irreversibly open the membranes of biological cells or lead to explosive electron field emission from metallic surfaces. The high peak-to-average power ratio can also suppress competing heating processes. Another set of benefits can result from the short pulse duration, which allows one to exploit the time

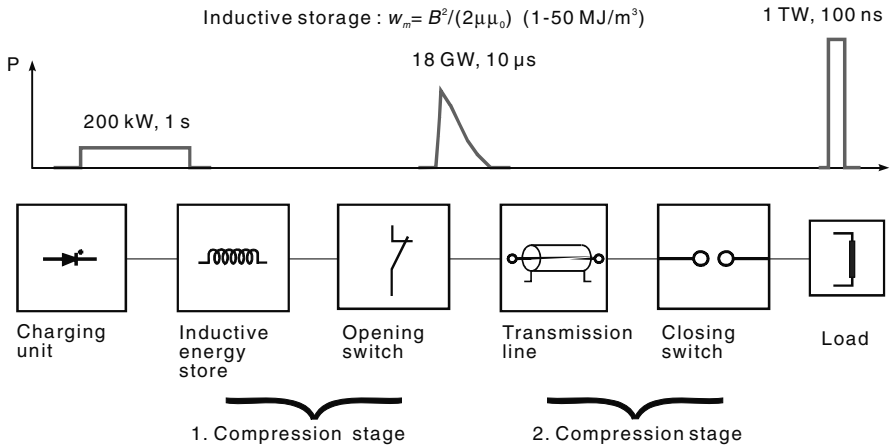


Fig. 1.4. Generator with inductive energy storage and opening switch. Only the first compression stage uses inductive storage. The later stages are capacitive and need a closing switch. As previously, we have assumed losses of about 50%

domain (e.g., in radar and flash X-ray radiography) or to avoid competing processes (e.g., electric breakdown or heat losses).

Since World War II, the development of pulsed power has mainly been driven by military requirements, both for the advancement of pulsed-power-based weapons and for the evolution of new simulation and diagnostic tools. Considerable effort has been undertaken to develop pulsed-power-based weapon systems such as electromagnetic mass launchers and beam weapons. Despite this effort, except for pulsed radar, no weaponised pulsed-power system has yet evolved. But many systems have been built for military research and development programmes to study the effects of nuclear weapons, to determine the properties of materials under extreme shock wave loading, and to create strong pulses of hard X-rays to image fast explosives.

Recent progress in the development of reliable and affordable components for pulsed-power systems such as long-lived high-voltage capacitors and new types of high-power semiconductor switches has created new interest in utilising pulsed-power techniques for commercial and industrial purposes. In contrast to some military applications, economic considerations have the strongest impact on commercialisation.

The various categories of pulsed-power applications are summarised in Table 1.1. These applications are based on either the production of strong pulsed electric or magnetic fields, the formation of intense radiation sources (electrons, ions, X-rays, etc.), or the creation of electric discharges. Some of the applications which are already successful are the defibrillator and the lithotripter in medicine, and the sterilisation of food by intense X-ray pulses. The defibrillator and the lithotripter are based on pulsed electric fields and

Table 1.1. Classification of pulsed-power applications

Pulsed-power driver		
1 GW–100 TW		
1 kJ–100 MJ		
10 kV–50 MV		
Pulsed electric and magnetic fields	Intense radiation sources (electrons, ions, X-rays, light, microwaves)	Electric (plasma) discharges

on pressure pulses produced by electric discharges, respectively. A detailed discussion of the categories of applications contained in Table 1.1 will be given in Chaps. 10–12.

The book is divided into two parts. In the first part, we present the physical and electrical foundations of pulsed-power techniques. In the second part, we describe some of the most promising emerging applications.

2 Static and Dynamic Breakdown Strength of Dielectric Materials

2.1 Introduction

Gaseous, liquid, and solid dielectric substances serve both as insulators in generator components such as capacitors, high-voltage transmission lines, and transformers and as working media in switches. The properties of these devices are predominantly determined by the electric breakdown strength and the dielectric constant of the dielectric.

The electric strength of an insulant can be defined qualitatively as the maximum field stress that the material can withstand for a given time. Quantitatively, a wide range of phenomena are involved. The factors which affect the electric strength include especially the integrated field–time action, which is related to the failure probability: $\ln[1 - F(E, t)] = -\alpha \int_0^t E^b t^a dt$. Here $F(E, t)$ represents the probability of failure after time t , if the sample is stressed with an electric field E , which may also be a function of t ; α , b , and a are constants to be determined experimentally. Other factors affecting the electric strength are the sample geometry, the pressure, the temperature, and the electrode material.

Dielectric breakdown is a statistical phenomenon. One cannot predict with certainty the time of breakdown, one may only calculate the probability of breakdown under given conditions of field and geometry. At the microscopic level breakdown requires the presence of sufficiently energetic charged particles that have acquired enough energy from the applied electric field between two energy-dissipating collisions to ionise the material and to create more charged particles. In most cases electrons dominate the breakdown process, since their mobility is much larger than that of ions.

In order for an electron to acquire enough energy between collisions, its mean free path in the material must be sufficiently large. If we neglect the differences between the ionisation energies of different materials and take into account the fact that the mean free path depends essentially on the density of the material, the electric breakdown strength should be the same for all materials that have the same density. Figure 2.1 shows a plot of the static electric breakdown strength of various materials versus density. It is obvious that the electric strength is only weakly dependent on the state of the material, but strongly dependent on the density.

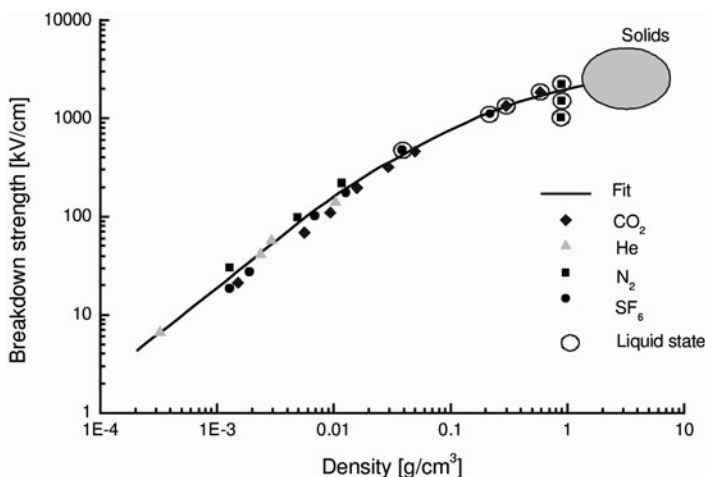


Fig. 2.1. Static insulation strength of various gases and liquids versus density [Cooke 1998]

While a gaseous or liquid dielectric is self-repairing after a breakdown, i.e., it recovers its previous electric strength, a solid dielectric material remains irreversibly destroyed. On the other hand, solid dielectrics are always necessary if mechanical forces have to be withstood. Liquids are generally preferred if large heat losses have to be removed.

Despite some similarities in the breakdown phenomena, there are also many differences, especially in the initiation and in the evolution of a discharge. Therefore it is necessary to discuss gases, liquids, and solids separately. In the following paragraphs we shall treat the breakdown strength of these materials phenomenologically, with an emphasis on the practical aspects and on formulae useful for the design of pulsed-power devices.

2.2 Gases

2.2.1 Static Breakdown

The electric strength of a gas is determined by the magnitude of its atomic and molecular reaction cross-sections for electron collisions. Of special interest are the ionisation and attachment cross-sections.

The concept of a reaction cross-section is based on the assumption that an interaction between an atomic projectile and an atom or molecule can only occur if the projectile passes through a certain area around the centre of the target atom or molecule. The cross-section can therefore be considered as the target area that must be hit in order to obtain a certain reaction (ionisation, excitation, attachment, etc.). Consequently, if we have n atoms

per unit volume in a gaseous layer of thickness dx , each with a cross-section σ , then we have $nA dx$ targets within an area of A , which mask an area $nA dx \sigma$. The probability of a particle causing an interaction in this layer is therefore $\sigma n dx = \Sigma dx$. Hence, if N particles enter the layer, the number crossing it without any collisions is reduced by $dN = -\Sigma N dx$. After traversing a layer of thickness x , only $N(x) = N_0 \exp(-\Sigma x)$ particles have not experienced any interaction. The mean free path over which a particle can move without a collision is therefore given by

$$\lambda = \int_0^{\infty} \frac{x \Sigma N(x)}{N_0} dx = \frac{1}{\Sigma}. \quad (2.1)$$

Let us now consider electrons moving in an electric field E . On average, their kinetic energy will increase by $eE\lambda = (m/2)u^2$ between two collisions. Their velocity therefore grows by $u = \sqrt{2eE\lambda/m}$. If u is much larger than the thermal velocity, a velocity distribution is established that deviates from a Maxwellian distribution. The shape of this distribution $g(u) du$ develops under the influence of the electric field E and the gas density n , which determines λ . However, because of the energy dependence of the cross-section σ , λ depends on the energy too. To determine $g(u) du$ self-consistently is therefore a complex problem, which will not be treated here (see, e.g., [Llewellyn-Jones 1957]).

Let us assume we know the equilibrium velocity distribution function $g(u) du$ of a swarm of electrons moving in a gas under the influence of a homogeneous electric field. We would like to calculate the number of ionising collisions per second leading to growth of the swarm. $\tau_i = \lambda_i/u$ is the mean time between ionising collisions for electrons with velocity u . Consequently, the rate of ionisation is $1/\tau_i = u/\lambda_i = \Sigma_i u$. Hence the total number of electrons increases by

$$\frac{dN_e}{dt} = N_e \int_0^{\infty} \Sigma_i u g(u) du. \quad (2.2)$$

If we now replace dN/dt by $\delta N/\delta t + u \delta N/\delta x$, and assume that the swarm does not spread, i.e., we set $\delta N/\delta t = 0$ and introduce a mean swarm velocity $\langle u \rangle$, we can write $dN_e = N_e \alpha dx$, where

$$\alpha = \frac{\int_0^{\infty} \Sigma_i(u) u g(u) du}{\langle u \rangle}. \quad (2.3)$$

Here, α is called the *ionisation coefficient*. With these definitions, we can calculate the growth of an electron avalanche under the influence of an electric field:

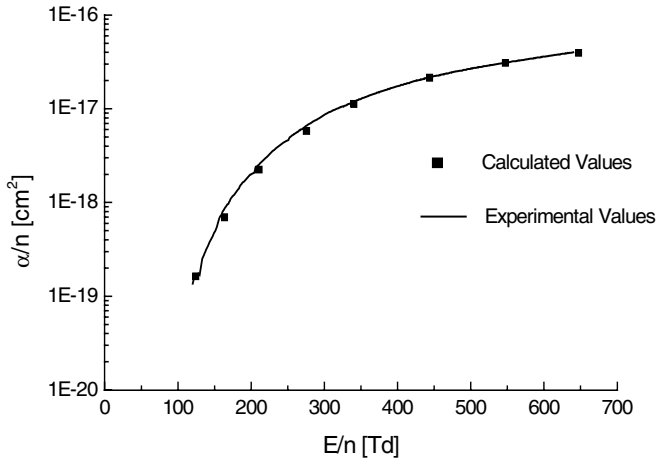


Fig. 2.2. Comparison of experimental data for α/n in nitrogen with values calculated from basic cross-section data [Meek and Craggs 1978]. Here, the old unit Townsend (Td) has been used, where $1 \text{ Td} = 10^{-17} \text{ V cm}^2$

$$N_e(x) = N_0 \exp(\alpha x). \quad (2.4)$$

It is important to realise that α/p is a unique function of E/p , where p is the gas pressure under normal conditions. This can be derived if we expand $g(u)$ into a Taylor series around $\langle u \rangle$ and take into account the fact that $\langle u \rangle$ must be proportional to the square root of the electric field E times the mean free path λ , which is inversely proportional to p . Consequently, we have

$$\frac{\alpha}{p} = F\left(\frac{E}{p}\right). \quad (2.5)$$

From the discussion, it is clear that one can calculate α/p or equivalently α/n from available cross-section data. Figure 2.2 shows a comparison of experimental data for α/n in nitrogen with calculated values.

Secondary electrons can be released from the cathode by ions that have drifted to the electrode, as well as by light quanta created by recombination and de-excitation processes. Hence there occurs a feedback from any previous avalanche to the next avalanche. If we assume that any electron that moves a distance dx in the avalanche liberates ωdx electrons from the cathode, then we can establish a balance as follows.

Let $N(x)$ be the number of swarm electrons at the position x . In travelling a distance dx , they increase their number through ionising collisions by $dN = N(x)\alpha dx$. Altogether, $N(d) = N(0)\exp(\alpha d)$ electrons reach the anode if $N(0)$ left the cathode and d is the distance between cathode and anode. In a stationary situation, each electron has released ωdx secondary electrons while travelling a distance dx . The total number of electrons leaving the cathode is therefore

$$N(0) = N_0 + \omega \int_0^d N(x) dx, \quad (2.6a)$$

$$N(0) = N_0 + \frac{\omega}{\alpha} N(0) (e^{\alpha d} - 1). \quad (2.6b)$$

Solving for $N(0)$ and replacing the result into the equation for $N(d)$, we finally obtain

$$N(d) = \frac{N_0 e^{\alpha d}}{1 - (\omega/\alpha) (e^{\alpha d} - 1)}, \quad (2.7)$$

where N_0 is the number of electrons released from the cathode by external processes. We can see that the avalanche grows without limit if the condition $\gamma (e^{\alpha d} - 1) = 1$ is fulfilled ($\gamma = \omega/\alpha$). This is called the *Townsend condition* for ignition. In this case, the insulation of the cathode–anode gap breaks down and a self-sustained discharge is created.

Since α/p is a unique function of E/p , and if one assumes further that ω/p is also a function of E/p (which has been experimentally confirmed), then the Townsend condition represents a functional relationship between the electrode separation d and the voltage at which breakdown occurs. Letting $\alpha/p = f(E/p)$ and $\omega/p = F(E/p)$, the Townsend condition can be rewritten as

$$\frac{F(E/p)}{f(E/p)} \left(e^{f(E/p)pd} - 1 \right) = 1. \quad (2.8)$$

Since $E = U/d$, (2.8) can, after solving for U , be expressed as

$$U_b = \Pi(pd), \quad (2.9)$$

which means that the breakdown voltage U_b of a uniform-field gap is a unique function Π of the product of the pressure and the electrode separation for a given gas and electrode material. This relationship is called the *Paschen law* [Paschen 1889].

In certain regimes, the functional relationship between α/p and E/p can be approximated by

$$\frac{\alpha}{p} = A e^{-Bp/E}, \quad (2.10)$$

where A and B are constants for a given gas. Introducing this relationship into (2.8) and using the experimentally observed fact that γ is a slowly varying function of E/p over a wide range, and after solving for U_b , (2.9) becomes

$$U_b = \frac{Bpd}{\ln[Apd/\ln(1 + 1/\gamma)]}. \quad (2.11)$$

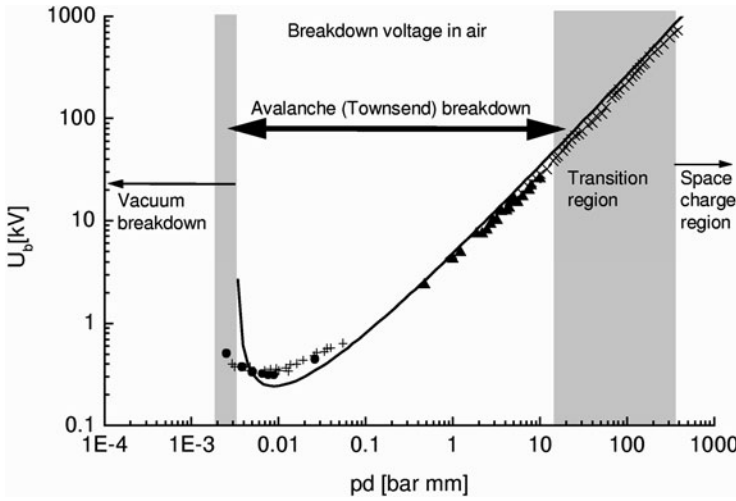


Fig. 2.3. Measured and calculated Paschen curves for atmospheric air

Table 2.1. Experimentally determined values of the gas constants A and B

Gas	A (1/(mm bar))	B (kV/(mm bar))	Range of E/p for validity (kV/(mm bar))
Air	1130	27.4	11–45
N ₂	977	25.5	8–45
H ₂	376	9.8	11–30
He	210	2.6	2–11
Ar	1020	13.5	8–45
CO ₂	1500	34.9	37–75

From this equation, it can be seen that at large and small values of pd , the breakdown voltage U_b increases. Consequently, U_b must go through a minimum, which is called the Paschen minimum. Calculation of this minimum breakdown voltage from (2.11) gives

$$U_{b \min} = e \ln \left(1 + \frac{1}{\gamma} \right) \frac{B}{A}. \tag{2.12}$$

Similarly, the minimum value of pd is found to be

$$pd_{b \min} = e \frac{\ln(1 + 1/\gamma)}{A}. \tag{2.13}$$

With a voltage lower than $U_{b \min}$, it is impossible to cause the breakdown of a gap with a uniform field distribution, no matter what the pressure or spacing. Figure 2.3 shows the measured Paschen curve for atmospheric air, in

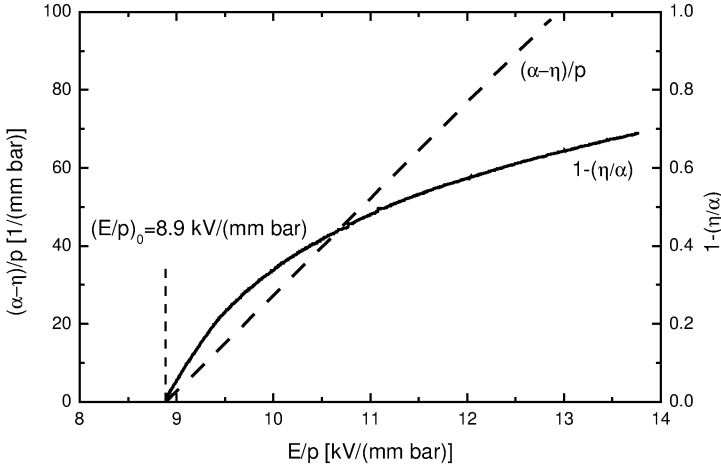


Fig. 2.4. Effective ionisation coefficient $(\alpha - \eta)/p$ and weight function $1 - (\eta/\alpha)$ describing the probability that an electron creates further avalanche electrons, for SF_6

comparison with a theoretical curve derived from (2.11) using the parameters listed in Table 2.1.

Theoretically, U_b should go to infinity at a certain value of pd , because it becomes impossible to create electron avalanches below this value. In practice, this does not happen, because at very high field strengths field emission of electrons from the electrodes occurs.

The most commonly used high-strength gas is SF_6 . SF_6 belongs to a group of *electronegative gases*, which are characterised by the ability to attach electrons to the molecule, which then becomes a negative ion. To describe the breakdown properties of these gases, we must consider the attachment coefficient η . η defines the attachment probability of an electron per unit path length. Similarly to α/p , η/p is a unique function of E/p . In addition to SF_6 , some other compounds containing halogens (Cl, F, I, etc.) are electronegative gases, and so is O_2 . The effective ionisation coefficient α_e is defined as the difference between α and η :

$$\alpha_e = \alpha - \eta = pf \left(\frac{E}{p} \right). \quad (2.14)$$

Electron avalanche formation becomes possible only if α_e is greater than 0. For SF_6 , this is the case if E/p is greater than 8.84 kV/(mm bar). $(\alpha - \eta)/p$ can be expressed as a linear function of E/p (see Fig. 2.4):

$$\frac{(\alpha - \eta)}{p} = k \left[\frac{E}{p} - \left(\frac{E}{p} \right)_0 \right]. \quad (2.15)$$

For SF_6 , $k = 27.7$ kV and $(E/p)_0 = 8.84$ kV/(mm bar). Using these parameters and the linear relationship (2.15) to determine the static breakdown

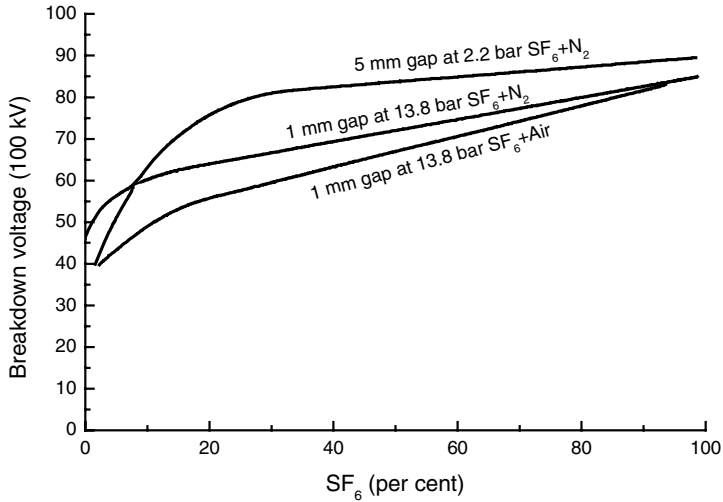


Fig. 2.5. Dependence of breakdown voltage on the SF₆ content for mixtures of SF₆ with air or nitrogen

Table 2.2. Relative electric strengths of gases

Air	1
Nitrogen	1
SF ₆	2.5
C ₅ F ₈	5.5
Hydrogen	0.5

voltage U_b for a uniform field, we obtain

$$U_b = pd8.84[\text{kV}/(\text{mm bar})] + 0.5 \text{ kV}. \quad (2.16)$$

A characteristic of SF₆ is that it maintains a high electric strength even if it is diluted with another gas (see Fig. 2.5). Vapours of higher strength than SF₆ are known, but most of them liquefy at atmospheric pressure and room temperature. Table 2.2 compares the relative electric strengths of various gases.

Another useful approximate relation for the breakdown voltage can be derived if a quadratic ansatz is used for the specific ionisation coefficient, which is especially valid for gases that are not electronegative or are only weakly so:

$$\frac{\alpha_e}{p} \sim \left[\frac{E}{p} - \left(\frac{E}{p} \right)_0 \right]^2. \quad (2.17)$$

Using this relationship and solving for U_b , we obtain

Table 2.3. Constants to be used in (2.18)

Gas	$(E/p)_0$ (kV/(bar mm))	c (kV/(bar mm) ^{1/2})
CO ₂	3.21	5.88
Air	2.44	2.12
N ₂	2.44	4.85
H ₂	1.01	2.42

Table 2.4. Field enhancement factors for various electrode geometries^a

Configuration	
Concentric cylinders	$\delta = (R/r - 1)/\ln(R/r)$
Equal spheres	$\delta \approx X/2r$ for $X/r \gg 1$; $X = d - 2r$
Equal parallel cylinders	$\delta \approx X/(2r \ln(X/r))$ for $X/r \gg 1$; $X = d - 2r$

^a δ , maximum stress/mean stress; R , r , radii; d , distance between centres.

$$U_b = \left(\frac{E}{p}\right)_0 pd + c(pd)^{1/2}. \quad (2.18)$$

Equation (2.18) is valid only for larger values of pd . Table 2.3 lists the constants to be used with (2.18) for various gases.

The mean breakdown strength can change considerably if a gap is bounded by spherical or cylindrical electrodes. This is especially true if the distance d between the electrodes is not small compared with their radii R , i.e., $d > R$. This effect is taken into account by introducing a field enhancement factor δ into the formula (2.18):

$$U_b = \frac{(E/p)_0 pd + c(pd)^{1/2}}{\delta}, \quad (2.19)$$

where δ is defined as the ratio between the maximum and the mean stress in the gap. Table 2.4 contains formulae for δ for various geometric configurations.

For *very inhomogeneous* field configurations (needle geometries), (2.18) can still be used if, instead of d an effective electrode distance d_{eff} is used. In such a geometry, the avalanche moves into an ever lower field. Consideration of the effective ionisation coefficient suggests that if the field falls to about 80% of the field at the electrode within the 20th-generation distance, the avalanche dies out (see the discussion about streamer breakdown below). Therefore, d_{eff} has been defined as the distance where the field has dropped to about 80% of its maximum value. For spherical and cylindrical electrodes, $d_{\text{eff}} = 0.115r$ and $0.23r$, respectively, where r is the radius of curvature.

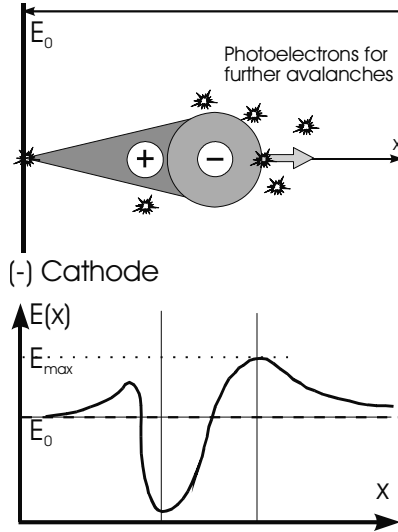


Fig. 2.6. Effect of space charge produced by an avalanche on the electric field in a gap. Ions are rather immobile and form a dipole field together with the electrons removed from the ions. This field will enhance the initially applied electric field E_0 at the avalanche head

2.2.1.1 Space Charge Effects

So far, we have neglected the space charge that is created in the electron avalanche. This is no longer justified if the avalanche has increased to 10^6 to 10^8 particles in a gas at atmospheric pressure. The relatively immobile ions stay behind in the avalanche tail, and the mobile electrons form the spherical avalanche head. We can easily estimate the electric field created by an avalanche containing N charged particles. Since the charge density grows by a factor of e over a distance $1/\alpha$, we may write

$$E_{SC} = \frac{eN}{4\pi\epsilon_0(1/\alpha)^2} = 1.5 \times 10^{-7} \frac{N}{(1/\alpha)^2} \text{ V/cm} . \quad (2.20)$$

For $N = 10^7$ and $\alpha^{-1} = 10^{-2}$ cm, we obtain $E_{SC} = 15 \text{ kV/cm}$, which can be a large fraction of the applied field.

Qualitatively, the field varies around the avalanche as shown in Fig. 2.6. Compared with the applied field, the field behind and ahead of the avalanche is increased by the space charge and reduced between the electron and ion clouds. According to Raether [Raether 1964], UV light emitted in recombination and de-excitation events creates electrons by photoionisation ahead of and behind the avalanche, initiating further avalanches, which finally form a conducting bridge between the anode and cathode. Because of the higher

fields at the ends of the avalanche, electrons created there can cause ionisation more efficiently. This kind of discharge development is called the streamer mechanism. A streamer need not necessarily start at the cathode. If the critical charge density is reached in the volume of the discharge gap, streamers start to grow towards both the anode and the cathode. Creating photoelectrons at larger distances from the main streamer can advance the growth of the breakdown channel rapidly. At atmospheric pressure, velocities as high as 100–1000 cm/ μ s have been observed. Raether determined the critical stage of the avalanche from experimental observations in a cloud chamber. He observed that streamers developed when $\alpha x_{cr} \sim 20$, where x_{cr} is the average position of the cloud when it becomes critical. Using this value, we can calculate the critical number of electrons in the avalanche at atmospheric pressure:

$$N_{cr} = e^{\alpha x_{cr}} = 10^8. \quad (2.21)$$

This number has been confirmed by Monte Carlo simulations [Kunhardt and Tzeng 1988]. The corresponding charge carrier density is $\sim 10^{14}$ cm $^{-3}$. It is not surprising that at this density, space charge (Debye) shielding begins to occur in the streamer channel.

2.2.2 Pulsed Breakdown

So far, we have considered the static breakdown voltage only, i.e., we have assumed that the voltage across the gap rose slowly, such that delays in the formation of a breakdown channel were unimportant.

However, if we apply a fast-rising pulse across the gap, we must take into account the fact that it takes a finite time before breakdown can occur. In detail, we can distinguish the following time lags in the formation of a gas breakdown channel, as illustrated in Fig. 2.7: t_0 is the time until the static breakdown voltage U_b is exceeded (U_b is considered as the reference voltage), t_s is the statistical delay time until an electron able to create an avalanche occurs,

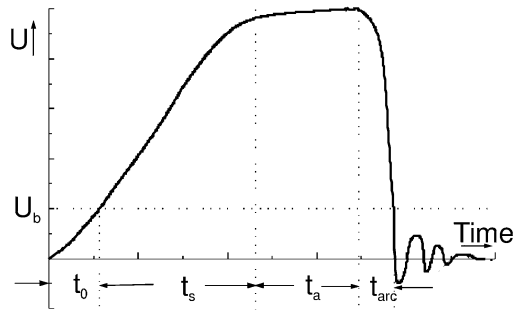


Fig. 2.7. Delay and build-up times determining the dynamics of breakdown in a gas-insulated gap

Table 2.5. Mobility of SF₆ ions in Ar/SF₆ mixtures

	2% SF ₆ in Ar	5% SF ₆ in Ar	10% SF ₆ in Ar
μ_{mix} (1 bar)	2.2 cm ² V ⁻¹ s ⁻¹	2.0 cm ² V ⁻¹ s ⁻¹	1.71 cm ² V ⁻¹ s ⁻¹
μ_{mix} (2 bar)	1.2 cm ² V ⁻¹ s ⁻¹	1.08 cm ² V ⁻¹ s ⁻¹	0.92 cm ² V ⁻¹ s ⁻¹

t_a is the avalanche build-up time until the critical charge density is reached, and t_{arc} is the time required to establish a low-resistance arc across the gap.

The *statistical delay time* t_s results from the statistics of electron appearance in the gap. Free electrons can be created by illuminating the gap volume or the cathode surface with electromagnetic radiation. In particular, UV light, X-rays and γ -radiation from radioactive sources are very effective in ionising gas atoms and in inducing photoemission. The electrons that initiate the self-breakdown of a gap can result from various sources.

Natural radioactivity and cosmic radiation produce between 0.1 and 10 free electrons per cm³ per second in a gas at atmospheric pressure, depending on the geographical location and other local conditions. These electrons can attach to the gas molecules and create a stationary concentration of a few thousand negative molecular ions per cm³ within a few minutes in a stored electronegative gas. In SF₆, a concentration of 2500 SF₆⁻ ions per cm³ has been measured after 5 minutes [Kindersberger 1986]. When such a gas is exposed to an electric field, the attached electrons can be liberated through collisional neutralisation and contribute to the rate of free-electron generation. The rate of electron detachment per volume element \dot{n}_δ depends on the density of negative ions n_n present in the gas volume, the ion drift velocity u_n , and the coefficient of collisional electron detachment δ :

$$\begin{aligned}\dot{n}_\delta(t) &= \delta n_n u_n, \\ u_n &= \mu_{\text{mix}} E.\end{aligned}\tag{2.22}$$

The mobility μ_{mix} depends on both the kind of ion and the gas composition. Mobility values for SF₆ ions in various mixtures of argon and SF₆ are given in Table 2.5. The dependence of δ/n on the reduced electric field for SF₆ ions in SF₆ is shown in Fig. 2.8.

At electric fields above a few times 100 kV/cm, an increasing number of electrons can leave the metal surface through the tunnel effect. The current density of these field-emitted electrons can be described by the Fowler–Nordheim equation [Fowler and Nordheim 1928]:

$$\begin{aligned}j &= \frac{1.54 \times 10^{-6} \beta^2 E^2}{\phi} \exp \left\{ -\frac{6.83 \times 10^{-7} \phi^{3/2} \theta(y)}{\beta E} \right\}, \\ \theta(y) &= 0.956 - 1.06y^2, \\ y &= 3.8 \times 10^{-4} \frac{\sqrt{\beta E}}{\phi}.\end{aligned}\tag{2.23}$$

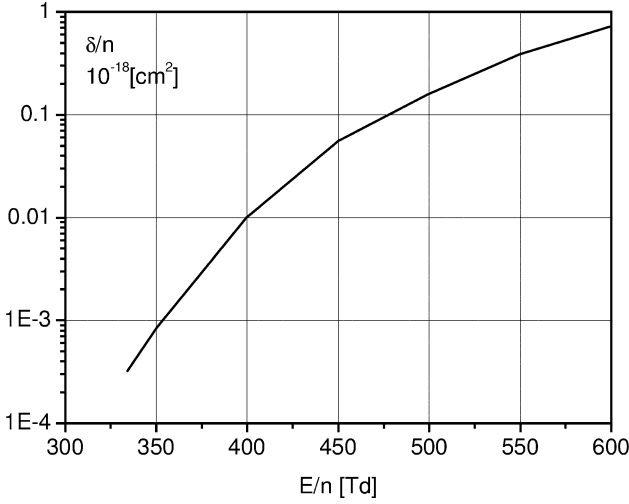


Fig. 2.8. Detachment coefficient d/n for SF_6 ions in SF_6 [Hilmert and Schmidt 1991]

Here, the current density j is obtained in A/cm^2 if the electric field E is given in V/cm and the work function ϕ in eV . β is an enhancement factor that takes into account the special conditions at localised emission centres on the metallic surface. The most important emission centres are dielectric inclusions, metallic microprotrusions (called whiskers), and adsorbed gases [Korolev and Mesyats 1999]. For dielectric inclusions and whiskers, the electric-field dependence of the emission can be described by the Fowler–Nordheim equation (2.23). The importance of field enhancement at the emission sites becomes obvious if one calculates the number of electrons per second using (2.23). To generate 10^6 electrons per second from a flat metallic surface of area 1 cm^2 , an electric field of $1.2 \times 10^7 \text{ V}/\text{cm}$ is required. However, for a localised emission site possessing a field enhancement of $\beta = 100$, the same number of electrons is obtained from an area of 10^{-12} cm^2 at a field of only $2.4 \times 10^5 \text{ V}/\text{cm}$.

In summary, the total number of electrons appearing in the gap is the sum of three source terms:

$$\dot{N}(t) = \dot{N}_{0n} + \dot{N}_F(t) + \dot{N}_\delta(t). \quad (2.24)$$

Only the first term which represents the number of naturally occurring electrons in the gap is independent of time. $\dot{N}_F(t)$, which describes the rate of field-emitted electrons, is obtained by integrating j/e (2.23) over the cathode surface. $\dot{N}_\delta(t)$, the rate of electron detachment, is obtained by integrating (2.22) over the gap volume.

Not every electron released into the gap is able to initiate an avalanche even if the voltage is above the static breakdown value. This is especially

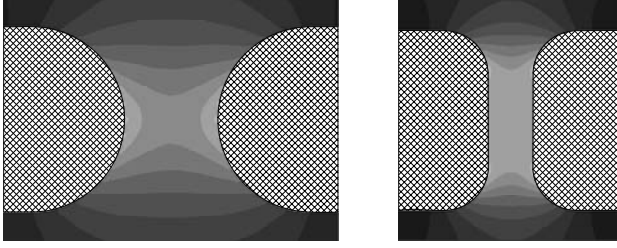


Fig. 2.9. Distribution of equipfield surfaces between two different electrode configurations. The greyscale steps represent 10% changes in the field strength

true for electronegative gases. Avalanches can grow only in those parts of the gap volume where the local field strength exceeds a certain critical value. For electronegative gases, the critical field strength E_{crit} is that field at which the ionisation coefficient α becomes larger than the electron capture coefficient η (see Fig. 2.4).

The probability for a single electron to initiate an avalanche is given by the local value of $1 - \eta/\alpha$ [Legler 1961]; $g(E/p) = 1 - \eta/\alpha$ can be used as a weight function for each electron released into the gap.

To determine the production rate of avalanche-effective electrons, we must therefore multiply each surface or volume element where an electron has been created by $g(E(t, x, y, z)/p)$.

$$\begin{aligned} \frac{dN_a}{dt} = & \int_F g\left(\frac{E(t, x, y, z)}{p}\right) \frac{j(E(t, x, y, z))}{e} dA \\ & + \int_V g\left(\frac{E(t, x, y, z)}{p}\right) [\delta(E(t, x, y, z)) n_n \nu_n(E(t, x, y, z)) + \dot{n}_0] dV, \end{aligned} \quad (2.25)$$

where \dot{n}_0 is the rate of naturally produced electrons per volume element. Figure 2.9 shows equipfield surfaces corresponding to contour plots of the weight function $g(E(t, x, y, z)/p)$ for two specific electrode configurations.

We can identify dN_a with the probability $\beta(t) dt$ that a breakdown occurs in the time interval $t, t + dt$ assuming that it did not occur up to time t . Using this definition, we obtain from the theory of conditional probability [Papoulis 1965]

$$F(t) = 1 - e^{-\int_0^t dN_a/dt dt}. \quad (2.26)$$

Here $F(t)$ is the probability that a breakdown has occurred before time t . The corresponding probability density $f(t)$ is given by

$$f(t) = \frac{dN_a}{dt} e^{-\int_0^t dN_a/dt dt}. \quad (2.27)$$

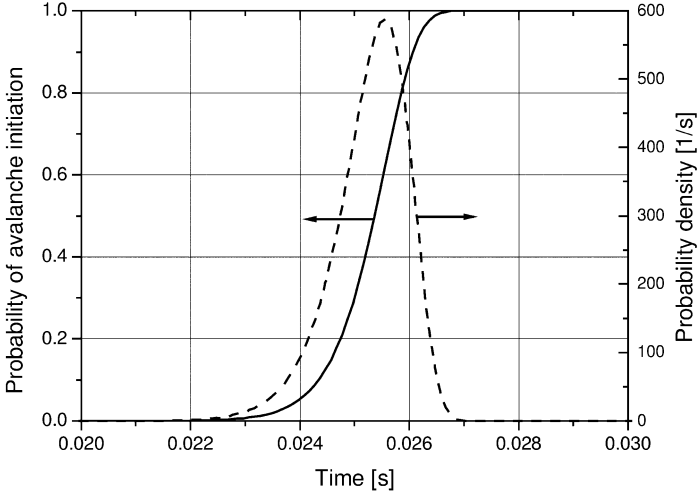


Fig. 2.10. Probability of avalanche initiation and the corresponding probability density in a 1 cm gap insulated with dry nitrogen. The voltage across the homogeneous gap rises at a rate of 6 MV/s

As an example, we shall consider the time distribution for the initiation of self-breakdown in a 1 cm gap filled with 1 bar of dry nitrogen and possessing a homogeneous field distribution. Using (2.17), we calculate a static breakdown voltage of 31 kV. We assume that the gap is ramped at 6 MV/s. We assume that the negative electrode is covered with 100 emission sites of area 10^{-10} cm², each with an enhancement factor of 100. We want to calculate the probability $F(t)$ for breakdown, and the probability density $f(t)$ as a function of time, assuming that only field emission contributes to the production of electrons in the gap. Evaluating (2.23) and (2.25)–(2.27), we obtain the results shown in Fig. 2.10. It takes only 5.2 ms to reach the static breakdown voltage, but the mean time to initiate an avalanche is 25.4 ms. At that time, the field strength in the gap has reached 152 kV/cm.

After the first electron avalanche has been formed, breakdown can develop in two different ways. During *Townsend breakdown*, several generations of successive avalanches can develop until a quasi-stable glow discharge or a glow-to-spark transition occurs. In the *streamer* mechanism of breakdown, a single avalanche is strong enough to create the critical number of electrons before the anode is reached. Electrons escaping from the avalanche head create a field distortion, which finally drives the self-propagation of the avalanche. In general, the *build-up times* t_a for these two cases will be very different.

For Townsend breakdown, we define the build-up time as the time that elapses until, in a certain generation, a critical number of avalanches appears in the gap. Since the Townsend mechanism inherently assumes that secondary

electrons are released from the cathode through interaction with photons and ions, we can expect that successive avalanche generations will start from quite different positions on the cathode surface and thus distribute the discharge over rather a large volume. Assuming that the electric field in the gap is not distorted by space charge and that the probability of ionisation depends only on the local electric field, Legler has calculated the distribution of build-up times for this case [Legler 1955]. He obtained the following for the mean build-up time of an avalanche starting with a single electron from the cathode:

$$\bar{t}_a = \bar{k} \frac{d}{\mu_e E} = \frac{\ln(e^C N_{\text{crit}}(\mu - 1))}{\ln \mu} \frac{d}{\mu_e E}. \quad (2.28)$$

Here we have assumed a homogeneous gap with a distance d between the electrodes; \bar{k} is the mean number of avalanche generations until the critical number N_{crit} is reached; C is the Eulerian constant, equal to 0.577; $\mu = \gamma(e^{\alpha d} - 1)$ is the feedback factor, describing the number of electrons released per avalanche from the cathode; μ_e is the electron mobility; and E is the electric field.

Owing to the build-up of positive-ion space charge near the anode, field enhancement occurs outside the space charge cloud and an ionisation wave propagates towards the cathode and back from the cathode towards the anode, until a stable glow discharge is established [Doran 1968].

For streamer breakdown, the overvoltage must be sufficiently large that the critical electron number N_{crit} is established in the gap during a single avalanche. This is the case if the overvoltage is about 15–20% above the static breakdown level. It has been said previously that about 10^8 electrons must be created in an avalanche propagating in a gas at atmospheric pressure before the streamer condition is reached, i.e., $\alpha x_{\text{cr}} \sim 18$. If the average electron drift velocity u_{drift} is known, we can calculate t_a from the relation $t_a = x_{\text{cr}}/u_{\text{drift}} = 18/(\alpha u_{\text{drift}})$. However, since the electron drift velocity depends on the electric field strength, this is difficult to evaluate, especially for a non-homogeneous field geometry.

For technological purposes, the *area-time relationship* is sometimes useful. This needs only a geometrical factor and the shape of the voltage pulse to determine t_a . However, it can be applied only if the statistical delay time t_s is very short compared with the build-up time. There is no strong derivation of this relationship, but some plausibility considerations have been given [Kind 1958]. The avalanche growth velocity $u(x, t)$ depends on the gap geometry and on the voltage above a reference voltage U_0 , which is close to the static breakdown voltage, i.e., on $U(t) - U_0$. We assume that this dependence can be described by a separation of variables:

$$u(x, t) = K(x) [U(t) - U_0] = \frac{dx}{dt}.$$

$K(x)$ is determined by the gap geometry only. Integration yields

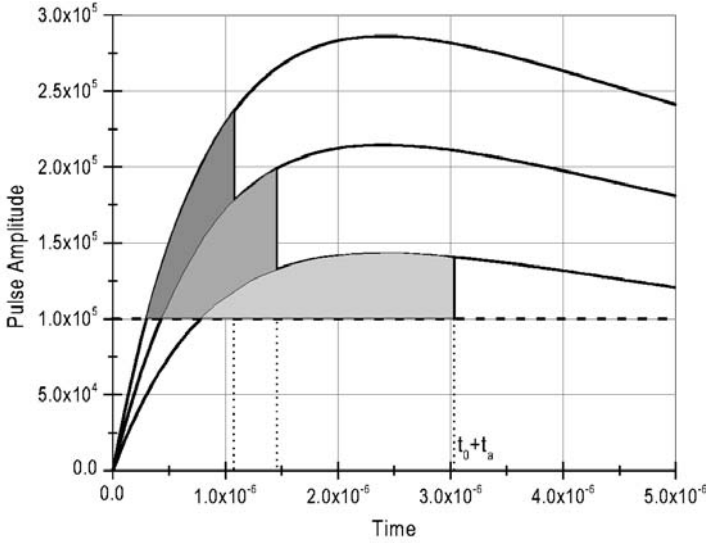


Fig. 2.11. Representation of different pulse shapes to illustrate the area–time relationship. The duration of the avalanche build-up time is determined by the requirement that $F_1 = F_2 = F_3$

$$\int_0^d \frac{dx}{K(x)} = \int_{t_0+t_s}^{t_0+t_s+t_a} [U(t) - U_0] dt = F. \quad (2.29)$$

The physical content of this relationship is that for a given gap geometry, only the time integral of the voltage above U_0 determines the avalanche build-up time, i.e., if F has been determined for one pulse shape, it can be used to calculate t_a for any other pulse shape. This is illustrated in Fig. 2.11.

2.2.3 Spark Formation

A conducting channel exists between the anode and the cathode after a streamer has bridged the high-voltage gap. Depending on the impedance of the high-voltage source, an intense current starts to heat the channel and to ionise it further until a low-resistance channel is established. To describe the transition from a streamer channel to a low-resistance arc channel, several models have been proposed in the literature. The most widely used is the spark law empirically obtained by Toepler [Toepler 1924, 1927]. A physical substantiation has been given by Pfeiffer [Pfeiffer 1971]. Following his argument, we assume that a weakly conducting column exists and that its conductivity is increased by collisional ionisation:

$$dn_e = n_e \alpha dx. \quad (2.30)$$

Substituting dx by $u_e dt$ and setting $u_e = \mu_e E$, we obtain

$$dn_e = n_e \alpha \mu_e E dt. \quad (2.31)$$

Taking into account the fact that the mean current density can be written as $j = n_e \mu_e e E$ and integrating over the time t since channel formation, we obtain the following for the mean electron density $n_e(t)$:

$$n_e(t) = \frac{\alpha}{e} \int_0^t j dt. \quad (2.32)$$

Here u_e is the electron drift velocity, μ_e is the electron mobility, and E is the mean electric field in the spark channel.

Assuming a homogeneous current density distribution in the column we can express the spark resistance as

$$R_f(t) = \frac{U}{I} = \frac{Es}{n_e(t) \mu_e e E \pi r_f^2} = \frac{s}{\alpha \mu_e \int_0^t I dt}, \quad (2.33)$$

where s is the channel length and r_f is the radius of the spark channel.

Toepler's spark law says that the resistance is inversely proportional to the charge that has been flowing through the channel. Since the column is heated by the current flow, it expands. This was not considered in the derivation of Toepler's law. Therefore this law is valid only for a limited time after channel formation, typically for 10 ns in a gas at atmospheric pressure.

The spark law derived by Weizel and Rompe [Rompe and Weizel 1944, Weizel and Rompe 1947] is based on similar assumptions. In particular, these authors also neglected channel expansion. Consequently, they arrived at a similar expression:

$$R_f(t) = \frac{s}{\sqrt{2 \frac{a}{p} \int_0^t I^2 dt}}. \quad (2.34)$$

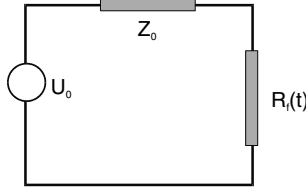
Here a is a constant and p is the gas pressure.

A different approach was followed by Braginskii [Braginskii 1958]. He allowed for the thermal expansion of the plasma channel, but assumed a specific conductivity for the channel plasma that was independent of time. The resulting spark law is given by (2.35):

$$R_f(t) = \frac{s}{\pi \sigma b^2 \int_0^t I^{2/3} dt}. \quad (2.35)$$

Table 2.6. Spark constants for various gases [Pfeiffer 1971]

Gas	$k_T = 1/\alpha\mu_e$ (10^{-4} V s/cm)	a (atm cm ² /V ² s)	σb^2 (10^4 A ^{1/3} cm/V s)
Air	0.5–0.6		
N ₂	0.4	1.1	3.5
CO ₂	0.5	1.0	3
Argon	0.085	25	10

**Fig. 2.12.** Model of a spark discharge circuit

Here b is a constant depending on the density, the conductivity and the thermodynamic properties of the plasma, and σ is the mean plasma conductivity in the channel. In Table 2.6, we summarise various constants for the spark laws.

Using Toepler's relationship, we shall now derive an equation for the spark current, and the characteristic times determining the current increase and the voltage decrease across the spark. For this purpose, let us consider the simple circuit sketched in Fig. 2.12.

In this model, we have neglected the inductance of the spark and the shunt capacitance. U_0 is the ignition voltage and Z_0 is the impedance of the driving source. The maximum current flowing in the circuit is

$$I_{\max} = \frac{U_0}{Z_0 + R_f} \approx \frac{U_0}{Z_0}. \quad (2.36)$$

Neglecting R_f is justified here, since generally $Z_0 \gg R_f$. With $y = I/I_{\max}$ and assuming Toepler's relation, we obtain the following for the circuit in Fig. 2.12:

$$\begin{aligned} dt &= \frac{k}{E_0} \frac{dy}{y(1-y)^2}, \\ t &= \frac{k}{E_0} \left(\ln \frac{y}{1-y} + \frac{1}{1-y} + C \right). \end{aligned} \quad (2.37)$$

The constant C is determined by assuming that the spark current begins with $y = I/I_{\max} = 10^{-3}$. In this case $C = 5.906$. In Fig. 2.13, I/I_{\max} has been plotted as a function of time for a spark in N₂ initiated at $E_0 = 10^5$ V/cm.

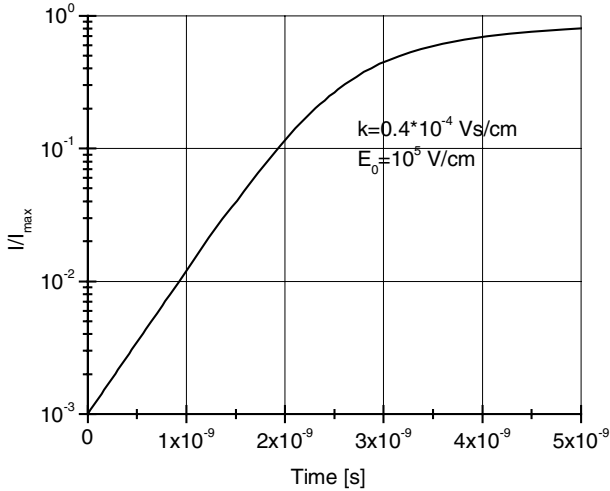


Fig. 2.13. Spark current as a function of time, relative to the maximum possible current, for the circuit of Fig. 2.12

Using (2.37), we can calculate the 0.1 to 0.9 rise time of the current, $\tau_{0.1-0.9} = 13.2 k/E_0$, and the e-folding time, $\tau_r = 6.84 k/E_0$.

Other relationships have been derived for τ_r in the literature. A widely used formula, empirically derived by J.C. Martin [Martin et al. 1996] from a number of experiments and supported by calculations, is the following relationship:

$$\tau_r = \frac{88}{Z_0^{1/3} E_0^{4/3}} \sqrt{\frac{\rho}{\rho_0}} \quad (\text{ns}), \quad (2.38)$$

where Z_0 is the impedance driving the channel, in ohms; E_0 is the field at the beginning of breakdown, in units of 10 kV/cm; ρ is the density of the gas; and ρ_0 is the density of air under normal conditions.

In this subsection we have shown that the breakdown of a gas gap is dependent upon the time history of the voltage across the gap when it exceeds the static breakdown voltage. If a pulse is sufficiently short, it may well happen that a breakdown does not occur even though the voltage has surpassed the breakdown value for a short time. This may happen if the streamer build-up time and the time for the formation of a conducting channel between the electrodes are larger than the pulse duration. J.C. Martin [Martin et al. 1996] therefore investigated the mean breakdown field for a point-plane geometry with a voltage ramp generator and fitted the results to the following expression:

$$E_{\text{bm}}^{\pm} t_{\text{eff}}^{1/6} d^{1/6} = K^{\pm} \left(\frac{p}{p_0} \right)^n, \quad (2.39)$$

Table 2.7. Empirical gas breakdown parameters for point–plane electrodes

Parameter	Air	Freon	SF ₆
K^+	22	36	44
K^-	22	60	72
n	0.6	0.4	0.4

where the + or – sign denotes the polarity of the point electrode, d is the gap spacing in centimetres, K and n are fitting constants, given in Table 2.7, t_{eff} is the equivalent time to breakdown (in microseconds) if the pulse is a square wave with a duration of t_{eff} , and p/p_0 is the ratio of the pressure of the gas in the gap to atmospheric pressure. E_{bm} is in kV/cm. The range of validity of this formula is $10^5 \text{ Pa} < p < 5 \times 10^5 \text{ Pa}$.

2.3 Liquids

2.3.1 Basic Electrical Processes

Even today, there is no comprehensive theory of breakdown in liquids. However, the basic processes of breakdown initiation can be divided into two categories, those associated with the bulk liquid and those occurring at the electrodes. In our discussion, we largely follow the work of Lewis presented in a series of fundamental papers [Lewis 1985, 1987, 1993, 1994a, b, c, 1996, 1998].

2.3.1.1 Processes in the Bulk

Charge in the bulk liquid can arise from molecular dissociation or from injection at an electrode. Dissociation does not lead to a net charge in the liquid. However, electron transfer through the electrodes leads to either an excess or a deficiency of electrons in the bulk. Charge transport occurs through molecular electronic states or through collective states of clusters of short-range order appearing in the liquid.

The electronic states of a liquid develop from those of individual molecules. A gas molecule can have two characteristic charge states: a positive ion, where the molecule has lost an electron, and a negative ion, in which an electron has been attached to the molecule. The electronic state of the positive ion has an energy $W_+(0)$, corresponding to the ionisation potential, and the negative ion has an energy $W_-(0)$, corresponding to the detachment potential. In the liquid, these ionised states are modified by the collective polarisation response of the surrounding molecules, and the energy levels corresponding to the fully polarised states shift to $W_+(\infty)$ and $W_-(\infty)$, respectively (Fig. 2.14). The energy associated with this response, $W(0) - W(\infty)$, consists of two parts: one component related to the polarisability of the molecular orbitals, and another

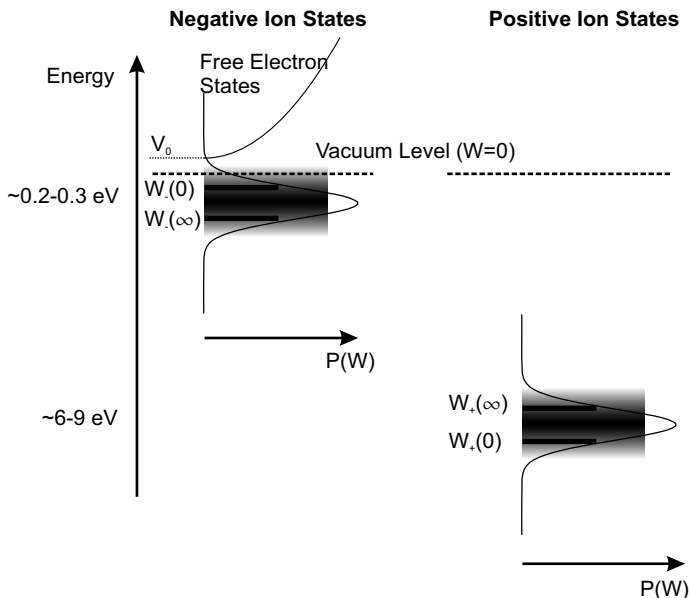


Fig. 2.14. Electronic energy states for positive and negative ions in a liquid. $W_-(\infty)$ and $W_+(\infty)$ correspond to fully localised states due to complete collective polarisation. The energy levels are broadened into Gaussian distributions $P(W)$ by thermal agitation. Electrons with energies greater than V_0 can be considered as quasi-free

component representing the collective dielectric response of the more remote molecules. When the state of an ion changes by gain or loss of an electron, molecular reorganisation occurs on a much slower timescale than that needed to relocate the electron. Because of thermal agitation, each electron level will be replaced by a Gaussian distribution of levels centred on it. This is also true for all states between $W_-(0)$ and $W_-(\infty)$ corresponding to various degrees of polarisation. Thus we obtain two broadened bands of Gaussian shape related to the two kinds of ions and the electron and hole transport in the bulk liquid can be described by a band model similar to that for amorphous solids. Impurities such as oxygen can trap electrons in states much below $W_-(\infty)$.

(Excess) charge carriers can stay in localised, quasi-localised and quasi-free mobile states in the conduction band. Quasi-free states can exist above $W_-(0)$ for electrons and below $W_+(0)$ for holes. Carriers can be considered free if they move through a sequence of states in the bands without staying long enough to induce the full electronic polarisation. The energy state of a free excess electron depends on a superposition of attractive and repulsive forces from the surrounding molecules. In the quasi-free state, these forces compensate each other. In general, the electron energy V_0 at which this happens lies above the vacuum level. In the case of n-hexane, this energy is about 0.1 eV.

The quasi-localised states lie around $W_-(\infty)$ and $W_+(\infty)$ in the band gap between $W_-(0)$ and $W_+(0)$. These states correspond to different charge carrier mobilities. Electrons and holes which have become fully localised drift as ions with their accompanying polarisation shells (polarons), with mobilities less than $10^{-5} \text{ m}^2 \text{ V}^{-1} \text{ s}^{-1}$. By means of thermal fluctuations, incident radiation or a high electric field, an electron or hole can be released from the polarisation shell and become quasi-free. In this state, the mobility becomes greater than $10^{-3} \text{ m}^2 \text{ V}^{-1} \text{ s}^{-1}$. In the region between, an electron can be considered as being in a quasi-localised state which is characterised by strong variations of the local potential in the unperturbed liquid. In a molecular cluster existing in the liquid, the electrons move in a periodic potential. Under the action of an electric field, the potential wells are reduced both in height and in width. Initially, quasi-localised electrons move by resonance tunnelling, as shown in Fig. 2.15. Since they must reach an empty state of equal energy, they will have an excess energy above the ground state after tunnelling. This energy is predominantly dissipated as phonon energy, leading to heating of the molecules along the electron path. At even higher electric fields, some electrons will be able to jump over the potential well (Fig. 2.15 again). During this “hopping” process, the energy difference between the initial and the final state is again dissipated as heat or through the emission of photons. At a transition between clusters, the potential well may become higher and broader and thus hinder electron movement.

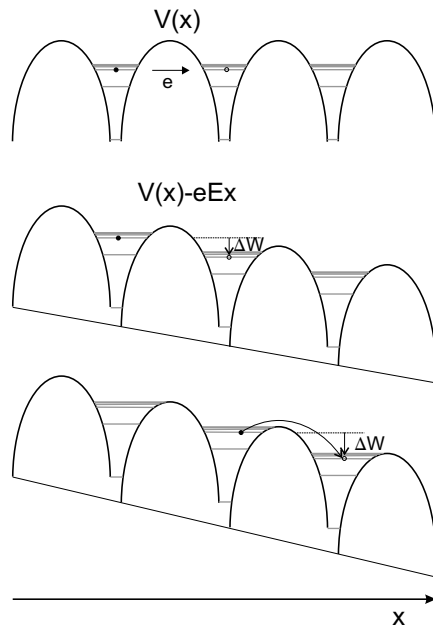


Fig. 2.15. Transfer of excess electrons between molecular states by resonance tunnelling under the influence of an electric field

In the quasi-free state, the mobility of electrons (or holes) is determined by scattering collisions with the liquid molecules, in which they excite vibrational modes and lose their energy gained from the electric field. The probability of a free electron to become trapped again depends on, among others things, its kinetic energy during its drift motion in the electric field.

During transit through a liquid, electrons can thus exist for some time in quasi-free and for some time localised states, and it is possible to describe their motion by an effective mobility depending on the times spent in the free and trapped states, t_f and t_t , respectively:

$$\mu_e = \frac{\mu_f t_f + \mu_t t_t}{t_f + t_t}. \quad (2.40)$$

Here μ_f and μ_t represent the mobilities in the free and trapped states, respectively. The time in the trap is determined by the thermal activation energy E_t necessary to liberate the electron:

$$t_t = t_0 \exp\left(\frac{E_t}{kT}\right), \quad (2.41)$$

where t_0 is the reciprocal of an attempt-to-escape frequency. For hydrocarbons, a value of 0.24 eV has been suggested for E_t in the literature [Fueki et al. 1972].

At high electric fields t_t will be much reduced, because the potential barrier localising an electron will be lowered on the anodic side, as shown in Fig. 2.15. For most of its transit time, the electron then travels in the conduction band, where its drift velocity is limited by collision processes as mentioned before. At very high fields the drift velocity can exceed the thermal velocity and the rate of energy acquisition from the field can become quite high. In hydrocarbon at 10^8 V/m, this rate is of the order of 10^{14} eV/s. This energy is dissipated by stimulating various molecular vibrational modes with typical quantum energies $h\nu$ of a few tenths of an eV. If the energy of the electron becomes larger than $h\nu$, the cross-section for inelastic collisions drops rapidly and the electron can gain sufficient energy to excite the next mode in terms of energy, up to molecular dissociation and ionisation. Ionisation is very important in the context of breakdown, since it generates a second electron and a positive ion or hole, and an avalanche can build up in the liquid. However, since only about 100 meV per molecule is needed to raise the temperature of a liquid from normal temperature to its boiling point, a region of low density (RLD) may have been created long before avalanching occurs in the liquid at normal density. In this low-density region, electron avalanches can build up at much lower electric fields and a growing gas channel can form, which becomes the starting point of a streamer similar to that in gases (see below). At the streamer head, the electric field is much enhanced, favouring self-propagation of the channel. This mechanism explains the observed independence of the streamer propagation velocity within certain limits.

Positive ions in a dielectric liquid will move with a mobility akin to that of ion motion in electrolytes, which is of the order of 10^{-7} to $10^{-8} \text{ m}^2 \text{ V}^{-1} \text{ s}^{-1}$. However, a positive ion in a liquid may be considered as a molecular hole state, and transport of a hole through the valence band can be much easier than ion motion. Nevertheless, the conditions for hole transport will be more stringent than those for free-electron transport, and reported hole mobilities in liquids are typically a factor of 10 smaller than the electron mobility at equal field strength. Hole transport requires the quantum-mechanical resonance tunnelling of an electron between an occupied and an empty state of equal energy. The probability of tunnelling through a potential barrier $V(x)$ at energy W depends on the following factor:

$$\exp \left[\frac{-4\pi}{h} \int_{x_1}^{x_2} \sqrt{2m(V(x) - W)} dx \right], \quad (2.42)$$

where m is the effective electron mass, and x_1 and x_2 are the spatial limits of $V(x)$ at W . If an electric field is applied, the width of the potential barrier will decrease and the tunnelling rate will increase. In a field of 10^8 V/m , an electron will gain an energy of 75 meV in each transfer step. This energy will be locally dissipated, leading to local molecular heating along the hole track.

2.3.1.2 Electrode Processes

Electrode processes play a dominant role in the initiation of breakdown in liquids. Especially under pulsed conditions, breakdown develops from the electrodes in the majority of cases. Excess electrons (or holes), which play an important role in the evolution of a breakdown, may be injected from metallic electrodes into the liquid. This process is very much determined by the detailed structure of the electrode–liquid interface. The situation at a metal–dielectric interface in equilibrium (zero applied voltage) is shown in Fig. 2.16 [Lewis 1994b]. The cloud of electrons moving around the positive ion cores of the metal extends partially into the liquid.

To this negatively charged surface layer, a monolayer of ions and molecules will be chemically or physically bonded and form the *inner Helmholtz layer* (IHL). This layer can be highly structured, especially if the attached molecules are polar. Therefore, its electrical properties are very different from those in the bulk liquid.

Beyond the IHL, there is a transition layer – the *outer Helmholtz layer* (OHL) – where the ions approach the equilibrium polarisation in the bulk liquid. Beyond the OHL is a diffuse region, the *Gouy–Chapman space-charge layer*, where excess ions of one sign exist. The Gouy–Chapman layer results from the fact that the ions attracted into the Helmholtz layers are not sufficient to compensate all of the charge on the electrode, and the residual electric field results in an additional charged layer. In a liquid with a low ion concentration, this layer can extend far into the liquid.

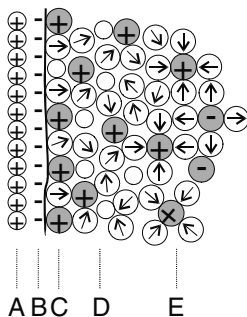


Fig. 2.16. The metal–liquid interface: A positive metal cores; B outer electron cloud; C inner Helmholtz layer; D outer Helmholtz layer; E Gouy–Chapman space charge layer

The IHL may become a double layer, especially if the ions moving to the surface are not neutralized immediately. This can be favoured by a dielectric layer (oxide or hydrocarbon) covering the metallic surface. Under these conditions, the electric field can be as high as 10^9 V/m. The potential-energy difference across the double layer changes the effective work function of the metal [Dekker 1964]. It also supports electron transfer through the oxide layer.

A model that describes electron transfer from a metal through a dielectric layer into vacuum has been described by Latham [Latham 1981]. With little modification, it can be adapted to the passage of electrons into a liquid. According to this model, electrons traversing the dielectric layer under the action of an electric field will be accelerated, entering the liquid as hot electrons. The Latham model predicts a current–voltage characteristic similar to the Fowler–Nordheim equation, but with parameters of very different meaning.

Lewis [Lewis 1987] has suggested that similar layers on the anode electrode will enhance hole injection into the liquid.

If a potential difference is applied between the electrodes, negative ions and electrons will be repelled from the cathode and positive ions and holes will be attracted. The opposite occurs at the anode. If the charge transfer through the metal interface is difficult, ions cannot be neutralised at the electrodes and the electrodes will become increasingly polarised. This results in an effective increase in the resistance of the overall system. The charge accumulated at the metal surface can significantly modify the potential-energy distribution from the classical image charge law.

The applied voltage will create a maximum in the potential distribution, moving towards the electrode as the applied voltage increases. At fields greater than 10^9 V/m, this maximum moves to the electrode within an atomic distance. In this case the effects of the IHL are reduced. If polar molecules such as water exist in the liquid, they can attach to the electrode with a high degree of organisation, changing the potential barrier drastically. Charge transfer at the metal–liquid interface can occur only between states of equal

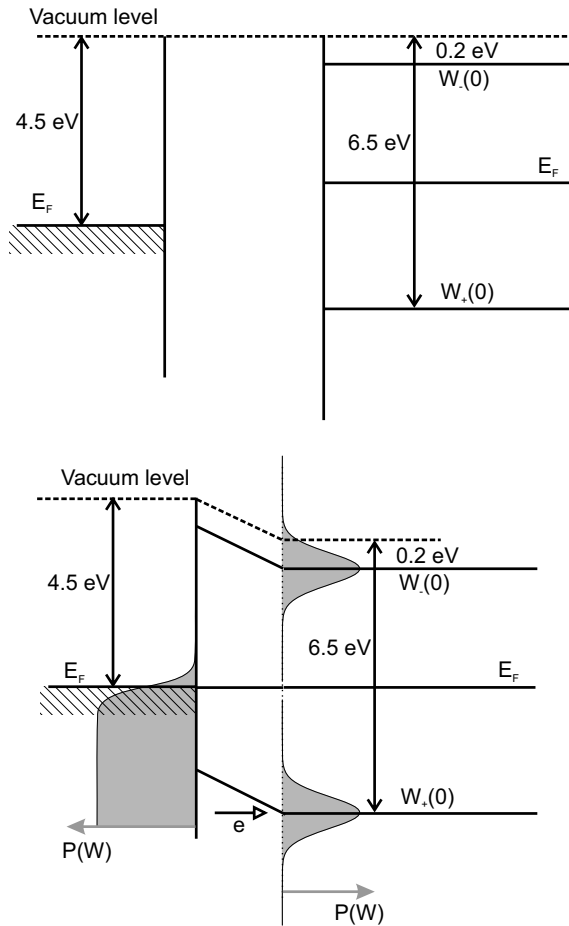


Fig. 2.17. Conditions at an interface between a metal cathode and a dielectric liquid, before (*top*) and after (*bottom*) contact. Electron transfer to negative-ion states W_- is energetically difficult, but easy to positive-ion states W_+ . However, the transfer rate depends on the number of empty states in the liquid boundary layer. An overlap between occupied free-electron states in the metal and empty W_- states in the liquid boundary may occur at high electric fields

energy. Electron transfer at the cathode to a W_- state has a low probability, since the Fermi level in the metal lies below the Gaussian distribution of W_- states (see Fig. 2.17). On the other hand, transfer to W_+ states becomes easy, since the band of these states is well below the Fermi energy. Similar considerations hold for the anode, where electron transfer from W_- states is easily achievable. The rate of charge transfer will depend on the density of occupied states in the emitting material that overlap with the density of empty states in the receiving zone and, of course, on the tunnelling probability.

2.3.2 Streamer Breakdown

Depending on their route, we distinguish between positive and negative streamers. Positive and negative streamers propagate towards the cathode and anode, respectively. In addition, streamers of both polarities are classified as primary, secondary, and tertiary streamers according to their structure, initiation field strength, and propagation velocity. Table 2.8 summarises the observed streamer modes.

Slow streamers have a bush-like shape, while fast ones become filamentary. Schlieren diagnostics have shown that a streamer consists of a gaseous phase. Therefore the breakdown strengths of liquids should increase with pressure. An increase by a factor of 3–4 has indeed been observed at 40 bar for transformer oil. On the other hand, temperature has a minor effect. During propagation between electrodes, the streamer velocity passes through a minimum. If the voltage amplitude or the pulse duration is insufficient, the streamer comes to rest and the streamer channel decays into a string of bubbles.

Table 2.8. Summary of streamer modes in transformer oil [Badent 1996]

	Structure	Velocity (km/s)	Initiation field strength (MV/m)	Diameter of main branch (μm)	Lumi- nescence
<i>Positive polarity</i>					
Primary	Filamentary or umbrella	2–3	400–600	10–50	No
Secondary	Fir-like branch	11–32	1200–1600	80–90	No
Tertiary	Thin channel with little branching out	> 100	> 2000	80–90	Yes
<i>Negative polarity</i>					
Primary	Leafless tree-like head	1–16	300–400	30–70	No
Secondary	Leafless tree-like head; little branching out	3–55	300–400	30–70	No
Tertiary	Thin channel with little branching out	> 65	400–2000	30–70	Yes

2.3.2.1 Cathode Initiation

The primary process for the initiation of a negative streamer is the injection of hot electrons into the liquid as described above, either from a dielectric (oxide) emission site or from a metallic microprotusion. Such an emission site need not necessarily be located on the electrode surface but can also be related to a contaminant particle in the liquid. Nevertheless, in most cases the emission will originate from the electrodes, especially under pulsed-electric-field stress. If a sufficiently large electron current density is injected into the liquid, a gas bubble of critical size and density may form at the electrode surface. Jones and Kunhardt have analysed the situation and derived the result that a necessary condition for the formation of a stable nucleation site is that a specific energy density of 10^9 J/m^3 (for water) must be deposited adiabatically in the liquid to create enough superheating [Jones and Kunhardt 1995a, b]. This criterion holds for a wide range of power densities and external pressures. Considerably less energy is required to expand the nucleation site to a critical size with a sufficiently low density ($n < n_c$) such that electron impact ionisation can take place and a gas streamer can grow to the critical size $\alpha r_c = 18$. Here α is the ionisation coefficient and r_c is the radius of the bubble; $\alpha r_c = 18$ is the condition necessary to initiate a gas streamer (see Sect. 2.2). For water, r_c and n_c are of the order of 10^{-6} m and $1.4 \times 10^{26} \text{ m}^{-3}$, respectively.

It is still not quite obvious by what mechanism large electron current densities can be launched into the liquid to achieve the required superheat. An unrealistically large local field enhancement seems necessary to deliver the necessary electron tunnel current. Also, the amount of tunnel current is limited by the number of available states in the liquid boundary layer, and it seems unlikely that enough free electrons can be launched. Electrons transferred to W_+ states will become localised, and emission to W_- states is energetically difficult. Therefore it has been suggested recently that electrocapillarity might play an important role in the injection of electrons into the liquid [Lewis 1998]. Electrocapillarity creates a tensile stress perpendicular to the applied electric field, and can produce voids in the liquid and small cracks in the liquid boundary layer. Another scenario for creation of a low-density region is by stimulated liberation of gas dissolved in the liquid. This can occur preferentially at rough surfaces with cracks.

Field emission into empty zones is facilitated and can therefore inject enough electrons to start a streamer in the liquid. But emission will be stopped soon, because of the build-up of a negative space charge in the liquid, which weakens the field at the emission site but enhances it in the liquid in front of the space charge. Depending on the strength of the electric field, various mechanisms of electron transport can occur in the liquid, as discussed in Sect. 2.2. The different electron mobilities associated with these processes will lead to different heating rates along the electron path and create a region of lower density, and finally a gaseous channel. Electrons in this channel

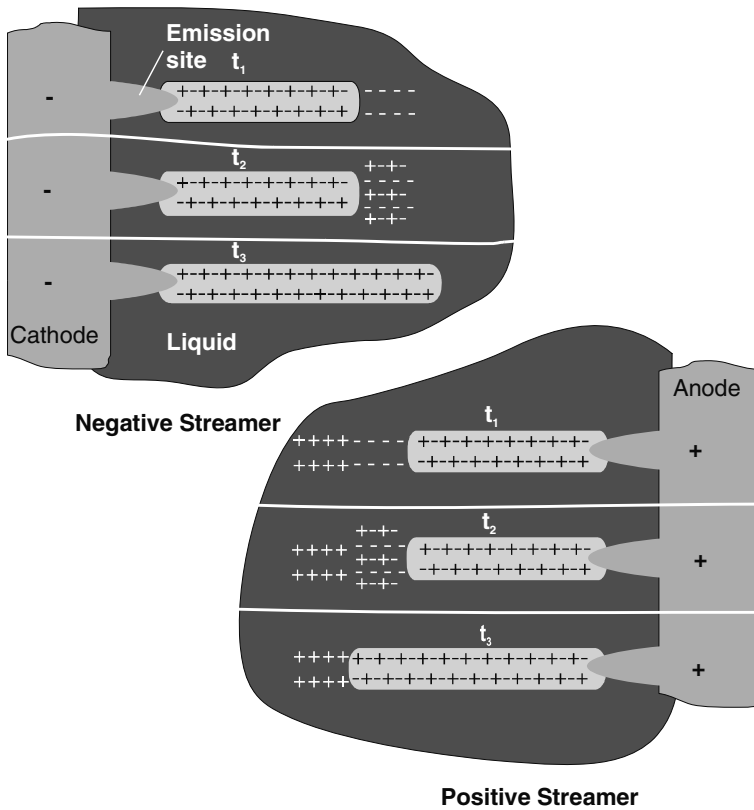


Fig. 2.18. Possible scenario for the advancement of negative and positive streamers in a liquid. Injection of hot electrons from an emission site on the cathode leads to local heating in the liquid and, if the electric field is sufficiently large and the excess electrons can be considered as quasi-free, causes extension of the gaseous streamer channel. On the anode side, electrons liberated from traps and molecules with a low ionisation potential become attracted to a field-enhanced zone and again can deposit enough energy in the liquid if the local field is high enough to form a region of low density. The positive space charge left behind can enhance the local field

can be accelerated towards the streamer tip and into the liquid, where they form a new space charge cloud and start another heating and evaporation cycle. An important aspect of this cycle is that the region between the space charge cloud in the liquid ahead of the channel and the boundary of the gaseous channel becomes heated sufficiently to form a region of low density before the space charge build-up repels further electrons (Fig. 2.18). If that happens, streamer propagation stops and the streamer decays. Another requirement is that the trailing end of the discharge channel becomes sufficiently conductive to maintain the potential at the front sufficiently close to that at the electrode.

When the streamer approaches the anode, the field at its tip increases and another, more effective electron transport mechanism may become possible, leading to a larger heating rate and thus a faster propagation of the streamer, thus causing the initiation of a secondary or, if the field becomes very high, a tertiary streamer [Badent 1996].

It has been observed that if the trapping distance of electrons from the streamer head is reduced, by adding an electron scavenger to the liquid, streamer propagation is accelerated [Devins et al. 1981]. This can be explained by the model described above if one considers the fact that less time is needed to form an RLD because the electron energy is now released within a smaller volume. However, additives that reduce the ionisation potential should not have a strong effect on the streamer velocity. Both effects have been observed experimentally.

2.3.2.2 Anode Initiation

Anode initiation of a streamer seems even less well understood. According to Lewis [Lewis 1987], a positive streamer can be initiated by hole injection from an oxide microregion on the anode surface. Hole injection can occur not only at the liquid–metal interface, but also at the liquid–plasma boundary of a streamer. However, hole propagation in the liquid can occur only through electron resonance tunnelling, which has a rather low probability at the observed breakdown fields.

Another mechanism for the anode initiation of streamers, discussed by Badent [Badent 1996], is the liberation of electrons from traps, quasi-localised states, or molecules with a low ionisation potential through field ionisation in the vicinity of a microprotrusion on the anode. These electrons become accelerated towards the field-enhancing site on the metal anode (Fig. 2.18). The space charge associated with this electron cloud will further enhance the field around the microprotrusion, and finally break down the path between the electron cloud and the tip of the microprotrusion depositing enough energy to create an RLD. The ions left behind in the liquid create a space charge cloud, which reduces the field between the cloud and the front end of the gaseous breakdown channel but can increase it towards the cathode side. To advance the gaseous streamer channel, the RLD must have been created before the positive space charge of ionised molecules reduces the field in front of the streamer tip below a critical value. Again, field enhancement at the streamer tip can be maintained only if the channel conductivity becomes sufficiently large.

This description of positive-streamer initiation and advancement is consistent with the experimental observation that electron scavengers such as SF₆ or CCl₄ do not have an effect, but low-ionisation-potential additives result in an increase of the streamer velocity [Beroual 1993].

2.3.2.3 Water

Water is a rather important dielectric liquid in pulsed-power applications. It has a relatively high electric breakdown strength (up to 3×10^7 V/m) for sub-microsecond electric stress and, owing to its high permittivity, can store quite large energy densities for short times. Most of the electrical characteristics of organic dielectric liquid insulators discussed in the previous sections are also valid for water. Nevertheless, some differences must be mentioned. Compared with the molecules of organic liquids, water molecules have a simple structure and intramolecular electron transport becomes unimportant. The water molecule possesses a large dipole moment and the properties of water in a metal-liquid boundary layer are likely to be very different from those in the bulk. The orientation of a water molecule near a metal surface depends on the polarity. It has been found, from X-ray scattering, that an oxygen-up orientation occurs at the cathode, while an oxygen-down orientation occurs at the anode. Also, a much greater density than that in bulk water has been determined for the first layer [Toney et al. 1994]. It is expected that this structure will have a strong impact on electron transfer and on the formation of gaps in the boundary layer due to electrocapillarity.

A small fraction (10^{-7}) of water molecules is always dissociated into H^+ and OH^- . These ions lead to a residual conductivity of 4×10^{-6} S/m even for very clean water. Therefore water is inadequate for DC-insulation. The ions can also move to the electrodes and influence the structure of the boundary layer and thus the charge transfer to the electrodes. Nevertheless, ionic currents do not contribute to the initiation of breakdown for submicrosecond pulses. This has been demonstrated even for salt solutions with concentrations up to 1 M [Jones and Kunhardt 1994]. Water can also dissolve large quantities of gases (N_2 , O_2 , and CO_2), which can lead to the formation of gas bubbles and thus facilitate the appearance of a streamer. It has been found that the dynamic breakdown strength of water increases with pressure and that the time lag to breakdown in doubly distilled water without gas becomes more than 50% larger [Jones and Kunhardt 1994].

2.3.3 Practical Considerations

Like gaseous media, liquids have the great advantage of self-repairing after breakdown, i.e., they restore their previous electric strength. Water, which is largely used in short-pulse applications, has, in addition, the benefit of a high dielectric constant ($\epsilon \approx 81$), which allows one to store high energy densities.

In highly purified liquids, the electric strength is of the order of 100 MV/m. Unfortunately, liquids are easily contaminated, and many contain solid particles and dissolved gases. If the voltage is applied continuously, the solid impurities line up parallel to the field and distort it, so that breakdown can occur at a relatively low voltage. The lining up is a fairly slow process and is unlikely to affect the strength for pulses shorter than 1 ms. In general, the

effect of impurities is small for short-duration pulses, i.e., shorter than a few microseconds.

In addition to solid particles, dissolved gas is of importance for the dielectric strength of a liquid. Under the action of the electric field, dissolved gas may come out of solution, forming a bubble. Most liquids have a higher dielectric constant than have gases. Therefore the field in a gas bubble is enhanced, and since anyway the strength of a gas is lower than that of a liquid, ionisation and avalanche formation can occur in the bubble. The discharges in the bubble attack the liquid so that more gas is created and the bubble grows.

The most important liquid insulant is mineral oil. It is used both as an insulating and a cooling medium in transformers, feedthroughs, and capacitors. Mineral oil can absorb moisture, which reduces its insulating strength [Küchler 1996]. The ability of oil to dissolve water increases with temperature. Therefore the insulating quality of oil has to be kept under surveillance, especially for unsealed systems. Partial discharges decompose the mineral oil, producing H_2 , CH_4 , C_2H_4 , and other gases, which can accumulate in certain positions and lead to a catastrophic failure of a high-voltage system. The composition of the gases dissolved in the oil can be used as a diagnostic tool to identify the type of failure, i.e., corona discharge, sparking or arcing.

Because of their tendency to become contaminated, liquids should not be used to insulate DC fields greater than 10 MV/m. Very often, they are used in combination with solids, where they serve to fill voids and push away gaseous inclusions. Oil-impregnated paper has been widely used as an insulator in high-voltage capacitors.

From the discussion in the preceding paragraphs, it is evident that the electric breakdown strength of liquids must be time-dependent. In pulsed-power systems, the insulating liquid is very often stressed for a short duration. J.C. Martin and co-workers at Aldermaston have measured the electric strength of transformer oil and water in the microsecond regime and derived various empirical formulae that are quite useful in the design of pulse generators [Martin et al. 1996]. These formulae will be presented below. However, attention should be paid to the range of their applicability and to the fact that they are approximate. It is also important to note that the breakdown voltage derived from these formulae corresponds to a 50% probability of breakdown. To determine the field for a higher safety margin, the field has to be evaluated using Weibull statistics (see below).

2.3.3.1 Uniform Field Distribution

Since the pulsed breakdown of a liquid originates from the electrodes, the breakdown field should depend on the area. For a uniform field and pulse durations in the range $10\ \mu\text{s} > t > 0.1\ \mu\text{s}$, the breakdown field is approximately given by

$$Et^{1/3}A^{1/10} = k_{\pm}, \quad (2.43)$$

where E is the electric field above the static breakdown threshold in MV/cm, t is in μs , and A is the electrode area in cm^2 . t is the effective pulse duration, defined as the time during which the voltage is greater than $0.63V_{\text{max}}$. For the constant k , we have:

- Transformer oil: $k_{\pm} = 0.5$.
- Water: $k_{+} = 0.3 \quad k_{-} = 0.6$.

For a weakly diverging field, (2.43) has to be applied to the maximum field at the electrodes, taking into account the polarity effect, and for A , one has to choose the area of the electrode which is stressed to more than 90% of the maximum field. For much shorter times, $7 \text{ ns} < t < 30 \text{ ns}$, and voltages between 0.4 and 1.1 MV, a slightly different equation has been derived for water [VanDevender 1976]:

$$Et^{0.39}A^{0.06} = 0.304 \times d^{0.65} . \quad (2.44)$$

To fit the experimental data, VanDevender found it necessary to include a dependence on d , the electrode separation. All quantities here should be used with the same units as in (2.43); d is in cm.

Under short-duration electric stress, the electric strength of water becomes comparable to that of other liquid insulators. At $1 \mu\text{s}$, its strength is around 40 MV/m. If water is used as a dielectric in pulse-charged systems, it has to be deionised, not primarily because impurities affect its pulse breakdown strength, but just to limit the ohmic conduction losses. As stated before, owing to the dissociation of its molecules, completely deionised water has a residual conductivity $\sigma = 4 \times 10^{-6} \text{ S/m}$. Its self-discharge time constant is $\tau = \epsilon\epsilon_0/\sigma = 180 \mu\text{s}$. In contact with air, the conductivity increases up to $\sigma = 10^{-4} \text{ S/m}$ owing to dissolution of CO_2 , leading to $\tau = 7.3 \mu\text{s}$. Therefore energy can be stored only for a rather short time in water-insulated systems, determined by the shorter of the two time constants for breakdown (2.43) and self-discharge.

2.3.3.2 Strongly Non-Uniform Field Distribution

The mean streamer velocity has been measured for point–plane and edge–plane configuration in a number of liquids for voltages from 0.1 to 5 MV. These formulae are especially useful in the design of liquid switches.

In the range 0.1–1.0 MV, the following expression has been given for mineral oil and other organic liquids:

$$u = d/t = kU^n , \quad (2.45)$$

where u is the mean streamer velocity, given in $\text{cm}/\mu\text{s}$, and U is the applied pulse voltage, given in MV. Note that u depends on U and not on the electric field E , reflecting the fact that E at the streamer tip is determined only by

Table 2.9. Parameters to be used in (2.45)

Liquid	k_+	n_+	k_-	n_-
Oil	90	1.75	31	1.28
Glycerine	41	0.55	51	1.25
CCl_4	168	1.63	166	1.71

the applied voltage and the radii of the streamer filaments. The parameters to be used in (2.45) are listed in Table 2.9.

In the range 1–5 MV, the difference between positive and negative streamers in the case of oil disappears, and the following relationship becomes valid for both polarities:

$$u d^{1/4} = 6.35 \times 10^{-5} U^{1.6}. \quad (2.46)$$

For water, the relationships look rather different. In the range 0.1–1 MV and for pulse durations > 100 ns, we have

$$\begin{aligned} ut^{1/2} &= 2.21 \times 10^{-2} U^{0.6} && \text{for positive points,} \\ ut^{1/3} &= 4.02 \times 10^{-4} U^{1.1} && \text{for negative points,} \end{aligned} \quad (2.47)$$

where u is in m/s, U in volts, and t in seconds. From (2.47), we can derive expressions for the breakdown field strength by introducing $u = d/t$ and $E_{\text{br}} = U/d$:

$$\begin{aligned} E_{\text{br}} &= 5.74 \times 10^2 d^{2/3} / t^{0.833} && \text{for positive points} \\ E_{\text{br}} &= 1.22 \times 10^3 / (d^{0.0909} t^{0.606}) && \text{for negative points} \end{aligned} \quad (2.48)$$

Plotting these breakdown field strengths shows that they increase rapidly with decreasing pulse duration (Fig. 2.19). The strongly time-dependent breakdown strength of water is the basis for some pulsed-power applications discussed in Chap. 11.

2.4 Solids

2.4.1 General Observations

The phenomenon of dielectric breakdown in solids is linked inseparably to the progressive destruction of the dielectric medium by electronic or ionic charge carriers that have acquired sufficient energy from the electric field. Although the mean free path of an electron in a solid is a debatable concept, it is quite instructive to discuss the question of what mean free path would be necessary at a given field strength for an electron to gain the energy required for various kinds of damage in solids.

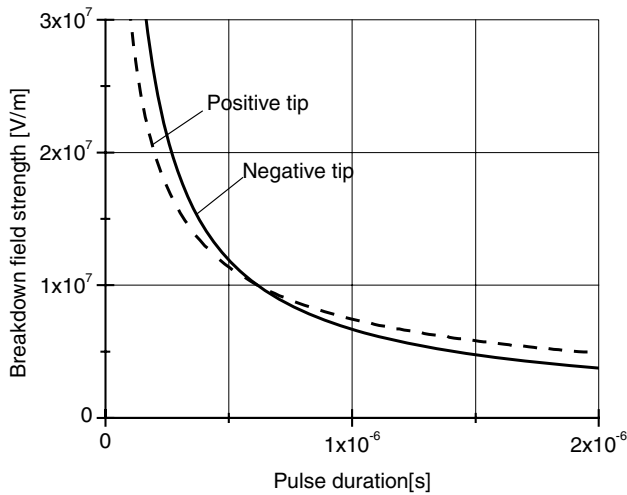


Fig. 2.19. Mean pulsed breakdown strength in water for a point-plane or edge-plane geometry. These graphs have been derived from the empirical formulae given in (2.48), which were derived for pulse durations greater 100 ns and pulse amplitudes between 0.1 and 1 MV. The plot has been calculated for a gap of 4 cm

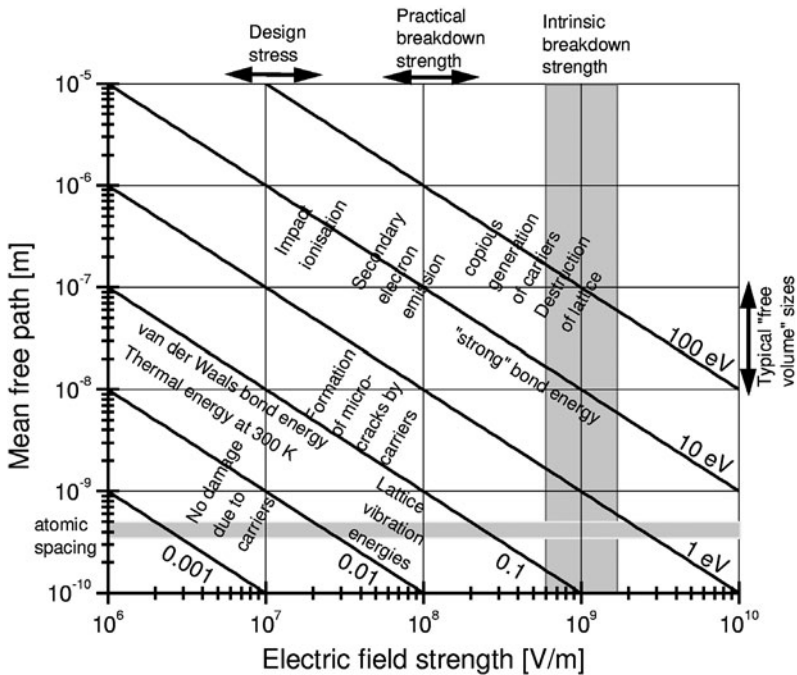


Fig. 2.20. Relationship between the electric field E , the mean free path ℓ , and the energy acquired by a carrier in a mean free path

Table 2.10. Dielectric constants and breakdown strengths of insulator materials

Insulator material	Dielectric constant ϵ	Breakdown strength (MV/m)
Air	1.0	3.0
Aluminium oxide	7.0	11.8
Barium titanate composite and filler	500–6000	2.0
Kapton	3.6	275
Impregnated paper	6	78
Lucite	3.3	20
Mylar	2.5	200
Polyethylene	2.2	177
Polypropylene	2.5	378
Polysulphone	3.1	315
Pyrex glass	4–6	20
SF ₆	1.0	8 (per atm)
Teflon	2.0	59
Transformer oil	2.2	10–40
Water	80	20 (for $t < 10 \mu\text{s}$)

In Fig. 2.20, lines of equal energy gain have been plotted in a coordinate system of mean free path and electric field. Strong binding energies in solids are typically of the order of several eV, while the energies required for impact ionisation are of the order of 10–20 eV. Table 2.10 summarises the static electric breakdown strength of a number of insulators. The practical electric breakdown strength of solid insulators is typically in the region of 100 MV/m. Using these data, we can conclude that a mean free path of between 0.1 and 1 μm is required to break bonds and to ionise material at the observed breakdown field strength. Such path lengths may occur only in some crystalline materials such as alkali halides, where, in addition, an energetic tail in the electron energy distribution resulting from energy accumulated over several successive collisions can be created. However, the chance of inducing electron avalanches in 2-D or 1-D lattices such as those of polymers is very small. One must therefore conclude that damage can be done only if either the damage threshold is reduced or electrons are allowed to move over significantly longer free paths. It is likely that a combination of both phenomena occurs in solids.

Before we consider possible mechanisms that can create the necessary conditions for breakdown, we shall summarise some general experimentally observed features of breakdown in solids.

The magnitude of the breakdown field depends on a number of factors, such as the time dependence of the electric field, the geometry of the sample, and the nature of the electrodes. In general, one finds a progressive reduction

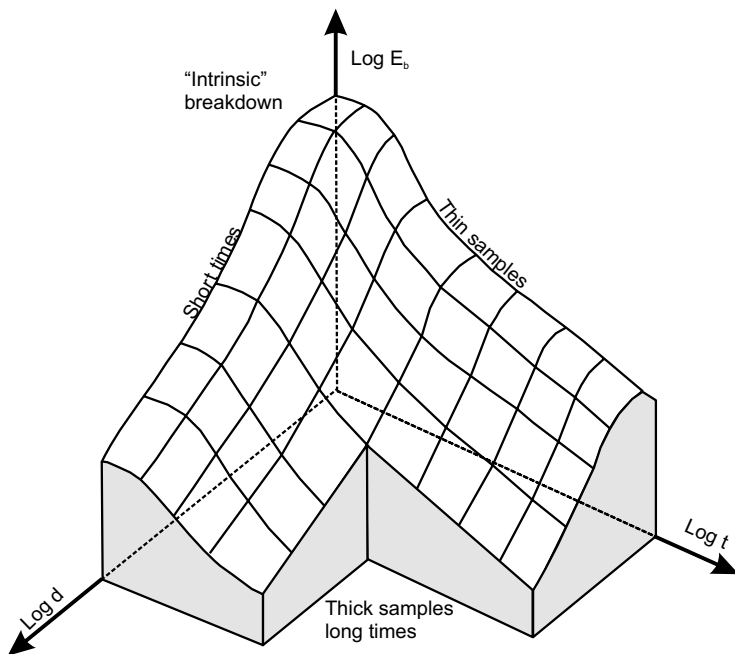


Fig. 2.21. Schematic representation of the relationship between the breakdown field E_b , the time to breakdown t , and the sample thickness d

of breakdown strength with increasing thickness, while the time dependence can be described by Weibull statistics (see below).

The dependence on time and thickness is shown schematically in Fig. 2.21. The highest breakdown strengths are achieved for the shortest times and thinnest samples. The area around the origin in Fig. 2.21 is called the ‘intrinsic’ breakdown strength. This is the strength that a material without defects and without external influences – for example charge injection from metallic electrodes – would have. The ‘intrinsic’ strength is between two and three orders of magnitude above the design stress in technological applications. The highest recorded values of the breakdown field E_b for a number of different materials lie between 100 and 1000 MV/m, although not for the alkali halides, whose highest breakdown strength is below 100 MV/m.

Most insulating materials show a temperature-independent breakdown strength between cryogenic temperatures and a critical temperature, where it drops drastically.

The general features of the experimental evidence about breakdown in solids can be summarised as follows [Jonscher and Lacoste 1984]:

- The breakdown has statistical characteristics. It follows a Weibull distribution (see below) that contains a time–field–strength integral, reflecting the memory effect of the material.

- The ‘intrinsic’ breakdown strength lies in a very narrow band for physically and chemically very different materials.
- The final result of a breakdown is always the formation of a narrow plasma channel. Other visible features precede and accompany breakdown, but the channel does not have to proceed along these features.
- Electronic charge carrier injection from the electrodes accelerates the breakdown.

The presence of macroscopic defects inside the material (e.g., voids or conducting inclusions) shortens the time to breakdown. The ageing of the electric strength of a material is strongly affected by charge carrier injection and trapping. Some other factors are electrically induced mechanical stress, which can lead to the formation of microvoids, and the diffusion of impurities.

2.4.2 Charge Transport, Injection, and Breakdown

On the basis of the general observations described in the previous subsection a phenomenological model of the breakdown of solids has been formulated by Jonscher and Lacoste [Jonscher and Lacoste 1984]. In this model, it is assumed that damage is done continuously to the material prior to the onset of the final breakdown. However, nothing is said about the molecular mechanism of this damage. Nevertheless, future improvements in the dielectric breakdown strength of solid insulators require a detailed understanding of the fundamental electrical properties of these materials. Electrical breakdown must at least begin at a molecular level. Therefore we shall discuss charge transport, charge injection, and breakdown in this subsection first at a molecular level, following some descriptions in the literature [Lewis 1984, 1989, 1990; Lewis and Bowen 1984; Ieda 1984; Zeller et al. 1984].

2.4.2.1 Charge Transport

The most important solid insulators today in pulsed-power technology are organic polymeric dielectrics such as polyethylene or cast epoxy. These dielectrics consist of long-chain molecules with strong covalent bonding in the chains and weak van der Waals bonding between chains. They can form both regular crystalline and amorphous regions. A schematic illustration of the structure of a semi-crystalline polymer is shown in Fig. 2.22. The crystalline lamellae (about $1\ \mu\text{m}$ long and $10\ \text{nm}$ thick) consist of linear, parallel chains forming a stable orthorhombic grid, interrupted by amorphous regions of thickness $1\text{--}10\ \text{nm}$. Crystalline regions can be linked by chains traversing the amorphous regions. Depending on the production method, up to 80% of the volume of polyethylene can become crystalline. Impurities, including gases and water, are relatively easy incorporated in amorphous regions.

The complex structure of polymers renders the modelling of electrical conduction in them quite difficult. Within the periodic potential distribution

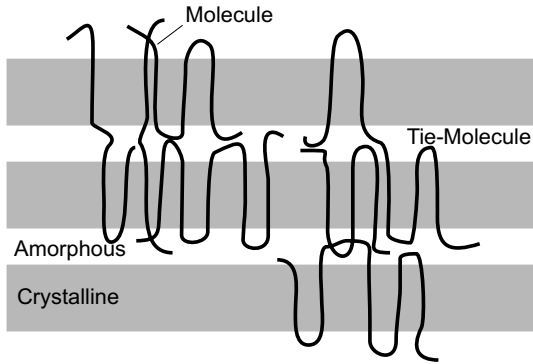


Fig. 2.22. Schematic representation of the lamellar structure of a semi-crystalline polymer. A tie molecule links two crystalline regions. Chain ends, kinks, loops, and folds occur in the amorphous regions, and parallel chains form the crystalline lamellae

along a chain, spatially extended electron states give rise to the formation of a structure of separated bands corresponding to the conduction and valence bands in a semiconductor (Fig. 2.23).

Because of the weak bonding between chains, it is justified to assume that the electronic states of a polymeric solid are similar to those of isolated chain molecules. Since the electron affinity of a polyethylene chain is negative – its conduction band is about 1 eV above the vacuum level – free-electron transport will follow interchain rather than intrachain paths [Lewis 2002]. Electrons will move in the periodic potential along the chain surface. Holes, however, can exist only in valence band states. Their transport must therefore occur intramolecularly. Both transport mechanisms will be easier along chains that happen to lie in the field direction. Chain ends, folds, kinks, and branching will interrupt the periodicity and lead to charge localisation. Further transport can proceed only by hopping or tunnelling between localised states. The situation is similar to that described in Sect. 2.2 for electron transport between zones of short-range order in a liquid. The electron transfer rate is very sensitive to the nature of the potential barrier. A simplified expression has been derived by Redi and Hopfield [Redi and Hopfield 1980] and modified by Lewis [Lewis 1990]:

$$P_{ab} = \nu_{ab} \exp(-2\alpha_{ab}R) \exp(-W_{ab}/kT) , \quad (2.49)$$

where ν_{ab} is an attempt-to-escape frequency, of the order of 10^{12} – 10^{13} s⁻¹; α_{ab} takes account of the overlap of the wave functions of states at sites a and b a distance R apart; and W_{ab} is the energy difference between the states at a and b, including the reorganisation energies Λ_a and Λ_b (see below).

In addition to being trapped on the basic molecular chains, electrons or holes can become trapped at dopant impurities. Dopant (Na^+ , K^+ , Cl^- , and

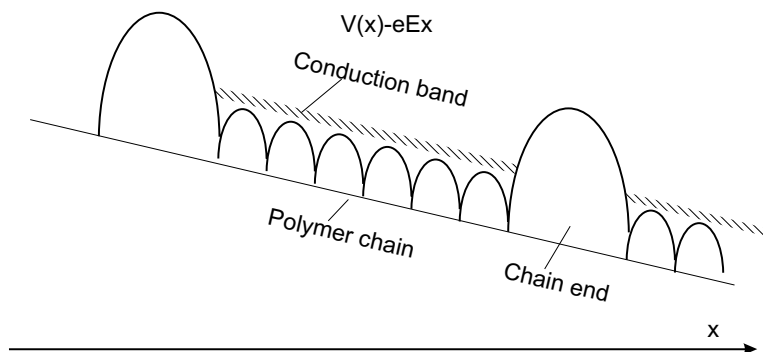


Fig. 2.23. Band structure for a section of an extended polymer chain coinciding with the field direction. At very large fields, excess electrons liberated from traps can move quasi-freely in a conduction band along the chain. At the chain ends, they must tunnel through a potential well to reach the next chain

O_2) densities of $10^{23}/m^3$ have been found in polyethylene. Acceptors and donors of this kind lead to reorganisation of the surrounding polymer matrix depending on their charge state. The reorganisation energy Λ associated with this has the same effect as that discussed for dielectric liquids in Sect. 2.2. When a charge is transferred to or from such a site, the polarisation will relax in accordance with the new charge state. Therefore Λ will depend on the length of time the charge state remains unchanged. The same considerations hold for charge carriers trapped on the polymer molecules.

The residence or trapping time t_{tr} in any localised state, which is inversely proportional to P_{ab} , is strongly dependent on the energy difference W_{ab} between the states. For representative values of ν_{ab} and $\alpha_{ab}R$, the residence time is 6 hours for $W_{ab} = 1$ eV and 10^{-9} s for $W_{ab} = 0.2$ eV.

2.4.2.2 Metal–Dielectric Contact

The large band gap of insulating polymers (> 8 eV) makes it very unlikely that mobile charge carriers can be created thermally. The only way to produce mobile charge carriers will be by the introduction of appropriate dopants or by injection of electrons or holes from metallic electrodes.

A metal electrode in contact with a dielectric solid will transfer charge into the solid. Measurements have shown that about 1 in 10^3 polymer surface states become either oxidised or reduced owing to this charge transfer [Bouatou and Lowell 1988]. The mechanism of this transfer is again by resonance tunnelling involving empty and occupied electronic states of the metal around the Fermi energy, and the acceptor and donor states of the polymer surface. The situation is parallel to that shown in Fig. 2.17 for a metal–dielectric-liquid contact. Since donor and acceptor states can coexist at the polymer surface, both electrons and holes can be exchanged between the metal and the

polymer surface, although in separate locations. Under the action of a strong electric field, the sign of the injected charge can change locally, since the energy bands of the dielectric move relative to the Fermi level. If the charge remains at surface states, further tunnelling will stop and current flow across the surface will become blocked.

At high electric fields, more charge carriers will be transferred, since higher-lying states become accessible. At the same time, charge may be transported away from the interface into the interior of the polymer, thus reducing the blocking action. This can proceed through tunnelling processes along molecular chains parallel to the field direction. At even larger electric fields, electrons can reach excited states. Decay from these excited states will remove energy from the electrons to the molecule and heat it. Ultimately, at the highest fields, electrons can reach the band of extended conduction states (see Fig. 2.23). Here, the only energy-dissipating mechanism becomes scattering from lattice vibrations, and kinetic energies sufficient for ionisation can be reached. However, this conduction band will still be limited by the extent to which the chain coincides with the field direction. In parallel to (2.48), an effective mobility can be defined, taking into account the different times spent by a charge carrier in the conduction band and in traps.

2.4.2.3 Breakdown

Electrons and holes injected from metal electrodes or liberated from shallow traps and subsequently stored in molecular states can concentrate significant energy densities. It has been suggested that, similarly to the processes in conducting polymers [Skotheim 1986], reducing or oxidising agents play an important role in the creation of quasi-free electrons and holes in the bulk material. Thus it is not only charge injection from the metal surface that can lead to local space charge concentrations. Under the action of a strong electric field, these charge carriers can be released in a short time in a cascade of tunnelling processes, and establish a preferred path for further charge transfer. It is assumed that the energy released in this process can create new defects and extend existing defects.

This phase may be called the conditioning phase [Jonscher and Lacoste 1984]. In polymers such as polyethylene, the electrical and mechanical properties are closely related. Strong electric fields can change the morphology of the insulator and create microvoids. If the density of defects becomes sufficiently high, they can merge and form defect clusters. A cluster allows much freer movement of charge carriers entering into it. Therefore these carriers can gain more energy and extend the cluster, which starts to grow along the field lines. Electrons can now acquire an energy corresponding to a mean free path of many interatomic spacings. At this stage, trees may become visible in the material.

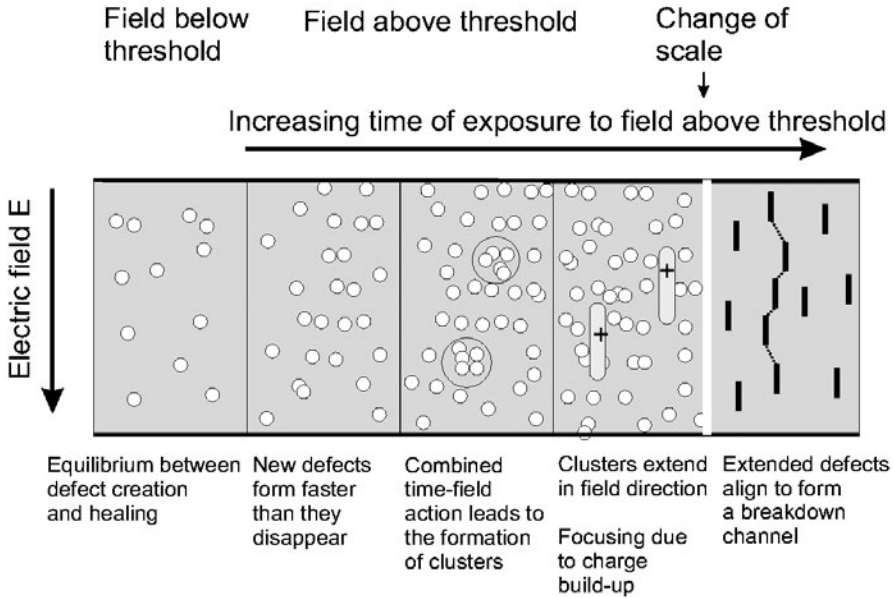


Fig. 2.24. Schematic illustration of the temporal evolution of defect formation under the action of an electric field, leading to the ultimate breakdown of the dielectric material

At low rates, a (thermal) healing process may compensate for the defect production, explaining the existence of a threshold field below which no breakdown is expected, however prolonged the exposure.

An important feature of cluster growth is self-focusing. This occurs after a plasma has been created inside a cluster. Since the electrons are much more mobile than the ions, they will leave the cluster and the cluster will become positive, attracting electrons that may be present in the neighbourhood. The situation becomes comparable to the initiation of a streamer in a liquid.

With an increasing number of randomly distributed elongated clusters, a favourable alignment may be created, where a current can link mutually favourably positioned defects. At this point, a thermal breakdown channel will be created. A schematic illustration of the cumulative model described here is shown in Fig. 2.24 [Jonscher and Lacoste 1984].

From the previous discussion, it becomes plausible that for thick samples the breakdown strength depends on the volume of the stressed material. Neglecting the time dependence, which is allowable for pulse durations of more than 100 ns, C.L. Martin has empirically determined the following expression for the breakdown field:

$$E V^{1/10} = k. \quad (2.50)$$

Table 2.11. Values of k for some plastics

Material	k
Polyethylene	2.5
Perspex	3.3
Mylar	3.6

Table 2.11 contains some values of k for plastic materials. For non-homogeneous fields, the maximum field and the volume in which the field exceeds 90% of the maximum field have to be used.

It is also understandable that the breakdown strength of a solid decreases with the number of pulses. This reduction is a very strong function of the ratio between the operation field E_{op} and the breakdown field E_{b} :

$$N_{\text{life}} = (E_{\text{b}}/E_{\text{op}})^n . \quad (2.51)$$

Here N_{life} is the expected number of pulses that the insulator will survive, E_{op} is the operation field, and n is an exponent that depends on the material ($n = 8$ for polyethylene, and $n = 16$ for mylar).

A technologically important observation is that for very short pulses, the breakdown strength of some liquids – especially water – is higher than that of many solids. This is especially true for multicomponent and compound materials containing many defects, pores, or boundary surfaces. This fact is the basis of the electro-impulse fragmentation described in Chap. 11.

2.5 Statistical Interpretation of Breakdown Strength Measurements

The empirical formulae given above are based on the interpretation of experimental data with the help of reliability theory. In reliability theory (see, e.g., [Barlow and Proscan 1975]), one defines the relative expected failure rate $\xi(S) dS$ for a stress S through

$$dn(S) = -n(S)\xi(S) dS , \quad (2.52)$$

where $dn(S)$ corresponds to the number of samples that fail if the stress is raised from S to $S + dS$ assuming that $n(S)$ samples have survived the stress S . By integrating (2.52), we obtain

$$\begin{aligned} \ln \frac{n(S)}{n_0} &= - \int_0^S \xi(S') dS' , \\ \frac{n(S)}{n_0} &= \Psi(S) = e^{-\int_0^S \xi(S') dS'} . \end{aligned} \quad (2.53)$$

If we assume that all samples obey the same statistical distribution, we can also say that $\Psi(S)$ represents the probability that a single sample will survive under the action of S . $F(S) = 1 - \Psi(S)$ is then the probability of failure for that sample, and $f(S)$ is the correlated probability density distribution function:

$$f(S) = \xi(S) e^{-\int_0^S \xi(S') dS'} . \quad (2.54)$$

To determine the failure rate for a specific technological system, it is necessary to find an expression for the relative expected failure rate ξ . In the case of decaying radioactive nuclei, for example, the relative decay rate $\xi(t)$ is constant ($\xi(t) = \alpha$), i.e., it does not depend on past history, and we obtain the well-known exponential law of radioactive decay:

$$\frac{n(t)}{n_0} = e^{-\alpha t} . \quad (2.55)$$

For technological systems, however, very often the failure rate increases exponentially with the stress:

$$\xi(S) = aS^\alpha . \quad (2.56)$$

In this case, one obtains the Weibull failure distribution,

$$F(S) = 1 - e^{-aS^{\alpha+1}/\alpha+1} . \quad (2.57)$$

If we define $\langle S \rangle$ as the value of S at which the probability of failure is $1 - 1/e = 63\%$, we can write this as

$$F(S) = 1 - e^{-(S/\langle S \rangle)^B} , \quad (2.58)$$

where $B = \alpha + 1$. Equation (2.58) is the simplest form of a (two-parameter) Weibull distribution. As discussed previously, in general we have a threshold S_0 below which no failure of the system occurs, independent of the duration of the stress. This can be represented with a three-parameter Weibull distribution, which is applicable for $S > S_0$:

$$F(S) = 1 - e^{-[(S-S_0)/\langle S \rangle]^B} . \quad (2.59)$$

Plotting $\ln[1/(1 - F)]$ on a double logarithmic scale results in a straight line, from which the parameters of the distribution can be derived (see Fig. 2.25).

Measurements of breakdown fields are generally made using small samples. Therefore, it becomes necessary to extrapolate the results to larger samples. Here we shall consider how this extrapolation is performed. For this purpose, we assume that a large insulator can be subdivided into N smaller sections, whose (identical) probability distributions for survival $\Psi(S/\langle S \rangle)$ are

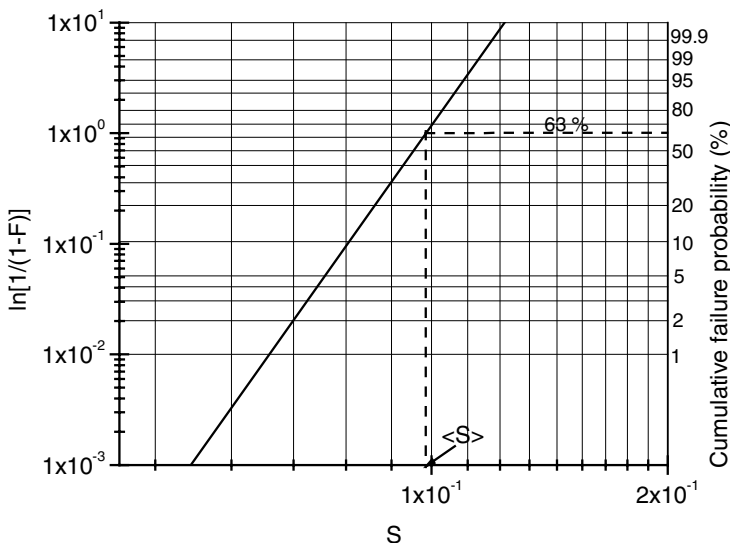


Fig. 2.25. Weibull distribution plot of (2.58). On the *right axis*, the cumulative failure probability F corresponding to each value of $\ln[1/(1 - F)]$ is plotted. For $F = 63\%$, one can read $\langle S \rangle$ from the abscissa. The gradient of the double logarithmic plot gives the exponent B

known. Then, according to the theory of statistics, we obtain the following for the probability $\Psi(S/\langle S_N \rangle)$ that the large insulator survives the stress S :

$$\Psi\left(\frac{S}{\langle S_N \rangle}\right) = \left[\Psi\left(\frac{S}{\langle S \rangle}\right)\right]^N. \tag{2.60}$$

We suppose further that the probabilities of survival for the small and the large insulator obey the same distribution (2.58) but with the appropriate mean breakdown strengths $\langle S \rangle$ and $\langle S_N \rangle$. Using (2.58), we can determine the scaling of $\langle S_N \rangle$ with the size (area or volume) of the insulator:

$$\left[\Psi\left(\frac{S}{\langle S \rangle}\right)\right]^N = e^{-(S/\langle S \rangle)^B N} = e^{-(SN^{1/B}/\langle S \rangle)^B} = e^{-(S/\langle S_N \rangle)^B} = \Psi\left(\frac{S}{\langle S_N \rangle}\right). \tag{2.61}$$

Thus we have $\langle S_N \rangle = \langle S \rangle/N^{1/B}$. N is proportional either to the area, i.e., $N = A_N/A_1$ (liquids under pulsed stress, thin sheets, etc.) or to the volume, i.e., $N = V_N/V_1$ (thick solid insulators). In evaluating statistical experimental data, the variance is useful:

$$\begin{aligned} \left(\frac{\sigma}{\langle S \rangle}\right)^2 &= \Gamma\left(1 + \frac{2}{B}\right) - \Gamma^2\left(1 + \frac{1}{B}\right), \\ \frac{\sigma}{\langle S \rangle} &= 10\% \Rightarrow B = 10. \end{aligned} \tag{2.62}$$

where Γ is the well-known gamma function. In some cases, a simple calculation of the variance allows a determination of the size-scaling exponent.

It has been discussed previously that the quantity which determines the stress on an insulator is proportional to the product $\int_0^t (E - E_0)^\mu t^\nu dt$, and for a step pulse, the failure probability F therefore has the following form (for $E > E_0$):

$$F(E, t) = 1 - e^{-ct^a(E-E_0)^b}. \quad (2.63)$$

To determine the parameters of this distribution experimentally, a step pulse of fixed field amplitude $E = E_a$ is applied to the sample and the time of breakdown is observed. The time distribution of breakdown events is obtained from $F(E, t)$ by differentiation:

$$f(E_a, t) = cat^{a-1} (E_a - E_0)^b \exp \left[-ct^a(E_a - E_0)^b \right]. \quad (2.64)$$

This distribution has a maximum at

$$t_p = \left(\frac{a-1}{ca} (E_a - E_0)^{-b} \right)^{1/a}, \quad (2.65)$$

and a mean time to breakdown given by

$$\langle t_b \rangle = \Gamma \left(\frac{1+1}{a} \right) c^{-1/a} (E_a - E_0)^{-b/a}, \quad (2.66)$$

where Γ is the gamma function.

A Weibull plot of the time in (2.63) will give a and the field dependence of the mean time to breakdown, and (2.66) will yield both E_0 and b/a when $\langle t_b \rangle$ has been measured for several values of E_a . From the value $F \left[ct^a(E_a - E_0)^b = 1 \right] = 0.632$, one can determine c . So all the parameters can be obtained from a series of measurements using different values of E_a .

Finally, we would like to point out again that the empirical formulae presented in the previous sections are valid for a 50% failure probability. If one wants a higher degree of reliability, one has to go back to the corresponding Weibull distribution in order to calculate the allowed stress. We shall illustrate this with an example.

For the case where there is a higher stress at the positive electrode and a uniform field distribution at this electrode, the breakdown strength of water is given by (2.43), which relates the field strength E above a threshold, the time t , and the area A , as follows:

$$Et^{1/3}A^{1/10} = k_+ = 0.3, \quad E \text{ in MV}, \quad t \text{ in } \mu\text{s}, \quad A \text{ in cm}^2.$$

We assume that $t = 0.050 \mu\text{s}$ and $A = 10 \text{ m}^2 = 10^5 \text{ cm}^2$, and seek the field strength at which the probability of breakdown is 10%. The stress variable

is $S = Et^{1/3}$. The 50% value $S_{0.5}$ is equal to $k_+/A^{1/10}$, from which we can directly infer that $B = 10$.

Thus S obeys the following Weibull distribution (Fig. 2.25):

$$F\left(\frac{S}{\langle S \rangle}\right) = 1 - e^{-(S/\langle S \rangle)^B}. \quad (2.67)$$

The relationship between $S_{0.5}$ and $\langle S \rangle$ is given by

$$\langle S \rangle = \frac{S_{0.5}}{(\ln 2)^{1/B}} = \frac{k_{\pm}}{(A \ln 2)^{1/10}}. \quad (2.68)$$

For our example, we obtain $\langle S \rangle = 9.84 \times 10^{-2}$. Next, we must determine $S_{0.1}$ for $F = 0.1$, i.e., $\ln(\ln(1/0.9)) = 10 \ln(S_{0.1}/\langle S \rangle)$, and therefore $S_{0.1} = \langle S \rangle e^{-0.225}$. Consequently, we have $S_{0.1} = 7.85 \times 10^{-2}$ and $E_{0.1} = 0.213$ MV/cm.

3 Energy Storage

Any electric energy storage device suitable for pulsed-power applications should meet the following list of requirements:

- high energy density;
- high breakdown strength;
- high discharge current capability;
- long storage time (low rate of energy leakage);
- high charging and discharging efficiency;
- large power multiplication (= ratio of power during charging to power during discharging);
- repetition rate capability and long lifetime;
- low specific cost.

It is evident that some of these requirements are in conflict and, depending on the kind of application and the spatial and environmental constraints, a compromise has to be found.

3.1 Pulse Discharge Capacitors

Despite the disadvantage in stored energy density, most pulsed-power systems are still based on high-voltage energy-storage capacitors. The main reason is that reliable, repetitive, fast closing switches are easier to build than the opening switches necessary to realize generators based on inductive storage. In addition, the energy hold time of capacitors is much longer than that of inductive storage devices, which is more convenient for some applications.

If the capacitance is C , the stored energy is $W_C = (1/2)CU^2$, where U is the charging voltage. The capacitance C is proportional to the area A and the relative dielectric constant ε , and inversely proportional to the thickness d of the dielectric: $C = \varepsilon\varepsilon_0 A/d$. A simple sketch showing the most important elements of a capacitor is presented in Fig. 3.1. In many capacitors, the metal electrodes are contacted by metallic tabs, which are either pressed or soldered to the electrodes. An insulating margin around the metal electrodes prevents flashover between the electrodes.

The lumped circuit model of a ‘real’ capacitor is shown in Fig. 3.2. The series resistance R_s is generally of the order of 0.1Ω . It is due to the leads,

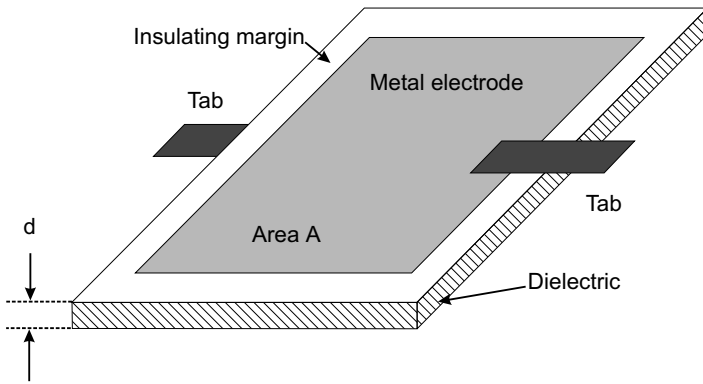


Fig. 3.1. Elements of a parallel-plate capacitor

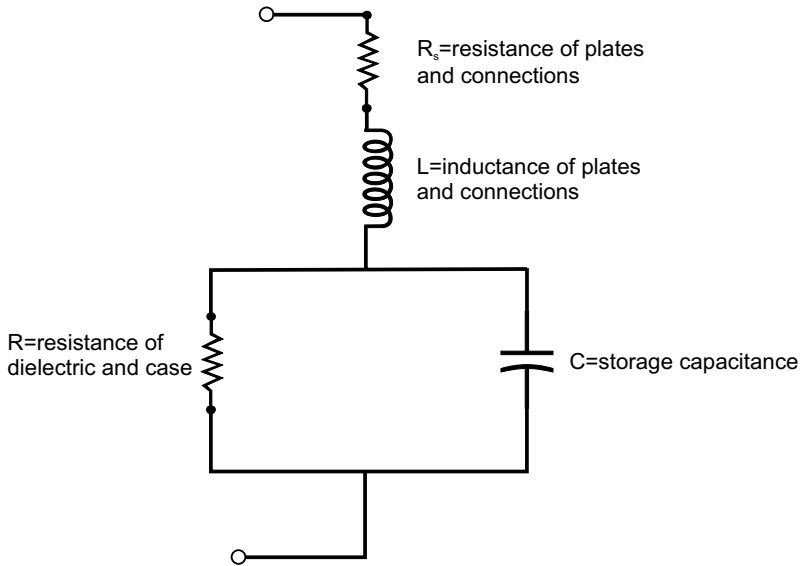


Fig. 3.2. Lumped circuit model of a capacitor

the tab contacts, and the electrodes. The parallel resistance R represents the current leakage path through the dielectric and over the case material. The inductance L associated with the internal arrangement of the capacitor is a limiting factor on the peak current that can be extracted: $I_p = U(C/L)^{1/2}$. The capacitance and the leakage resistance depend on the temperature, voltage, humidity, and storage time. The variation with temperature for a capacitor using castor-oil-impregnated paper as the dielectric is shown in Fig. 3.3. Even larger changes of the dielectric constant with temperature are found for epoxy and Mylar [Sarjeant and MacDougall 1997].

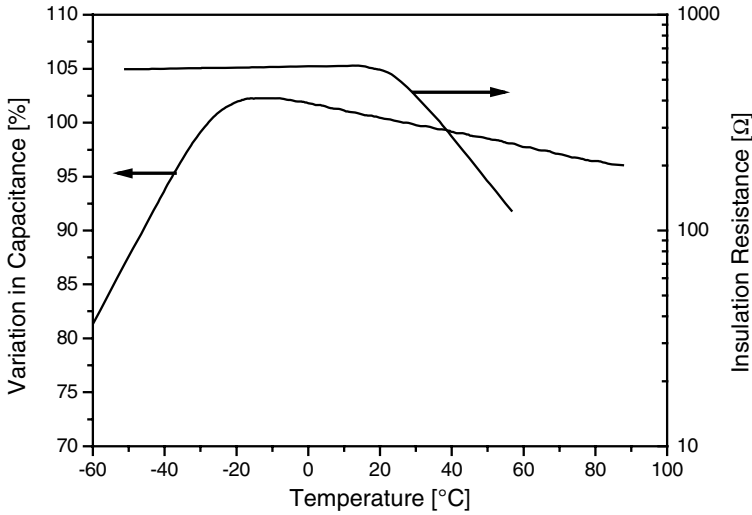


Fig. 3.3. Variation of capacitance and insulation resistance versus temperature for a capacitor using oil-impregnated paper as the dielectric

Table 3.1. Properties of some dielectric materials used for the insulation of high-voltage capacitors. Here E_{DB} is the static breakdown field

Material	ϵ	E_{DB} (kV/cm)	$\text{tg}(\delta)$
Impregnated paper	3–4	200–800	0.01–0.03
Epoxy	3.5	320	0.014
Mylar	3	400	0.001
Polypropylene	2.55	256	0.0005
Teflon	2.1	216	0.0002
Kapton	3.4	2800 (25 μm)	0.01
Plexiglas	3.3	200	0.009
Transformer oil	3.4	400	0.0002
Aluminiumoxide	8.8	126	0.01
Bariumtitanate	1143	30	0.01
Glass (borosilicate)	4.84	157	0.0036

In addition to its electric strength, some further important properties of a dielectric material are its dielectric constant ϵ and its loss factor $\text{tg} \delta$. These parameters are listed in Table 3.1 for some common dielectric materials.

The high-voltage strength of a capacitor is determined not only, and sometimes not even predominantly, by the breakdown strength of its dielectric,

but also by the shape, the area, and the metal used for the terminals and their bonding to the insulator that fills the case. In addition, the electric strength is also influenced by the conditions of operation. Temperature, pressure, humidity, and voltage reversal can all affect the breakdown threshold.

When a capacitor is charged or discharged quickly its instantaneous capacitance differs from the static value. This phenomenon results from the finite relaxation time of the polarisation, which is also responsible for the dielectric losses that occur in capacitors. We shall treat this effect by assuming an alternating field is applied to the capacitor. In general, both the polarisation P and the displacement D will lag behind in phase relative to the applied electric field E .

If we consider an oscillating field E of frequency ω ,

$$E = E_0 \cos \omega t, \quad (3.1)$$

we have

$$D = D_0 \cos(\omega t - \delta) = D_1 \cos \omega t + D_2 \sin \omega t, \quad (3.2)$$

where δ is the phase angle, $D_1 = D_0 \cos \delta$, and $D_2 = D_0 \sin \delta$.

For most dielectrics, D_0 is proportional to E_0 but the ratio D_0/E_0 is generally frequency-dependent. To describe this situation, one may thus introduce two frequency-dependent dielectric constants:

$$\begin{aligned} \varepsilon'(\omega) &= \frac{D_1}{E_0} = \frac{D_0}{E_0} \cos \delta, \\ \varepsilon''(\omega) &= \frac{D_2}{E_0} = \frac{D_0}{E_0} \sin \delta. \end{aligned} \quad (3.3)$$

According to (3.3), we have the relation:

$$\operatorname{tg} \delta = \frac{\varepsilon''(\omega)}{\varepsilon'(\omega)}. \quad (3.4)$$

Since $\varepsilon''(\omega)$ and $\varepsilon'(\omega)$ are frequency-dependent, the phase angle δ is frequency-dependent too. We shall now show that the energy dissipated in the dielectric in the form of heat is proportional to $\varepsilon''(\omega)$. The current density in the capacitor is equal to

$$j = \frac{dq}{dt} = \frac{dD}{dt} = \omega(-D_1 \sin \omega t + D_2 \cos \omega t), \quad (3.5)$$

where use has been made of (3.2). Here q is the surface charge density on the capacitor plates. Thus the energy density w dissipated in the dielectric per unit volume and time is given by

$$w = \frac{\omega}{2\pi} \int_0^{2\pi/\omega} jE dt. \quad (3.6)$$

By substituting for j and E , one easily finds

$$w = \frac{\omega}{2} E_0^2 \varepsilon'' = \frac{\omega}{2} E_0 D_0 \sin \delta \approx \left(\frac{\omega}{2} \right) E_0 D_0 \operatorname{tg} \delta. \quad (3.7)$$

It is correct to call $\sin \delta$ the loss factor; however, frequently $\operatorname{tg} \delta$ is taken as the loss factor. This is allowable only for small values of δ .

In general, the dielectric polarisation may be considered as the sum of two contributions:

$$P = P_s + P_d, \quad (3.8)$$

where the subscripts s and d refer to the spontaneous and the dipolar polarisation, respectively. P_s is due to electronic and atomic polarisation, which occurs very fast, while P_d appears in substances composed of molecules that have permanent electric dipole moments. If the field is suddenly switched on, P_d relaxes to the final, static value with a time constant τ . We can therefore assume that P can be expressed by

$$P = P_s + P_{dst} \left(1 - e^{-t/\tau} \right). \quad (3.9)$$

The static value is $P_{st} = P_s + P_{dst}$. Since the energy density w in a capacitor is given by

$$w = \frac{1}{2} \varepsilon_0 E^2 + \frac{1}{2} P E, \quad (3.10)$$

we have a fast term whose time dependence can be neglected at the usual switching speeds (not less than a nanosecond) in pulsed-power generators, and a relaxation term which affects the charging and discharging of capacitors.

As illustrated in Fig. 3.4, it takes some time before the capacitor has reached its final charge. In this figure, we have assumed ideal capacitors without resistance and inductance and a voltage source with zero impedance. In the case of discharge into a short circuit, an ideal switch was assumed. In practice, it may happen that the spark in a gas switch extinguishes before the capacitor has been completely discharged, because the voltage has dropped below a critical value. In this case the polarisation may continue to relax to the static value, which will be less than the preceding value, and the capacitor voltage can rise again, leading to a hazardous situation if the capacitor is not grounded continuously before it is handled. This situation is indicated by the horizontal dashed line in Fig. 3.4. Continuous grounding is also necessary because electrons which previously had penetrated into the dielectric may diffuse out and recharge the capacitor.

The complex impedance of a capacitor can be defined as

$$Z = R_{csr} + i \left(\omega L - \frac{1}{\omega C} \right), \quad (3.11)$$

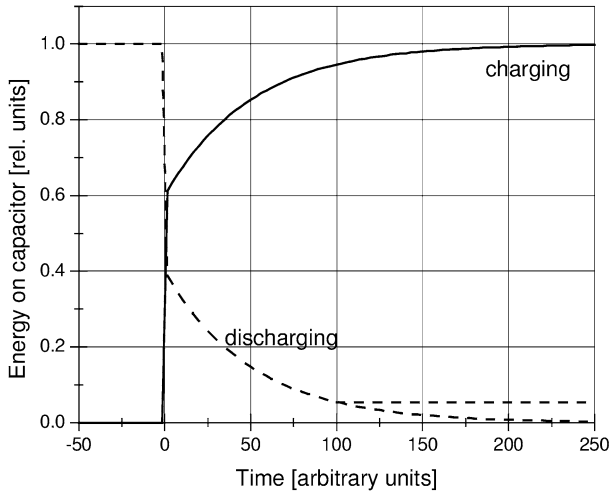


Fig. 3.4. Typical response of a dielectric to a square-wave voltage pulse (*curve labelled ‘charging’*) and to sudden switching of an ideal capacitor into an ideal short circuit (*curve labelled ‘discharging’*)

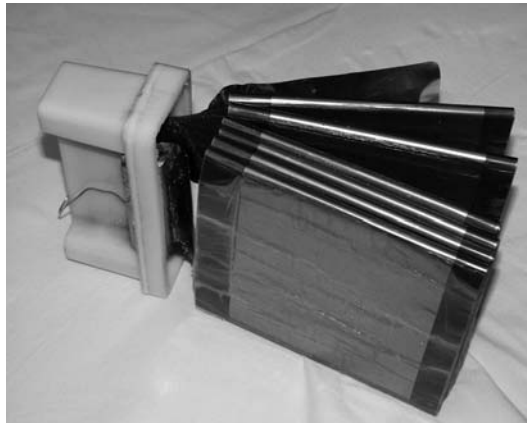


Fig. 3.5. 60 kV, 0.2 μF power capacitor consisting of six roll-ups. The case has been dismantled. The capacitor terminals are embedded in the plastic head on the left

where R_{esr} is the equivalent series resistance, which in most cases is equal to R_{s} (see Fig. 3.2). At the self-resonant frequency $\omega_{\text{r}} = 1/(LC)^{1/2}$, the inductive and the capacitive reactance cancel each other, and $Z = R_{\text{esr}}$. In general, it is necessary to stay much below ω_{r} to avoid large power losses inside the capacitor, which could destroy it. As shown in Fig. 3.5, a power capacitor can consist of several packs rolled up from a stripline such as that sketched in Fig. 3.1. Therefore, depending on the position of the tab, the minimum discharge time can be limited by the two-way transit time between the stripline end and the

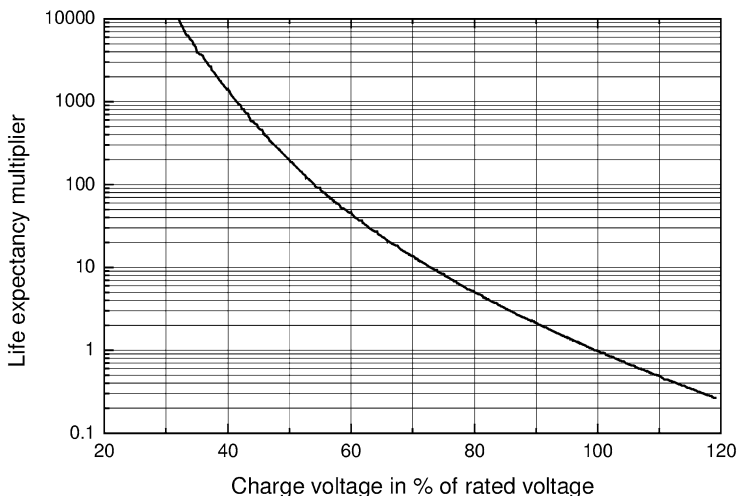


Fig. 3.6. Life expectancy of a capacitor versus charge voltage

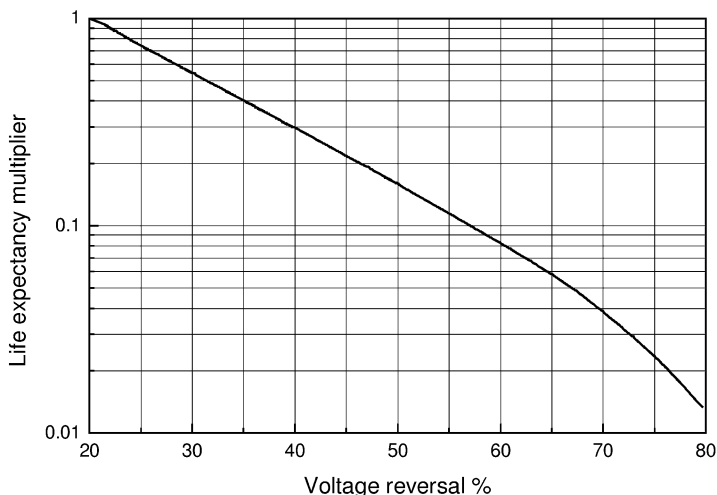


Fig. 3.7. Voltage reversal coefficient of life

tab position and may become larger than the LC ringing time. Consequently, a fast capacitor also requires stacks with a short path to the terminals.

Capacitor lifetime can be affected strongly by the ratio of charge to rated voltage and by voltage reversal. The sensitivity to voltage reversal can be understood on the basis of the breakdown models discussed in Chap. 2. If charge has been injected from the metallic-cathode side into the dielectric, the space charge field associated with it can add to the external field during voltage reversal and the total field can exceed the local breakdown stress and cause damage to the material. Figures 3.6 and 3.7 show the life expectancy as

a function of the percentage of the rated voltage and as a function of voltage reversal, respectively, for some high-energy-density capacitors. For industrial pulsed-power applications, a shot life of greater than 10^8 is often required. This can be achieved either by operating capacitors much below their rated voltage or by designing them with very conservative dielectric insulation, i.e., with a large size and low energy density.

Failure in capacitors results mainly from three sources: surface tracking along the insulating margin at the edges of capacitor sections, breakdown at voids or impurities in the dielectric, and arcing at pressure-contacted tabs or in other sections of the capacitor. Arcing produces gasification of materials and builds up pressure in the capacitor case. It can be avoided if all contacts are soldered or welded. Surface tracking can be eliminated by resistively grading the field distribution at the capacitor edge. This can be achieved, for example, by impregnating the paper with a dilute solution of copper sulphate in water. However, the problem with this technique is that it increases the loss current in the capacitor and reduces the hold time dramatically. A breakdown in the dielectric need not necessarily destroy the capacitor if the metal conductor is a thin film which can carry only a limited current density. If a breakdown occurs at a small spot, current will flow from the capacitor plates through the fault and evaporate the metal in the immediate neighbourhood of such a spot and, except for a small loss of capacitance, the capacitor will remain functioning [Slenes et al. 2001]. This self-clearing process is illustrated in Fig. 3.8.

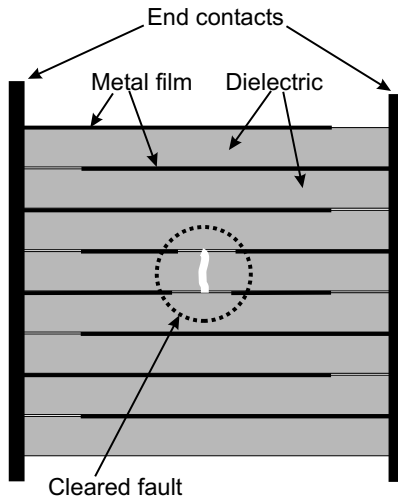


Fig. 3.8. Metallized-film capacitor stack with cleared breakdown spot

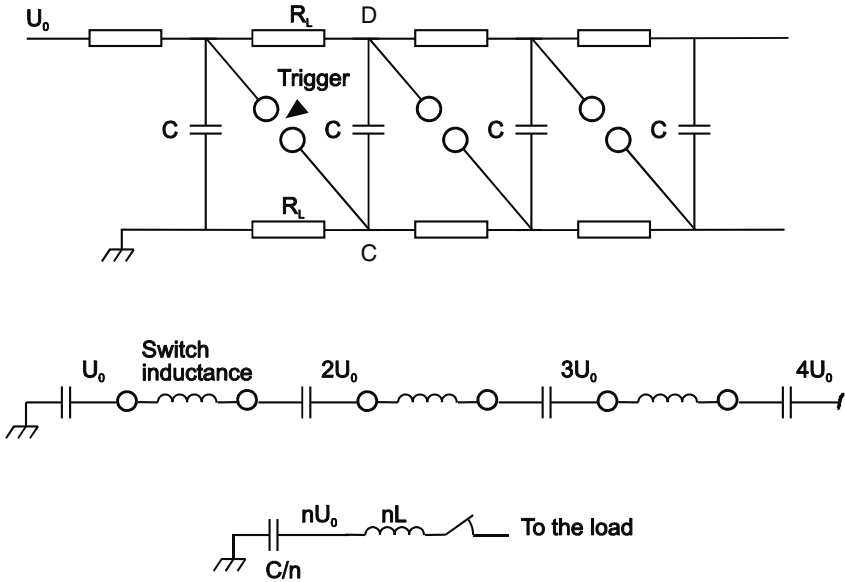


Fig. 3.9. Marx generator circuit with unipolar charging through the resistors R_L (top). Configuration of Marx after firing of all switches (middle). Lumped circuit model of erected Marx generator (bottom)

3.2 Marx Generators

3.2.1 Classical Marx Generators

In general, high-voltage pulse capacitors are built for operating voltages below 100 kV. The main reason for this is that transformers for high-power charging supply units become prohibitively large above 100 kV. To produce pulses with larger amplitudes, Marx generator circuits can be used. The basic circuit was patented by Erwin Marx in 1923 [Marx 1923, 1924]. The fundamental principle of this generator is to charge several capacitors in parallel and then to switch them into a series configuration for discharging. Thus the output voltage becomes the charging voltage multiplied by the number of capacitor units. Figure 3.9 illustrates a simple Marx generator circuit with unipolar charging neglecting stray capacitances. The capacitors are charged through the resistors R_L while the switches are open.

If the first switch is closed, the voltage at point C is driven to the charging voltage U_0 . Therefore the voltage at point D must jump to $2U_0$. At this instant, the second gap has a voltage $2U_0$ across it and, if properly designed, must break down. This process proceeds until all gaps have fired sequentially. At this time, the Marx generator is said to have been erected. The time for this process is normally of the order of a microsecond.

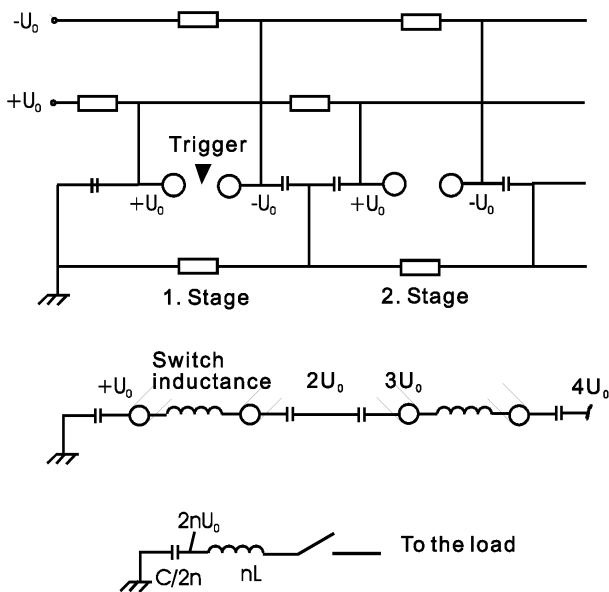


Fig. 3.10. Marx generator with bipolar charging. Compared with the simple circuit of Fig. 3.9, only half the number of switches are required. Stray capacitances have been neglected again

Another Marx circuit, shown in Fig. 3.10, uses bipolar charging. In this design, the number of switches is only half that for the simple circuit. Initially, the voltage across each switch is $2U_0$. After it has been erected, the Marx generator is equivalent to the circuit shown in the middle part of Fig. 3.10, which can be reduced further to the circuit drawn at the bottom. Here L is the inductance resulting from the capacitor, from its connections to the switch, and from the closed switch itself. The total capacitance C_M of the erected Marx generator is $C/2n$, while the total inductance L_M equals $nL_s + 2nL_c$, where n is the number of stages and L_s and L_c are the inductances of the switch and capacitor, respectively. Of course, the stored energy is $W_M = 2n(1/2)CU_0^2$. The impedance of the Marx generator is $Z_M = (L_M/C_M)^{1/2} = n[2(2L_c + L_s)/C_0]^{1/2}$. This determines the power that the generator can deliver to a load.

The smaller the impedance, the larger is the available power. Since the impedance increases with the number of stages n , it becomes more and more difficult to raise the power of Marx generators to the terawatt level and above. Therefore, the major task of Marx generators in ultra-high-power generators is to pulse-charge an intermediate storage (water or oil) capacitor. As the breakdown strength of water depends on the duration of the electric-field stress, charging must happen quickly if a high energy density is to be obtained. To obtain complete energy transfer, the capacitance of the intermedi-

ate storage device must equal the capacitance of the erected Marx generator. Consequently, the charging time is proportional to the oscillation period τ of the Marx generator.

By expressing C_M and L_M through the stored energy and the voltage of the erected Marx generator, we see from (3.12) that, for a fixed voltage pulse amplitude, the charging time is proportional to the square root of the stored energy W_M :

$$\begin{aligned} \tau &\propto \sqrt{L_M C_M}, & C_M &\propto \frac{W_M}{U_M^2}, & L_M &\propto U_M, \\ \tau &\propto \sqrt{\frac{W_M}{U_M}}. \end{aligned} \quad (3.12)$$

Thus, to achieve high energy densities and short, high-power pulses it may be more beneficial to synchronise several Marx generators of reduced pulse energy to charge one water capacitor.

Let us reconsider the simple Marx generator of Fig. 3.9. After all switches but the last one have closed, each capacitor begins to discharge through two resistors in parallel. The time constant of this discharge process is

$$\tau = \frac{1}{2} R_L C_0. \quad (3.13)$$

If a load is connected to the output of the Marx generator, the generator discharges with a time constant that depends on the load impedance. This time constant must be short compared with τ if most of the energy is to be delivered to the load. Dissipating energy in the charging resistors is undesirable both during charge and discharge, since it reduces the generator efficiency. Sometimes inductors are used instead of resistors in the charging circuit. In this case the time constant for self-discharge after switch closure becomes

$$\tau = 2\pi \left(\frac{1}{2} L_L C_0 \right)^{1/2}. \quad (3.14)$$

In this case also τ must be made several times larger than the duration of the output pulse.

Modern power supplies are able to charge the capacitors with a constant current (see Sect. 6.3). However, because of the serial chain of charging resistors, each capacitor in a Marx configuration is charged at a different rate. An approximate expression for the charging time constant of the n th capacitor is given by

$$\tau_n = R_L C_0 n^2. \quad (3.15)$$

In this case the difference ΔU_0 in voltage between the first and the last capacitor after charging for a time t is given by

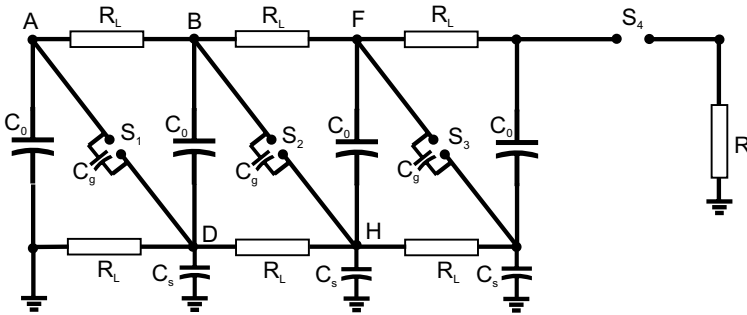


Fig. 3.11. Marx generator with stray capacitances C_s between stage capacitors and ground, and C_g across switches. Stray capacitances between A, B, F, etc. and ground have been assumed to be negligible

$$\frac{\Delta U_0}{U_0} = \frac{R_L C_0 n^2}{t}. \tag{3.16}$$

Any tolerable ratio $\Delta U_0/U_0$ determines a minimum charging time t . For repetitive operation, this can limit the repetition frequency.

Triggering the Marx generator means starting the erection process by external-command control at a preselected instant in time. The general design goals are to achieve a low prefire probability, a large operating range, and a small jitter. By ‘jitter’, we mean the statistical standard deviation of the switching time. Most Marx generators use triggerable three-electrode spark gaps as switches in the first stage and self-breaking spark gaps in the later stages. Triggering is achieved by applying an ignition pulse to the trigger electrode of the three-electrode spark gap (see Sect. 4.1.1).

In our previous discussion of Marx generator erection, we neglected stray capacitances. Stray capacitances appear between the stage capacitors and ground, represented by C_s , and between the switch electrodes, represented by C_g . Stray capacitances may also occur between points A, B, F, etc. and ground. C_g also includes the mutual capacitance between capacitor cases. They are of paramount importance for the operation of a Marx generator. We shall discuss their effect on the basis of the more realistic Marx circuit presented in Fig. 3.11. Here the distributed stray capacitance C_s has been lumped into discrete capacitances per stage.

We assume that each capacitor has been charged to U_0 and that the spark gap switch S_1 has been triggered. The stray capacitance at point D tries to hold that point at ground. Generally, the stage capacitance C_0 is much larger than C_s and the latter will rapidly charge to a value very close to U_0 . Then point B will jump to a potential $2U_0$. The next switch gap, S_2 , will fire only if it is overvolted sufficiently long. The stray capacitances C_g of switch S_2 and C_s at point H form a capacitive voltage divider, and the potential drop across S_2 is therefore given by

$$\Delta U = \frac{2U_0}{1 + C_g/C_s}. \quad (3.17)$$

In designing a Marx generator one must take care that the ratio C_g/C_s is sufficiently small. This can be achieved, for example, by placing a grounded conducting plate close to the case of the storage capacitor C_0 .

However, even with this measure, the overvoltage across S_2 does not last very long. As point D is charged to U_0 , point H will charge to the same potential, since D and H are connected through the charging resistor R_L . In parallel with this process, point F tends to charge to $2U_0$, since it is connected to B, which is at $2U_0$. If C_0 is large compared with C_s , it can be considered as a voltage source of magnitude $-U_0$, and the potential at H would also tend to U_0 by this process alone. Since both processes act in parallel, the time constant for charging C_s at H is $1/2R_L C_s$. The main point here is that the overvoltage across switch S_2 is reduced, with that time constant, and it will finally approach U_0 again. Hence the switch must be designed such that it breaks down at an overvoltage ΔU with a delay much less than $1/2R_L C_s$. We can extend the preceding discussion to the subsequent switches. However, since the overvoltage becomes increasingly larger, it becomes easier and easier to break down the other gaps.

To prevent prefire of the Marx generator, each switch must be operated with a sufficient safety margin. We can define this safety factor as the ratio m between the switch breakdown voltage U_b and the operating voltage U_0 . Thus, to achieve breakdown, the overvoltage across the gap must be greater than mU_0 . From the discussion of the Marx generator shown in Fig. 3.11, it is clear that m cannot be larger than 2. Indeed, it should be much less than 2 if reliable switching is to be obtained.

Instead of triggering one switch, one could trigger the first k gaps. Although this increases the overvoltage of the $(k + 1)$ th gap to

$$\Delta U = kU_0 \frac{2}{1 + \sqrt{1 + 4C_g/C_s}}, \quad (3.18)$$

this does not enlarge the safety factor m very much since, as we shall see later (Sect. 4.1), reliable triggering of three-electrode spark gaps is possible only for $m < 1.5$.

The generator concept shown in Fig. 3.9 is the example of an $n = 1$ Marx generator, i.e., the erection wave is capacitively coupled to the next gap. A section of a unipolar Marx generator where the coupling is across every two gaps ($n = 2$) is sketched in Fig. 3.12 [Nation 1979]. The system is arranged such that there is a large coupling capacitance C_c across every two gaps. To understand the rationale behind this design, we assume that the previous $(p - 1)$ gaps have closed so that the potential at point A is pU_0 . As in the previous case, the gap capacitance C_g and the coupling capacitance C_c form a voltage divider, and the potential at point B is

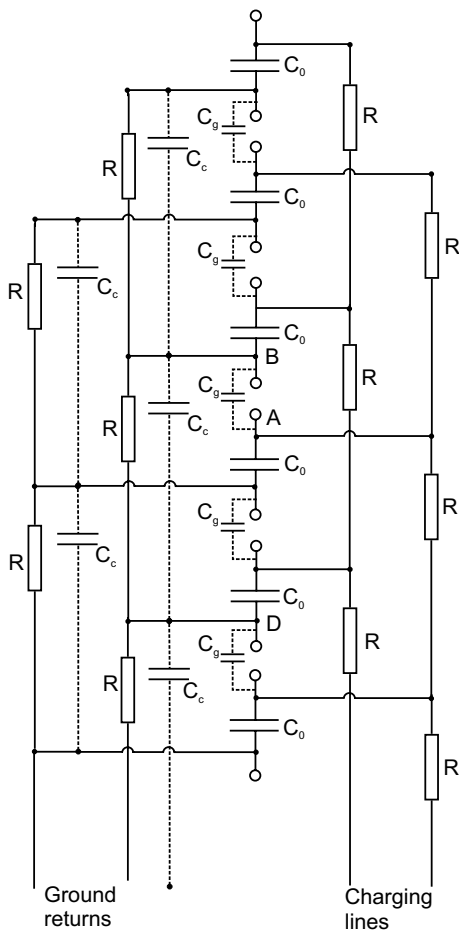


Fig. 3.12. $n = 2$ Marx generator with capacitive coupling across every two gaps

$$U_B = (p - 2)U_0 + \frac{2U_0 C_g}{C_g + C_c}. \tag{3.19}$$

Hence the potential difference across the gap AB is

$$\Delta U = \frac{2U_0}{1 + C_g/C_c}. \tag{3.20}$$

As the capacitor C_c discharges through R , the potential difference approaches $2U_0$ (instead of U_0 for the $n = 1$ Marx generator). This is a characteristic of a $n = 2$ Marx generator, in which the coupling capacitors C_c are made large and the charging and ground return resistors also bridge two gaps. In an $n = 3$ Marx configuration, the coupling capacitors and the charging resistors straddle three gaps and an overvoltage of $3U_0$ can be achieved.

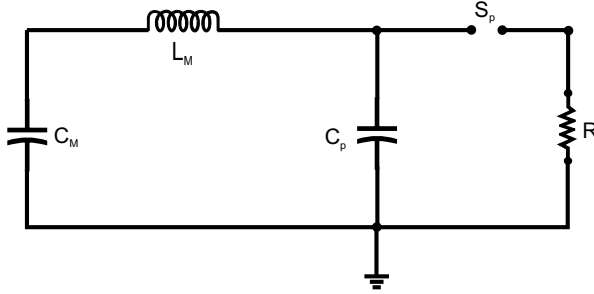


Fig. 3.13. Peaking-capacitor circuit

However, in this case at least the first two switches must be triggered. An advantage of the high- n Marx configurations is that they are relatively free of self-breakdown problems. However, they tend to erect more slowly. The reliability of sequential switching can be improved if a UV-transparent line of sight exists between adjacent gaps. By this means, a pre-ionisation of the subsequent switch gaps can be obtained, reducing the breakdown delay.

If the Marx generator is placed in a metallic tank, the stray capacitance can be estimated by the following rule of thumb: the Marx column itself is considered to be a metallic conductor, and the capacitance between this conductor and the tank calculated on this assumption is then divided by the number of Marx stages to obtain the stray capacitance of each stage.

Since a Marx generator is an oscillatory circuit, the voltage at the capacitors can reverse. As we know already that this reduces the capacitor lifetime, it is desirable to prevent it. A crowbar switch at the exit of the generator that fires just when the voltage starts to reverse can accomplish this task. In general, triggering of the crowbar switch is necessary, since the voltage will be low at the time of reversal.

The rise time of the output of a Marx generator can be improved by using a peaking capacitor. A possible configuration is shown in Fig. 3.13. Here, the Marx generator has been represented by the serial capacitance and inductance of the erected generator. The peaking circuit consists of an extra capacitor C_p and an extra switch S_p . C_p is charged to $U_p = U_M 2 C_M / (C_M + C_p)$.

3.2.2 LC Marx Generator

A special variant of the Marx-generator is the LC generator shown in Fig. 3.10, which was first proposed by Fitch at Maxwell Labs [Fitch 1964]. Therefore this configuration is also called a Fitch generator.

As illustrated in Fig. 3.14, consecutive capacitors are charged with opposite polarity. Therefore, the sum of the voltage between the output and ground is zero at first. When the switches are closed, an oscillating discharge occurs, reversing the charge of every second capacitor, and after half a period

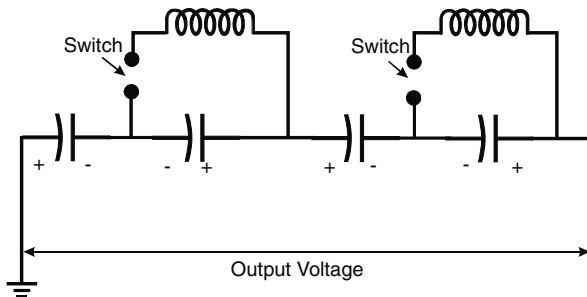


Fig. 3.14. Simplified representation of an *LC* Marx generator

the output voltage becomes nU_0 , where n is the number of capacitors. The advantage of this configuration is that the inductance has a minimum, since the inductance of the switches is located outside the erected Marx circuit. A difficulty is that all switches must be fired with very low jitter, because otherwise an overvoltage can appear in certain stages. The output voltage as a function of time is given by $U(t) = (1/2)nU_0 [1 - e^{-t/2\tau} \cos(\omega t)]$; here $\omega^2 = 1/LC$, and $\tau = L/R$, where R is the sum of the switch, capacitor, and wiring resistances.

3.2.3 Basic Pulsed-Power Energy Transfer Stage

It has been mentioned already that a Marx generator is used very frequently to rapidly charge an intermediate storage capacitor. Thus we have the situation shown in Fig. 3.15, where an initially charged capacitor is discharged into an initially empty capacitor. Because of its importance for pulsed-power technique, this transfer process will be treated in detail below.

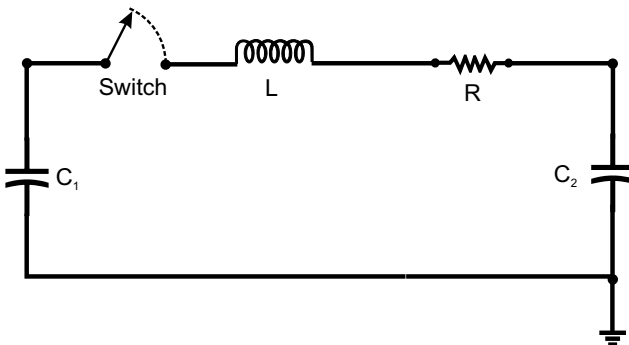


Fig. 3.15. Basic circuit diagram for the evaluation of the energy transfer from C_1 to C_2

We consider the energy balance as follows:

$$\frac{1}{2} C_1 U_1^2 + \frac{1}{2} L I^2 + \int R I^2 dt + \frac{1}{2} C_2 U_2^2 = W_0 ; \quad (3.21)$$

$$\frac{d}{dt} : C_1 U_1 \frac{dU_1}{dt} + L I \frac{dI}{dt} + R I^2 + C_2 U_2 \frac{dU_2}{dt} = 0, \quad (3.22)$$

$$U_1 + L \frac{dI}{dt} + R I + U_2 = 0, \quad (3.23)$$

$$\frac{Q_1}{C_1} + L \frac{dI}{dt} + R I + \frac{Q_2}{C_2} = 0; \quad (3.24)$$

$$\frac{d}{dt} : L \frac{d^2 I}{dt^2} + R \frac{dI}{dt} + I \frac{C_1 + C_2}{C_1 C_2} = 0; \quad (3.25)$$

here, W_0 is the energy initially stored in the capacitor C_1 .

Using the abbreviations

$$\begin{aligned} \tau &= \frac{L}{R}, \\ C &= \frac{C_1 C_2}{C_1 + C_2}, \\ \omega_0^2 &= \frac{1}{LC}, \\ \omega^2 &= \left| \frac{1}{LC} - \frac{1}{(2\tau)^2} \right|, \end{aligned}$$

we can write (3.25) as

$$\frac{d^2 I}{dt^2} + \frac{1}{\tau} \frac{dI}{dt} + \omega_0^2 I = 0. \quad (3.26)$$

A solution of the differential equation (3.26) is obtained by using the ansatz $I = Ae^{\lambda t}$, with the initial conditions $I(0) = 0$ and $dI/dt(0) = U_0/L$. For the characteristic roots $\lambda_{1,2}$, we obtain

$$\lambda_{1,2} = -\frac{1}{2\tau} \pm \sqrt{\frac{1}{4\tau^2} - \omega_0^2}. \quad (3.27)$$

For further treatment we have to distinguish three cases:

1. $\omega_0 \tau > 1/2$. In our context, this is the most important case, and the solution is

$$I = \frac{U_0}{\omega L} e^{-t/2\tau} \sin \omega t \quad (3.28)$$

$$I_{\max} \approx \frac{U_0}{(L/C)^{1/2} + 0.8 R}. \quad (3.29)$$

In this case, we calculate the following for the output voltage:

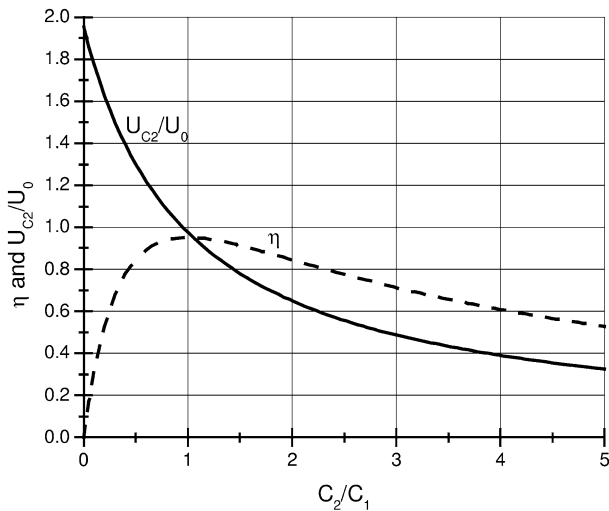


Fig. 3.16. Relative energy transfer η and relative voltage on C_2 as a function of C_2/C_1

$$U_{C_2}(t) = \frac{\int_0^t I(t') dt'}{C_2} = \frac{U_0 C_1}{C_1 + C_2} \left[1 - e^{-t/2\tau} \left(\cos \omega t - \frac{1}{2\omega\tau} \sin \omega t \right) \right],$$

$$U_{C_2}(\text{max}) = \frac{U_0 C_1}{C_1 + C_2} \left[1 + e^{-\pi/2\omega\tau} \right]. \tag{3.30}$$

For the relative energy transfer, we obtain

$$\eta = \frac{C_1 C_2}{(C_1 + C_2)^2} \left(1 + e^{-\pi/2\omega\tau} \right)^2. \tag{3.31}$$

The residual voltage on C_1 is

$$U_{C_1}(t) = \frac{U_0 C_1}{C_1 + C_2} + \frac{U_0 C_2}{C_1 + C_2} \left(\cos \omega t + \frac{1}{2\omega\tau} \sin \omega t \right) e^{-t/2\tau},$$

$$U_{C_1}(\text{min}) = \frac{U_0}{C_1 + C_2} \left(C_1 - C_2 e^{-\pi/2\omega\tau} \right). \tag{3.32}$$

Figure 3.16 shows the relative energy transfer to and the relative voltage on C_2 as a function of the ratio C_2/C_1 . The energy transfer is complete if R is small and $C_1 = C_2$. A voltage magnification (‘ring-up’) of < 2 can be achieved if $C_2 < C_1$.

2. $\omega_0\tau = 1/2$. In this case, the critically damped case, we have

$$I(t) = \frac{U_0}{L} t e^{-t/2\tau}, \tag{3.33}$$

and the voltage on capacitor C_2 is

$$U_{C_2} = \frac{U_0}{1 + C_2/C_1} \frac{1}{2\tau} \left\{ 2\tau - (t + 2\tau) e^{-t/2\tau} \right\}. \quad (3.34)$$

Obviously, the relative energy transfer turns out to be less than 1/4.

- $\omega_0\tau < 1/2$. For completeness, we present, finally, the result for the third case:

$$I(t) = \frac{U_0}{\omega L} e^{-t/2\tau} \sinh \omega t. \quad (3.35)$$

Here, we calculate the following for the voltage on capacitor C_2 :

$$U_{C_2} = \frac{U_0}{C_2\omega L} \frac{2\tau e^{-t/2\tau} (2e^{t/2\tau} - 2\omega\tau \cosh \omega t - \sinh \omega t)}{1 - 4\omega^2\tau^2}. \quad (3.36)$$

3.3 Inductive Energy Storage

A generator using capacitive energy storage can be considered as a current amplifier. Generators that use inductive storage are voltage amplifiers. As stated in Chap. 1, in an inductive storage device the energy is stored in the magnetic field. The energy density in an inductive storage system can be up to two orders of magnitude higher than in a capacitive system, even if one takes into account the volume necessary for the dielectric insulation. The basic circuit of an inductive generator is shown in Fig. 3.17.

The inductance L is charged from a current generator with an internal impedance R_g while the opening switch is closed and the closing switch is open. The current through the inductor rises to a maximum value $I_0 R_g / (R_g + R)$:

$$I(t) = I_0 \frac{R_g}{R + R_g} \left(1 - e^{-[(R+R_g)/L]t} \right). \quad (3.37)$$

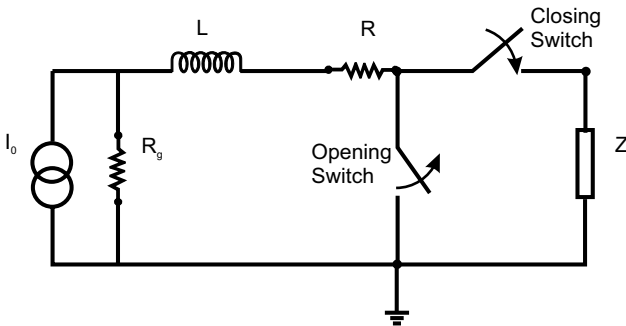


Fig. 3.17. Basic circuit of a pulsed-power generator with inductive storage

The time constant τ_L for charging is $L/(R + R_g)$. If the load current I_0 is large, charging of the inductor must occur rapidly and the storage time must be short, because otherwise the energy loss in the resistance of the inductor windings and the switch becomes unacceptably large and the overall efficiency of the system drops. To achieve fast charging of the inductor, the current source must have a high internal impedance and a large power.

3.3.1 Power and Voltage Multiplication

Let us assume that the storage inductance has been charged at time $t = 0$ and that the current flowing through the inductor is now $I_1(0)$. We neglect R , introduce a parasitic inductance L_2 , and replace the current source by a pulsed voltage source $U_0 = I_0 R_g$, which is able to deliver a current pulse of magnitude I_0 for a duration of τ_p , as shown in Fig. 3.18. If we require that $I_1(0)$ should come close to I_0 , then L_1/R_g must be small compared with τ_p . At time $t = 0$, the opening switch opens instantaneously from zero resistance to a final resistance R_s . Part of the load current $I_1(0)$ is then diverted from the switch through the parasitic inductance L_2 into the load R_l . If $I_1(t)$ and $I_2(t)$ are the currents flowing through the storage inductor and through the load, respectively, we have

$$0 = R_g I_1 + L_1 \frac{dI_1}{dt} + R_s (I_1 - I_2) , \quad (3.38)$$

$$0 = R_l I_2 + L_2 \frac{dI_2}{dt} + R_s (I_2 - I_1) . \quad (3.39)$$

This system of coupled differential equations has two characteristic roots τ_{\pm} :

$$\tau_{\pm} = \left[\frac{R_l + R_s}{2L_2} + \frac{R_g + R_s}{2L_1} \right] \times \left[1 \pm \sqrt{1 - \frac{4L_1 L_2 [(R_l + R_s)(R_g + R_s) - R_s^2]}{[L_1 (R_l + R_s) + L_2 (R_g + R_s)]^2}} \right] . \quad (3.40)$$

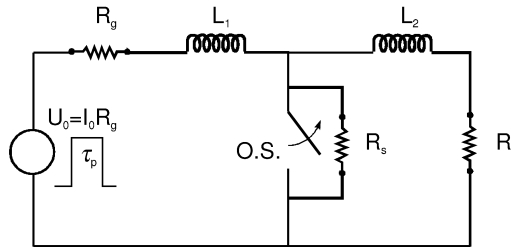


Fig. 3.18. Simplified circuit diagram for the analysis of power and voltage multiplication with a generator based on inductive energy storage

Equation (3.40) can be simplified for $R_s \gg R_l, R_g$, and $L_1 \gg L_2$. Under these conditions, we have

$$\begin{aligned}\tau_+ &= \frac{L_2}{R_s}, \\ \tau_- &= \frac{L_1}{R_g + R_l}, \\ \tau_+ &\ll \tau_-.\end{aligned}\tag{3.41}$$

Finally, using the initial conditions $I_1(0) = I(0)$ and $I_2(0) = 0$, we find

$$I_1(t) \approx \frac{L_1 I(0)}{L_1 + L_2} \left[e^{-t/\tau_-} + \frac{L_2}{L_1} e^{-t/\tau_+} \right],\tag{3.42a}$$

$$I_2(t) \approx \frac{L_1 I(0)}{L_1 + L_2} \left[e^{-t/\tau_-} - e^{-t/\tau_+} \right],\tag{3.42b}$$

$$I_s(t) = I_1 - I_2 \approx I(0) e^{-t/\tau_+}.\tag{3.42c}$$

In this case, the switching time τ_s within which the current through the opening switch decays is given by $\tau_s = \tau_+$. Since $\tau_+ \ll \tau_-$, the load current $I_2(t)$ is determined by τ_- . The current flowing in the storage inductor L_1 before and after switch opening $I(t)$ (3.37) and $I_1(t)$ (3.42a), respectively, the switch current $I_s(t)$ after the start of opening, and the load current $I_2(t)$ are plotted in Fig. 3.19.

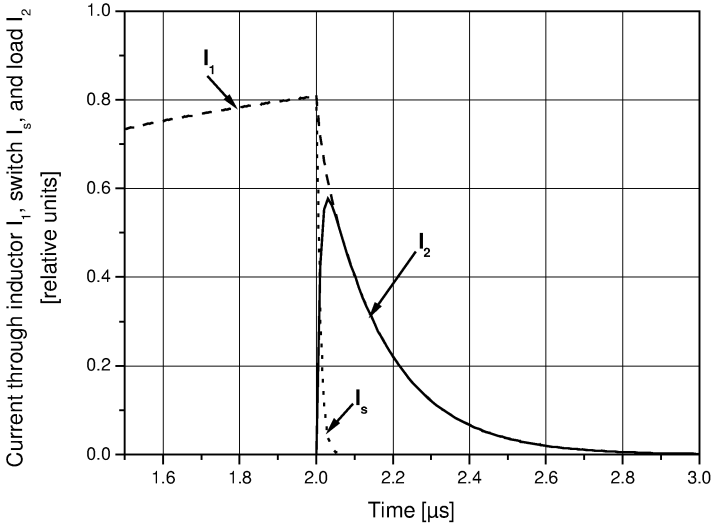


Fig. 3.19. Inductor, load, and switch currents in a generator based on inductive storage and opening switches. ($L_1 = 1 \mu\text{H}$, $L_2 = 0.1 \mu\text{H}$, $R_g = 1 \Omega$, $R = 0.1 \Omega$, $R_s = 10 \Omega$, $R_l = 5 \Omega$)

The power $P = I_2(t)R_l$ generated in the load has a maximum value of

$$P_m = \frac{R_l L_1^2 I(0)^2}{(L_1 + L_2)^2} \left(1 - \frac{2}{x} (\ln x + 1) \right),$$

$$x = \frac{R_s L_1}{L_2 (R_g + R_l)} \gg 1. \quad (3.43)$$

To calculate the power multiplication factor M , we have to compare P_m with the maximum power that the source would have delivered to the load if the inductor were absent. Of course, this is the power into a matched load, i.e., when $R_l = R_g$:

$$P_{al} = \frac{I_0^2 R_g}{4}. \quad (3.44)$$

Therefore we obtain

$$M = \frac{P_m}{P_{al}} \approx \frac{4R_l}{R_g} \frac{L_1^2}{(L_1 + L_2)^2} \left(1 - e^{-R_g \tau_p / L_1} \right)^2 \left(1 - \frac{2}{x} (\ln x + 1) \right). \quad (3.45)$$

M increases linearly with the ratio R_l/R_g . We see also that it is desirable to keep the parasitic inductance L_2 as small as possible. The voltage multiplication factor M_V also grows in proportion to R_l/R_g :

$$M_V \propto \frac{R_l}{R_g} \frac{L_1}{L_1 + L_2} \frac{I(0)}{I_0}. \quad (3.46)$$

3.4 Rotors and Homopolar Generators

A non-superconducting inductive storage system dissipates its energy with a time constant L/R . If we require an efficient use of energy, the inductor must be charged in a time that is short compared with L/R . For large devices storing multimegajoule energies, we therefore need a pulsed current source of very large power. For this purpose, it is necessary to store the energy intermediately, for example, in a flywheel. The kinetic energy of a flywheel is

$$W_{kin} = \frac{1}{2} \Theta \omega^2, \quad (3.47)$$

where Θ is the moment of inertia and ω is the angular velocity. The specific stored energy can reach values as high as 300 MJ/m³ (see Chap. 1), and total energies of more than 100 MJ are possible. A flywheel can transfer its energy only in a time that is greater than 10 ms in most cases. A suitable pulsed high-current generator that is based on a flywheel is the homopolar generator, whose principle is shown in Fig. 3.20.

In a homopolar generator, the flywheel also serves as a rotor. The generator can be considered to be a mechanical capacitor of very high, variable

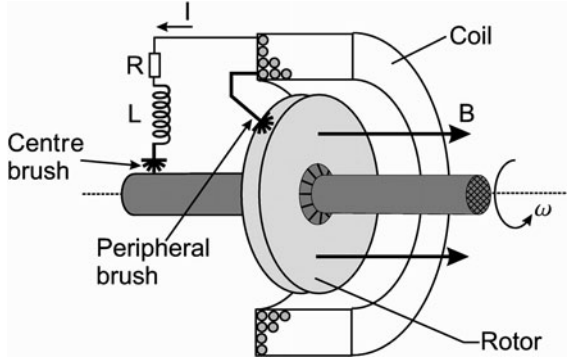


Fig. 3.20. Basic set-up of a self-exciting homopolar generator

equivalent capacitance. Its operation is based on Faraday's law. For the loop voltage, we obtain

$$U = -\frac{d}{dt} \int \vec{B} \cdot d\vec{A} = -\int \frac{\partial}{\partial t} \vec{B} \cdot d\vec{A} - \oint (\vec{B} \times \vec{u}) \cdot d\vec{s}. \quad (3.48)$$

We can derive this relationship if we consider the electric field in the rest frame of the flywheel. Using the well-known formula for the transformation of fields in a moving frame, we have

$$\vec{E}' = \vec{E} + \vec{u} \times \vec{B}. \quad (3.49)$$

Hence the voltage acting between two points on the rotor in Fig. 3.20 is

$$\begin{aligned} U &= \oint (\vec{E} + \vec{u} \times \vec{B}) \cdot d\vec{s} = \int \text{curl } \vec{E} \cdot d\vec{f} + \oint (\vec{u} \times \vec{B}) \cdot d\vec{s} \\ &= -\int \frac{\partial \vec{B}}{\partial t} \cdot d\vec{f} - \oint (\vec{B} \times \vec{u}) \cdot d\vec{s}. \end{aligned} \quad (3.50)$$

The first term on the right-hand side can be neglected, if the building-up of B (in case of a self-exciting generator) is sufficiently slow. The second term in (3.50) creates a potential drop along a radius of the rotor.

In a self-exciting generator, the magnetic field B is created by the output current of the rotor [Driga et al. 2001]. Therefore the induced voltage must be proportional to the current I and the angular velocity ω :

$$U = \alpha I \omega, \quad (3.51)$$

where α is a machine parameter.

Considering the electric circuit we have:

$$L \frac{dI}{dt} + IR = \alpha I \omega \quad (3.52)$$

where L is the total (constant) inductance of the generator, which in most cases is identical to the storage inductance, and R is the total resistance of the rotor, the coil, and the contact brushes. A second equation can be derived from energy conservation:

$$\frac{1}{2}\Theta\omega^2 + \frac{1}{2}LI^2 + \int_0^t I^2 R dt = \frac{1}{2}\Theta\omega_0^2, \quad (3.53)$$

where ω_0 is the initial angular velocity of the rotor. Differentiating with respect to the time t and using the relation

$$\frac{dI}{dt} = (\alpha\omega - R)\frac{I}{L} = \alpha(\omega - \omega_c)\frac{I}{L} \quad (3.54)$$

derived from (3.52), we obtain

$$\Theta \frac{d\omega}{dt} = -\alpha I^2. \quad (3.55)$$

The current can rise only if the initial angular velocity ω_0 is greater than some critical value $\omega_c = R/\alpha$. By eliminating the time t from (3.54) and (3.55), we can derive a differential equation relating I to ω :

$$\begin{aligned} \frac{L}{\Theta} \frac{dI}{d\omega} &= \frac{\omega_c - \omega}{I}, \\ I^2 + \frac{\Theta}{L}(\omega - \omega_c)^2 &= \frac{\Theta}{L}(\omega_0 - \omega_c)^2 + I_0^2 = A, \end{aligned} \quad (3.56)$$

where A is a constant. Using this equation to express $\omega - \omega_c$ in (3.54) through I , we obtain finally a differential equation for $I(t)$:

$$L \frac{dI}{dt} = \alpha I \left[(\omega_0 - \omega_c)^2 + \frac{L}{\Theta} (I_0^2 - I^2) \right]^{1/2}. \quad (3.57)$$

By integrating (3.57), we obtain the following solution:

$$\begin{aligned} I(t) &= \frac{\sqrt{A}}{\cosh\left(\alpha(t - t_0)\sqrt{A/\Theta L}\right)}, \\ t_0 &= \frac{1}{\alpha} \sqrt{\frac{\Theta L}{A}} \ln\left(\frac{\sqrt{A}}{I_0} + \sqrt{\frac{A}{I_0^2} - 1}\right). \end{aligned} \quad (3.58)$$

The maximum current is reached when the hyperbolic cosine is equal to 1:

$$I_{\max} = (\omega_0 - \omega_c) (\Theta/L)^{1/2}. \quad (3.59)$$

Here, we have assumed that I_0 , the initial current in the system, is small. We then have the following simplified expression for t_0 :

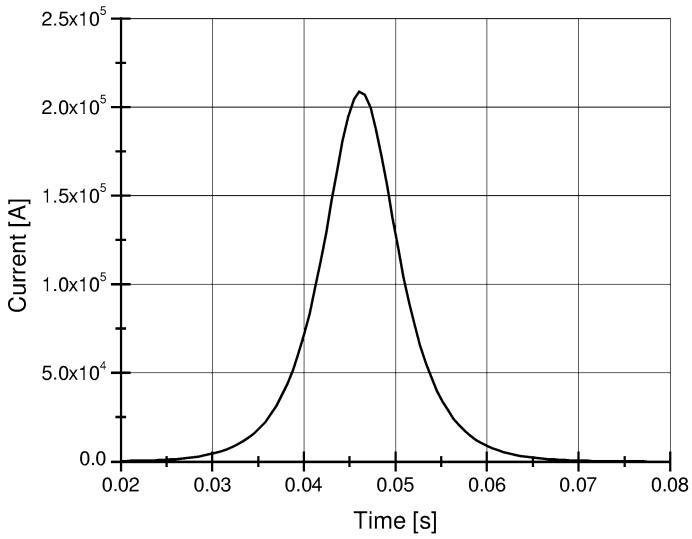


Fig. 3.21. Output current pulse of a homopolar generator

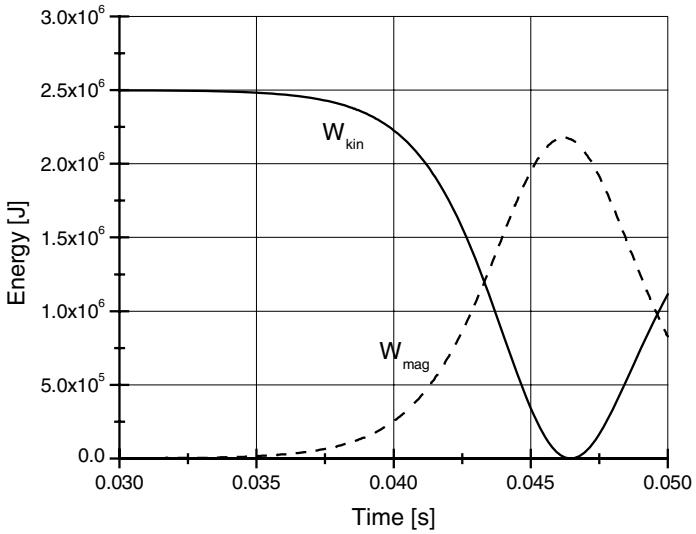


Fig. 3.22. Evolution of the kinetic energy W_{kin} and the magnetic energy W_{mag} for a self-exciting homopolar generator

$$t_0 = \frac{L}{R} \frac{\ln(2I_{\max}/I_0)}{\omega_0/\omega_c - 1}. \quad (3.60)$$

The efficiency for the transformation of stored kinetic energy into magnetic energy in the inductive storage device is given by

$$\eta = \frac{L_s I_{\max}^2}{\Theta \omega_0^2} \approx \frac{L_s}{L} \left(1 - \frac{\omega_c}{\omega_0}\right)^2. \quad (3.61)$$

From this equation, we can read off at least qualitatively the influence of the various parameters of the system. A satisfactory efficiency can be achieved only if the storage inductance is comparable to the total inductance and if $\omega_c \ll \omega_0$.

In Fig. 3.21, we have plotted $I(t)$ for a system with the following parameters: $\Theta = 5 \text{ kg m}^2$, $L = 10^{-4} \text{ H}$, $\alpha = 3 \times 10^{-5} \text{ s}$, $R = 2 \times 10^{-3} \text{ } \Omega$, $\omega_0 = 1000/\text{s}$, $\omega_c = 66.6/\text{s}$, $W_{\text{kin}} = 2.5 \text{ MJ}$, $L_s/L = 0.8$, and $\eta = 0.7$. Using the expression for $I(t)$, we can derive the evolution of both the kinetic energy of the rotor and the magnetic energy of the inductor. This is shown in Fig. 3.22.

There are a few disadvantages associated with the homopolar generator:

- The generator voltage is low, in general.
- There are contact problems, and appreciable wear of the brushes due to the high rotor velocity.

To produce a higher output voltage from a homopolar generator, it is advantageous to separate the exciting and the storage coils [Lupton et al. 1981].

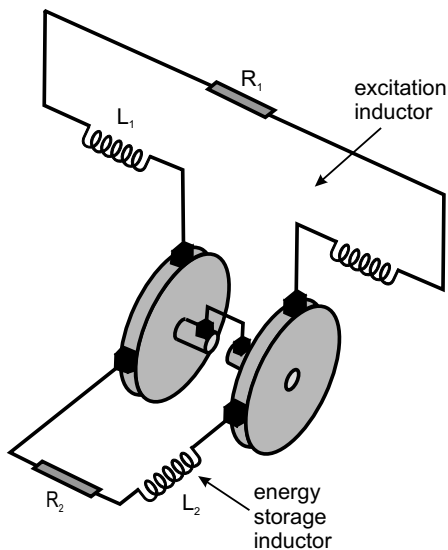


Fig. 3.23. General scheme of a self-exciting homopolar generator with separate excitation and storage inductors

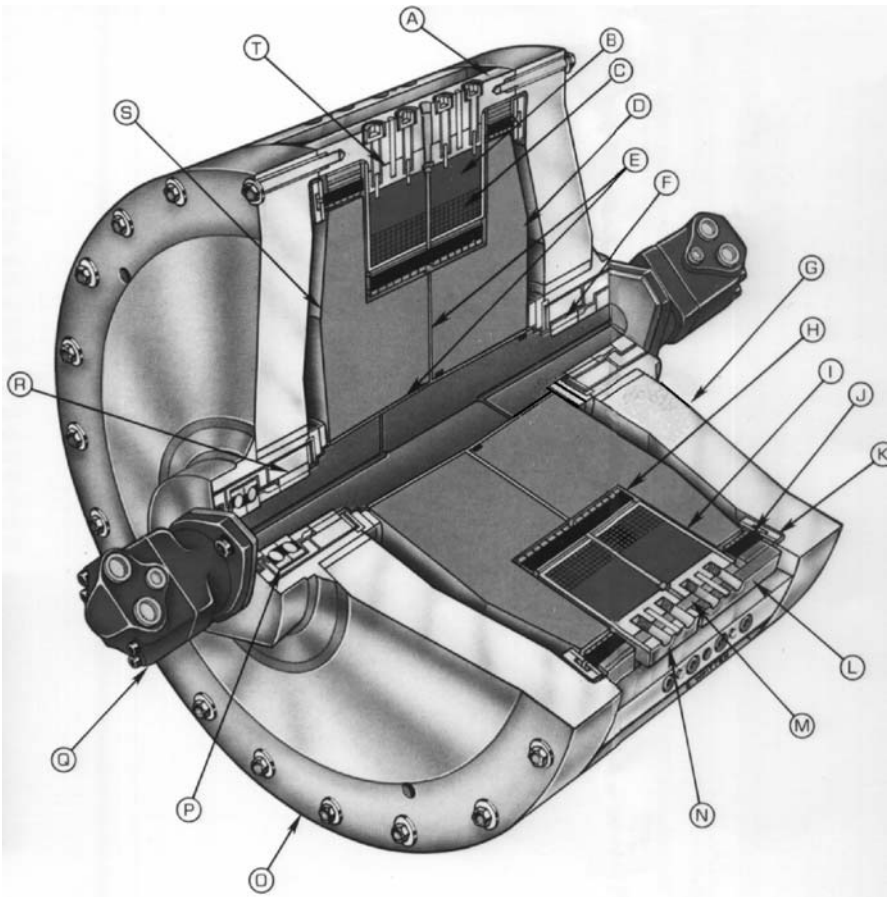


Fig. 3.24. Technical details of a compact pulsed homopolar generator: A, stator support bar; B, stator iron; C, field coil; D, removable rotor section; E, ceramic insulator; F, radial bearing; G, stator support cone; H, inner brush assembly; I, compensating plate; J, outer brush assembly; K, outer brush manifold; L, output terminal-outer brush; M, insulator; N, output terminal-inner brush; O, stator support cone; P, thrust bearing; Q, hydraulic motor; R, radial bearing; S, permanent rotor section; T, inner brush air manifold (OIME Inc., Odessa, Texas)

Such a set-up is shown in Fig. 3.23. This simplifies the insulation of the energy storage inductor. In this case, the basic differential equations describing the circuit are

$$\begin{aligned}
 \alpha I_1 \omega &= L_1 \frac{dI_1}{dt} + R_1 I_1, \\
 &= L_2 \frac{dI_2}{dt} + R_2 I_2,
 \end{aligned}
 \tag{3.62}$$

and

$$\Theta \frac{d\omega}{dt} = -\alpha I_1 (I_1 + I_2) . \quad (3.63)$$

For the special case where $R_1/L_1 = R_2/L_2$, we can derive the efficiency from these equations:

$$\eta = \frac{L_2 I_{\max}^2}{\Theta \omega_0^2} = \frac{L_1}{L_1 + L_2} \left(1 - \frac{\omega_c}{\omega_0} \right)^2 . \quad (3.64)$$

That is, if $L_1 \gg L_2$, the largest fraction of the energy initially stored in the rotor is transferred to the storage inductor.

Figure 3.24 presents the technical design of a homopolar generator and of the corresponding rotor.

4 Switches

After the energy storage device, the switch is the most important element of a high-power pulse generator. High-power switching systems are the connecting elements between the storage device and the load. The rise time, shape, and amplitude of the generator output pulse depend strongly on the properties of the switches in the pulse-forming elements. Generators with capacitive storage devices need closing switches, while generators with inductive storage devices require opening switches. We shall start with a discussion of several types of closing switches.

4.1 Closing Switches

In this case, the switching process is associated with voltage breakdown across an initially insulating element. This breakdown can either occur automatically as a result of an overvoltage or be initiated by an externally supplied trigger pulse.

4.1.1 Gas Switches

Gas switches are commonly applied in high-power pulse generators. They are easy to use, can handle very large currents and charges, and can be triggered precisely. Various gas switches are available that operate in very different pressure regimes. Figure 4.1 shows the range of gas pressures and operating voltages for some of the most important types of gas-filled switches [Frank et al. 1991].

The properties of the switches listed in Fig. 4.1 will be discussed below in some detail. Many applications require a precisely controlled initiation of the voltage breakdown. The trigger method applied has a big influence on the ignition delay and its variance (jitter).

For all switching systems, the operation of the switch can be divided into the four phases schematically shown in Fig. 4.2:

- I. Trigger phase (build-up of a trigger discharge).
- II. Transition phase (transition from a high to a low switch impedance, also called ‘commutation’).

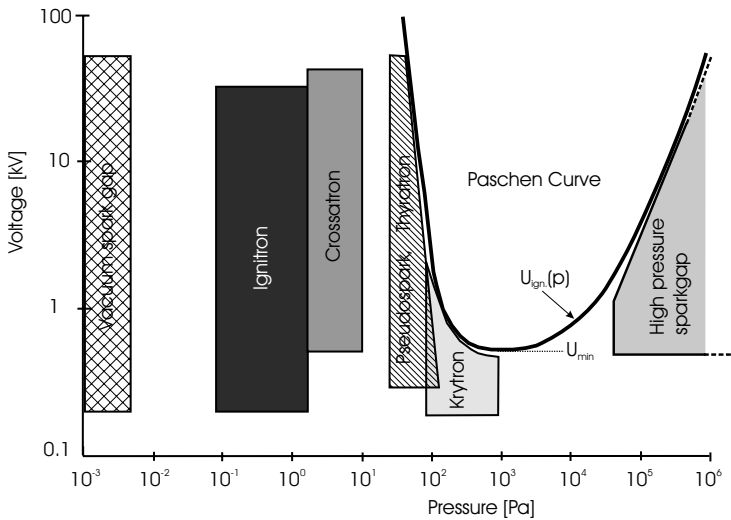


Fig. 4.1. Range of gas pressures and operating voltages for various types of gas switches. In addition, the Paschen curve for air is shown for a fixed gap width of 3 mm. Above this curve, switch operation becomes impossible since the breakdown strength is exceeded

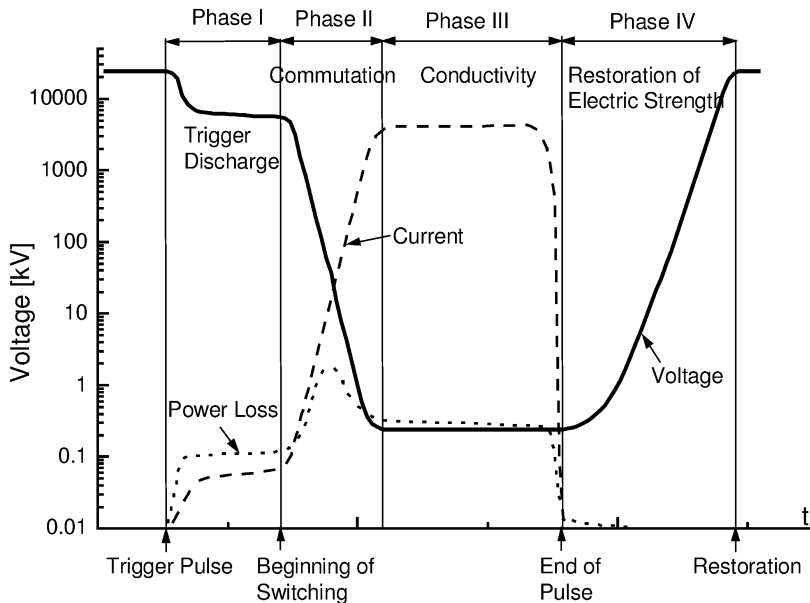


Fig. 4.2. Evolution of voltage, current, and power loss in a gas-filled switching system

III. Stationary phase (constant conductivity of the switch).

IV. Recovery phase (restoration of the previous electric strength).

Considerable energy consumption occurs only during the commutation phase, where the voltage drops while the current increases strongly. We can estimate the energy loss W_V during commutation if we assume that voltage decay and current growth occur in a synchronised manner and linearly:

$$W_V = \int_0^{\tau_s} U(t)I(t) dt = U_m I_m \int_0^{\tau_s} \left(1 - \frac{t}{\tau_s}\right) \frac{t}{\tau_s} dt = \frac{U_m I_m \tau_s}{6} \approx 0.2 U_m I_m \tau_r, \quad (4.1)$$

where U_m and I_m are the maximum voltage and current, respectively, of the pulse, τ_s is the switching time, and τ_r is the pulse rise time ($\tau_r \approx 0.8\tau_s$). In a repetitive system, this is the energy that must be removed by cooling.

4.1.1.1 Gas-Filled Spark Gaps

A spark gap can break down either because its breakdown voltage has been exceeded or because the breakdown strength has been reduced by certain events (UV radiation, plasma diffusion, etc.) inside the spark gap. The important design parameters of a spark gap are:

- the self-breakdown, or hold-off, voltage U_b ;
- the variance of U_b , which determines the probability of prebreakdown;
- the operation range, i.e., the range of voltages that can be held off with sufficiently low prebreakdown probability and can be reliably triggered;
- the jitter, i.e., the time variance of ignition;
- the switching time t_s , which describes the decay of the impedance (resistance and inductance);
- the prebreakdown inductance and capacitance;
- the repetition rate capability;
- the lifetime and cost.

Triggering can be achieved either by a laser pulse or by a high-voltage pulse at an auxiliary electrode. The general set-up and the main components of a three-electrode spark gap are presented in Fig. 4.3.

A wiring diagram for a three-electrode spark gap is presented in Fig. 4.4. We speak of longitudinal overvoltage triggering if the voltage amplitude of the trigger pulse added to the applied operating voltage is sufficient to break down a partial gap. Ignition of the second partial gap occurs if its breakdown voltage is less than the operating voltage. If a coupling capacitor C_c is used to decouple the trigger source from the generator, the potential of the trigger electrode floats very close to zero because the capacitances of the partial gaps are much smaller than C_c . In this case the necessary conditions for

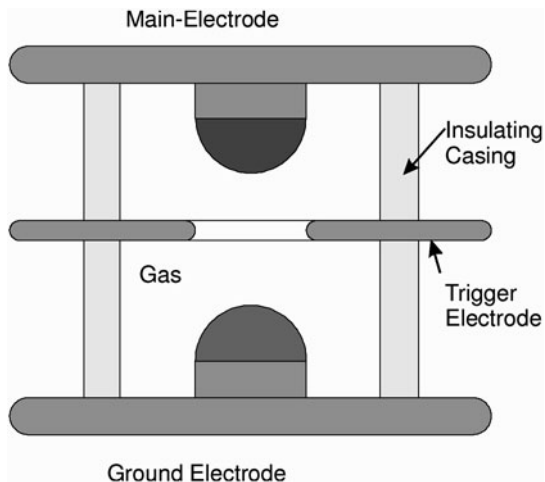


Fig. 4.3. Components of a three-electrode spark gap

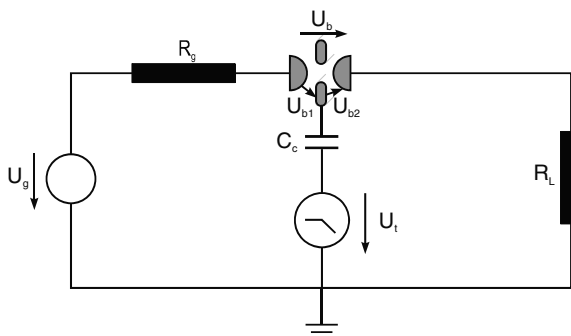


Fig. 4.4. Wiring diagram of a three-electrode spark gap (U_g = generator voltage, U_t = trigger voltage, U_b = breakdown voltage, U_{b1} , U_{b2} = breakdown voltages of the partial gaps, R_g = generator impedance, R_L = load impedance, C_c = coupling capacitor)

longitudinal overvoltage triggering can be summarised as follows: $U_g + U_t > U_{b1}$, $U_g > U_{b2}$, $U_t < U_{b2}$. From this we can conclude that $U_{g\min} = U_{b2}$ and, since $U_{t\max} = U_{b2}$, we have $U_{g\min} + U_{t\max} = 2U_{b2} \geq U_{b1}$, i.e., at the limits we have $U_{b2} = (1/2)U_{b1}$. For a symmetric spark gap configuration this means that the trigger electrode should be positioned at $2/3$ of the gap spacing from the main electrode. Of course, we must also meet the condition $U_g < U_{b1}$ if the trigger electrode is floating. Therefore the operating range of such a three-electrode spark gap is $U_{b2} < U_g < 2U_{b2}$ or, if we express U_{b2} through U_b , $(1/3)U_b < U_g < (2/3)U_b$. A better utilisation of the breakdown strength U_b of the complete gap and a larger operating range can be obtained if we set the trigger electrode at $1/3$ of U_g with the help of a resistive divider, as shown in Fig. 4.9 later. In this case we have $(1/3)U_b < U_g < U_b$.

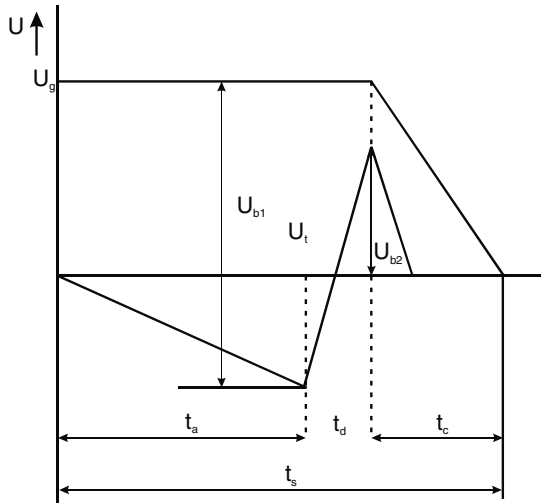


Fig. 4.5. Evolution of the voltages at the trigger and main electrodes of a three-electrode spark gap using longitudinal overvoltage triggering (t_a = trigger actuating time, t_d = switching delay, t_c = commutation time, t_s = switching time)

Figure 4.5 shows schematically the evolution of the voltages across a three-electrode spark gap with a floating trigger electrode ($U_f = 0$). The potential distribution in the gap of a three-electrode switch with the trigger electrode clamped at $(1/3)U_g$ is shown in Fig. 4.6 during various phases of operation. Longitudinal overvoltage triggering is characterised by the fact that both partial gaps break down because of overvoltage. Through the applied overvoltage and the UV radiation from the first spark, the breakdown occurs very rapidly. This results in a very short and only slightly varying switching time and switch delay time.

If the operation voltage of the three-electrode gap is smaller than the breakdown strength of the second gap, another breakdown mechanism develops. This is illustrated in Fig. 4.7. This kind of triggering is called longitudinal plasma triggering. In this case, the second gap can fire only if its breakdown strength is continuously reduced by UV radiation from the spark channel plasma of the first gap. The switching time and switch delay time have much larger values than in the previous case.

Figures 4.5 and 4.7 suggest that longitudinal triggering can occur only for opposite polarities of the operating and triggering voltages. This restriction is no longer necessary for the trigatron switch configuration shown in Fig. 4.8. However, in this case also, the best trigger performance is achieved if the polarities of the trigger pulse and the operation voltage are opposite. Trigratrons are normally operated with charging voltages in the range of 80–99% of the static self-breakdown voltage U_b . Triggering down to less than 50% of U_b is possible; however, the delay and the jitter at such a low voltage are generally

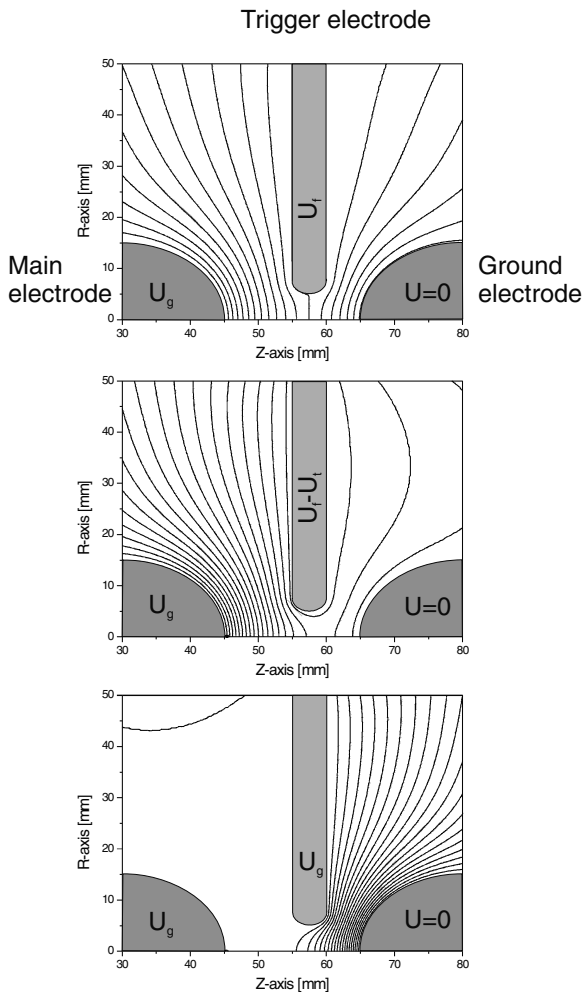


Fig. 4.6. Potential distribution in a three-electrode spark gap switch, before ignition (*top*), after application of a trigger signal (*centre*), and after breakdown of the first gap (*bottom*)

quite high. The switching of a trigatron is determined by the following sequence of events. Upon arrival of the trigger pulse, streamers begin to grow in the vicinity of the trigger pin tip and propagate across the main gap. After the streamer has reached the opposite electrode, the applied field causes the ionisation density in the channel to grow. Concurrently, the gap between the trigger pin and the adjacent main electrode also undergoes a streamer breakdown process. The final result is usually two thermalised arcs, connecting the trigger pin to the opposite electrode and the adjacent electrode. Sometimes it is also possible that the gap between the trigger electrode and the adjacent

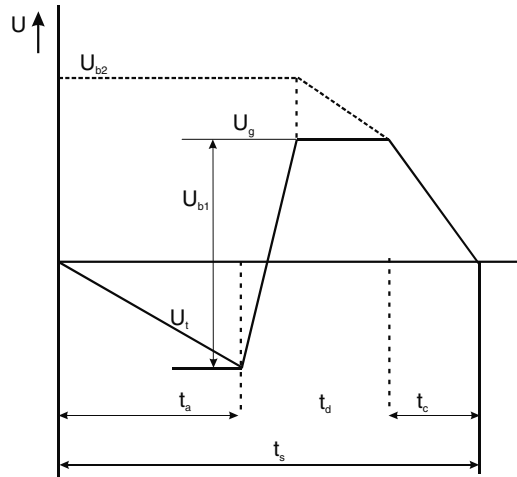


Fig. 4.7. Breakdown sequence in the longitudinal-plasma-triggering mechanism

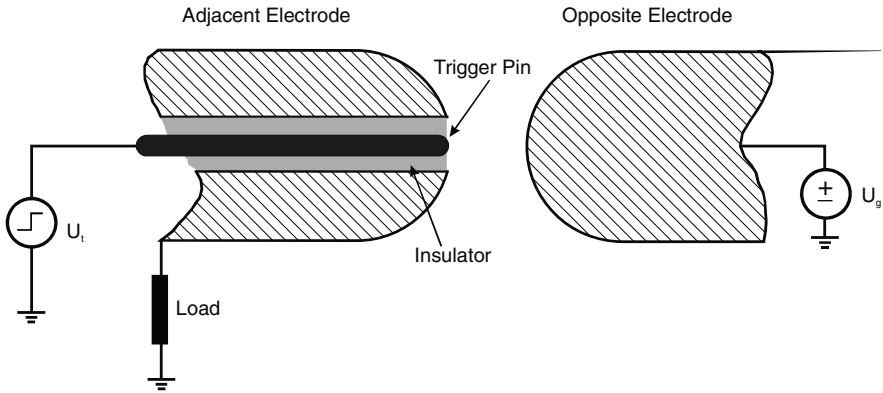


Fig. 4.8. Schematic drawing of a trigatron spark gap

electrode breaks down first. This is especially the case if the trigger pulse and the operation voltage have the same polarity. Then the main gap breaks down because of the UV radiation emitted from the first arc.

4.1.1.2 Analysis of Trigger Circuit

The evolution of the trigger voltage – and therefore the switch delay – is determined by the trigger generator circuit, as well as by the main discharge circuit. Figure 4.9 presents the equivalent-circuit model of a capacitive discharge circuit containing a triggered three-electrode spark gap with a clamped trigger electrode.

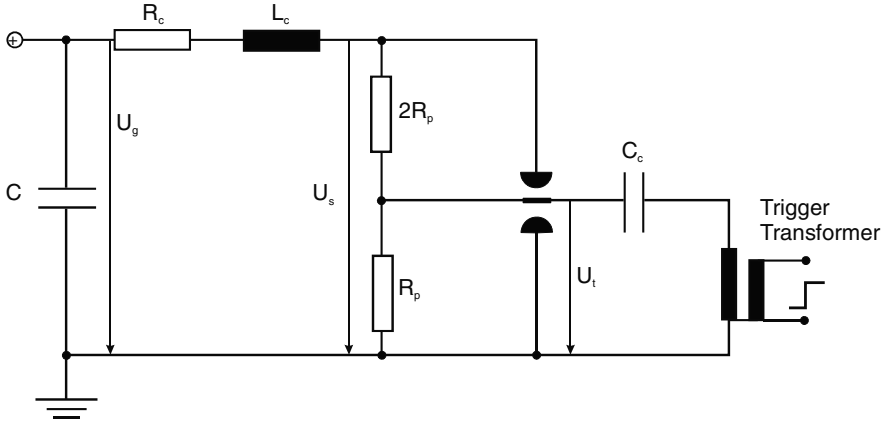


Fig. 4.9. Circuit diagram of three-electrode trigger set-up

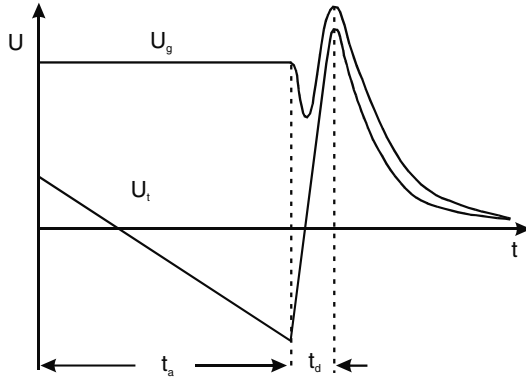


Fig. 4.10. Characteristics of the voltage across the switch and at the trigger electrode

It is assumed that the storage capacitor C has been charged to the voltage U_g and that the trigger electrode has been preset by a high-impedance voltage divider to one-third of that value. In addition to an inductance L_c , the circuit contains a damping resistor R_c . The trigger pulse, generated by a pulse transformer, is coupled to the trigger electrode through a coupling capacitor C_c . Figure 4.10 presents the general evolution of the transient voltage at the trigger and high-voltage electrodes. To determine the influence of the various circuit parameters on the rise time of the ignition pulse, we must evaluate the set-up of Fig. 4.9. For this purpose, we attribute capacitances C_1 and C_2 to the partial gaps. C_2 and C_c carry a voltage $U_2 = (1/3)U_g$ before application of the trigger pulse. At time $t = 0$, the pulse transformer produces a voltage ramp $U_t = St$. Assuming that $C_1 = C_2 \ll C_c < C$, we obtain the following for the voltage at the trigger electrode:

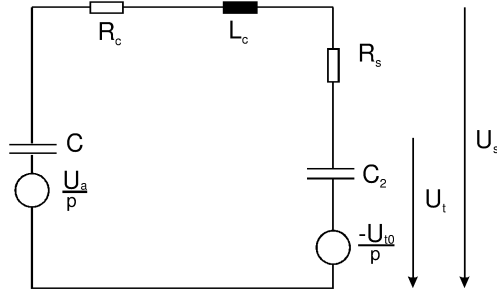


Fig. 4.11. Equivalent circuit of the discharge configuration after breakdown of the first switch gap

$$\begin{aligned}
 U_t &= \frac{U_g}{3} - S \left[t - \frac{\sin(at)}{a} \right], \\
 a &= \sqrt{\frac{2C_2 + C_c}{2C_2C_cL}} \approx \sqrt{\frac{1}{2C_2L}}.
 \end{aligned} \tag{4.2}$$

At the end of the trigger activation time t_a , the gap between the trigger electrode and the high-voltage electrode breaks down, and the potential of the trigger electrode switches from the momentary value of the trigger voltage to the charging voltage U_g . Simultaneously, a reduction of the voltage U_s across the spark gap is observed, which, however, reverses after a short time and exceeds the applied voltage U_g (see Fig. 4.10).

The equivalent circuit for calculating the voltage reversal at the trigger electrode is presented in Fig. 4.11. Here R_s is the spark gap resistance, which has been assumed to be time-independent. At time $t = 0$, the stray capacitance C_2 has been charged to $-U_{t0}$. For small damping and $C \gg C_2$, and using the abbreviations $R_t = R_c + R_s$ and

$$\omega = \sqrt{\frac{C_2 + C}{C_2CL_c} - \left(\frac{R_t}{2L_c}\right)^2} \approx \sqrt{\frac{1}{C_2L_c} - \left(\frac{R_t}{2L_c}\right)^2}, \tag{4.3}$$

we obtain the following for the voltage functions:

$$\begin{aligned}
 U_s(t) &= -U_{t0} + (U + U_{t0}) \left(1 - e^{-R_t/2L_c t} \left(\cos \omega t + \frac{R_t - R_s}{2\omega L_c} \sin \omega t \right) \right), \\
 U_t(t) &= -U_{t0} + (U + U_{t0}) \left(1 - e^{-R_t/2L_c t} \left(\cos \omega t + \frac{R_t}{2\omega L_c} \sin \omega t \right) \right).
 \end{aligned} \tag{4.4}$$

Neglecting the ohmic resistance, we have an oscillation with an amplitude $2U + U_{t0}$. Thus, depending on the degree of damping, the potential at the trigger electrode can exceed the static operation voltage U appreciably.

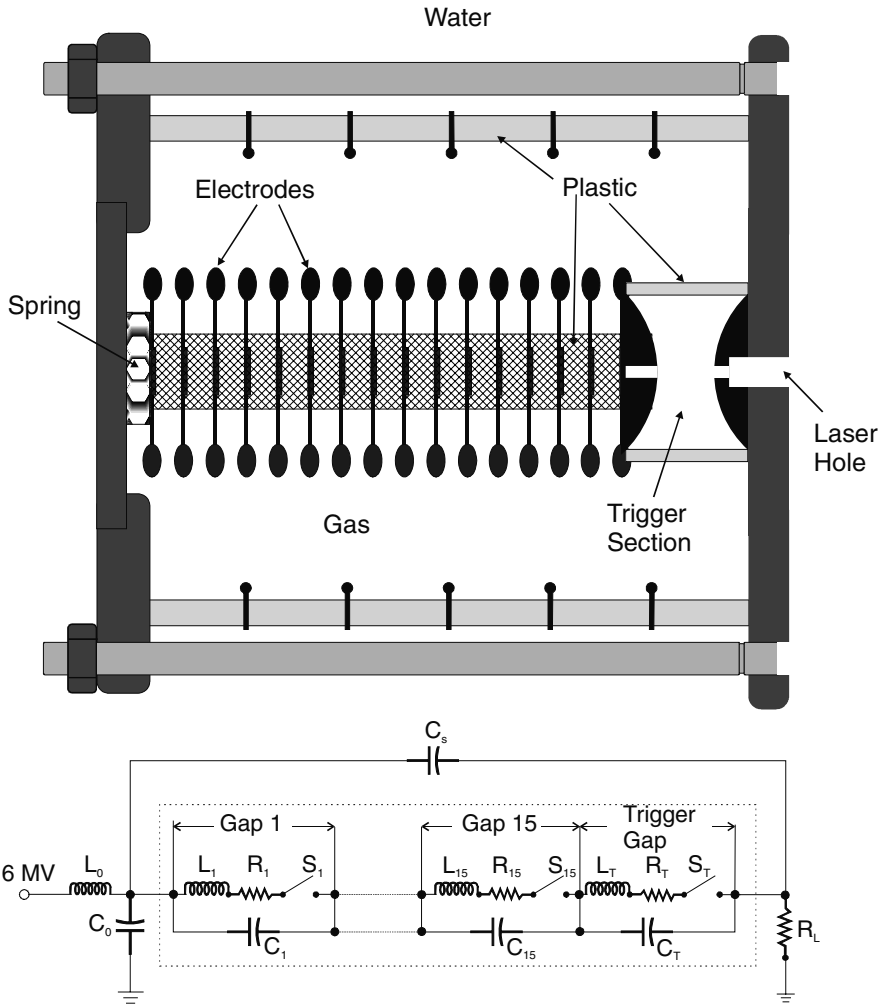


Fig. 4.12. General set-up of a high-power laser-triggered spark gap for 6 MV and 0.5 MA operating voltage and current, respectively

4.1.1.3 Multistage Spark-Gap Switch with Laser Triggering

Simply scaling a three-electrode spark gap to multimegavolt operating voltages would lead to large gaps, making the jitter and inductance unacceptably high. However, multimodular high-power pulse generators need very exact synchronisation of megavolt pulses generated by separate generator modules. Laser triggered multistage spark gaps have been developed to serve this purpose. The general features of such a switch, developed at Sandia National Laboratory [Humphreys et al. 1985], are shown in Fig. 4.12, which also contains its equivalent-circuit model.

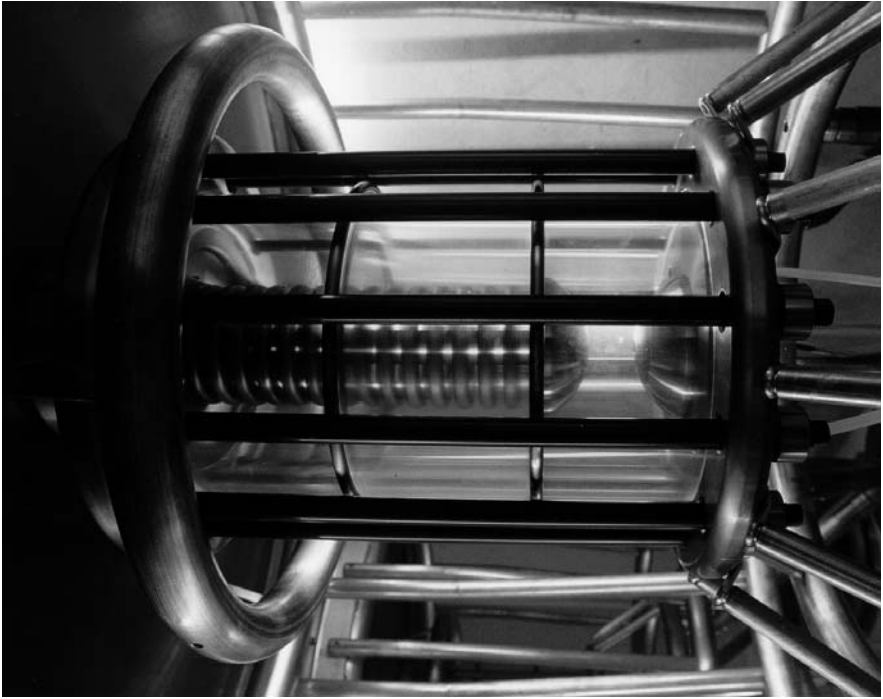


Fig. 4.13. A 4 MV version of a multigap spark switch

This switch has been designed for an operating voltage of up to 6 MV and a switch current of 0.5 MA. It consists of 15 equal spark gaps and a trigger section. A central stack of insulating discs supports 15 toroidal electrodes. Plastic rods outside the housing hold the stack together, and a spring in one of the base plates maintains a compressive force on the stack. In general, the operating voltage is around 90% of the self-breakdown value. With this setting, a prefire probability of 0.1% has been achieved. Because of the toroidal geometry of the electrodes, the gap capacitances are small. Their values relative to the trigger gap capacitance C_T have been chosen such that 20% of the operating voltage occurs across the trigger section. The switch is 68 cm long and has an overall diameter of 61 cm.

To trigger the 5.7 cm wide first gap, a UV laser pulse (KrF) with a 25 mJ pulse energy is necessary. The laser pulse is focused with a long-focal-length lens into the centre of the trigger section. A needle-shaped spark of centimetre length is created in the focal spot of the laser. It enhances the electric field in the gap and accelerates streamer propagation. Approximately 1 ns after the application of the laser pulse, a breakdown occurs in the trigger gap. The capacitance C_T is discharged rapidly, and the voltage increases across the remaining gaps. Gap 15 feels this voltage increase first. Thus an ignition wave

propagates to the other gaps and ignites them sequentially. The switching sparks appear at the rim of the disc-shaped electrodes, and several channels are created since dU/dt becomes very fast (see below). Consequently, a rather small spark inductance of only 100 nH, out of a total inductance of 400 nH, is generated. The trigger delay is around 20 ns and the jitter is less than 0.4 ns.

The equivalent circuit shown in the lower half of Fig. 4.12 includes an intermediate storage capacitor C_0 , which is charged from a Marx generator through an inductance L_0 to a level of up to 6 MV.

A 4 MV version of a multigap spark switch is shown in Fig. 4.13.

4.1.1.4 Pulse Rise Time

The rise time of a pulse, which of course corresponds to the voltage decay across the switch, is the sum of a resistive and an inductive term:

$$\begin{aligned}\tau_{\text{tot}} &= \{\tau_{\text{L}}^2 + \tau_{\text{R}}^2\}^{1/2}, \\ \tau_{\text{tot}} &= \frac{U}{(dU/dt)_{\text{max}}}.\end{aligned}\quad (4.5)$$

The voltage decay across an inductance L , connected to a generator with impedance Z , is determined by the time constant $\tau_{\text{L}} = L/Z$. Generally, an exact calculation of the time-dependent inductance L of a spark gap is impossible. However, for most practical cases it can be approximated by the inductance of a thin cylindrical wire on the axis of a metallic tube. If the wire has a radius r_i and a length ℓ and if the inner radius of the tube is r_a , we obtain

$$L = \ell \frac{\mu_0}{2\pi} \ln\left(\frac{r_a}{r_i}\right) = 2\ell \ln\left(\frac{r_a}{r_i}\right) \approx 14\ell \text{ (nH)} \quad (4.6)$$

for ℓ in cm. For the resistive phase of a spark channel in a liquid or a gas, the following expression has been derived in the literature [Martin et al. 1996]:

$$\tau_{\text{R}} = \frac{88}{Z^{1/3} E^{4/3}} \left(\frac{\rho}{\rho_0}\right)^{1/2} \text{ ns}, \quad (4.7)$$

where E is the electric field strength, measured in MV/m, and ρ_0 is the density under normal conditions. For solids of density 1 g/cm^3 , i.e., for most organic insulators, one finds

$$\tau_{\text{R}} = \frac{2320}{Z^{1/3} E^{4/3}} \text{ ns}. \quad (4.8)$$

Here, again, the value of E in MV/m has to be inserted.

4.1.1.5 Multichannel Spark Gaps

Multichannel spark gaps can reduce the switch inductance and shorten the resistive phase. Thereby, pulses with shorter rise times can be produced. In addition, the wear of multichannel switch electrodes is smaller because the energy loss is distributed over a larger area.

We want to answer the question of under what conditions several channels might occur in a spark gap with extended electrodes. After the first channel has fired and taken a large fraction of the maximum possible current, the voltage across the gap breaks down and the formation of further channels is prevented. Small voltage reductions can have a large effect on channel formation, because the electron multiplication coefficient α is a strong function of the field strength. The time interval during which new channels can be created will therefore be only a fraction of the voltage decay time τ_{tot} :

$$\Delta t = f\tau_{\text{tot}} . \quad (4.9)$$

(If we count all channels that reach more than 50% of the maximum current in a channel, $f = 0.1$.)

We must add a transit time, which is the time in which the information can spread to the other channels that a channel has fired, to Δt . If the length of the switch electrodes is ℓ and the number of channels on this electrode is n , we have

$$\tau_{\text{trans}} = \frac{\ell}{nc} . \quad (4.10)$$

Since the channels will not be homogeneously distributed, we must again take only a fraction f_2 of the transit time, where $f_2 = 0.8$. Thus we obtain the following for the time interval in which further channels can appear:

$$\Delta t = 0.1\tau_{\text{tot}} + 0.8\tau_{\text{trans}} . \quad (4.11)$$

Δt depends on the number of channels: the inductive term of τ_{tot} is $\sim 1/n$, the resistive term is $\sim 1/n^{1/3}$, and the transit time term is $\sim 1/n$.

Each spark gap has a variance of its breakdown voltage, which can be characterised by the standard deviation $\sigma_a(U)$. For a pulse of rise time t_r , we can transform this variance into a time variance. The relations can be derived from Fig. 4.14.

By the index ‘a’, we indicate that we are dealing here with the absolute variance. We can easily see that the time jitter of channel initiation $\sigma_a(t)$ is equal to $\sigma_a(U)/(dU/dt)$. Thus the number of channels can be calculated from the requirement

$$2\sigma_a(t) < \Delta t = 0.1\tau_{\text{tot}} + 0.8\tau_{\text{trans}} . \quad (4.12)$$

Therefore, to achieve the largest possible number of channels, we must reduce $\sigma_a(U)$ and decrease the pulse rise time dU/dt as much as possible.

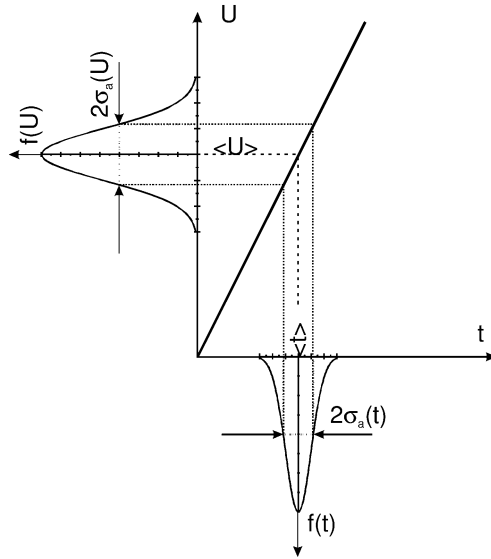


Fig. 4.14. Relation between the standard deviation of voltage breakdown $\sigma_a(U)$ and the time variance $\sigma_a(t)$

4.1.1.6 Thyratrons

The thyatron, especially the hydrogen thyatron, emerged from efforts during World War II to develop effective military radar systems. After the war it became also the switching workhorse in many accelerator systems. Like spark-gap switches, thyratrons are gas-filled switching devices. However, their operating gas pressure is much lower and they use a triode configuration (see Fig. 4.15). Most thyratrons use hydrogen at a base pressure of 30–80 Pa. In contrast to vacuum tubes, the thyatron is characterized by the presence of a plasma, which allows the passage of large currents without significant electrode erosion.

Thyratrons operate on the left-hand side of the Paschen minimum (see Fig. 4.1). Their hold-off voltage is limited by field emission, which sets in at fields larger than 10^5 V/cm. Generally, the anode–grid distance is of the order of 2–3 mm, which limits the hold-off voltage to values of around 40 kV. The hold-off voltage capability can be improved if a bias voltage is applied to the control grid. The distance between the control grid and the cathode corresponds to the Paschen minimum U_{\min} for hydrogen. If a trigger pulse of amplitude $U > U_{\min}$ is applied to the grid a glow discharge is initiated between the cathode and the grid. The anode and cathode communicate electronically: electrons from the glow discharge plasma can migrate rapidly through the openings in the grid to the main discharge region between the grid and the anode. By charge carrier multiplication, a conducting plasma bridge is then created between the anode and the grid, and the thyatron

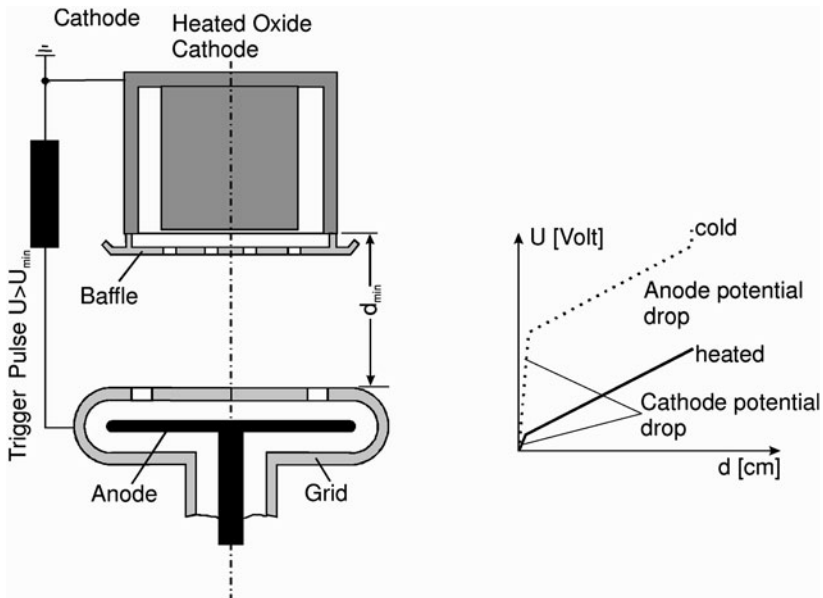


Fig. 4.15. Principal features of a thyatron with heated cathode (*left*), and potential drop with a heated cathode (*solid line*) and without one (*right*). The grid surrounds the anode such that the pd value excludes the possibility of a long-distance discharge

closes. In its left half, Fig. 4.15 shows the principal features of a thyatron with a thermionic cathode.

The typical operating voltage of a thyatron is of the order of several times 10 kV. After ignition, the voltage drops to about 100 V. Therefore, an appreciable power loss occurs, which must be dealt with by cooling. Thyratrons achieve trigger delays of the order of 200 ns and a jitter of a few nanoseconds. To regain the initial hold-off voltage, the anode voltage must become slightly negative for 25–75 μ s, which is the time needed for the plasma to decay.

An essential feature of the thyatron is that it uses a thermal electron source. An important advantage of the hot cathode is the absence of a marked cathode potential drop (Fig. 4.15, right). With a cold cathode, a potential drop is necessary to accelerate the ions towards the cathode to maintain secondary-electron production. Energetic ions, however, lead to erosion of the cathode and therefore to a limited lifetime. To prevent fast electrons from the cathode glow discharge directly reaching the anode and causing damage there, all thyratrons use a baffle as a screening element. The holes in the baffle and in the grid are shifted relative to each other to prevent a direct line of sight between cathode and anode.

Initially, thyratrons used glass envelopes and their lifetime was limited to only 500 hours. Ceramic housings made them more rugged and shock-

and vibration-resistant, and allowed effective cooling of the anode. This, in addition to TiH reservoirs to maintain the hydrogen pressure at a constant level, improved their lifetime characteristics. Nowadays thyratrons achieve operating times of 10^5 hours at repetition rates of a few kilohertz and average operating power at the megawatt level.

4.1.1.7 The Pseudospark Switch

Like a conventional thyatron, the pseudospark switch operates in a low-pressure regime, at high values of E/p . In this regime, the mean free paths of electrons and ions become comparable to the electrode spacing. Therefore most electrons reach the anode without any ionising collisions in the gas.

Introducing a hollow cathode into the configuration, as shown in Fig. 4.16, changes the field configuration and increases the possible discharge path lengths. The diameter of the aperture determines the field penetration into the hollow cathode. With the help of a small number of initial electrons, which can be created, for example, by a triggered discharge in the hollow cathode, a pseudospark discharge can be initiated. At the beginning, most electrons are runaway electrons, i.e., they become accelerated to energies comparable to the potential drop between the anode and the cathode. (Owing to this mechanism, pseudospark channels can also be used to create very high-current-density electron beams.)

The switching mechanism, however, is based on the build-up of a highly ionized plasma [Christiansen and Hartmann 1990, Frank and Rath 1990]. Plasma build-up occurs first inside the hollow cathode, owing to the relatively low E/p values in this region. Electrons from the hollow cathode lead to ionisation, mainly on the symmetry axis of the arrangement. Ions left behind in this region drift back into the hollow cathode, forming a positive space charge (virtual anode) and, finally, distorting the static electric field inside the

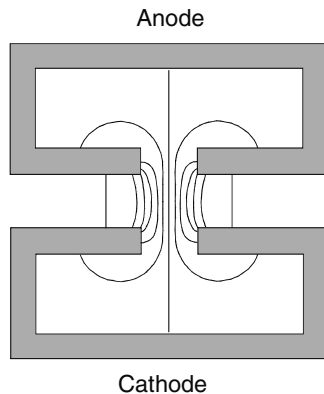


Fig. 4.16. Electric-field configuration in a two-electrode pseudospark system

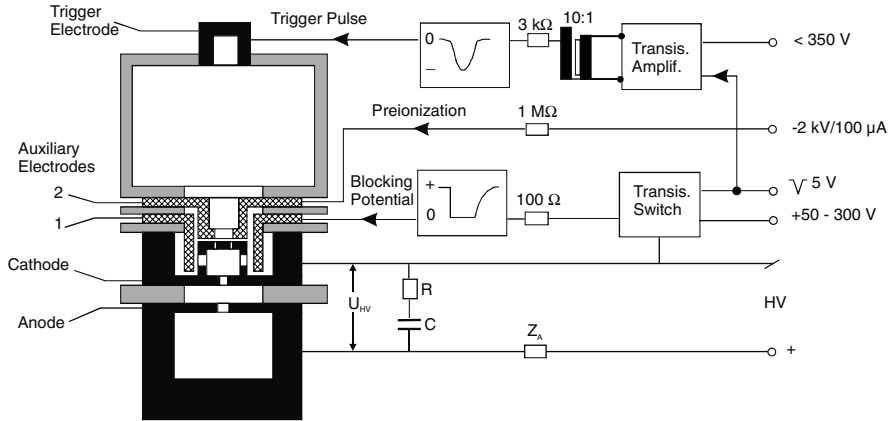


Fig. 4.17. Pseudospark switch arrangement, including a schematic of the trigger section. Triggering is achieved with the help of a glow discharge created in the upper part of the switch. (All metallic parts are either shown in black or cross-hatched. Insulators are grey.) [Frank and Rath 1990]

hollow cathode. This makes the electron production rate greater than the loss rate first in the hollow cathode and, subsequently, also in the anode–cathode gap. Thus a low-resistivity plasma is established, and breakdown of the gap occurs. A dense plasma layer established close to the wall of the cathode hole mediates the current transfer between the channel and the metallic wall. Its properties determine the total current in the switch and therefore the impedance of the closed switch. The current flow between this plasma layer and the metallic wall is carried by ions, while electrons carry the current between the layer and the channel. It has been found [Urban 2002] that the final value of the switch impedance and the time of its establishment depend on the cathode material.

The delay and the jitter of breakdown also depend on the number of initial electrons in the hollow cathode, which can be created by various methods. Of these methods, a pulsed glow discharge has proven to be most advantageous with respect to lifetime and repetition rate capability. A jitter of less than 10 ns and a delay of 0.5 μs have been achieved with this method.

A pseudospark switch arrangement is drawn in Fig. 4.17. In this set-up, the main switch is separated from the trigger section by a cage, which forms the hollow cathode and protects the trigger section, increasing its lifetime.

A low-current glow discharge ($I < 1 \text{ mA}$) starting from the auxiliary electrode 2 provides a weak ionisation inside the trigger section. To trigger the switch, a pulsed discharge ($I < 1 \text{ A}$) is generated by applying a negative pulse of 3 kV to the trigger electrode. It is also possible to apply a positive bias of up to 300 V to the auxiliary electrode 1 to influence the field configuration in the hollow cathode through holes on the side of the cage. This blocking po-



Fig. 4.18. General view of a metal–ceramic pseudospark switch

tential suppresses undesirable pre-firing of the main switch. When triggering takes place at the cathode, charge carrier injection causes the formation of a positive space charge within the hollow cathode. A pseudospark discharge then starts after a delay of 10–40 ns. Pseudospark switches of 40 kV switching voltage and 20 kA switching current are commercially available as sealed systems with H_2 and D_2 gas filling. Figure 4.18 shows a photograph of such a metal-ceramic pseudospark gap.

4.1.1.8 Ignitrons

The basic ignitron device is a very high-current, high-voltage switch with a liquid mercury pool cathode and an ignitor pin dipping into the liquid-metal reservoir. The whole assembly is contained in a stainless steel tube, vacuum-sealed with glass insulators at the anode feedthrough. Under normal conditions, the internal mercury pressure is of the order of 5 Pa. An ignitron can switch a pulse charge of up to 2000 C. For heavy-duty operation, it can be air or water cooled. Some devices also contain internal splash and deionisation baffles.

Figure 4.19 shows a typical ignitron configuration. The anode is usually massive to prevent an impulsive temperature rise during conduction. Anode cooling is effected only through the anode stem and through radiation to the cooled walls. Molybdenum anodes are used in devices that cannot exclude current reversal or backfires. The cathode consists of a mercury pool at the bottom of the stainless steel tube. The ignitor serves as the triggering electrode and is insulated from the cathode by a glass feedthrough. The ignitor

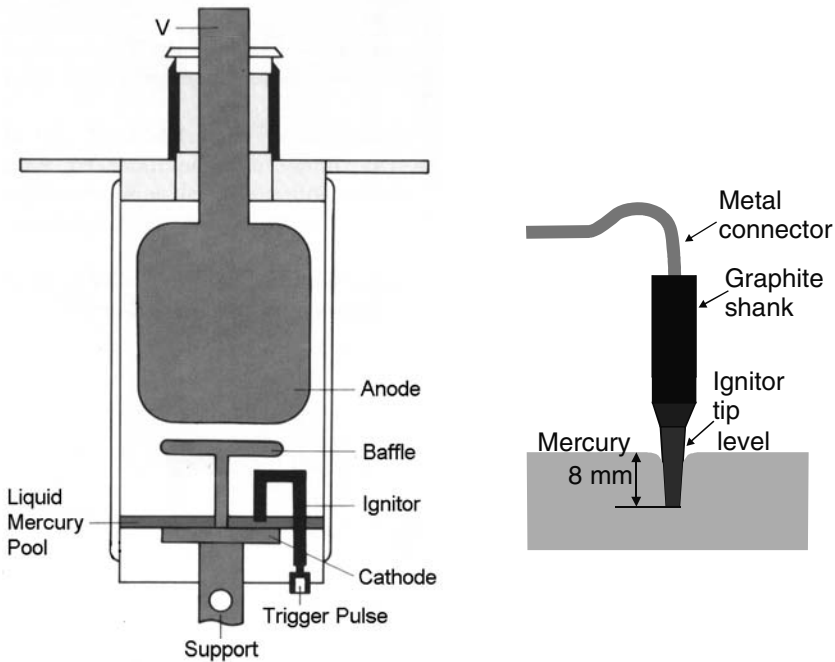


Fig. 4.19. High-voltage ignitron with splash baffle, and with a schematic illustration of the ignitor pin set-up. An enlarged view of the mercury contact to the trigger pin is shown on the *right*

material is a refractory semiconductor such as silicon carbide or boron carbide that is not wetted by mercury. Therefore a negative meniscus with a relatively high resistance forms at the mercury–ignitor interface. The electrical power in the ignitor circuit is thus mainly dissipated in a small volume near this interface. The resulting high power density creates an intense source of mercury vapour and free electrons. Cathode hot spots can spread over the entire surface of the mercury in about 50–100 ns. Therefore the mercury vapour pressure rises rapidly in the cathode–anode space, and the pd value approaches the Paschen minimum. Since at the same time free electrons are present, an ionisation avalanche develops and the device becomes conductive. Ignitrons exhibit current rise times of typically 300–500 ns.

Conduction of the anode–cathode current will cease only after the current has dropped below a critical value such that no more additional vapour is produced and after additional time to allow recombination and recondensation of mercury. The mercury vapour must be forced to recondense back into the pool. Mercury condensed on the glass seals can lead to failure of voltage hold-off and, in the worst case, can cause breakdown and destruction of the insulators. Ignitrons are limited to a repetition rate of 1 Hz.

The primary end-of-life mechanism for ignitron devices is ignitor wetting. This results in a progressive decrease of the resistance at the ignitor–mercury interface and leads to failure of ignition. The wetting is caused by electrochemical reactions involving impurities diffusing to the ignitor interface.

Nowadays, ignitrons are being progressively eliminated because of the unsettled question of the disposal of mercury-containing waste.

4.1.1.9 Krytrons

The krytron is a low-pressure gas discharge device with a tetrode configuration, sealed in a glass tube with a cold cathode. It operates at 1.3 kPa of helium gas pressure. There is no gas reservoir. A special design of the anode–grid area, together with the applied gas pressure, allows a relatively large hold-off voltage. A short trigger delay time of about 30 ns and fast commutation are achieved through an already existing plasma created by a glow discharge between a special keep-alive electrode and the cathode.

A krytron pack with an integrated trigger transformer is shown in Fig. 4.20. The current and voltage rise times are below 1 ns, and the maximum switch current and voltage are around 3 kA and 8 kV, respectively. A pulse length of up to 10 μ s and a repetition rate of 1 kHz can be achieved. The trigger plasma spreads into the space between a control grid and the cathode. Switching is initiated by a positive pulse at the control grid, which, except for a small opening, surrounds the anode. A ^{63}Ni β -emitter is also enclosed in the glass tube. This serves to create a weak permanent pre-ionisation such that faultless switching is guaranteed even after a long period of rest, and it makes the krytron to large extent immune to many environmental factors. A disadvantage is the limited lifetime of 10^6 discharges, which is determined by gas consumption and electrode erosion.

Krytrons are still widely used in fast trigger generators and Pockels cell drivers, but they are also ideal for use in the detonating circuitry of bombs.

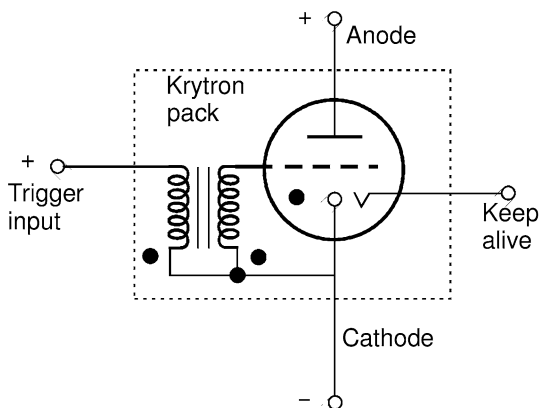


Fig. 4.20. Schematic of krytron pack including a trigger transformer

4.1.1.10 Triggered Vacuum Gap (TVG)

The triggered vacuum gap shown in Fig. 4.21 is a three-electrode system pumped down to 0.001 Pa. It is closed by injection of a plasma cloud. The hold-off voltage depends only on the properties of the electrode surfaces. Currents of up to 10 kA can be switched at voltages of up to 100 kV. If the device is cooled, repetition rates of several kHz are possible.

The gas-plasma mixture is created with the help of an auxiliary arc, burning between two electrodes inserted into one of the main electrodes. In many cases, the auxiliary electrodes are made of titanium loaded with hydrogen. Hydrogen is desorbed from the titanium hydride reservoir at the foot of the moving arc, which is accelerated by self-magnetic forces.

The jitter of the TVG is of the order of 30 ns, and the switching time is around 100 ns. An important advantage of this switch is its positive current-voltage characteristic, which makes it suitable for set-ups with several switches in parallel. Of further advantage are the small dimensions, the large dynamic range, and the absence of a heated cathode. However, the lifetime of both the trigger system and the main electrodes is rather limited.

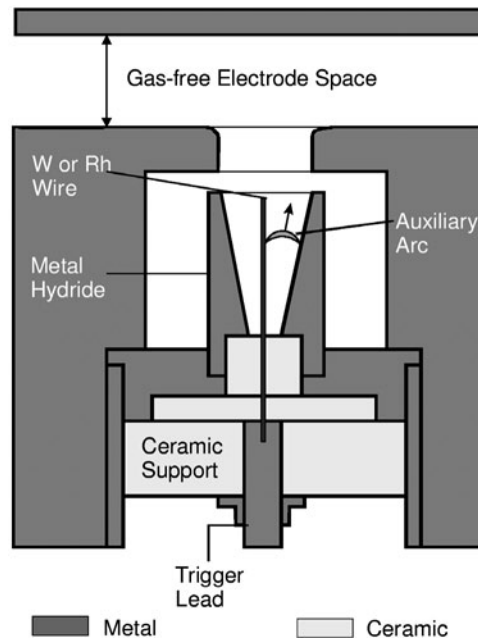


Fig. 4.21. Sectional view of a triggered vacuum switch with a coaxial plasma gun for triggering

4.1.2 Semiconductor Closing Switches

The limiting switching characteristics of semiconductor devices are primarily associated with the relatively low mobility and density of charge carriers in the plasma and with the comparatively low operating temperature. Thus a large volume of the conducting region is required to conduct large currents. The relatively small carrier drift length in the plasma does not allow one to increase the interelectrode distance as is done in gas discharge devices, and hence the primary way in which the switching power can be increased is by increasing the area of the current-carrying channel. These facts have to be observed with all types of semiconductor switches.

4.1.2.1 Thyristors

The thyristor (or silicon-controlled rectifier SCR) is a four-layer device with the sequence $p^+n^-pn^+$. This structure has three p - n junctions and, as illustrated in Fig. 4.22, can also be visualised as a combination of an n - p - n and a p - n - p transistor sharing a common collector junction. Each transistor section is supplied with a driving current to the base from the collector of the other transistor. The gate is usually connected to the p -type base of the n - p - n transistor. The doping profile of a thyristor is shown in Fig. 4.23 (ABB 2001).

Because of their high doping concentrations, the outer layers are called emitters, and the two inner zones can be considered as bases because of their weak doping concentrations. The semiconductor element itself is a thin silicon single-crystal disc of up to 70 cm^2 in area. Heat losses generated during operation are removed through the metal end plates contacting the Si disc. To improve the efficiency of heat removal, water-cooled copper plates can be pressed against the metal contacts of the thyristor.

We can distinguish three modes of operation of a thyristor:

- the reverse blocking state;
- the forward blocking state;
- the conducting, or on state.

If a reverse bias is applied to the thyristor (anode negative with respect to cathode), electrons start to move to the cathode and holes to the anode. This current flow enlarges the space charge region at junctions J_1 and J_3 and decreases it at junction J_2 . The applied voltage U_{rev} is taken by J_1 and J_3 ; $U_{\text{rev}} = U_1 + U_3$. Since the doping concentrations in the bases are very different (see Fig. 4.23), most of the voltage is held by J_1 . The reason for this is that J_3 reaches avalanche breakdown at a rather low reverse bias and thus can easily conduct rather large currents. Therefore the reverse-bias characteristic of the thyristor is determined mainly by the p - n - p transistor structure.

When a positive potential is applied to the anode, the electric field accelerates electrons towards the anode and holes towards the cathode. This

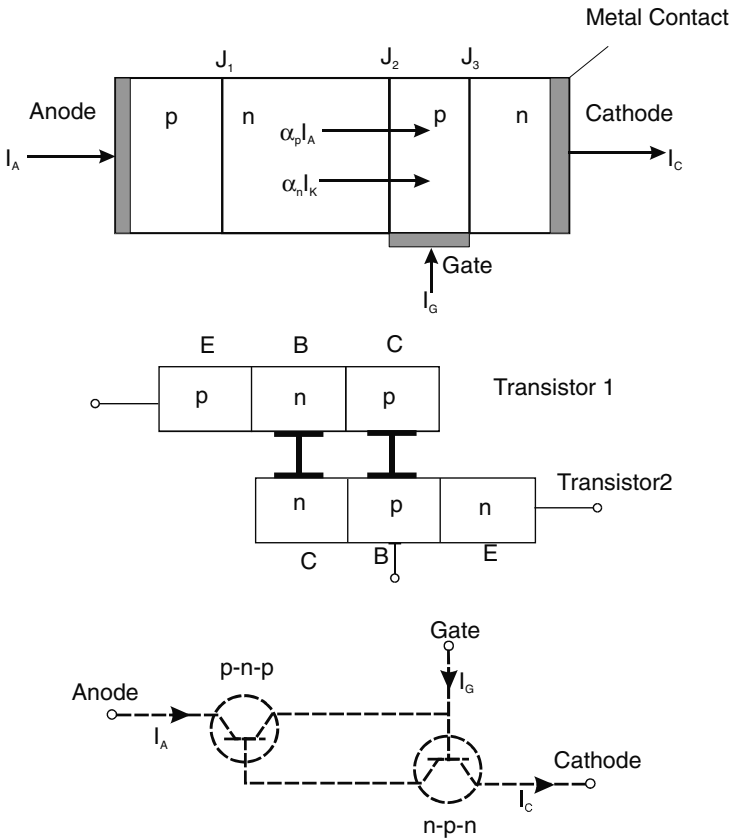


Fig. 4.22. Structure of thyristor, and two-transistor equivalent circuit

enlarges the space charge region at J_2 , and the electric field across J_2 increases. J_2 becomes reverse biased and blocks the flow of any substantial current, despite the fact that the two other junctions are forward biased. The device is in the forward blocking state. During any transient change of currents and fields in the thyristor structure, we can consider the conducting paths outside the stationary space charge zones as quasi-neutral (electron-hole plasma), since the dielectric relaxation time $\tau_R = \epsilon_0 \epsilon_p / \sigma$ is always less than 10^{-10} s. A forward-blocking capability will exist as long as the applied potentials are below the breakdown potential of junction J_2 .

We now consider the situation when the device is in the forward blocking state. If sufficiently high positive bias is applied to the gate, holes begin to stream into the p-base towards the cathode, and initiate emission of electrons from the cathode through junction J_3 to neutralize the holes. A large charge carrier density builds up at the boundary x_5 of the base and creates a density gradient that drives the electron-hole plasma towards J_2 , spreading it over

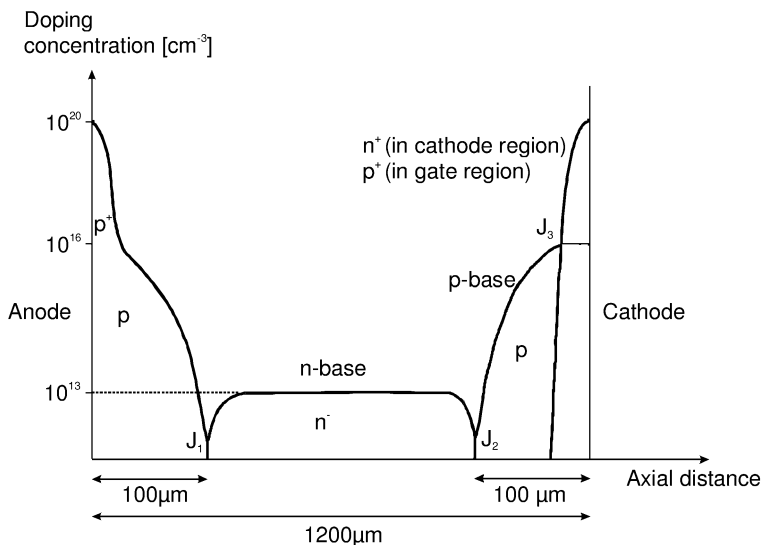


Fig. 4.23. Doping profile of the layers of a thyristor

the complete base (Fig. 4.24). At J_2 , the electrons are accelerated by the electric field towards the n-base and the accompanying holes are held back. The electrons in the n-base provoke the injection of holes through junction J_1 , producing a plasma density gradient in the n-base analogous to that in the p-base.

When the plasma arrives at J_2 , electrons are kept back and holes are accelerated across, driving the junction J_3 even more into the conducting state. Now a critical charge density is reached in the p-base, and a regenerative feedback with a total loop gain exceeding 1 sets in. As the current through the device increases part of the applied voltage is dropped along the current path and at the external load resistance, and the potential at J_2 decreases. The junction capacitance is discharged because not all charge carriers separated at J_2 are compensated any longer by charge carriers of opposite polarity streaming in through J_1 and J_3 . Finally, the voltage drop becomes so large that J_2 switches from the blocking into the conducting state. All three junctions are now forward biased and the device is turned on.

The switching point is a sensitive function of the magnitude of the gate current, so that a family of current–voltage characteristics can be plotted with the gate current I_g as a parameter (Fig. 4.25).

Without any external action, the thyristor cannot come back from the conducting to the blocking state. For the thyristor to regain its initial blocking capability, the excess charge density must be removed below a critical value of the stored charge. To extinguish the thyristor, two methods are generally applied:

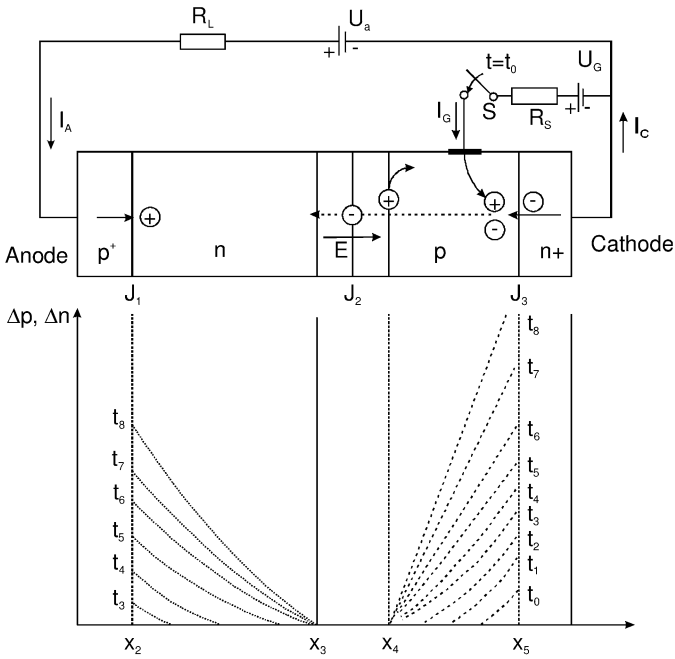


Fig. 4.24. Time sequence of charge carrier densities during switch-on [Gerlach 1979]

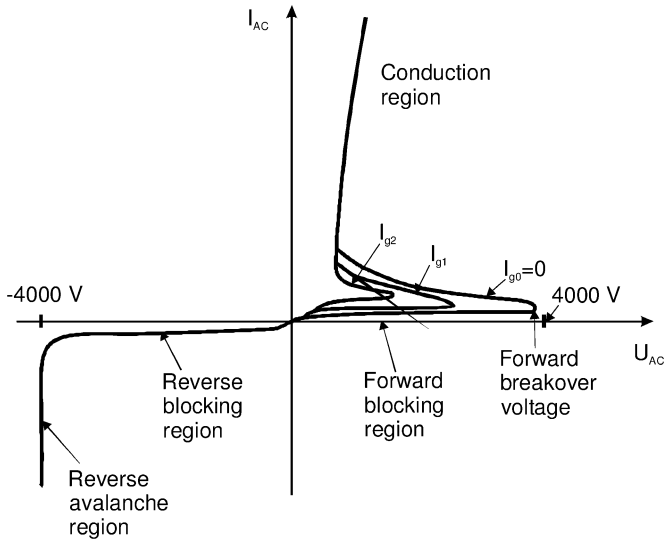


Fig. 4.25. Family of thyristor U-I characteristics

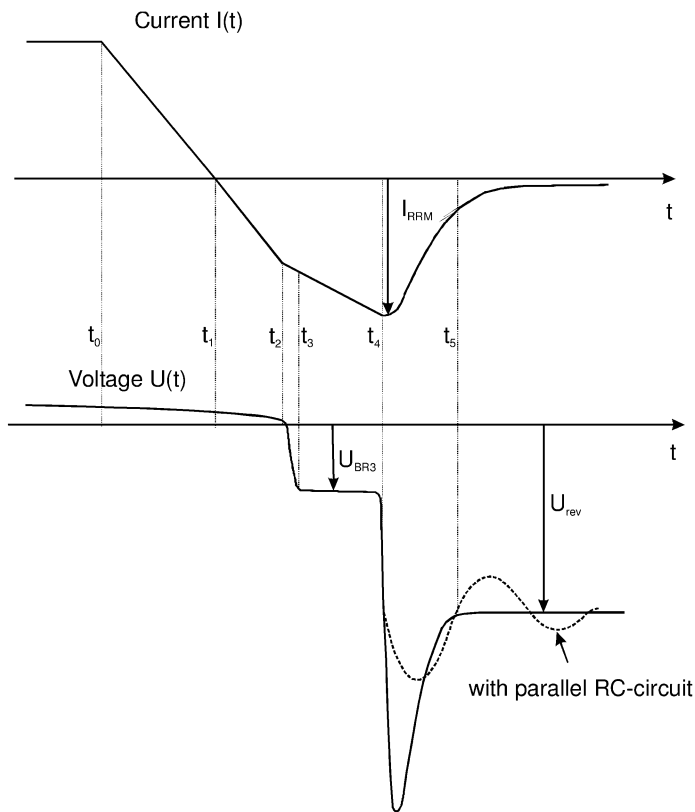


Fig. 4.26. Voltage and current in a the thyristor during commutation [Gerlach 1979]. A large inductive voltage peak during current fall-off can destroy the thyristor. To avoid this, an RC element parallel to the thyristor can be used to limit the voltage amplitude

- commutation of the current by polarity inversion;
- commutation of the current, supported by gate-assisted turn-off.

A reverse current can only flow unimpeded until the surplus charge at the emitter junctions J_1 and J_3 has been removed and a blocking voltage begins to build up. When this occurs, the space charge region expands into the bases, extracting further charge carriers. Nevertheless, the reverse current begins to decay rapidly. Initially it declines with a constant gradient $dI/dt = -U_{\text{rev}}/L$, where L is the inductance in the circuit (Fig. 4.26). At this time, recombination of charge carriers can be neglected.

Even after the zero crossing at t_1 , the current continues to flow with the same gradient. After the excess charge has been removed from the p-base adjacent to J_3 , a blocking potential begins to build up at time t_2 and the thyristor voltage $U(t)$ becomes negative. At the same time, the current

gradient shrinks. However, this reduction remains small in general, since J_3 cannot hold a large blocking voltage. Because of the large doping concentration in the p-base, its breakdown voltage U_{BR3} does not reach more than 10–20 V. At time t_4 , the surplus charge has been removed from in front of the p-emitter, and J_1 begins to take a blocking voltage. As the barrier layer at J_1 expands, the current gradient drops and it becomes zero when $U(t)$, the voltage across the thyristor, equals U_{rev} . Since the charge carrier density at J_1 has already fallen very much at this instant, the current level I_{RRM} which has been reached can no longer be maintained now. The thyristor current approaches zero and, since $dI/dt > 0$, the thyristor voltage exceeds the applied reverse voltage: $U(t) = -(U_{rev} + L dI/dt)$. A large dI/dt can lead to breakdown and destroy the thyristor. After the thyristor current has dropped to zero, the remaining charge carriers disappear in 10–100 μs by recombination.

Instead of the thyristor being triggered electronically, it can also be switched on by a light pulse. Photons with energies larger than the band gap can generate electron–hole pairs either in the space charge zone of junction J_2 or in the bases. These charge carriers behave analogously to those injected from a gate. Those generated in the highly doped emitter regions do not contribute to the current, since their life is very short in these zones. To initiate switching of the thyristor, the photocurrent must induce an anode current above the magnitude at which regenerative feedback produces a loop gain greater than 1.

In gate turn-off (GTO) thyristors, the interface of the gate contact with the p-base is larger than the area of the n-emitter interface (Fig. 4.27). The switch-on process is similar to that of a conventional thyristor. Switching off

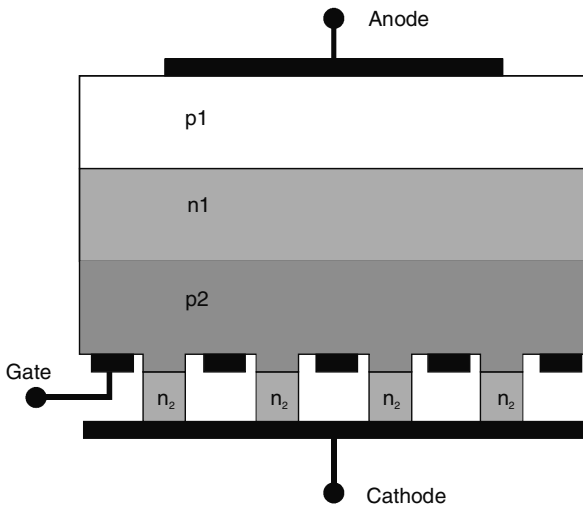


Fig. 4.27. Structure of a GTO thyristor

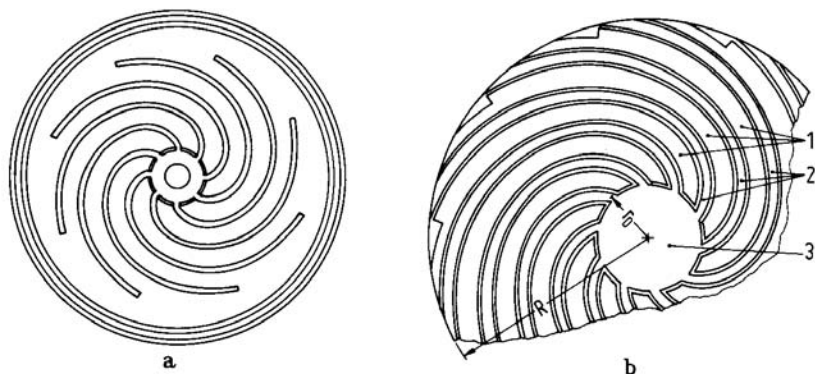


Fig. 4.28. Spiral gate stripe geometry of a high-current thyristor [Gerlach 1979]. 1, emitter stripes; 2, gate leads, 3, central gate contact

is achieved by application of a negative bias to the gate with respect to the cathode. Thus holes are sucked away from the boundaries of the n-emitters. To maintain charge neutrality, electrons are pushed from these regions to a small channel at the centre of the n-emitter. If the channel radius becomes smaller than the diffusion length, the charge carrier density declines and electron injection from the n-emitter stops.

Special gate structures are necessary if the thyristor is to switch large currents. A critical point during switch-on of a thyristor is the fact that, initially, only a small channel in the vicinity of the gate conducts current. Only after the ignition delay time t_d does the thyristor begin to carry current over the complete area. The current spreads laterally with a velocity of $0.05\text{--}0.1\text{ mm}/\mu\text{s}$, which means that for large-area thyristors, several hundred microseconds would be needed to turn the whole area on. To protect the thyristor against damage by localised overheating, the current gradient must remain below a critical value dI_{cr}/dt . To allow a faster current rise, the gate electrode has been constructed in the form of spiral finger or strip contacts, as shown in Fig. 4.28. If a sufficiently powerful ignition pulse is applied to such a gate, the blocking junction J_2 starts to conduct simultaneously at all positions. To obtain homogeneous ignition, a rather large ignition current pulse is required for such a set-up. This is sometimes generated with the help of an auxiliary thyristor integrated on the same wafer.

Thyristors for pulsed-power applications are characterised by a much larger allowable current gradient than for conventional net thyristors. Current gradients of up to $30\text{ kA}/\mu\text{s}$ can now be realised with GTO-like structures and powerful gate drivers. Table 4.1 compares the characteristics of a typical phase control thyristor with that of a high-current thyristor switch. To obtain a reverse-conducting thyristor, a free-running diode can be integrated on the Si disc. This enables the use of semiconductor switches in oscillating capacitor discharges also. A low-inductance set-up is achieved by placing the



Fig. 4.29. Four-stage repetitive thyristor switch with integrated free-running diode and trigger circuit. Maximum operating voltage, 10 kV; peak current, 30 kA; maximum current rise, 20 kA/ μ s; repetition rate, 10–50 Hz. Water-cooling bodies are visible between the thyristor units. A single unit with a trigger circuit but without water cooling is shown at the *bottom*.

trigger unit on the same board as the thyristor itself. The thyristor and the trigger circuit comprise a common unit. To obtain a switch with a larger hold-off voltage, several thyristor units can be stacked in series as shown in Fig. 4.29.

In Table 4.1, U_{FRM} and U_{RRM} are the largest allowable peak values of a repetitive half-sine-wave pulse for forward and backward polarity, respectively; I_{TSM} is the maximum non-periodic pulse current for a pulse duration of t_p ; and I_{TRMSM} is the effective allowable continuous current.

Table 4.1. Comparison of a phase control and a pulsed-power thyristor

Eupec T 1501 N (phase control thyristor)	ABB 5SPY 36L4502 (high-current thyristor switch)
$U_{FRM} = 7\text{--}8\text{ kV}$	$U_{FRM} = 4.5\text{ kV}$
$U_{RRM} = U_{FRM}$ (symmetric)	$U_{RRM} = 18\text{ V}$ (non-symmetric)
$I_{TSM} = 45\text{ kA}$ for $t_p = 10\text{ ms}$	$I_{TSM} = 140\text{ kA}$ for $t_p = 50\ \mu\text{s}$
$I_{TRMSM} = 4000\text{ A}$	
$dI_{cr}/dt = 300\text{ A}/\mu\text{s}$	$dI/dt > 10\text{ kA}/\mu\text{s}$

As can be suspected from Fig. 4.29, the high complexity and the large dimensions of a high-voltage, high-current thyristor stack, which also lead to a large product cost, are the main drawbacks of thyristors and, up to now, have prevented their broad use in pulsed-power applications. This complexity is increased by the protective circuits necessary to prevent destruction of the device in case of any malfunction in the circuit.

4.1.2.2 IGBTs

The insulated-gate bipolar transistor (IGBT) combines the advantages of bipolar transistors (low resistance in the switched-on state) with those of field effect transistors (loss-free gate control). Single IGBT units have lower current capabilities than thyristors in the voltage range 1000–1800 V, but they can easily be arranged in parallel configurations and can easily be switched off, and they possess switch-on times of the order of several times 10 ns. The IGBT differs from the power FET configuration by an additional p^+ zone, which forms the collector (Fig. 4.30). The device consists of many small-size units (10^{-3} mm^2) connected in parallel, and a common large-area collector (several cm^2). A positive temperature coefficient ensures an equal and stable partition of the total current between the individual elements.

Analogously to a bipolar transistor, holes are injected into the n-base, and the switch-on voltage is reduced to the saturation value. The IGBT has a limited reverse-blocking capability. Therefore an external diode is sometimes used in parallel.

High-power IGBTs are now available with blocking voltages up to 4 kV and on-state currents of 3 kA. IGBTs are widely used in high-voltage power and charging units. However, the same arguments as for thyristors – high complexity and high cost – have up to now prevented their broad use as repetitive high-voltage switches in pulsed-power generators.

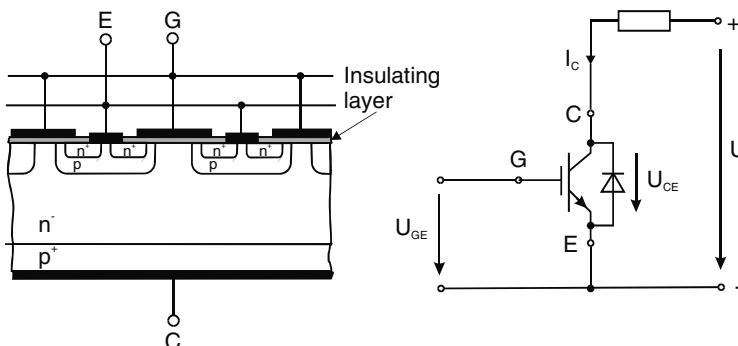


Fig. 4.30. General structure of an IGBT, and an IGBT switch set-up with an anti-parallel diode

4.1.2.3 Optically Activated Semiconductor Switches

Optically activated semiconductor switches are based on the creation of charge carriers with the help of an intense light source (a laser). The current inside the semiconductor must obey the continuity equation

$$\begin{aligned}\nabla j_n &= e(R_n - G_n) + e \frac{\partial n}{\partial t}, \\ \nabla j_p &= -e(R_p - G_p) - e \frac{\partial p}{\partial t},\end{aligned}\quad (4.13)$$

where $R_{n,p}$ are the recombination rates and $G_{n,p}$ are the generation rates of electrons (subscript 'n') and of holes (subscript 'p'). Electron and hole generation is caused either by optical excitation or by avalanche ionisation at sufficiently high electric fields:

$$eG_{av} = \alpha_n |j_n| + \alpha_p |j_p|. \quad (4.14)$$

Figure 4.31 presents the ionisation coefficients α_n and α_p as a function of the inverse field strength.

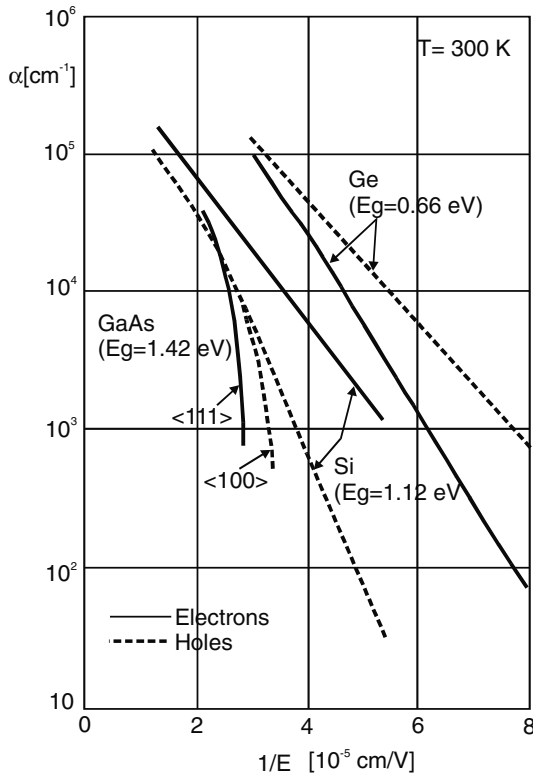


Fig. 4.31. Ionisation rate coefficients α_n and α_p

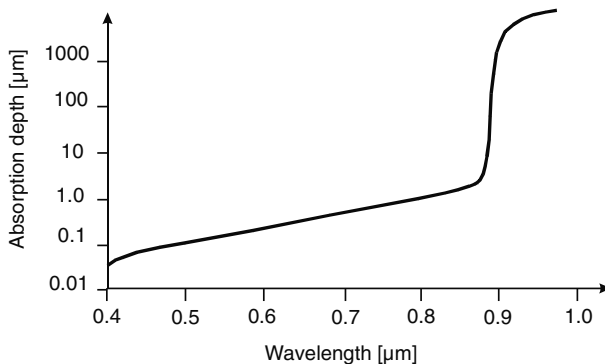


Fig. 4.32. Optical absorption depth in GaAs as a function of wavelength

One suitable semiconductor material for laser activation is GaAs [Loubriel et al. 1995, 1997]. Figure 4.32 shows the optical absorption depth in GaAs as a function of the wavelength. It is obvious that in order to obtain a sufficiently broad conducting channel in the material, the wavelength should be larger than $0.9\ \mu\text{m}$. Therefore a Nd:YAG laser, whose fundamental frequency is in the infrared region at $1.06\ \mu\text{m}$, is an appropriate light source.

A low-impedance stripline pulse generator using a multielement GaAs switch is shown in Fig. 4.33. Since the finite leakage current through the GaAs switches does not allow DC charging of the stripline, the line is pulse charged from another capacitor circuit, drawn in the upper half of the figure. With the help of an optical-fibre system, the beam from the Nd:YAG laser is split into a number of subbeams equal to the number of GaAs switch elements. The laser is fired when the stripline has reached its maximum charge.

An optically activated GaAs semiconductor switch can be operated in two regimes. In the linear photoconducting regime, the available number of charge carriers is determined only by the laser intensity. Here, the current density in the switch and the period of conduction are rather limited. It can be seen from Fig. 4.34 that the current through the switch follows the evolution of the laser power (left column of Fig. 4.34). The current flow stops after the number of charge carriers created by photoionisation has been consumed.

In the nonlinear regime, the number of charge carriers is increased by collisional ionisation and, as in a gas switch, increases exponentially. However, the switch impedance does not drop as much as it does in a spark-gap switch. There remains a voltage drop of typically $5\ \text{kV/cm}$ across the switch, and therefore the power loss in the switch is rather high (right column of Fig. 4.34). The middle column of Fig. 4.34 represents the transition between the linear and nonlinear operating regimes.

Thus, at present, the optically activated switch has found only limited application in situations where very fast switching at relatively low power is required. A big disadvantage is also that it cannot be applied in systems with DC charging.

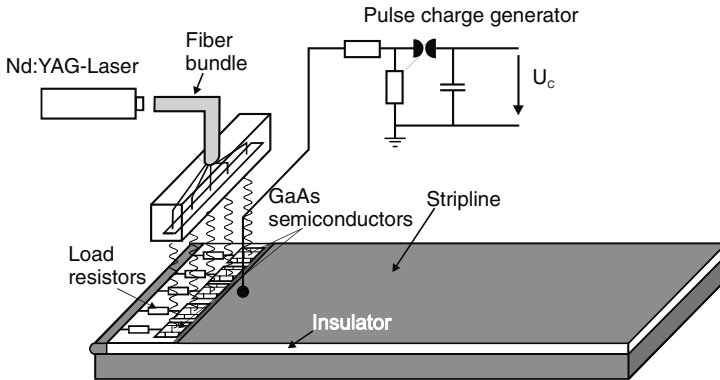


Fig. 4.33. Low-impedance stripline generator using laser-activated GaAs semiconductor switches. The stripline must be pulse charged from another capacitive generator in a time short compared with the RC discharge time of the stripline [Katschinski 1994]

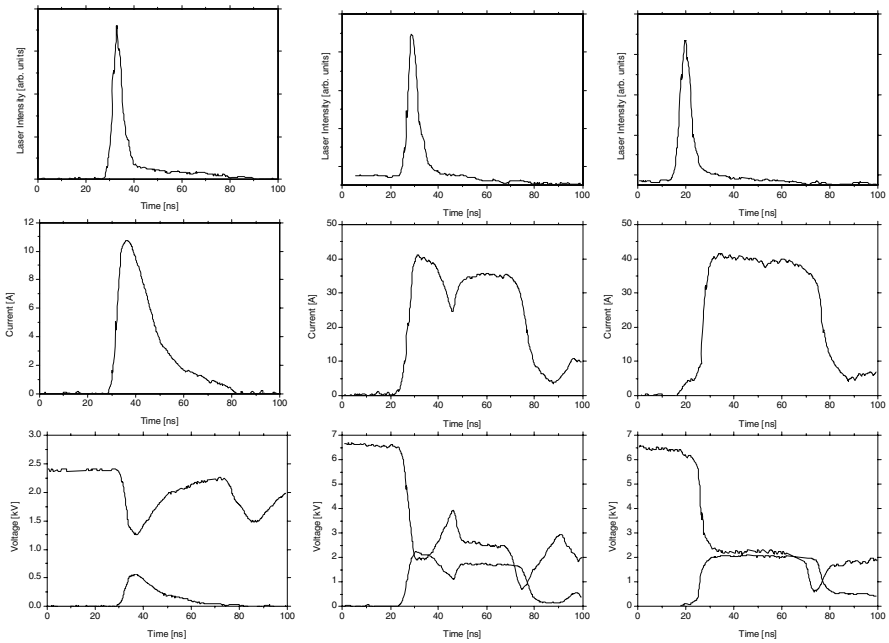


Fig. 4.34. A collection of signals measured with the set-up of Fig. 4.33. The stripline was charged to 2.4 kV (*left*) and 6.4 kV (*middle and right*). The left compilation demonstrates the typical performance in the linear photoconducting regime of operation, while the right sequence refers to the nonlinear avalanche regime. The diagrams in the central part of the figure show the transition between the two regimes. In the *bottom row* the voltage across the switch and across a load resistor are shown [Katschinski 1994]

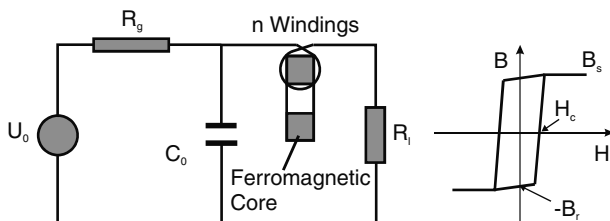


Fig. 4.35. Basic circuit with capacitive energy storage and a ferromagnetic switch. On the *right*, an ideal hysteresis loop is shown. Starting from the negative remanence point $-B_r$, the switch is driven into positive saturation at B_s .

4.1.3 Magnetic Switches

Magnetic switches are based on the saturation of a ferromagnetic core. They operate with relatively small losses and without wear. Figure 4.35 shows the basic circuit used with a magnetic switch.

While the capacitor is being charged, the coil, with a ferromagnetic core, has a high inductance at the beginning. When saturation of the core is reached by the leakage current flowing through the coil, the inductance drops abruptly by a factor of μ , which represents the relative permeability of the core material, and the switch is closed. In contrast to a transformer, which uses only a small part of the hysteresis loop to achieve linear coupling between two circuits, a magnetic switch always utilises the complete range from remanence to saturation. To obtain fast and distinct switch performance, the hysteresis loop should approximate a rectangular form, with an abrupt change of the permeability over several orders of magnitude when the saturation point is reached (Fig. 4.35).

The duration during which the switch can be considered open depends on the cross-section of the core and on the sum of its remanence and saturation inductions:

$$U(t) = \frac{d\Phi}{dt} = F \frac{dB}{dt},$$

$$\int U(t) dt = U_0 \tau = F(B_r + B_s). \quad (4.15)$$

Here U_0 is the mean pulse voltage and τ is the pulse duration. F is the cross-section of the core, and B_r and B_s are the remanence and the saturation induction, respectively. A suitable ferromagnetic material should have a high saturation inductance, a very steep hysteresis loop, and a small coercive force H_c . The commonly used ferromagnetic materials are ferrites, and ferromagnetic glasses such as Metglass¹ and the equivalent German brand

¹ Brand name of Allied Corporation, USA.

Vitrovac². Metglass and Vitrovac are metallic amorphous materials fabricated as very thin ribbon sheets by melt spinning, i.e., by rapid cooling of a thin molten layer. Metglass and Vitrovac have higher saturation inductances than ferrites but are conductive. Therefore cores made from these materials must be wound from thin ribbons with an intermediate layer of insulation. Nevertheless, the finite conductivity of Metglass and Vitrovac leads to differences between the static and the dynamic hysteresis loop. In general, the switching losses of magnetic switches can be divided into magnetisation and eddy current losses. The magnetisation, or hysteresis, losses are determined by the area of the hysteresis loop:

$$W_H = V \oint H dB, \quad (4.16)$$

where V represents the volume of the core and the integral has to be taken over the complete loop. Eddy current losses are induced in conducting materials by a time-varying induction. The power loss is proportional to the square of the induced voltage U :

$$P_{ec} \sim \frac{U^2}{\rho}, \quad (4.17)$$

where ρ is the specific resistance. At very high magnetization speed, the eddy current losses dominate and the effective hysteresis loop becomes broader and less steep, i.e., the switch deviates from ideality. Even cores fabricated from metallic-glass sheets as thin as $20 \mu\text{m}$ show this phenomenon at very high frequencies. For a thin sheet whose thickness d is very small compared with its width b and for sinusoidal boundary conditions $\underline{H}(\pm d/2, t) = \sqrt{2}H_0 \times \exp(i\omega t)$, the complex value of the magnetic induction is given by [Küpfmüller and Kohn 2000]

$$\underline{B} = \mu\mu_0 H_0 \frac{\cosh(\beta(1+i)x)}{\cosh(\beta(1+i)d/2)}. \quad (4.18)$$

Here H_0 is the effective value of the magnetic boundary field, and the absolute value of \underline{B} represents the effective value of the magnetic induction:

$$B(x) = \mu\mu_0 H_0 \sqrt{\frac{\cosh^2(\beta x) - \sin^2(\beta x)}{\cosh^2(\beta d/2) - \sin^2(\beta d/2)}}. \quad (4.19)$$

Here β is the inverse skin depth; $\beta = (\pi\nu\sigma\mu\mu_0)^{1/2}$, where ν is the frequency, σ is the conductivity, μ is the relative permeability, and μ_0 is the permeability of a vacuum. x runs from $-d/2$ to $d/2$. The function (4.19) has been plotted in the left part of Fig. 4.36 for $\beta d/2 = 2.5$.

² Brand name of Vacuum Schmelze Hanau.

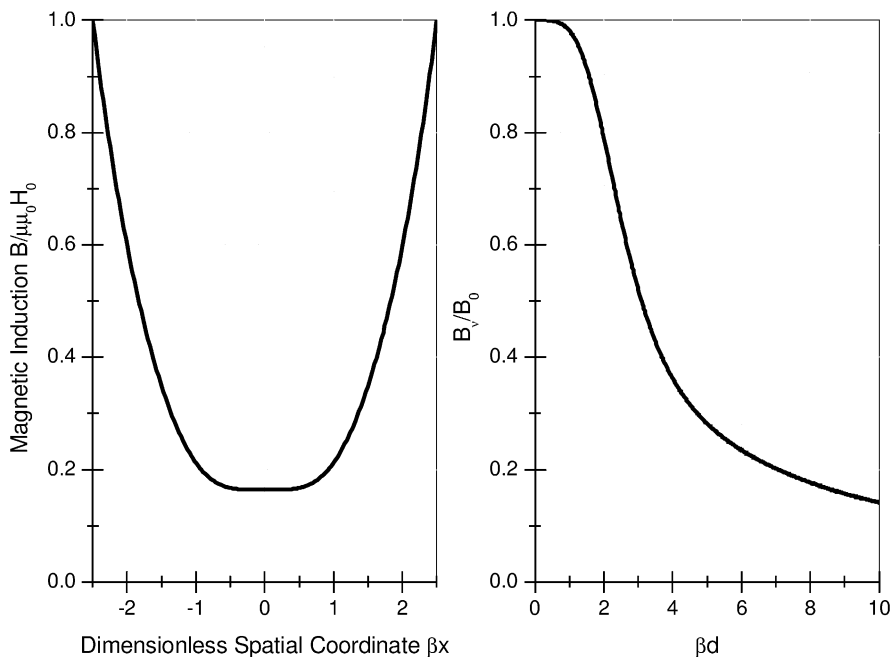


Fig. 4.36. Relative magnetic flux distribution in a thin sheet of thickness $\beta d = 2.5$ (*left*). Mean value of the magnetic induction versus βd (*right*)

We can use (4.19) to calculate the mean effective value of the magnetic induction as a function of the ratio between the sheet thickness and skin depth: βd . This is achieved by integrating (4.19) over the sheet and dividing by bd , where b is the width of the sheet. The result is given by (4.20) and plotted in the right part of Fig. 4.36. Here $B_0 = \mu\mu_0 H_0$.

$$B_\nu = \sqrt{2} \frac{\mu\mu_0 H}{\beta d} \sqrt{\frac{\cosh(\beta d) - \cos(\beta d)}{\cosh(\beta d) + \cos(\beta d)}}. \quad (4.20)$$

The time-dependent magnetic induction for the sinusoidal case considered can be obtained by multiplying (4.18) by $\exp(i\omega t)$. Taking the real part of the resulting expression, we obtain

$$B(x, t) = \sqrt{2} B(x) \sin\{\omega t - \varphi(x)\}. \quad (4.21)$$

Here $B(x)$ is given by (4.19), and $\varphi(x)$ is a spatially dependent phase factor given by

$$\begin{aligned} & \tan(\varphi(x)) \\ &= \frac{\sinh(\beta(d/2 - x)) \sin(\beta(d/2 + x)) + \sinh(\beta(d/2 + x)) \sin(\beta(d/2 - x))}{\cosh(\beta(d/2 + x)) \cos(\beta(d/2 + x)) + \cosh(\beta(d/2 - x)) \cos(\beta(d/2 - x))}. \end{aligned} \quad (4.22)$$

Equations (4.21) and (4.22) are also good approximations for transient sinusoidal pulses resulting, for example, from a Marx generator that discharges into a transmission line connected to a load through a magnetic switch.

To determine the characteristics of a switch for a specific pulse shape, one has to perform a Fourier analysis and calculate the effective inductance for each Fourier component. However, to obtain a rough estimate, it is often sufficient to evaluate (4.20) for the most dominant frequency. Of course, one must also take into account the packing fraction of the core, i.e., the ratio of the area of ferromagnetic material divided by the total area of the core, including the insulating layers.

Summarising, the advantages of magnetic switches result from their large degree of reproducibility, wear-free operation, and short recovery time. Their disadvantages result from their inability to produce an ideal rectangular pulse shape. In particular, the leakage current through the switch can create a long-lasting ‘foot’ preceding the main part of the pulse. Another disadvantage is that there is only one operating point, and that the switch has a relatively large volume.

4.1.4 Summary

In Table 4.2, we summarise some properties of the closing switches discussed in this section and give their ranges of operation.

4.2 Opening Switches

An opening switch is characterised by a sudden growth of its impedance [Schoenbach et al. 1984, Guenther 1987]. This can be initiated either by some external actuator or by some internal process, which may depend on the amount of charge conducted through the switch. The mechanism of opening can be of either resistive, inductive, or capacitive nature. An example of a resistive opening switch is the common fuse. Inductive opening switches can be realised by flux compression, such that $L(t) > L(0)$. A capacitive opening switch is obtained if $C(t) < C(0)$.

Independent of the opening mechanism, a good opening switch should meet the following requirements:

- long current conduction time;
- large current and small losses during conduction;
- fast impedance rise during opening;
- high impedance after opening and large voltage hold-off during current interruption;
- short recovery time (i.e., high repetition rate capability);
- long lifetime (small wear).

Table 4.2. Summary of properties of closing switch

Type	Hold-off potential (kV)	Peak current (kA)	Cumulative charge (A s)	Repetition rate (Hz) [commutation time (ns)]	Lifetime (number of pulses)	Remarks
Spark gap	1–6000	10^{-3} –1000	0.1–50	1–10 [1–1000]	10^3 – 10^7	Lifetime is determined by electrode erosion
Thyratron	5–50	0.1–10	10^{-3}	1000 [5–100]	10^7 – 10^8	Applied in lasers and accelerators
Ignitron	> 10	> 100	2000	1 [1000]	10^5 – 10^6	Applied in lasers and accelerators
TVG	0.5–50	1–10	40	1 [10–100]	$> 10^4$	
Pseudo-spark	1–50	1–20	1	1–1000 [> 10]	10^6 – 10^8	Similar to Thyratron
Krytron	8	3	0.01–0.1	< 1000 [1–10]	10^7	Very short delay and commutation time
Magnetic Switch	1000	100–1000		10 [5–10000]	10^8 – 10^9	Cannot be triggered; one operating point only
Thyristor	< 5	< 5	10^{-2}	10 [> 1000]	10^8	Can be stacked; expensive; complex
IGBT	< 4	3		100	10^8	Can be switched off
GaAs photoactivated switch	< 20	1–10	$< 10^{-4}$	< 10 [1–10]	10^2 – 10^3	Needs intense light source

4.2.1 Fuses

Perhaps the most widely known opening switch is the melting fuse. This consists of either a thin wire or a foil, embedded in a gaseous, liquid or granular medium. The opening mechanism is based on melting, boiling, or vaporisation of a conductor. Very fast opening (< 50 ns) is possible, and the conduction time can be determined by the type of material and its geometry. Figure 4.37 presents the increase in the resistivity of an aluminium wire as a function of the specific adiabatic energy deposition. The resistivity of most metals rises continuously with temperature both in the solid and in the liquid phase. The

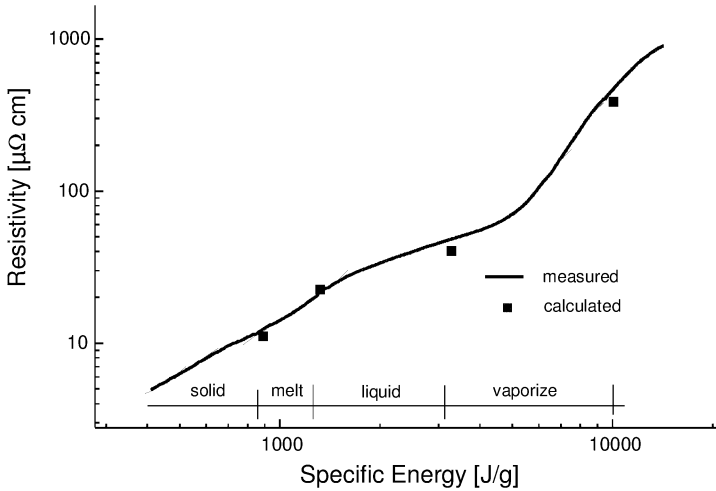


Fig. 4.37. Resistivity of a fuse as a function of specific energy deposition [Reinovsky et al. 1982]

resistance of a copper wire, for example, increases during this process by nearly two orders of magnitude. The high magnetic pressure associated with the current flowing through the fuse can maintain a high density and therefore metallic conductivity beyond the critical temperature. Only after the onset of expansion does the metallic conductivity disappear. For copper, this occurs at densities around $0.5\text{--}1 \text{ g/cm}^3$. If the density of the metal vapour becomes sufficiently small, electron avalanche processes can lead to the initiation of arcs in the vapour. The purpose of the surrounding medium is therefore to quench or prevent arc formation. Magnetohydrodynamic (MHD) instabilities and inhomogeneities in the fuse material can lead to early breaking of the fuse, causing an irregular distribution of the solid, liquid, and vapour sections. At the positions of breaks, successive arcs can be formed along the entire length of the switch. These phenomena demonstrate the importance of the surrounding medium for the performance of fuse opening switches. If the fuse is embedded in a gaseous medium or in a vacuum, it can at least in principle be operated repetitively, if the wire is replaced periodically by a suitable technique. The biggest advantage of fuse opening switches is their simplicity and the possibility to adapt their parameters to the experimental conditions by choosing the appropriate cross-section, length, and number of elements.

4.2.2 Mechanical Interrupters

The typical vacuum interrupter switch consists of two planar or disc electrodes, one fixed and the other movable, inside a vacuum envelope with a nominal gas pressure of 0.1 Pa or less. Such switches are used, for example,

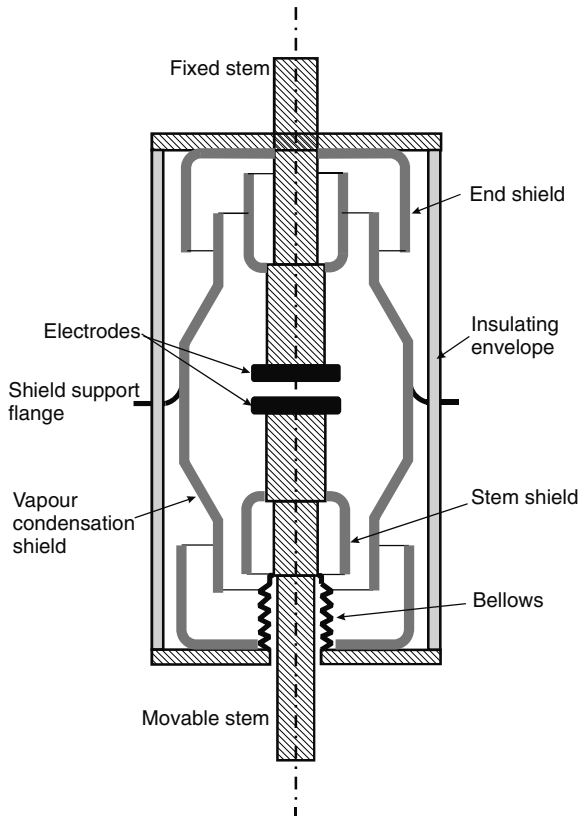


Fig. 4.38. Cross-section of a typical vacuum interrupter [Lafferty 1980]

in AC applications for electric utilities. Figure 4.38 shows a cross-section through a typical vacuum interrupter.

The movable electrode is attached to an actuator mechanism through a set of bellows to maintain the vacuum. In its closed position, a low resistance ($10\text{--}50\ \mu\Omega$) is provided by a tight metal-to-metal contact of the electrodes. To open the switch, the electrodes must be separated by an actuator. During the process of switch breaking, an arc is likely to be drawn between the electrodes, sustained by metal vapour evaporated from the electrodes. In unipolar systems a current counter-pulse must be applied to decrease the power input to the arc and to allow the residual arc plasma to recombine. After zero current has been reached in the switch, a rate of voltage rise (dU/dt) as high as $24\text{ kV}/\mu\text{s}$ is possible.

A circuit diagram showing the principle of a counter-pulse arrangement is shown in Fig. 4.39. Until time t_1 , the entire loading current flows through the closed switch S_0 . The switches S_1 and S_2 are open. At time t_1 , switch S_1 closes and the capacitor C_1 , charged previously to U_1 , discharges through

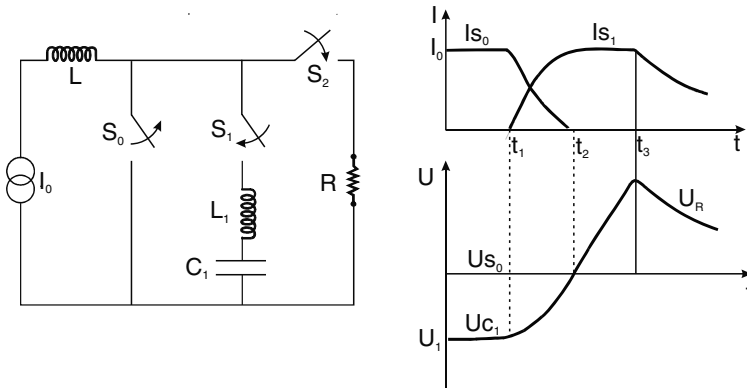


Fig. 4.39. Counter-pulse circuit diagram, and current and voltage traces during operation

the inductance L_1 and the switches S_1 and S_0 . The direction of current flow is chosen such that the current through S_0 is reduced. At time t_2 , when the current through S_0 passes through zero, the actuator is activated to open the switch. After the opening of S_0 , the capacitor C_1 is recharged, this time, however, with opposite polarity. The rate of voltage rise dU/dt is equal to $I_0/C_1 = \text{const.}$ if $L \gg L_1$ (i.e., $I_0 = \text{const.}$). At time t_3 , S_2 is closed and the stored energy is transferred to the load.

The standard vacuum interrupter shown in Fig. 4.38 allows repetitive operation up to a few tens of hertz. Its opening speed can reach tens of microseconds.

4.2.3 Superconducting Opening Switches

This switch utilises a transition from a superconducting state into a state of normal conduction. Superconducting opening switches are commonly applied in conjunction with superconducting energy storage. The main problem with the superconducting switch consists of the additional cooling necessary to remove the heat flowing into the cryogenic coolant during opening.

The opening process can be initiated by three different trigger or quenching methods: by the current itself, by an external pulsed magnetic field, or by pulse heating. The repetition rate depends on the speed of recovery to the superconducting state. Figure 4.40 shows schematically the arrangement of a switch that is opened with the help of a pulsed magnetic field, whose strength exceeds the critical field of the superconductor.

4.2.4 Plasma Opening Switches

The plasma opening switch is suitable for high currents and short switching times. It consists of a plasma bridge of low density (10^{13} – 10^{15} cm^{-3}),

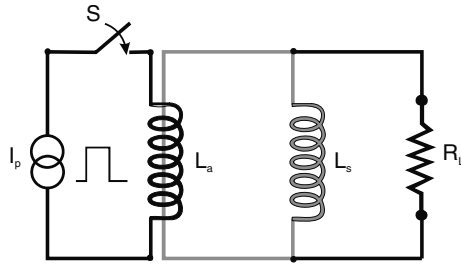


Fig. 4.40. Superconducting energy storage device L_s with a superconducting opening switch activated by a pulsed-magnetic field coil L_a , which creates a field above the critical value in a section of the superconducting circuit. The resistance of this section must become larger than the load resistance R_L to divert the current into the load effectively

established before the inductive storage device has been charged, between its terminals (Fig. 4.41). Various kinds of plasma generators are used to establish the plasma bridge.

A coaxial system whose operation is started by gas injection is shown in Fig. 4.42. The gas is made into a plasma by an auxiliary electric pulse before the coaxial inductor is charged. Depending on the plasma density, the plasma bridge begins to erode after a certain amount of charge has been conducted through it. Thereby, the switch passes from a state of high conductivity to a state of low conductivity.

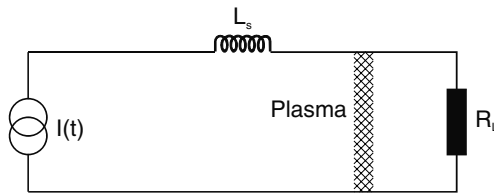


Fig. 4.41. Illustration of the principle of an inductive storage device with a plasma opening switch

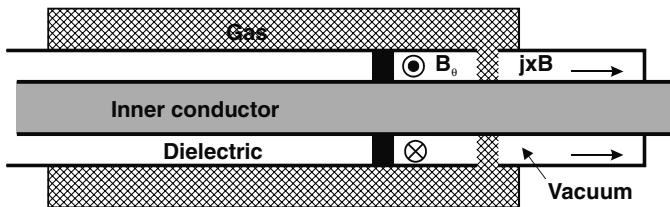


Fig. 4.42. Schematic illustration of a coaxial system with an injected pulsed gas column which is transformed into a plasma by an applied electric pulse

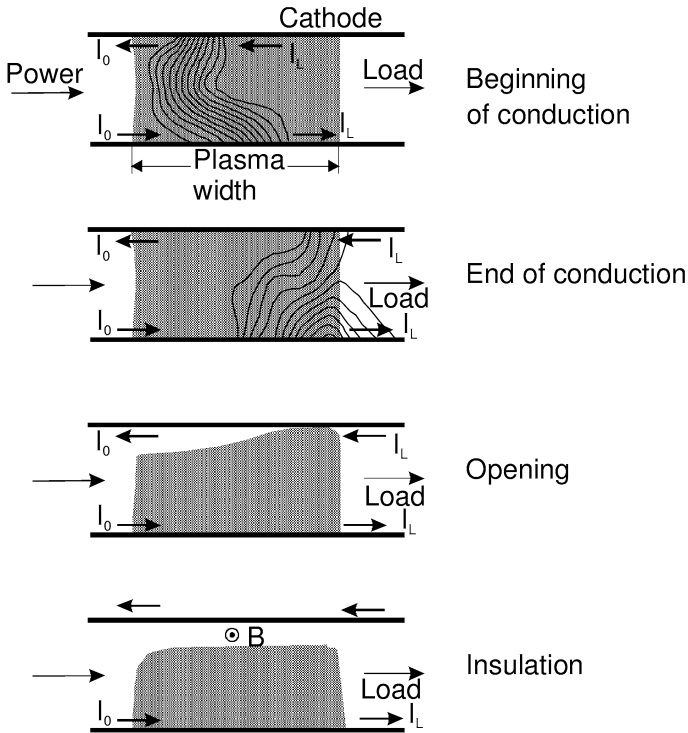


Fig. 4.43. Illustration of the operation phases of a plasma opening switch. The contour lines in the first two sketches represent constant-current contours, i.e., the total current flowing past these locations. They have been inferred from measurements [Shpitalnik et al. 1998, Arad et al. 2003]. The usefulness of a plasma opening switch is determined by the degree of insulation obtained after opening

The behaviour of plasma switches is very complex and depends not only on the plasma density but also on the injection velocity, the ion mass, density gradients, and the conditions at the electrodes, as well as on the impedance of the load into which the current is commutated. Generally, three phases of operation of a plasma opening switch can be distinguished. These operation phases are illustrated schematically in Fig. 4.43.

During the conduction phase, the current and, concurrently, the magnetic field penetrates into the plasma. The evolution of the magnetic field in the highly conductive plasma can be expressed by an equation derived from Faraday's law, a generalized Ohm's law with the neglect of electron inertia, and Ampère's law with the neglect of the displacement current. We can obtain the generalized Ohm's law from the equations of motion for the two-fluid hydrodynamics [Artsimowitsch and Sagdejew 1983] of a quasi-neutral plasma with equal numbers of electrons and singly charged ions ($n_e = n_i = n$):

$$\begin{aligned}
nm_i \frac{d\vec{u}_i}{dt} &= -\nabla p_i + en\vec{E} + en(\vec{u}_i \times \vec{B}) - m_e(\vec{u}_i - \vec{u}_e)\nu_{ei}n, \\
nm_e \frac{d\vec{u}_e}{dt} &= -\nabla p_e - en\vec{E} - en(\vec{u}_e \times \vec{B}) + m_e(\vec{u}_i - \vec{u}_e)\nu_{ei}n. \quad (4.23)
\end{aligned}$$

Here u_e and u_i are the electron and ion velocities, respectively, m_e and m_i are the electron and ion masses, p_e and p_i are the electron and ion pressures, E is the electric field, B is the magnetic induction, e is the electron charge, and ν_{ei} is the collision frequency between ions and electrons. The last terms on the right-hand side of (4.23) therefore represent the drag force density. Multiplying the first of these equations by m_e and the second by m_i , subtracting the second equation from the first, and neglecting terms of the order m_e/m_i and assuming significant changes of the current density only for times $t \gg 1/\nu_{ei}$, i.e., ignoring the inertia terms on the left-hand side, we obtain

$$\vec{E} = \vec{u} \times \vec{B} + \frac{\vec{j}}{\sigma} - \frac{\vec{j} \times \vec{B}}{en} - \frac{\nabla p_e}{en}. \quad (4.24)$$

Here, we have introduced the conductivity $\sigma = (ne^2/m_e)/\nu_{ei}$. Substituting (4.24) into Faraday's law, we obtain the most general equation for the description of magnetic-field penetration into a conducting fluid:

$$\frac{\partial \vec{B}}{\partial t} = \vec{\nabla} \times (\vec{u} \times \vec{B}) - \vec{\nabla} \times \left(\frac{\vec{j} \times \vec{B}}{en} \right) + \frac{\Delta \vec{B}}{\sigma \mu_0}. \quad (4.25)$$

Here, the first term on the right-hand side is the convection term. This is formally the same as the vorticity in an inviscid fluid [Sommerfeld 1950]. If this term dominates, i.e., if the electrical conductivity is large, we can interpret this equation as meaning that the magnetic lines of force move with the fluid; the field is frozen into the plasma. In this case, the magnetic flux through any contour following the motion of the material remains constant in time, and the dominating effect will be pushing of the plasma by the $\vec{j} \times \vec{B}$ force. This pushing can result in a 'snowplough' movement if the plasma density is high. The second term in (4.25) is the Hall term. It is expected to dominate for scale lengths $\ell = [(1/n)dn/dx]^{-1}$ that are smaller than the inertial length of the ions, i.e., $\ell \ll c/\omega_{pi}$, where ω_{pi} is the ion plasma frequency and c is the speed of light. If the Hall field dominates, the magnetic field can penetrate with a velocity given by $u_H = B/(2\mu_0 en\ell)$. In this case, the magnetic-field velocity u_H becomes larger than the ion velocity u_i . The last term in (4.25) describes the general process of diffusion into a conductor.

In order to conduct currents of several hundred kiloamps or up to megaamps for a duration of microseconds a plasma density of 10^{15} – 10^{16} per cm^3 is required. At these high electron densities, plasma pushing by the magnetic field as expressed by the first term in (4.25) is an adequate model to describe the conduction phase. The plasma flow switch discussed below is an example of a switch where this applies.

To conduct currents for less than 100 ns with subsequent opening in less than 10 ns, a plasma density of around 10^{13} per cm^3 is necessary. Under these conditions, the magnetic field penetrates owing to the Hall term, the second term in (4.25). The complete theory developed to describe this situation is called electron magnetohydrodynamics (EMHD) [Kingsep et al. 1990].

For intermediate densities, both terms in (4.25) become relevant. Intermediate densities may also develop during the conduction phase in a high-density switch. Plasma switches containing several different ion species behave in an even more complex way: separation of the ion components can occur, and the lighter ion component may be pushed towards the load [Maron et al. 2002].

Opening of the plasma switch occurs if the plasma becomes pushed out of the gap or if it is eroded. The impedance of the open phase is very much determined by self-magnetic insulation in the gap initially filled with plasma resulting from the current flowing downstream of the load (Fig. 4.43). Thus it is obvious that the losses of the switch grow with the load impedance and that the plasma opening switch is useful mainly for low-impedance loads. This also limits the attainable power and voltage multiplication (see Sect. 3.3).

4.2.5 Plasma Flow Switches

The plasma flow switch operates at much higher plasma densities (10^{15} cm^{-3}) than does the fast plasma opening switch. Therefore it is well suited for conduction times in the microsecond range. It is based on the magnetohydrodynamic acceleration of a plasma bridging a gap between two electrodes, as discussed before. A sudden increase in the gap width causes interruption of the current-carrying contact and initiates the opening process (Fig. 4.44).

4.2.6 Semiconductor Opening Switches (SOSs)

Current interruption in semiconductor opening switches depends either on the production of charge carriers in the intrinsic material by an external pulsed radiation source, such as a laser or an electron beam, where the carriers disappear if the source is shut off, or on charge injection into the base of a p^+nn^+ structure in a time that is short compared with the lifetime of the charge carriers in the material, and subsequent local or global depletion of the accumulated charge carriers by the reverse current. As we saw in the earlier section on optically activated semiconductor switches, the first principle of control cannot be used for high-power switching.

To understand the physical principles of semiconductor opening switches based on the second scheme, let us consider first the recovery processes in silicon power rectifiers [Benda and Spenke 1967]. The structure of a power rectifier is similar to that of a p^+in^+ (or ‘pin’) diode. The ideal pin diode consists of an intrinsic layer sandwiched between a heavily doped p-type (p^+) region and a heavily doped n-type (n^+) region. In practice, this is difficult to

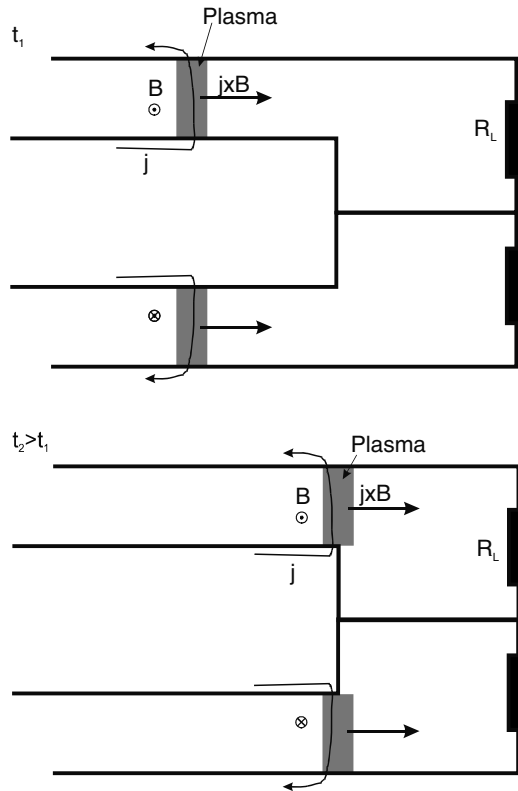


Fig. 4.44. General scheme of a plasma flow switch: conduction phase (*top*) and beginning of opening phase (*bottom*)

achieve, so a psn diode is used, where 's' represents the lightly doped middle layer, which can be p- or n-type. A typical doping concentration of such a diode structure obtained by diffusion is shown in Fig. 4.45.

The step recovery diode (SRD), which is commonly used for frequency multiplication, shares a similar structure with the power rectifier. Although they are far from perfect, both diodes show certain features of an opening switch. During forward operation, the middle region of the structure shown in Fig. 4.45 is 'swamped' by holes from the left and by electrons from the right. This leads to a strong increase in the carrier concentrations in the middle region, which for reasons of neutrality must be equal: $n(x, t) = p(x, t)$, where $n(x, t)$ is much greater than the doping concentration. Because of this strong increase in the concentration, pair generation and recombination are no longer balanced. Since recombination predominates, the current of the holes coming from the left is taken over by the electrons meeting the holes from the right. This takes place not only in the middle region but also in the highly doped regions.

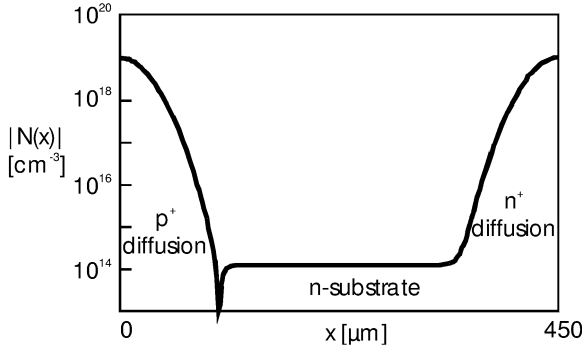


Fig. 4.45. Distribution of doping concentration in a power rectifier or SRD diode

For diodes with abrupt junctions (pin diodes) this leads to the following carrier distribution in the middle region:

$$n(x) = \frac{\tau j_F}{2eL_d} \left(\frac{\cosh x/L_d}{\sinh d/L_d} - B \frac{\sinh x/L_d}{\cosh d/L_d} \right). \tag{4.26}$$

Here τ is the lifetime of charge carriers in the middle region, j_F is the forward current density, e is the value of the electronic charge, L_d is the diffusion length, $2d$ is the width of the middle region of the rectifier, $B = (\mu_n - \mu_p) / (\mu_n + \mu_p)$, and μ_n and μ_p are the electron and hole mobilities, respectively. Equation (4.26) is also approximately valid for psn diodes.

The average value of the charge carrier concentration is

$$\bar{n} = \frac{j_F \tau}{2de}. \tag{4.27}$$

Thus the forward current density has to take account of the fact that, within a lifetime τ , the stored charge per unit area $2den$ is destroyed exactly once by recombination.

We now assume that at time $t = 0$, the polarity of the rectifier is reversed from the forward load current density j_F to the reverse current density j_R . This instant in time, however, is not the switching time that we want to consider, but the beginning of the removal of the stored charge from the middle region. As a large reverse current begins to flow, the concentration gradients at the right and left borders of the middle region change sign, and the charge carrier distribution changes as shown in Fig. 4.46. As soon as the concentration distribution reaches zero values at the boundaries, a space charge region develops there, which in the case of an intrinsic middle region (pin diode) is maintained by mobile charge carriers rather than by fixed ionised donors or acceptors. At the left border of the middle region in Fig. 4.46, holes are supplied from the stored charge in the middle, but no electrons can be supplied from the highly doped p region. Thus the electrons begin to disappear,

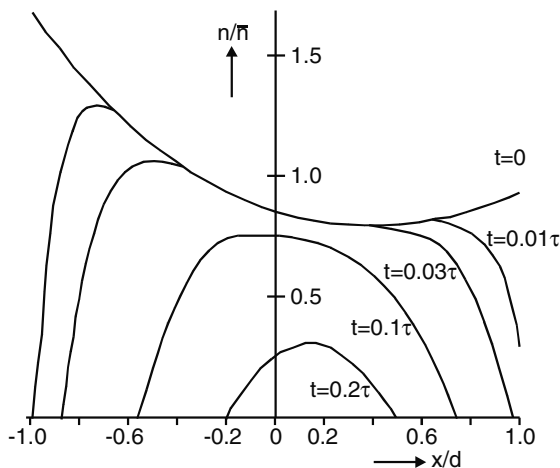


Fig. 4.46. Sweeping out of carriers from the swamped zone by a strong reverse current $j_R = 10j_F$ ($\mu_n = 3\mu_p$, $d = L_d$)

and the hole concentration remains uncompensated with respect to its charge at this border. Similar considerations apply to the right border of the middle region, where the electrons remain uncompensated. However, because of the difference in the hole and electron mobilities, the space charge and the voltage drop associated with it appear earlier at the left boundary than at the right. The carrier distribution in a pin rectifier during the sweeping-out process is schematically presented in Fig. 4.47. The holes flowing off to the left and the electrons flowing off to the right must be supplied by the stored charge. Hence this charge must decrease and finally disappear completely.

The ‘sweeping-out’ boundaries $x = -a_1(t)$ and $x = a_r(t)$ approach each other with a velocity that can be found by the following considerations. In the middle of the swamped zone, where the concentration gradient disappears, the carrier currents flow as pure field currents and have the same ratio as the mobilities:

$$\begin{aligned} |j_p| &= \frac{\mu_p}{\mu_n + \mu_p} j_R, \\ |j_n| &= \frac{\mu_n}{\mu_n + \mu_p} j_R. \end{aligned} \quad (4.28)$$

In the space charge zones, on the other hand, one type of carrier always carries the entire reverse current. Therefore, at $x = -a_1(t)$, the carrier currents jump discontinuously by

$$\Delta j_p = -\Delta j_n = j_R - \frac{\mu_p}{\mu_n + \mu_p} j_R = \frac{\mu_n}{\mu_n + \mu_p} j_R. \quad (4.29)$$

Consequently, during a time interval δt , at $x = -a_1$ a charge differential $\Delta j_p \delta t$ is swept out per unit area:

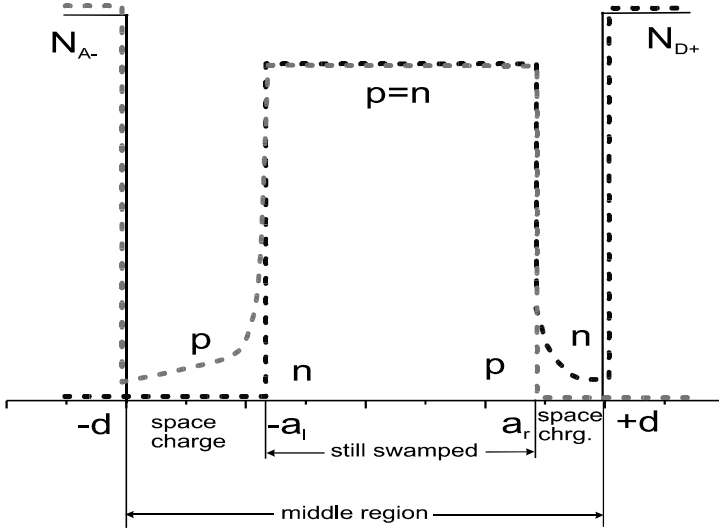


Fig. 4.47. Distribution of the charge carriers in a pin rectifier during the sweeping-out process

$$\Delta j_p \delta t = \frac{\mu_n}{\mu_n + \mu_p} j_R \delta t = e\bar{n} \delta a_1. \quad (4.30)$$

Thus we find the velocity of the left sweeping-out boundary to be

$$\left| \frac{da_1}{dt} \right| = \frac{\mu_n}{\mu_n + \mu_p} \frac{j_R}{e\bar{n}}. \quad (4.31)$$

Correspondingly, we have for the right boundary

$$\left| \frac{da_r}{dt} \right| = \frac{\mu_p}{\mu_n + \mu_p} \frac{j_R}{e\bar{n}}. \quad (4.32)$$

As soon as the build-up of the space charge zones has begun, the voltage across the rectifier starts to rise and, depending on the impedance of the driving circuit, the current drops, as shown in Fig. 4.48. A fast transition (short t_R) is generally unwanted in power rectifier applications, since it can lead to large inductive voltages in power circuits. Also, the entire reverse recovery transient is undesirable in power applications, since it is a source of power loss. Thus the power rectifier is optimised by minimising $t_R + t_S$ and, within that constraint, maximising t_R . On the other hand, SRDs are designed to achieve fast transients, but their s-layer is rather small and they cannot support large reverse voltages.

An improvement with respect to this situation is the drift step recovery diode (DSRD), which was first developed in the Joffe Institute in St Petersburg [Grekhov and Mesyats 1999]. In this diode, a short forward pump

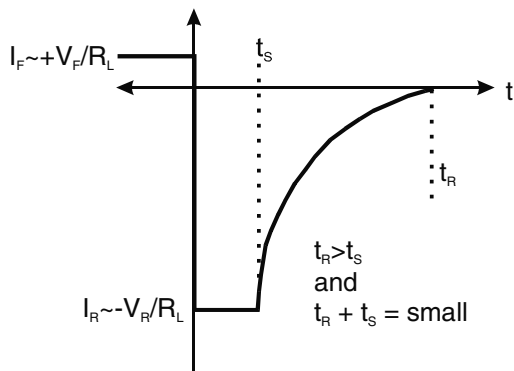


Fig. 4.48. Ideal reverse recovery transients for a power rectifier

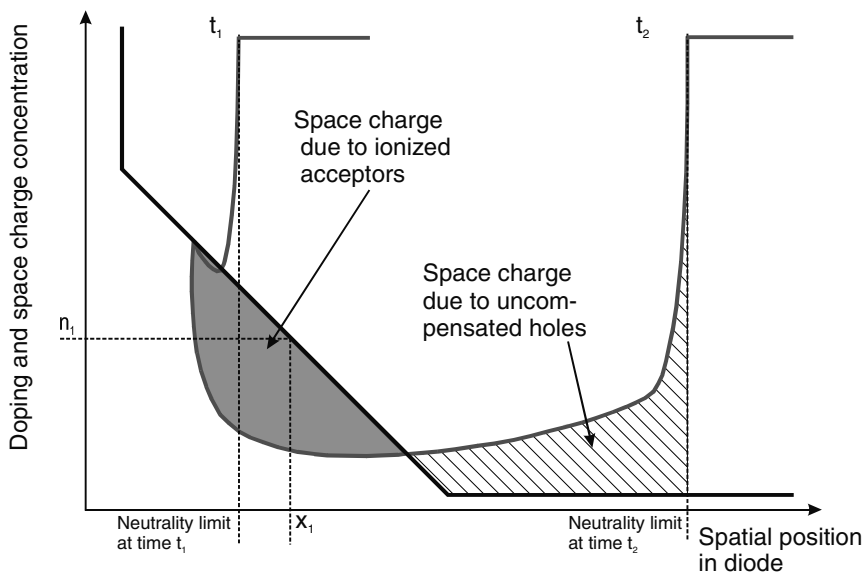


Fig. 4.49. Schematic illustration of the movement of the plasma front and the formation of space charge in a semiconductor opening switch during reverse-current operation

pulse is used to create a strongly inhomogeneous distribution in the plasma (holes + electrons), concentrated mainly at the p^+n junction. Owing to this profile, the speed of the sweeping-out process is increased by two orders of magnitude. Typically, opening times of 0.5–1.5 ns can be achieved at current densities of around 100–200 A/cm². The voltage hold-off of a single diode is about 1–1.5 kV. These diodes can be stacked without any voltage dividers to achieve voltage pulses of up to 50 kV.

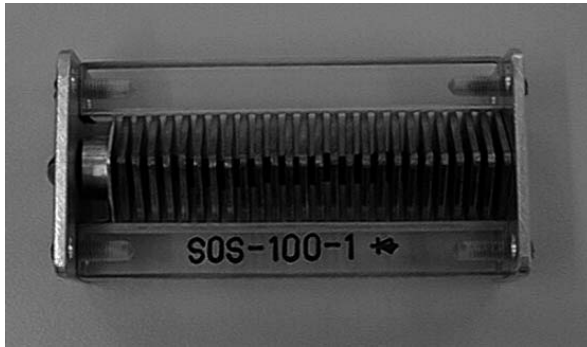


Fig. 4.50. 100 kV semiconductor-opening-switch (SOS) stack

However, the best performance is presently achieved with a switch called the SOS (semiconductor opening switch) [Lyubutin et al. 1996], where current densities of up to 60 kA/cm^2 have been interrupted in less than 10 ns. The operating voltage of a single SOS diode is around 1.5 kV. These diodes can be stacked too without any voltage dividers, and arrangements for 1 MV have been assembled. The SOS diode consists of a $p^+ - p - n - n^+$ structure. As in the power rectifier diode, holes and electrons enter the structure from the highly doped regions during forward pumping. The carriers need tens of nanoseconds to cross the base region where the field is high. On coming to the regions with high concentrations and low fields, they are retarded and accumulate in these regions. Therefore the greater part of the stored charge carriers are found in the form of a quasi-neutral electron-hole plasma at the boundaries of the highly doped regions. When the reverse current flows, two concentration fronts move into the base as described previously. Current interruption is initiated at those points where the plasma concentration is lowest (Fig. 4.49). As the plasma front moves to the middle, ionised acceptor and donor atoms remain uncompensated and a space charge region develops near the highly doped boundaries. Early in the opening process, when the electric field is high at these positions, avalanche multiplication of carriers takes place [Engelko and Bluhm 2004]. It is important to notice that the opening of the switch occurs without complete removal of the plasma from the base.

Figure 4.50 shows a stack of SOS diodes which, if placed in oil, can hold voltages of up to 100 kV during opening.

5 Pulse-Forming Networks

Many pulsed-power applications require a constant-voltage plateau. To create such pulses, various arrangements of LC elements are necessary. These arrangements are called pulse-forming networks.

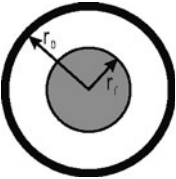
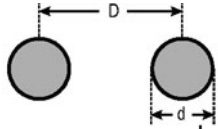
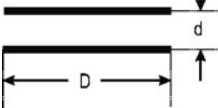
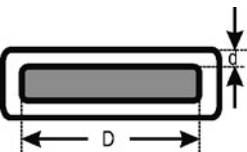
5.1 Transmission Lines

Transmission lines are the continuous borderline case of a network consisting of discrete LC elements. Let us consider a circuit element (L or C) of finite extent. We want to find a criterion for when it can be considered as a lumped circuit element and for when it has to be treated as an extended object. The answer depends on the time during which energy is extracted from or supplied to the element. If this time is long compared with the time it takes for an electromagnetic wave to move from one terminal of the element to the next, then the element can be treated as a lumped (or point-like) circuit element. In the opposite case, the element, must be treated as a transmission line. This leads sometimes to the confusing situation in which while the energy is supplied slowly the line can be treated as a lumped parameter, but when the energy is extracted rapidly it must be regarded as a distributed-parameter element.

Various transmission line geometries and the corresponding distributed parameters are listed in Table 5.1. L' and C' here are the inductance and the capacitance per unit length.

Let us consider first an infinitesimal section of a homogeneous coaxial transmission line, as shown in Fig. 5.1. The specific inductances of both conductors (inner and outer) have been summarised as L' . Further, we combine R'_1 and R'_2 , the resistances per unit length of the inner and outer conductors, into one element R' . G' is the conductance per unit length. With these simplifications, we arrive at the lumped circuit presented in the lower right part of the figure, which can be used to derive the differential equations with the help of Kirchhoff's laws. In general, all quantities are frequency-dependent because of the skin effect and because, also, the dielectric constant depends on the frequency. For the following derivation, we assume, however, that they are independent of the position x and of the voltage and current as well. In this case, the following differential equations can be derived, where the Laplace-transformed version has been adopted:

Table 5.1. Transmission line geometries and distributed parameters

<p>1. Coaxial transmission line:</p> $C' = 2\pi\epsilon / \ln(r_o/r_i)$ $L' = (\mu/2\pi) \ln(r_o/r_i)$ $Z_0 = \left((\mu/\epsilon)^{1/2} / 2\pi \right) \ln(r_o/r_i)$ $= 60(\mu_r/\epsilon_r)^{1/2} \ln(r_o/r_i)$	
<p>2. Double-wire line:</p> $C' = \pi\epsilon / \operatorname{arcosh}(D/d)$ $L' = (\mu/\pi) \operatorname{arcosh}(D/d)$ $Z_0 = \left((\mu/\epsilon)^{1/2} / \pi \right) \operatorname{arcosh}(D/d)$	
<p>3. Parallel-plate line:</p> $C' = \epsilon D/d$ $L' = \mu d/D$ $Z_0 = (\mu/\epsilon)^{1/2} (d/D)$	
<p>4. Stripline:</p> $C' = 2\epsilon D/d$ $L' = \mu d/2D$ $Z_0 = (\mu/\epsilon)^{1/2} (d/2D)$	

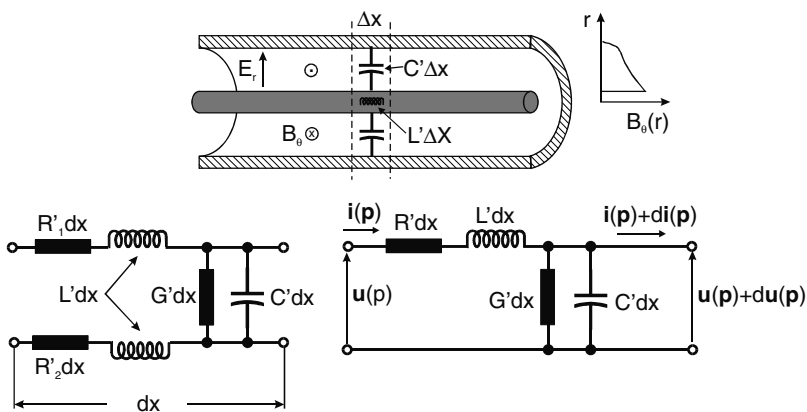


Fig. 5.1. Differential element of a homogeneous transmission line. The *lower right* part shows the reduced, lumped circuit model used for the derivation of the differential equations

$$\begin{aligned}\frac{d^2 \mathbf{u}(\mathbf{p})}{dx^2} &= (G' + \mathbf{p}C')(R' + \mathbf{p}L') \mathbf{u}(\mathbf{p}), \\ \frac{d^2 \mathbf{i}(\mathbf{p})}{dx^2} &= (G' + \mathbf{p}C')(R' + \mathbf{p}L') \mathbf{i}(\mathbf{p}).\end{aligned}\quad (5.1)$$

In the case of a lossless line ($R' = 0$, $G' = 0$), we obtain

$$\begin{aligned}\frac{d^2 \mathbf{u}(\mathbf{p})}{dx^2} &= \mathbf{p}^2 C' L' \mathbf{u}(\mathbf{p}), \\ \frac{d^2 \mathbf{i}(\mathbf{p})}{dx^2} &= \mathbf{p}^2 C' L' \mathbf{i}(\mathbf{p}).\end{aligned}\quad (5.2)$$

Solving these differential equations in x , we obtain

$$\mathbf{u}(x, \mathbf{p}) = \mathbf{u}_x(\mathbf{p}) = \left\{ \begin{array}{l} \vec{\mathbf{u}}_0(\mathbf{p}) e^{-\mathbf{p}\sqrt{L'C'}x} \\ \overleftarrow{\mathbf{u}}_0(\mathbf{p}) e^{\mathbf{p}\sqrt{L'C'}x} \end{array} \right\}. \quad (5.3)$$

Taking into account the following rule for the inverse Laplace transformation,

$$L\{u_x(t - T)\} = \mathbf{u}_0(\mathbf{p}) e^{-\mathbf{p}T}, \quad (5.4)$$

this leads to the following result:

$$u(x, t) = u_x(t) = \left\{ \begin{array}{l} \vec{u}_0(t - x\sqrt{L'C'}) \\ \overleftarrow{u}_0(t + x\sqrt{L'C'}) \end{array} \right\}. \quad (5.5)$$

The general solution is a linear combination of both solutions:

$$u_x(t) = \vec{u}_0(t - x/c) + \overleftarrow{u}_0(t + x/c). \quad (5.6)$$

In the equations above, we have adopted a notation that indicates by arrows above the letters the direction of wave propagation. In (5.6), we have replaced $L'C'$ by $1/c^2$, where c is the phase velocity of the wave. The first term shows that the wave amplitude at position x and time $t = t_1 + x/c$ is the same as that at position $x = 0$ and time $t = t_1$, i.e., we are dealing with a wave propagating in the positive x -direction with a velocity c . If c is frequency-independent, the propagation occurs without dispersion, i.e., the shape of the wave is conserved. The second term describes a wave travelling with the same velocity in the opposite direction. Similar equations are valid for the current pulse. Substituting the solution (5.3) into the circuit equation yields

$$\begin{aligned}\frac{d\vec{\mathbf{u}}_x(\mathbf{p})}{dx} &= -\mathbf{p}L' \vec{\mathbf{i}}_x(\mathbf{p}), \\ -\mathbf{p}\sqrt{L'C'} \vec{\mathbf{u}}_x(\mathbf{p}) &= -\mathbf{p}L' \vec{\mathbf{i}}_x(\mathbf{p}).\end{aligned}\quad (5.7)$$

From this result, we obtain the impedance Z_0 of the line:

$$\frac{\vec{u}_x(\mathbf{p})}{\vec{i}_x(\mathbf{p})} = \sqrt{\frac{L'}{C'}} = Z_0 = -\frac{\overleftarrow{u}_x(\mathbf{p})}{\overleftarrow{i}_x(\mathbf{p})}. \quad (5.8)$$

For the loss-free transmission line treated here, Z_0 is independent of the frequency. Therefore we also have

$$Z_0 = \frac{\vec{u}_0(t-x/c)}{\vec{i}_0(t-x/c)} = -\frac{\overleftarrow{u}_0(t+x/c)}{\overleftarrow{i}_0(t+x/c)}. \quad (5.9)$$

5.1.1 Terminations and Junctions

We consider first a lossless transmission line that is terminated with an arbitrary frequency-dependent impedance $Z(\mathbf{p})$ (Fig. 5.2). According to Ohm's law, the following relation must hold at the termination:

$$Z(\mathbf{p}) = \frac{\vec{u}_\ell(\mathbf{p}) + \overleftarrow{u}_\ell(\mathbf{p})}{\vec{i}_\ell(\mathbf{p}) + \overleftarrow{i}_\ell(\mathbf{p})}. \quad (5.10)$$

If we now replace the currents by the voltages of the incoming and reflected waves, using

$$\vec{i}_\ell(\mathbf{p}) = Z_0 \vec{u}_\ell(\mathbf{p}), \quad \overleftarrow{i}_\ell(\mathbf{p}) = -Z_0 \overleftarrow{u}_\ell(\mathbf{p}), \quad (5.11)$$

we obtain the following for the reflection coefficient ρ :

$$\rho = \frac{\overleftarrow{u}_\ell}{\vec{u}_\ell} = \frac{Z - Z_0}{Z + Z_0}. \quad (5.12)$$

Several special cases are important. The case $Z = Z_0$ is called the case of a matched load. This is equivalent to an infinitely long line, because nothing is reflected from the termination. $Z = 0$ is the short-circuit case. Here, the wave is completely reflected with an inverted voltage amplitude. $Z = \infty$ represents an open circuit, and here the voltage pulse is totally reflected with the same polarity.

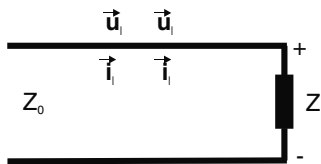


Fig. 5.2. Transmission line with impedance Z_0 , terminated with $Z(\mathbf{p})$

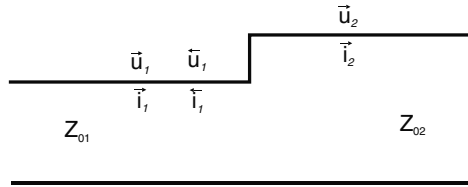


Fig. 5.3. Junction of two transmission lines

Similar considerations hold at a junction of two lines with impedances Z_{01} and Z_{02} (Fig. 5.3):

$$\rho = \frac{\vec{u}_r}{\vec{u}_1} = \frac{Z_{02} - Z_{01}}{Z_{02} + Z_{01}}. \tag{5.13}$$

At the junction of the two lines, we have

$$\vec{u}_1 + \vec{u}_r = \vec{u}_2. \tag{5.14}$$

Using this relation, we can calculate a transmission coefficient for the voltage pulse:

$$\frac{\vec{u}_2}{\vec{u}_1} = 1 + \frac{\vec{u}_r}{\vec{u}_1} = 1 + \rho. \tag{5.15}$$

For $Z_{01} = Z_{02}$, the reflection coefficient ρ is 0 and, consequently, the transmission coefficient is 1. However, for a reflection-free junction, the condition $Z_{01} = Z_{02}$ is necessary but not sufficient. If the geometry of a line changes abruptly, it becomes impossible to satisfy Maxwell's equations just by superposing the fundamental waves. In this case higher modes come into play. In Fig. 5.4, longitudinal sections through junctions between two cables of equal impedance but different mechanical dimensions are shown.

Only by a smooth transition such as that sketched in the right part of Fig. 5.4, can we achieve the condition that the fields are not disturbed too much and that reflections can be avoided for high frequencies. For higher wave modes that may have been created at a junction, the electric and magnetic field vectors are no longer perpendicular to each other and their phase velocity

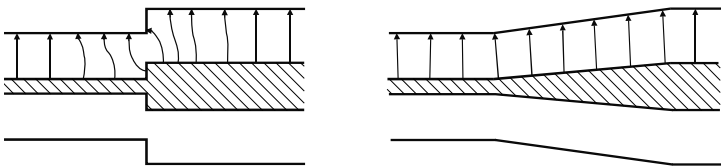


Fig. 5.4. Longitudinal sections through junctions between two cables of equal impedance but different mechanical dimensions [Lewis and Wells 1959]

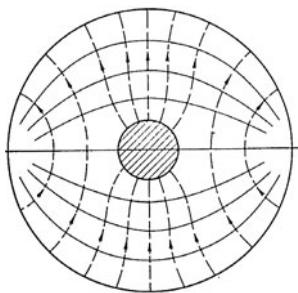


Fig. 5.5. Field line plot of the H_{11} wave mode in a coaxial transmission line. The *dashed lines* represent the electric field lines, and the *solid lines* show the magnetic field lines

becomes frequency-dependent. In addition, a limiting frequency exists for each mode, below which transmission is inhibited. The H_{11} (or TE_{11}) mode has the lowest cut-off frequency. A field line plot of the H_{11} mode in a coaxial cylindrical transmission line is drawn in Fig. 5.5.

The corresponding cut-off wavelength can be estimated from the following approximately valid relation: $\lambda_{co} = \pi(r_a + r_i)$, where r_a and r_i are the outer radius and the conductor radius, respectively.

Remark

H-modes (or TE (transverse electric) waves) have an axial component H_z of the magnetic field, and E_z is zero. E-modes (or TM (transverse magnetic) waves) have an axial component E_z of the electric field, and $H_z = 0$. The indices n , m describe the number of wave maxima in the various directions of the chosen coordinate system.

5.1.2 Transmission Lines with Losses

Energy losses during wave propagation are the result of three causes:

- the finite resistance of the conductors;
- the non-zero conductance and the high-frequency properties of the dielectric medium;
- radio emission in the case of an open system.

The relations for the Laplace-transformed voltage and current given by (5.3) remain valid if we replace L' by $L'(1 + R'/pL')$ and C' by $C'(1 + G'/pC')$. For sufficiently high frequencies, we always have $R' \ll \omega L'$ and $G' \ll \omega C'$. Taking this into account, we obtain the following for the low-loss case:

$$\begin{aligned}
 Z_0(p) &\approx \sqrt{\frac{L'}{C'}} \left[1 + \frac{R'/L' - G'/C'}{2p} \right], \\
 \frac{1}{c} &\approx \sqrt{L'C'} \left[1 + \frac{R'/L' + G'/C'}{2p} \right].
 \end{aligned}
 \tag{5.16}$$

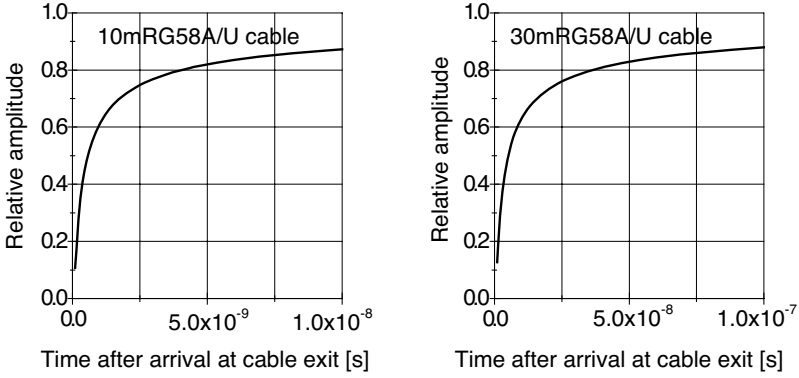


Fig. 5.6. Relative amplitude of a step pulse at the exit of a 10 and a 30 m long RG 58A/U coaxial cable. ($Z_0 = 50 \Omega$, $k = 1.14 \times 10^{-6}$ (at 1 GHz), $c/c_0 = 0.659$)

Both quantities are frequency-dependent. Introducing (5.16) into (5.3), we finally obtain the following for the damped wave:

$$\begin{aligned} \vec{u}_x(p) &= \vec{u}_0(p) e^{-a'x} e^{-p\sqrt{L'C'}x}, \\ a' &= \frac{R'}{2} \sqrt{\frac{C'}{L'}} + \frac{G'}{2} \sqrt{\frac{L'}{C'}} = a'_R + a'_G. \end{aligned} \quad (5.17)$$

In general, the term a'_G can be neglected for frequencies below 10^9 Hz. Owing to the skin effect, R' is proportional to $\omega^{1/2}$:

$$R' = \sqrt{\frac{\mu\omega\rho_a}{2}} R_a + \sqrt{\frac{\mu\omega\rho_i}{2}} R_i. \quad (5.18)$$

Therefore we can write $a' = k\sqrt{\omega}$. In this case, the amplitude of a pulse transmitted through a cable of length ℓ is attenuated according to (5.19):

$$\begin{aligned} u(\ell, t) &= u_0 \left(1 - \Phi \left(\frac{k\ell}{\sqrt{t - \ell/c}} \right) \right), \\ \Phi(s) &= \frac{2}{\sqrt{\pi}} \int_0^s e^{-q^2} dq. \end{aligned} \quad (5.19)$$

$\Phi(s)$ is the Gaussian error integral.

In Fig. 5.6, we have used (5.19) to plot the amplitude of a step pulse at the exit of a 10 m and a 30 m long RG 58A/U coaxial cable.

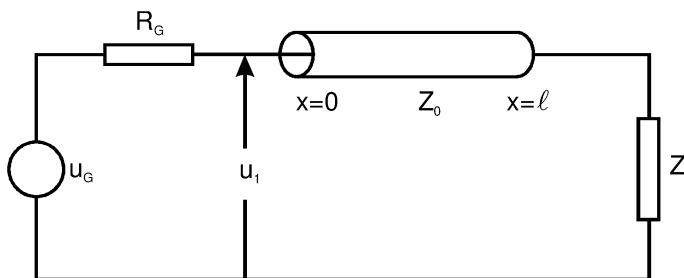


Fig. 5.7. Schematic of a short transmission line for input impedance calculation

5.1.3 The Finite Transmission Line as a Circuit Element

The most important features of a transmission line for its use as a circuit element are:

- the temporal delay that a signal experiences;
- its characteristic, resistor-like impedance;
- its signal reflection properties.

For slow signals or short cables, the input impedance of a cable with a non-matched termination is not Z_0 , i.e., purely ohmic, but complex. We can obtain the input impedance of a short cable of characteristic impedance Z_0 and length ℓ (Fig. 5.7) from the following considerations. The Laplace transform of the generator voltage $\mathbf{u}_G(\mathbf{p})$ is subdivided between the voltage drop at the generator impedance and the voltage drop at the input impedance:

$$\mathbf{u}_1(\mathbf{p}) = \frac{Z_1}{R_G + Z_1} \mathbf{u}_G. \quad (5.20)$$

On the other hand, the input voltage must be equal to the superposition of the forward-travelling wave and the reflected wave:

$$\begin{aligned} \mathbf{u}_1(\mathbf{p}) &= \vec{\mathbf{u}}_1(\mathbf{p}) + \overleftarrow{\mathbf{u}}_1(\mathbf{p}) = \vec{\mathbf{u}}_1(\mathbf{p}) \left(1 + \frac{\overleftarrow{\mathbf{u}}_1(\mathbf{p})}{\vec{\mathbf{u}}_1(\mathbf{p})} \right), \\ \frac{\overleftarrow{\mathbf{u}}_1(\mathbf{p})}{\vec{\mathbf{u}}_1(\mathbf{p})} &= \rho_Z e^{-2p\sqrt{L'C'}\ell}, \\ \rho_Z &= \frac{Z - Z_0}{Z + Z_0}. \end{aligned} \quad (5.21)$$

In general, R_G will not be matched either. Therefore, we must also consider the reflection of the returning wave at the cable input:

$$\rho_{R_G} = \frac{R_G - Z_0}{R_G + Z_0}. \quad (5.22)$$

Thus we have

$$\vec{\mathbf{u}}_1(\mathbf{p}) = \mathbf{u}_G(\mathbf{p}) \frac{Z_0}{Z_0 + R_G} + \vec{\mathbf{u}}_1(\mathbf{p}) \rho_{R_G} \rho_Z e^{-2\mathbf{p}\sqrt{L'C'}\ell}, \quad (5.23)$$

from which we obtain

$$\vec{\mathbf{u}}_1(\mathbf{p}) = \mathbf{u}_G(\mathbf{p}) \frac{Z_0}{(Z_0 + R_G) \left(1 - \rho_{R_G} \rho_Z e^{-2\mathbf{p}\sqrt{L'C'}\ell}\right)}, \quad (5.24)$$

and finally

$$\mathbf{u}_1(\mathbf{p}) = \mathbf{u}_G(\mathbf{p}) \frac{Z_0 \left(1 + \rho_Z e^{-2\mathbf{p}\sqrt{L'C'}\ell}\right)}{(Z_0 + R_G) \left(1 - \rho_{R_G} \rho_Z e^{-2\mathbf{p}\sqrt{L'C'}\ell}\right)}. \quad (5.25)$$

Comparing the last equation with (5.20), we calculate the following for the input impedance:

$$Z_1 = Z_0 \frac{1 + \rho_Z e^{-2\mathbf{p}\sqrt{L'C'}\ell}}{1 - \rho_{R_G} \rho_Z e^{-2\mathbf{p}\sqrt{L'C'}\ell}}. \quad (5.26)$$

For the special case of an open end, we have

$$Z_1 = Z_0 \frac{1 + e^{-2\mathbf{p}\sqrt{L'C'}\ell}}{1 - e^{-2\mathbf{p}\sqrt{L'C'}\ell}} = Z_0 \frac{\cosh\left(\mathbf{p}\sqrt{L'C'}\ell\right)}{\sinh\left(\mathbf{p}\sqrt{L'C'}\ell\right)}. \quad (5.27)$$

For the case $\omega(L'C')^{1/2} \ell \ll 1$ (which is equivalent to the case $\ell \ll \lambda$), we obtain the following by expanding the exponential function into a series and keeping just the first-order terms:

$$Z_1 \approx Z \frac{1 + \mathbf{p}\sqrt{L'C'}\ell Z_0 - Z/Z}{1 - \mathbf{p}\sqrt{L'C'}\ell Z_0 - Z/Z_0}. \quad (5.28)$$

From this, we derive the following for $Z \ll Z_0$ ($Z_0 = (L'/C')^{1/2}$):

$$Z_1 \approx Z + \mathbf{p}L'\ell, \quad (5.29)$$

i.e., the input impedance of a short transmission line is equivalent to a series connection of an inductance $L'\ell$ and the terminal impedance Z .

In the opposite case $Z \gg Z_0$, we obtain

$$Z_1 \approx \frac{1}{1/Z + \mathbf{p}C'\ell}. \quad (5.30)$$

Here the input impedance consists of a parallel connection of the cable capacitance $C'\ell$ and the terminal impedance Z .

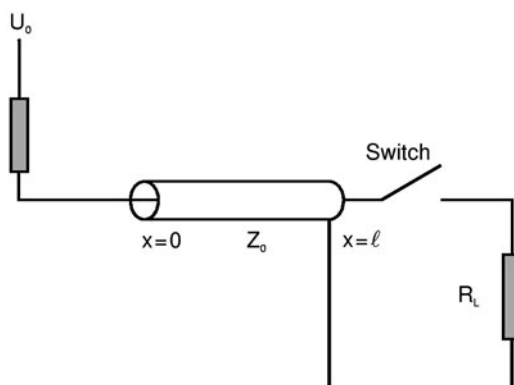


Fig. 5.8. Schematic of a transmission line circuit for the production of pulses

5.1.4 Production of Pulses with Lossless Transmission Lines

If we consider the charged transmission line shown in Fig. 5.8 from the load side, its impedance is given by (5.27), assuming that the connection to the charging unit has a very high impedance and may therefore be considered as an open end. If we introduce $T = (L'C')^{1/2} \ell$, which is the one-way transit time of a wave on the line, we may write the following for the Laplace transform of the current at the load end:

$$\begin{aligned}
 i(p) &= \frac{U_0}{p(R_L + Z_0 \coth(pT))} \\
 &= \frac{U_0}{p(R_L + Z_0)} \frac{1 - e^{-2pT}}{1 + Z_0 - R_L/Z_0 + R_L e^{-2pT}} \\
 &= U_0 \frac{1 - e^{-2pT}}{p(R_L + Z_0)} \left[1 - \frac{Z_0 - R_L}{Z_0 + R_L} e^{-2pT} + \left(\frac{Z_0 - R_L}{Z_0 + R_L} \right)^2 e^{-4pT} - \dots \right].
 \end{aligned} \tag{5.31}$$

Applying an inverse Laplace transformation, we obtain the following for the current in the time domain:

$$\begin{aligned}
 I(t) &= \frac{U_0}{Z_0 + R_L} \left\{ 1 - H(t - 2T) - \frac{Z_0 - R_L}{Z_0 + R_L} [H(t - 2T) - H(t - 4T)] \right. \\
 &\quad \left. + \left(\frac{Z_0 - R_L}{Z_0 + R_L} \right)^2 [H(t - 4T) - H(t - 6T)] - \dots \right\}
 \end{aligned} \tag{5.32}$$

where $H(t)$ is the Heaviside step function ($H(t) = 1$ for $t \geq 0$, and $H(t) = 0$ for $t < 0$). $I(t)$ has been plotted in Fig. 5.9 for $R_L/Z_0 = 1$, $R_L/Z_0 > 1$, and $R_L/Z_0 < 1$.

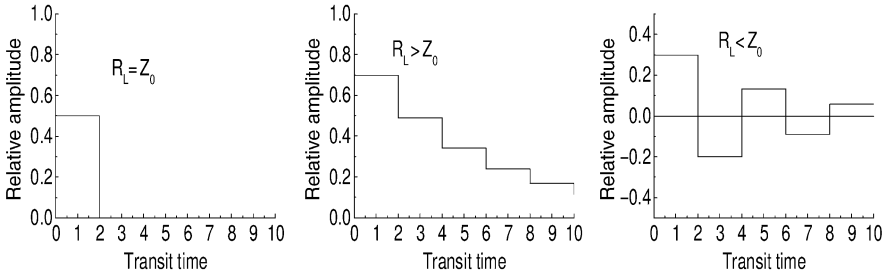


Fig. 5.9. Pulse shapes obtained for three different terminations of a cable

5.2 RLC Networks

Transmission lines are impracticable for creating rectangular pulses with a duration of more than 500 ns. Therefore circuits with discrete RLC elements are used to produce such pulses.

Before considering specific LC ladder networks, let us first discuss a transmission chain in a more general way. We refer to the chain shown in Fig. 5.10, consisting of a sequence of meshes with complex impedances Z_1 and Z_2 .

Applying Kirchhoff’s second law to the r th mesh of the chain, we obtain the following for the Laplace transform of the current:

$$i_r(p) [Z_1(p) + 2Z_2(p)] - i_{r-1}(p)Z_2(p) - i_{r+1}(p)Z_2(p) = 0. \tag{5.33}$$

The transfer function between two chain elements is defined through

$$i_{r+1}(p) = G(p)i_r(p). \tag{5.34}$$

After making the transition $p \rightarrow i\omega$, it is convenient to express the amplitude term through an exponential too:

$$G(i\omega) = g(\omega)e^{i\phi(\omega)} = e^{a(\omega)+i\phi(\omega)}. \tag{5.35}$$

Thus (5.33) becomes

$$i_r(i\omega) \left[Z_1(i\omega) + 2Z_2(i\omega) - Z_2(i\omega) e^{-[a(\omega)+i\phi(\omega)]} - Z_2(i\omega) e^{a(\omega)+i\phi(\omega)} \right] = 0, \tag{5.36}$$

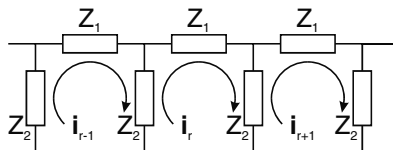


Fig. 5.10. Section of a generalised ladder network with complex impedances Z_1 and Z_2

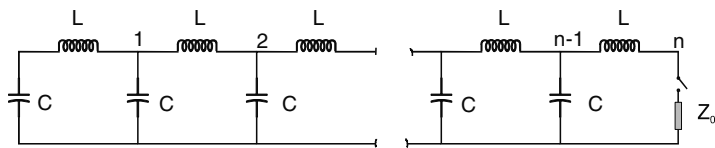


Fig. 5.11. Pulse-forming LC chain

and, consequently,

$$\frac{Z_1(i\omega) + 2Z_2(i\omega)}{Z_2(i\omega)} = 2 \cosh[a(\omega) + i\phi(\omega)]. \tag{5.37}$$

Applying the addition rules for the cosh function, we finally obtain

$$1 + \frac{Z_1(i\omega)}{2Z_2(i\omega)} = \cosh(a(\omega)) \cos(\phi(\omega)) + i \sinh(a(\omega)) \sin(\phi(\omega)). \tag{5.38}$$

We can now distinguish two limiting cases:

1. $g(\omega) = 1$, i.e., $a(\omega) = 0$. In this case no amplitude reduction occurs, but the shape of the pulse remains unchanged only if $\phi(\omega) = k\omega$ holds too. In that case the only effect that occurs if a wave propagates along the chain is a shift on the time axis. We have a delay chain.
2. The second case to be considered is $\phi(\omega) = 0$ and $a(\omega) = \text{const.} < 0$. In this case we have a frequency-independent attenuation of the pulse, i.e., an ideal attenuator. We shall not discuss this case further.

For a delay chain, (5.38) reduces to

$$\cos(\phi(\omega)) = 1 + \frac{Z_1}{2Z_2}. \tag{5.39}$$

The range of possible values for Z_1/Z_2 is therefore restricted to

$$-1 < \frac{Z_1}{4Z_2} < 0, \tag{5.40}$$

i.e., delay chains can be realised only if the ratio of the two complex resistances Z_1 and Z_2 is real and negative. Therefore only combinations of capacitances and inductances are suitable elements for such a chain. We could have concluded this already from our results on transmission lines. These results also suggest that a rectangular pulse can be approximated by the chain of LC combinations shown in Fig. 5.11, which is a direct replica of a transmission line.

Inserting the expressions for $Z_1 = i\omega L$ and $Z_2 = 1/i\omega C$ into (5.40), we have

$$-1 < \frac{-\omega^2 LC}{4} < 0. \tag{5.41}$$

This defines the frequency range within which wave propagation remains attenuation-free: the upper frequency of this range is $\omega_u = 2/(LC)^{1/2}$. Correspondingly, (5.33) becomes

$$\mathbf{i}_r(\mathbf{p}) \left(L\mathbf{p} + \frac{2}{\mathbf{p}C} \right) - \frac{\mathbf{i}_{r-1}(\mathbf{p})}{\mathbf{p}C} - \frac{\mathbf{i}_{r+1}(\mathbf{p})}{\mathbf{p}C} = 0. \quad (5.42)$$

In accordance with (5.34) and (5.35), we seek a solution of this set of differential equations in the form

$$\mathbf{i}_r(\mathbf{p}) = Ae^{r\theta} + Be^{-r\theta}. \quad (5.43)$$

Here we have used the abbreviation $\theta = i\phi(\omega)$, and, according to (5.37), we have the relationship $\cosh(\theta) = 1 + (LC/2)\mathbf{p}^2$.

A and B are constants that must be determined from the boundary conditions in the first and the last mesh. If the last element n in the chain is connected to a voltage source $\mathbf{u}_0(\mathbf{p})$ instead of the impedance Z_0 shown in Fig. 5.11, we obtain the following expression for the Laplace transform of the input current into the chain:

$$\mathbf{i}_n(\mathbf{p}) = C\mathbf{u}_0 \frac{\sinh(n\theta)}{\sinh((n+1)\theta) - \sinh(n\theta)}. \quad (5.44)$$

The input impedance of the network is then given by

$$Z(\mathbf{p}, n) = \frac{\mathbf{u}_0(\mathbf{p})}{\mathbf{i}_n(\mathbf{p})} = \frac{1}{\mathbf{p}C} \left[\frac{\sinh((n+1)\theta)}{\sinh(n\theta)} - 1 \right]. \quad (5.45)$$

For $n \rightarrow \infty$ this impedance converges, as expected, to the impedance of a finite line terminated with an open circuit (5.27):

$$\lim_{n \rightarrow \infty} Z(\mathbf{p}, n) = \sqrt{\frac{L}{C}} \coth \left(\mathbf{p} \sqrt{L_N C_N} \right), \quad (5.46)$$

where $L_N = nL$ and $C_N = nC$.

$Z_0 = (L/C)^{1/2}$ can be considered as the fundamental impedance of the discrete network. If we now assume that all capacitors in the chain have been charged to U_0 and that subsequently the chain will be connected to a load of impedance Z_0 by an ideal switch (Fig. 5.11), a pulse develops across the series connection of the load and chain impedances, and the Laplace-transformed pulse current in the matched load becomes

$$\mathbf{i}_n(\mathbf{p}) = \frac{U_0/\mathbf{p}}{\sqrt{L/C} + 1/\mathbf{p}C [\sinh((n+1)\theta)/\sinh(n\theta) - 1]}. \quad (5.47)$$

Introducing $p = 2/(LC)^{1/2} \sinh(\theta/2)$, we obtain

$$\mathbf{i}_n(\mathbf{p}) = CU_0 \frac{\sinh(n\theta)}{\sinh((n+1)\theta) + [2 \sinh(\theta/2) - 1] \sinh(n\theta)}. \quad (5.48)$$

In general, it proves to be impossible to invert this expression.

To determine the transit time of the pulse through the chain and thereby the pulse duration, we proceed as follows. The currents at both ends of the chain are linked by

$$\mathbf{i}_n(i\omega) = \mathbf{i}_1(i\omega)e^{in\phi(\omega)}, \quad (5.49)$$

and from (5.39) we have the following for the phase shift $\phi(\omega)$:

$$\phi(\omega) = \arccos\left(1 - \frac{\omega^2 LC}{2}\right) = \arccos\left(1 - 2\left(\frac{\omega}{\omega_u}\right)^2\right). \quad (5.50)$$

Expanding this into a series, we obtain

$$\phi(\omega) = \omega\sqrt{LC}\left[1 + \frac{1}{6}\left(\frac{\omega}{\omega_u}\right)^2 + \dots\right]. \quad (5.51)$$

For frequencies much smaller than ω_u , we can therefore approximate (5.49) by

$$\mathbf{i}_n(i\omega) \approx \mathbf{i}_1(i\omega)e^{in\omega\sqrt{LC}}. \quad (5.52)$$

Therefore, by an inverse transformation of (5.52) into the time domain, we find that the one-way pulse transit time on the chain is about $n(LC)^{1/2}$. The mean pulse amplitude obtained for a matched load is $U_0/2$ if the chain has been charged to U_0 . For the pulse duration, we obtain $2n(LC)^{1/2}$. The pulse shape achieved with five LC elements is plotted in Fig. 5.12.

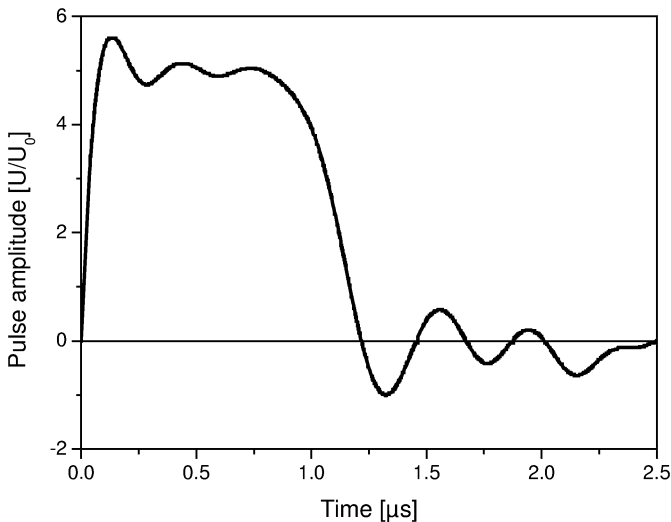


Fig. 5.12. Voltage pulse shape achieved across a matched load at the end of a network consisting of five LC elements

Although the general features of the pulse are as expected, there is a substantial overshoot at the beginning of the pulse and an undershoot at the end. In some applications, these imperfections are intolerable.

A Fourier analysis of the circuit shown in Fig. 5.11 uncovers the reason for this poor pulse shaping. The circuit approximates a sharp-edged square pulse with five terms. However, in the Fourier series expansion of a square pulse train, the terms decrease only as the inverse of the first power of n , i.e., the Fourier coefficients a_n are proportional to $1/n$. Therefore a large number of terms is required to obtain a good approximation of a square pulse.

Guillemin was the first to discover that much better pulse shaping can be obtained with fewer elements, if a slower pulse rise time is acceptable [Guillemin 1944, Glasoe and Lebacqz 1948]. Thus a much more constant pulse voltage plateau can be achieved. The terms in the Fourier series expansion of a trapezoidal pulse train, for example, decrease in proportion to $1/n^2$, and those for a pulse train with a parabolic rise and fall decrease in proportion to $1/n^3$. Nevertheless, it is not obvious that a synthesis method based on the Fourier method, which is normally used to analyse continuous pulse trains, is effective in solving a single-pulse problem.

As an example, we shall consider the Guillemin network for the reproduction of a trapezoidal pulse. To derive this network, we start from an analogy between a square and a trapezoidal pulse as shown in Fig. 5.13.

An ideal transmission line discharged into a short circuit creates a periodic bipolar square pulse with current amplitude $2I_0$. Discharging the line into a matched load leads to a single square pulse. The periodic bipolar waveform can be analysed as a Fourier series. We now assume that a network that is capable of reproducing a bipolar trapezoidal pulse into a short circuit also leads to a single trapezoidal pulse if it is terminated into a matched load. If this is correct, we need to find the network that is able to approximate the pulse train shown in Fig. 5.13c. The Fourier series expansion of this pulse train is

$$I(t) = 2I_0 \sum_{k=0} \frac{4}{(2k+1)\pi} \frac{\sin((2k+1)\pi a)}{(2k+1)\pi a} \sin \frac{(2k+1)\pi t}{t_p}. \quad (5.53)$$

Here t_p is the base of the trapezoid and at_p is the rise time of the bipolar trapezoidal pulse train (see Fig. 5.13c).

Each term of the Fourier series represents a sinusoidal partial current of amplitude $2I_0 b_k$ and frequency $(2k+1)/(2t_p)$, where

$$b_k = 2I_0 \frac{4}{(2k+1)\pi} \frac{\sin((2k+1)\pi a)}{(2k+1)\pi a}. \quad (5.54)$$

Such partial current terms can be created by the network shown in Fig. 5.14. The oscillating current in this network is

$$I_k(t) = U_0 \sqrt{\frac{C_k}{L_k}} \sin \left(\frac{t}{\sqrt{L_k C_k}} \right). \quad (5.55)$$

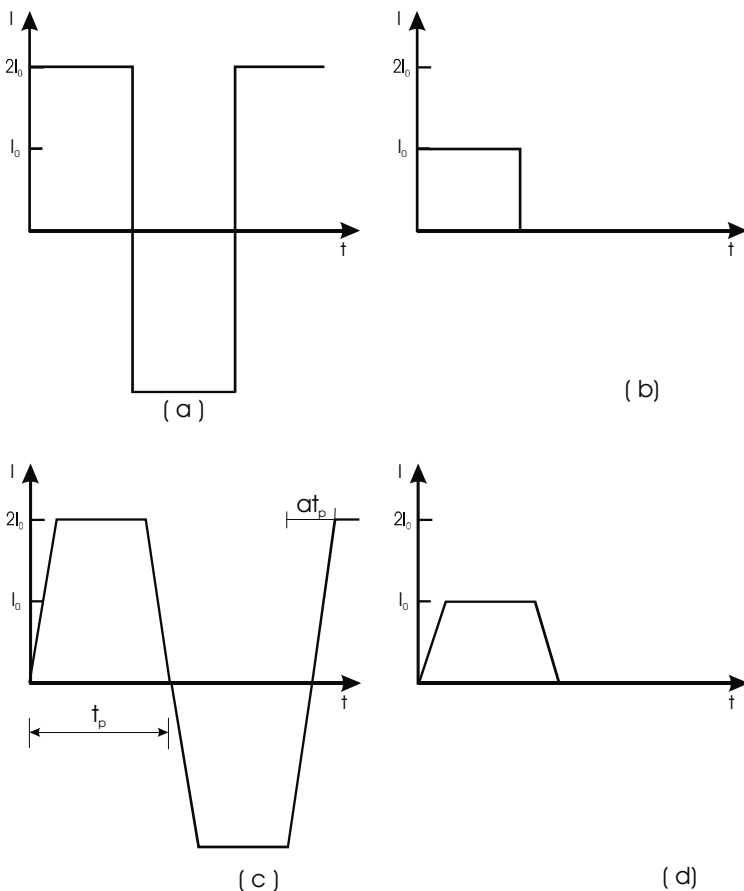


Fig. 5.13. Design concept for a Guillemin network. (a) Output current of an ideal transmission line into a short circuit. (b) Output current of the same line into a matched load. (c) Trapezoidal pulse from a Guillemin network with a short-circuit load. (d) Ideal discharge of a Guillemin network into a matched load

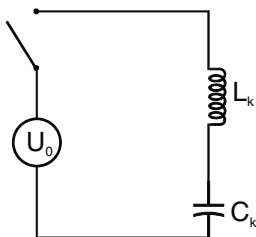


Fig. 5.14. Basic LC circuit to mirror a term of a Fourier series

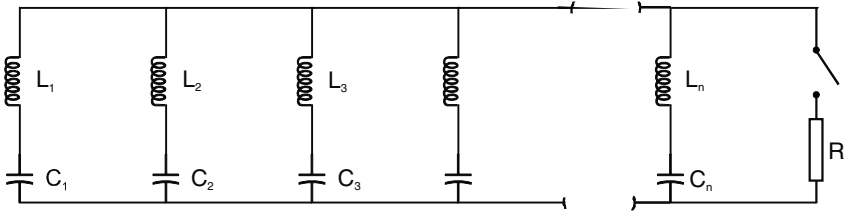


Fig. 5.15. Fundamental Guillemin network

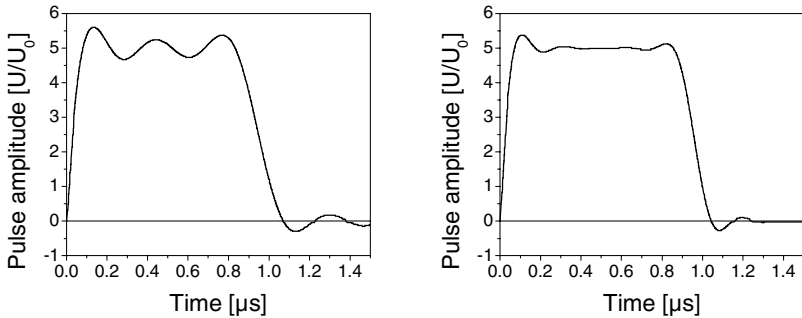


Fig. 5.16. Pulse voltage of a three-element (*left*) and five-element (*right*) Guillemin network into a matched load

L_k and C_k can be determined by comparison with the terms of the Fourier series:

$$\begin{aligned}
 L_k &= \frac{Z_0 t_p}{(2k + 1)\pi b_k}, \\
 C_k &= \frac{b_k t_p}{(2k + 1)\pi Z_0};
 \end{aligned}
 \tag{5.56}$$

$Z_0 = U_0/2I_0$ can be considered as the characteristic impedance of the network. Consequently, the resulting network for the creation of a trapezoidal pulse shape consists of a number of such LC circuits with values of L_k and C_k given by (5.56), connected in a parallel configuration. We call this the fundamental Guillemin network (Fig. 5.15).

Figure 5.16 shows the voltage pulses for discharges into matched loads for Guillemin networks consisting of three and five elements, respectively. It is obvious that the pulse shaping has been much improved. A major disadvantage of the Guillemin network is that all capacitors must have different capacitance values. In general, it is difficult to obtain high-voltage pulse capacitors with the necessary capacitance values from stock. Therefore the network shown in Fig. 5.15 can be difficult and expensive to build.

5.3 Circuit Simulation with LEITER

LEITER is a simple numerical program which is capable of simulating complex transmission line networks. It is especially useful for calculating systems in which loss-free transmission lines, characterised by their impedance Z_i and their electric length (wave transit time) τ_i , are the main elements. However, losses can also be treated by introducing lumped resistors at suitable positions in the network. In addition, LEITER can be used to simulate circuits containing lumped elements. For example, a lumped inductance can be represented by a short transmission line of very high impedance, and a lumped capacitance can be represented by a short transmission line of very low impedance:

$$L_i = Z_i \tau_i, \quad C_i = \frac{\tau_i}{Z_i}. \quad (5.57)$$

We have seen previously that the voltage, amplitude on a line can be considered as a superposition of waves travelling in the positive and negative x -directions:

$$U = \vec{U} + \overleftarrow{U}. \quad (5.58)$$

Correspondingly, we have the following for the current on a transmission line:

$$I = \frac{\vec{U} - \overleftarrow{U}}{Z}. \quad (5.59)$$

LEITER keeps track of the momentary values of the voltage amplitudes of waves travelling in both directions, taking into account the reflection and transmission coefficients at the ends of the line to determine the incoming and outgoing wave portions:

$$\begin{aligned} \rho &= \frac{Z_2 - Z_1}{Z_2 + Z_1}, \\ T &= \frac{2Z_1}{Z_2 + Z_1}. \end{aligned} \quad (5.60)$$

If, at the end of an element, several lines or combinations of lines and resistors are connected, Z_2 in (5.60) is replaced by the collective impedance of all elements connected. The transmitted portion is then divided up between all elements connected to this 'knot' allowing for losses in an interposed resistor if necessary.

The various types of knots that the program can handle are presented in Fig. 5.17. Knot types 6, 7, and 8 are ideal switches, which can either open or close at a certain time or close at a selectable voltage level. Type 9 describes the nonlinear impedance characteristic of an electron diode (called a pinch diode). With the help of type 10, it is possible to simulate a time-dependent

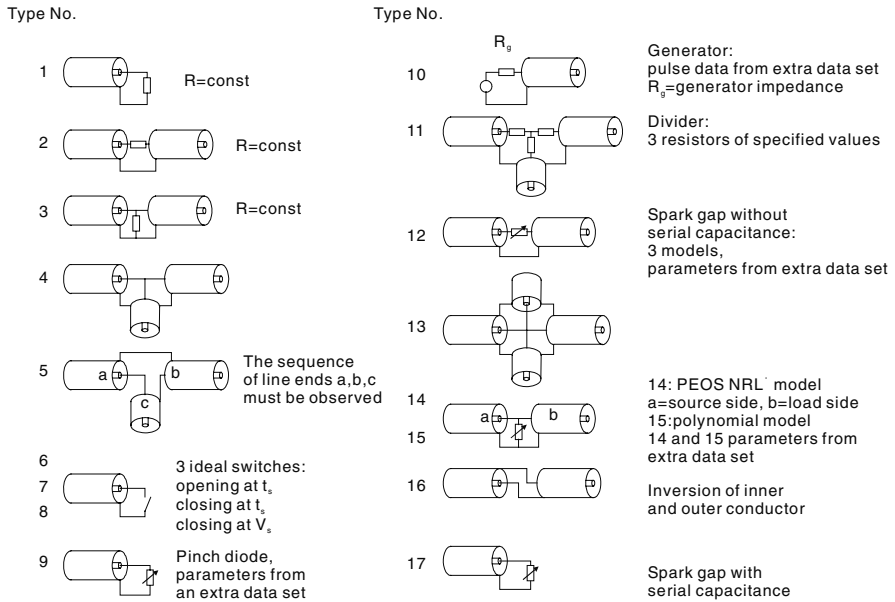


Fig. 5.17. The knot types available in the network program LEITER

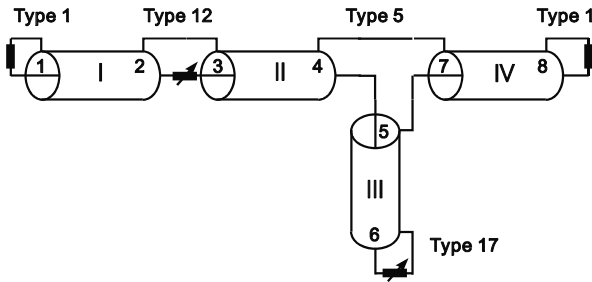


Fig. 5.18. A transmission line network for simulation with LEITER

voltage source. Type 12 allows one to calculate the resistive decay of a spark gap according to various preselectable spark laws (Töpler, Rompe-Weizel, or exponential). The inductance of the spark gap is represented by a short transmission line element. Type 14 describes a plasma opening switch. Type 17 simulates the resistance of a spark gap connected to the end of a line and can be used as a side branch in Type 5. The transit time and the impedance of the line determine the capacitance and inductance of the spark gap. A restriction on the application of LEITER is that it cannot treat reconnecting lines.

An example of a transmission line network is shown in Fig. 5.18. This consists of three line elements, each of impedance 5Ω . The first line has been charged to 1 MV. At the beginning of the simulation, the output switch of

Table 5.2. LEITER input parameter set for the example presented in Fig. 5.18 (additional comment lines start with an asterisk)*Simple transmission line network*

Total time	Time step	Plot initial time	Steps averaged
100	1.0000E-01	0	10

4 element specifications

	Transit time (ns)	Impedance (Ω)	U_0 (V)	I_0 (A)
'No. 1'	20.00	5.0000	1.0E+06	0.0000
'No. 2'	10.00	5.0000	0.0000	0.0000
'No. 3'	1.00	5.0000	0.0000	0.0000
'No. 4'	20.00	5.0000	0.0000	0.0000

5 node specifications

	Type	adjacent	end-#n	$A(i)$	Scope of $A(i)$
'No. 1'	1	1	0 0 0	5.0E+06	Ohm ending
'No. 2'	12	2	3 2 0	1.0E+01	Volt igniting
'TYP12A.DAT'	*Spark gap model according to Toepler				
'No. 3'	5	4	7 5 0 0		
'No. 4'	17	6	6 0 0	1.0E+05	Volt igniting
'TYP17B.DAT'	*Spark gap model with serial capacitance				
'No. 5'	1	8	0 0 0	5.00	Ohm ending

3 plot specifications

End #	Plot code	Scale	Colour
8	1	1.00E+06	1
6	1	1.00E+06	2
2	1	1.00E+06	3

this line closes. Line element III and the knot of type 17 at its end describe a switch with stray capacitance $C = \tau/Z$. The switch at the end of this line closes if the voltage amplitude reaches more than 100 kV. The last line of the total arrangement is terminated with a matched load of 5Ω . The input parameters are listed in Table 5.2. The results of the simulation are shown in Fig. 5.19.

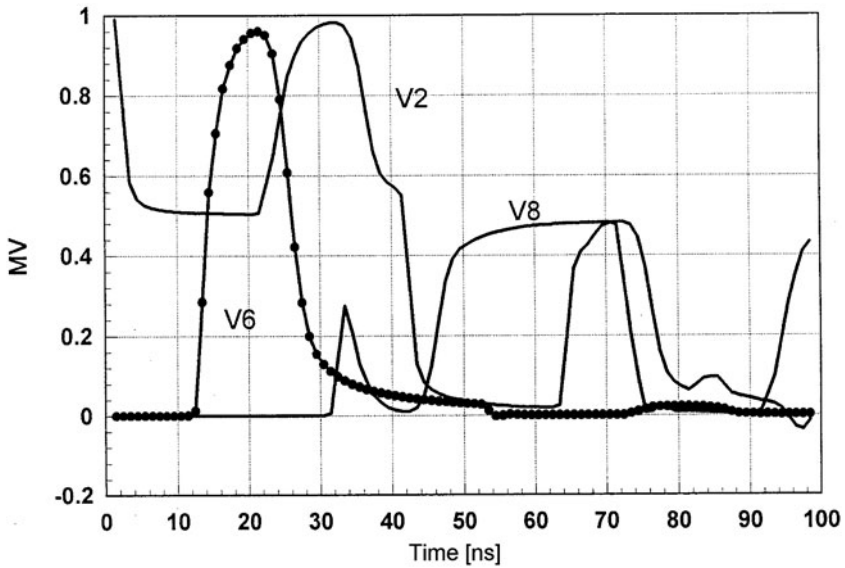


Fig. 5.19. Evolution of pulse voltage at the line ends 2, 6, and 8 in the circuit of Fig. 5.18. Since line II is of the same impedance as line I, the voltage at position 2 drops to half the charging voltage of line I as soon as the switch resistance has dropped to zero. A prepulse occurs at the load end (position 8), because the switch connecting lines II and IV has a stray capacitance, simulated by line III

6 Pulse Transmission and Transformation

6.1 Self-Magnetic Insulation in Vacuum Lines

Some tasks in science and technology require very intense pulsed radiation sources with a brightness of more than $100 \text{ TW/cm}^2 \text{ sr}$ and a radiation pulse energy of more than 1 MJ. To produce such sources, high-voltage pulses with an electric power of more than 100 TW must be compressed to electric power densities of more than 100 TW/m^2 and efficiently coupled to the device generating the desired radiation.

Most devices suitable for this task must operate in a vacuum environment. Therefore the high-voltage pulse must enter a vacuum vessel hosting the source through an insulating interface separating the liquid dielectric from the vacuum section. Figure 6.1 shows a design of such an interface, demonstrating the most important features.

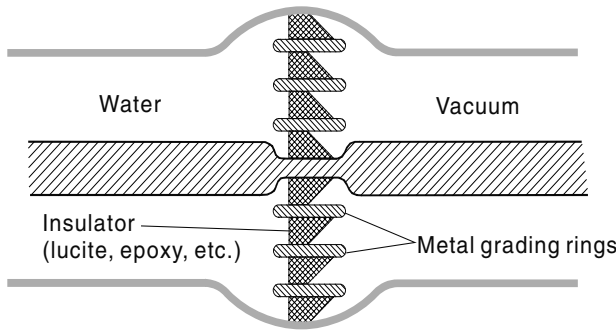


Fig. 6.1. Insulating interface in a transmission line passing from a water to a vacuum section

This interface consists of insulating rings separated by metallic grading rings. The metallic and dielectric rings are sealed to hold the high vacuum either by O-rings or by a direct metal-to-dielectric bond. It is the task of the metal grading rings to distribute the potential homogeneously over the interface on the vacuum surface. Effects involving both conductors and insulators determine sparking on the surface on the vacuum side. On metallic surfaces, electrons may be produced by field emission (see below). These elec-

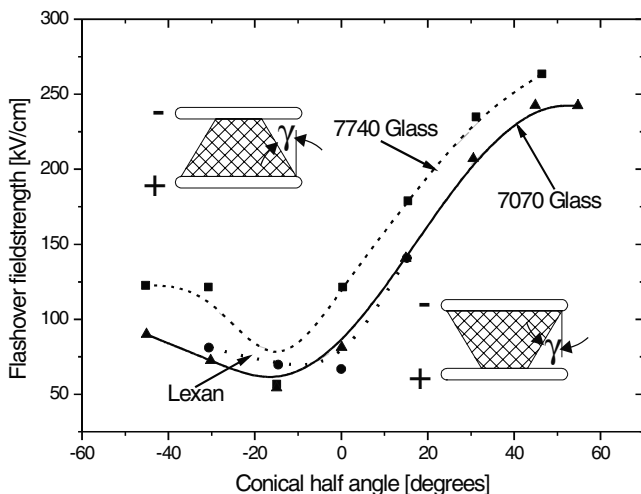


Fig. 6.2. Breakdown level for pulsed voltages as a function of the inclination angle between the insulator surface and the normal to the cathode

trons can be accelerated by the electric field and collide with the insulator surface. If the secondary-electron emission coefficient of the insulator is larger than one, positive charge is accumulated on the surface and further electrons can be attracted. Furthermore, adsorbates may be released by this electron bombardment and a gas layer can form above the surface. If a critical gas-density–thickness product is reached, electron avalanches can grow in the gas layer and create a surface breakdown. Of course, this requires an electric-field component tangential to the surface, which can be established by space charge built up on the insulator only.

To prevent the accumulation of space charge on the dielectric, the insulator sections have angled surfaces, such that all electrons are accelerated away from the surface and collected on the metallic rings. Measurements of the electric breakdown strength of dielectric cones as a function of inclination angle show that the insulator hold-off has a maximum for an angle of 45° [Milton 1972]. A graph of the breakdown level for pulsed voltages as a function of insulator angle is shown in Fig. 6.2.

In many cases, the dielectric–vacuum interface is the weakest element of a high-voltage pulse line under electric-field stress. The maximum field strength that can be held with an interface arrangement such as that shown in Fig. 6.1 has been determined empirically for pulsed systems [Martin et al. 1996]:

$$E_{DB} = \frac{7 \times 10^5}{t^{1/6} A^{1/10}} \text{ [V/m]}, \quad (6.1)$$

where t is the time duration (in s) during which the electric-field strength exceeds 87% of its maximum value, and A is the interface area measured

Table 6.1. Breakdown strength and transportable energy flux density

	Breakdown strength E (MV/m)	Energy flux density S (TW/m ²)
Transformer oil	60	15
Water	50	60
Insulator surface	20	1

in m². For pulse durations of a few times 10 ns, the breakdown strength is below 20 MV/m and therefore the power density that can be transported through the interface is below 1 TW/m². In general, the energy flux density of a planar wave is given by the absolute value of the Poynting vector,

$$S = \sqrt{\frac{\varepsilon\varepsilon_0}{\mu\mu_0}} E^2. \quad (6.2)$$

In Table 6.1 we compare the breakdown strength and the transportable power density for various dielectric media with those of a vacuum interface for pulse durations of 10–100 ns.

6.1.1 Vacuum Breakdown on Metallic Surfaces

At macroscopic field strengths above 20 MV/m, explosive electron emission with plasma formation occurs on metallic surfaces in vacuum. The plasma is a practically unlimited electron source with zero work function.

The physical processes leading to electron field emission are based on the quantum mechanical tunnelling effect. Strong electric fields reduce the width of the potential barrier that exists between the interior of the metal and the outside. To illustrate this effect, we consider a metal at absolute zero ($T = 0$) and assume the surface potential barrier to be a step function (Fig. 6.3).

The potential energy of an electron outside the metal is equal to $-eEx$. If the potential width d becomes of the order of 100 nm or less, electrons in the vicinity of the Fermi level will be able to tunnel through the barrier. The number of allowed states $Z(W) dW$ in an energy range between W and $W + dW$ for a free-electron gas is proportional to $W^{1/2}$. The electron distribution among these states is given by the Fermi–Dirac function $F(W)$, where

$$F(W) = \frac{1}{e^{(W-W_F)/kT} + 1}. \quad (6.3)$$

Thus $N(W) dW = Z(W)F(W) dW$ states are occupied in the energy interval W , $W + dW$. As the field strength becomes larger, more and more electrons below the Fermi level begin to contribute to the emission current. According to the derivation first carried out by Fowler and Nordheim [Fowler and Nordheim 1928], the emission current as a function of the field strength E for a triangular barrier may be written in the form

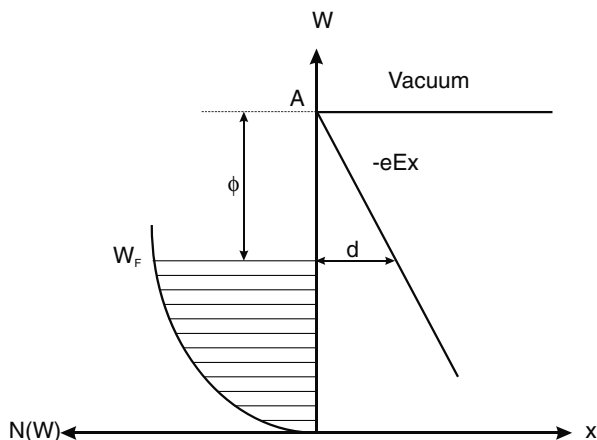


Fig. 6.3. Illustration of high-field electron emission by tunnelling. The vertical axis represents also the boundary between metal and vacuum

$$\begin{aligned}
 j &= \frac{1.54 \times 10^{-6} \beta^2 E^2}{\phi} \exp \left\{ -\frac{6.83 \times 10^7 \phi^{3/2} \theta(y)}{\beta E} \right\}, \\
 \theta(y) &\approx 0.956 - 1.06y^2, \\
 y &= 3.8 \times 10^{-4} \frac{\sqrt{E}}{\phi}.
 \end{aligned} \tag{6.4}$$

The current density j is obtained in A/cm² if the electric field E is given in V/cm and the work function ϕ in eV. Here we have also introduced a field enhancement factor β .

Setting the field strength to 25 MV/m in (6.4) results in a current density of 10 nA/cm². This is much less than the value observed experimentally under these conditions. Plotting measured values of $\ln(j/E^2)$ as a function of $1/E$ leads to a straight line with a gradient that is in agreement with (6.4) only if a field strength 100 times larger is assumed.

At present, several models are competing to explain this observation. The oldest and most popular of them is the whisker model [Mesyats 1998]. Here, a ‘whisker’ is a fine filamentary metallic protrusion, such as the one shown in Fig. 6.4, which leads to a local field enhancement.

From an analysis of the simple model shown in Fig. 6.4, we must conclude that a field enhancement of $\beta = 100$ means that the aspect ratio h/r of the whisker structure must be of the same order. However, such needles are rarely observed.

Careful investigations using electron tunnelling microscopy have discovered that, very frequently, dielectric inclusions are involved in the emission centres [Latham 1981]. In this case, the tunnelling current from the metal into the dielectric plays a dominant role, and the emission current obeys the same scaling with the electric field as in the Fowler–Nordheim equation.

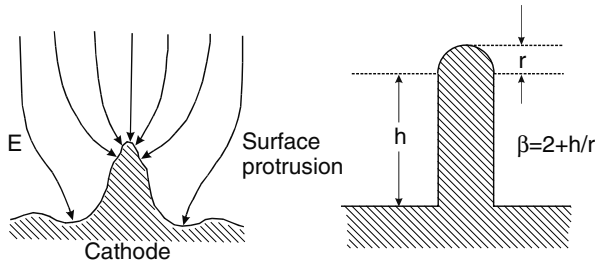


Fig. 6.4. Field distribution at the tip of a whisker, and a simple model to calculate the field enhancement factor β

A further idea in all models is that the current flowing through the emission site (whether a whisker or a dielectric inclusion) leads to strong heating and finally vaporises the site. The vapour is then ionised by succeeding electrons. However, an assessment of the possible heating rate has led to the conjecture that electron-stimulated desorption of adsorbates also plays an important role during vapour and plasma formation [Halbritter 1985, 1986].

6.1.2 Qualitative Description of Self-Magnetic Insulation

Summing up the previous subsection, we can state that at field strengths above 20 MV/m, a homogeneous plasma layer is created on a metallic surface in vacuum within a few nanoseconds. Thus, without magnetic insulation, an electron loss current can flow between conductors and prevent effective transport of pulse energy in a vacuum transmission line. Figure 6.5 illustrates qualitatively how the line current evolves after the onset of electron emission.

Before breakdown (top sketch), only a displacement current flows in the line. The magnetic field associated with this current would be too weak to affect the trajectories of electrons markedly, if there were any.

After the onset and increase of the electron loss current, electrons are deflected by the self-magnetic field of the total line current, first at the entrance to the line (second and third sketch).

If the current exceeds a critical value, the electron orbits can no longer reach the anode (fourth sketch). More and more sections of the line become magnetically insulated. An electron sheath forms on the negative conductor, and the impedance of the line deviates from the vacuum impedance.

As the loss zone propagates into the line, larger portions of it become magnetically insulated. The propagation velocity of the loss front is less than c , the speed of light. The conditions are similar to those occurring during the formation of a shock front in fluid dynamics. Therefore this kind of wave propagation is often called an electromagnetic shock wave. Figure 6.6 illustrates once more the conditions at the wave front. Here we have assumed that a voltage pulse ramping to a voltage plateau of 2 MV is launched at

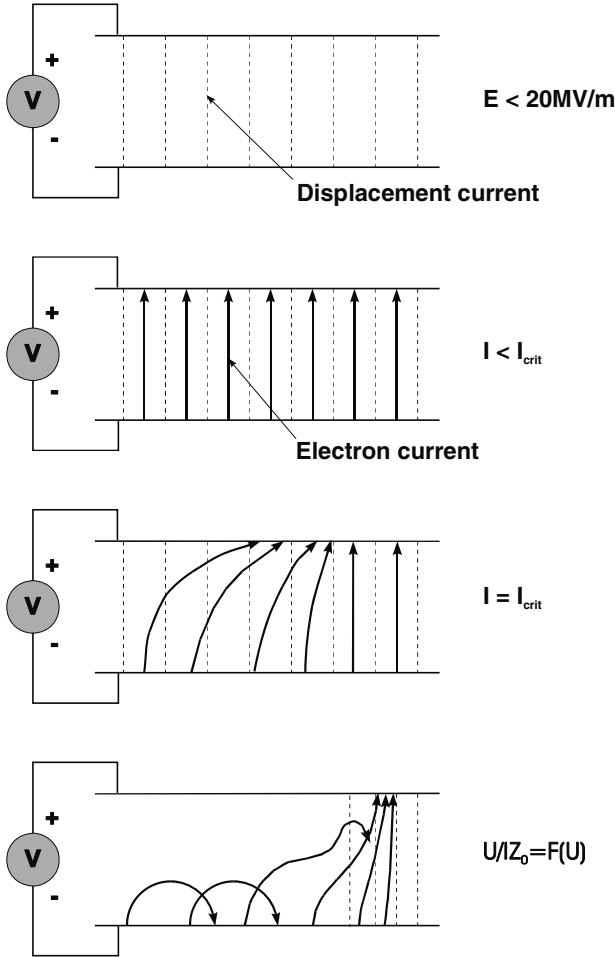


Fig. 6.5. Illustration of the various phases during the development of self-magnetic insulation in an extended transmission line

the line entrance. As long as the voltage ramp remains below the breakdown threshold, the wave propagates at the speed of light. This portion of the pulse leads to a precursor running ahead of the main pulse, which travels at a lower speed. The distance between the precursor and the main pulse grows with time. The rise time of the main pulse depends on the conditions at the loss front. Inside the loss front, the voltage drops from the plateau to the level of the precursor. In general, the width of the loss front is a few times the distance between the conductors.

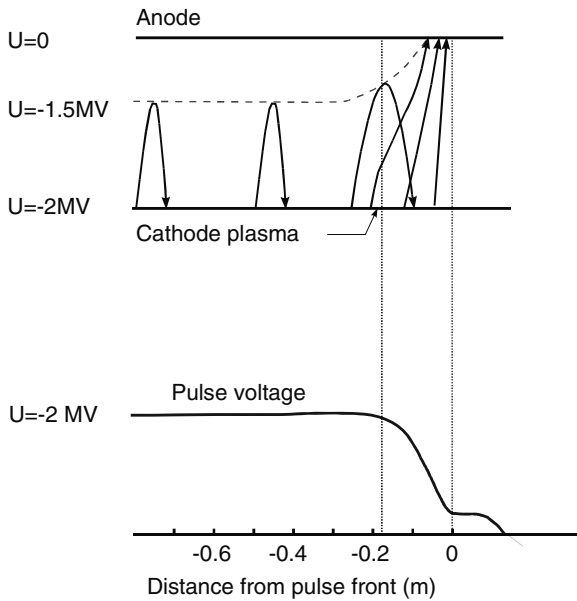


Fig. 6.6. Electron trajectories and corresponding development of the pulse voltage during propagation in a transmission line with progressing self-magnetic insulation

6.1.3 Quantitative Description of Self-Magnetic Insulation

For an exact description of self-magnetic insulation, it is necessary to solve Maxwell's field equations simultaneously with the Hamiltonian equations of motion. In addition, a model to treat the plasma formation at the cathode must be developed and coupled to the system of equations. In detail, the system of coupled differential equations (6.5)–(6.7) must be solved.

In general, this can only be done numerically. The method of solving this problem is the particle-in-cell (PIC) method [Birdsall and Langdon 1991]. Figure 6.7 shows the flow diagram of a PIC code. At the beginning, the field distribution must be determined for the given geometry. Then electrons are generated at positions on the cathode where the conditions for emission are fulfilled. In most cases this is a simple threshold condition for the electric field strength. During the next time step, the electrons are moved in the known fields, and thereafter the space charge and current densities are calculated. Using these quantities, the new fields can be determined, and particles are newly emitted and moved together with those remaining in the system from the previous time step in the modified fields. This sequence is carried out until convergence is achieved. Figure 6.8 shows an example of a PIC-code calculation for the electron density in a coaxial vacuum transmission line terminated with an electron diode [Illy et al. 1994]. Here the electric field is coupled into the line from a ring-shaped gap.

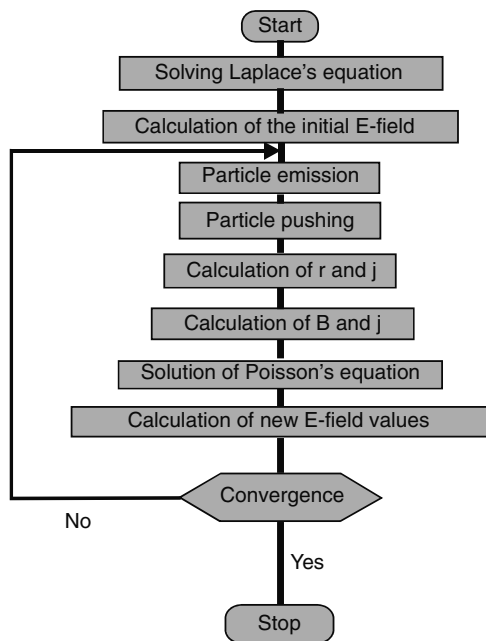


Fig. 6.7. Flow diagram of a particle-in-cell (PIC) code

The differential equations to be solved in a PIC code are given in their most general form by (6.5)–(6.7):

$$\begin{aligned}\Delta \vec{A} &= \mu_0 \varepsilon_0 \frac{\partial^2 \vec{A}}{\partial t^2} - \mu_0 \vec{j}, \\ \Delta \Phi &= \mu_0 \varepsilon_0 \frac{\partial^2 \Phi}{\partial t^2} - \frac{\rho}{\varepsilon_0}.\end{aligned}\quad (6.5)$$

Equations (6.5) represent Maxwell's field equations, where \vec{A} is the magnetic vector potential defined through $\vec{B} = \nabla \times \vec{A}$, and Φ is the scalar potential. The next equations are

$$\begin{aligned}H &= \sqrt{(m_0 c^2)^2 + c^2(\vec{P} - e\vec{A})^2} + e\Phi, \\ \dot{P}_i &= -\frac{\partial H}{\partial q_i}, \quad \dot{q}_i = \frac{\partial H}{\partial P_i}.\end{aligned}\quad (6.6)$$

Equations (6.6) are the relativistic Hamiltonian equations of motion for a charged particle in an electromagnetic field. Here q_i and P_i are the coordinates and the components of the canonical momentum, respectively; m_0 is the rest mass of the particle and c is the velocity of light in vacuum. The final equation considered is

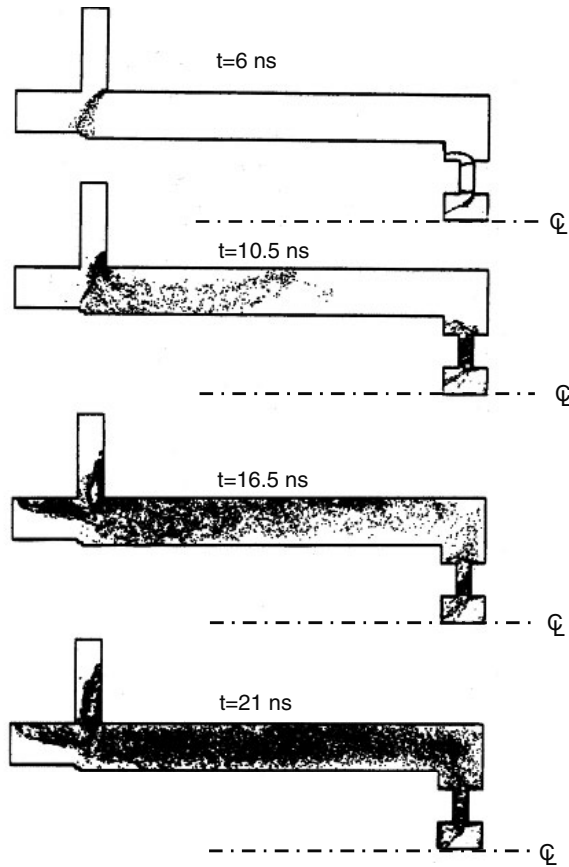


Fig. 6.8. Evolution of electron flow in a self-magnetically insulated transmission line terminated with an electron diode

$$n_c(\vec{r}, t) = f(E_c, \vec{r}, t). \quad (6.7)$$

Equation (6.7) describes the formation of a plasma at the metallic surface if the electric field exceeds a critical value E_c .

6.1.3.1 Analytical Models

Analytical models can lead to better insight into the parametric dependences of self-magnetic insulation [Baranchikov et al. 1978, Creedon 1975, Mendel et al. 1983, DiCapua 1983]. Therefore, in the following we shall consider such a model for stationary conditions at a large distance behind the loss front of the wave. That is, we have only a net current flow j_z in the z -direction. In addition, we assume a homogeneous coaxial line (Fig. 6.9). The set of coupled differential equations (6.5) can then be simplified:

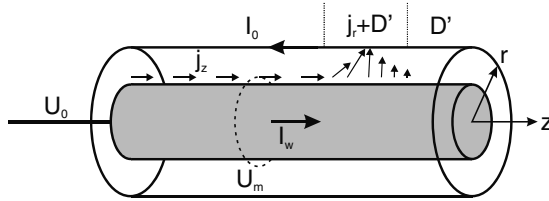


Fig. 6.9. Illustration of current components in a self-magnetically insulated transmission line

Potential equations:

$$\frac{1}{r} \frac{\partial}{\partial r} \left(r \frac{\partial A_z}{\partial r} \right) = -\mu_0 j_z,$$

$$\frac{1}{r} \frac{\partial}{\partial r} \left(r \frac{\partial \Phi}{\partial r} \right) = -\frac{\rho}{\epsilon_0} \tag{6.8}$$

Momentum conservation: $P_z = \gamma m_0 \dot{z} - e A_z = 0.$ (6.9)

Energy conservation: $\gamma m_0 c^2 - e \Phi = m_0 c^2,$ (6.10)

$$\beta = \frac{v}{c},$$

$$\gamma = \frac{1}{\sqrt{1 - \beta^2}} = 1 + \frac{e \Phi}{m_0 c^2}. \tag{6.11}$$

Here β is the particle velocity relative to the velocity of light, and γ is the relativistic factor (defined in (6.11)). In this cylindrical geometry, the self-magnetic field B_θ is related to the vector potential and the current by (6.12):

Self-magnetic field: $B_\theta = -\frac{\partial A_z}{\partial r} = \frac{\mu_0 I(r)}{2\pi r}.$ (6.12)

Condition at the anode: $\int_{r_c}^{r_a} \mu_0 \frac{I(r)}{2\pi r} dr = A_z^a = \frac{m_0 c}{e} \frac{\dot{z}_a}{c} \gamma_a.$ (6.13)

The last expression in (6.13) is derived from (6.9). If electrons just touch the anode tangentially, we have

$$\frac{\dot{z}}{c} = \beta_a.$$

(Generally $\beta_a \geq \dot{z}/c$ since there can be also a radial component of the particle velocity.) Electrons will not reach the anode if the following condition is fulfilled:

$$\text{Insulation condition: } A_z^a = \int_{r_c}^{r_a} \mu_0 \frac{I(r)}{2\pi r} dr \geq \frac{m_0 c}{e} \beta_a \gamma_a. \quad (6.14)$$

In general, the total line current I_0 is divided into an electron sheath current and a wall current flowing in the skin depth of the metallic cathode or in a plasma sheath on the cathode. However, the current distribution and the relative contributions of the two components to the total current are not known a priori. Therefore, there is also no unique interrelation between the total current I_0 and the insulation condition; i.e., the insulation condition is consistent with an infinite number of current distributions.

If there is only a wall current in the line, i.e., the electric field at the cathode remains below the field emission threshold, we can obtain the insulation condition for a probe electron launched at the cathode by integrating (6.14):

$$\frac{\mu_0}{2\pi} I_{\text{cr}} \ln \frac{r_a}{r_c} = \frac{m_0 c}{e} \beta_a \gamma_a. \quad (6.15)$$

Solving for I_{cr} , we obtain

$$I_{\text{cr}} = I_\alpha g \beta_a \gamma_a. \quad (6.16)$$

Here, the following abbreviations have been used:

$$I_\alpha = \frac{m_0 c^2}{e} \frac{2\pi}{\mu_0 c} = 8500 \text{ A},$$

$$g = \frac{1}{\ln r_a/r_c}; \quad (6.17)$$

g is a geometric factor.

I_{cr} is called the critical current. It is the wall current required in the line to prevent a particle launched at the cathode from reaching the anode. Of course, the critical current is not equivalent to the self-consistent insulation condition in the case of explosive electron emission from the cathode. To determine this condition, we must know the electron current density distribution in the gap between the inner and the outer conductor. Without additional assumptions about the characteristics of the electron flow, this distribution cannot be derived within the framework of our model. Quite generally, the electron trajectories shown in Fig. 6.10 are conceivable.

In a laminar electron flow, the particles stream in a force-free manner parallel to the electrodes. In a quasi-laminar flow, the electrons move on cycloidal trajectories, with return to the cathode. A common feature of both of these trajectory types is the conservation of canonical angular momentum (6.9) and total energy (6.10). Therefore a product of two delta functions can describe the distribution of particles in phase space.

In comparison, the flow presented in the lower section of Fig. 6.10 has a general energy and momentum distribution. However, numerical simulations

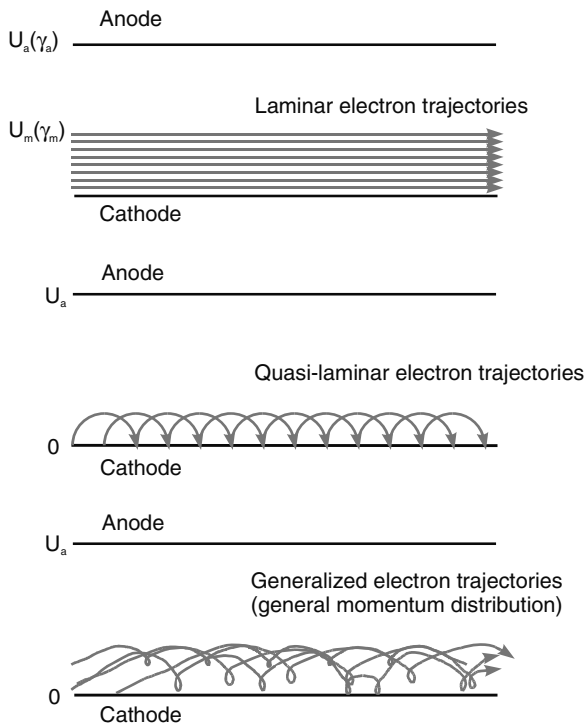


Fig. 6.10. Conceivable electron trajectories in a parallel plate vacuum transmission line

suggest that a laminar flow is a rather good approximation. For this kind of flow, we can derive the stationary solution in the following way [Creedon 1975]. First, we solve the relevant differential equations for the space charge region. Second, we combine this solution with that for the vacuum region between the sheath edge and the anode. We always assume that ions are not emitted from the anode side. For electrons streaming parallel to the z -axis, the radial momentum is zero, and we have

$$\begin{aligned} \dot{p}_r = 0 &= -e \frac{\partial \Phi}{\partial r} + ev_z \frac{\partial A_z}{\partial r} \\ &= -eE_r + ev_z B_\theta. \end{aligned} \tag{6.18}$$

Equation (6.18) describes the balance of force in the r -direction. This equation must be combined with the one-dimensional potential equations,

$$\begin{aligned} \frac{1}{r} \frac{\partial}{\partial r} \left(r \frac{\partial A_z}{\partial r} \right) &= -\mu_0 \rho v_z, \\ \frac{1}{r} \frac{\partial}{\partial r} \left(r \frac{\partial \Phi}{\partial r} \right) &= -\frac{\rho}{\epsilon_0}. \end{aligned} \tag{6.19}$$

From (6.18), we have $\partial A_z/\partial r = 1/v_z \partial\Phi/\partial r$, which can be introduced into the first of the equations (6.19), leading to

$$\begin{aligned} \frac{1}{r} \frac{\partial}{\partial r} \left(r \frac{1}{v_z} \frac{\partial\Phi}{\partial r} \right) &= -\mu_0 \rho v_z, \\ \frac{1}{r} \frac{\partial}{\partial r} \left(r \frac{\partial\Phi}{\partial r} \right) &= -\frac{\rho}{\varepsilon_0}. \end{aligned} \quad (6.20)$$

Now we use the second equation to eliminate r in the first, and, in addition, express v_z and Φ in terms of γ :

$$\begin{aligned} \frac{v_z}{c} &= \frac{\sqrt{\gamma^2 - 1}}{\gamma}, \\ \frac{e\Phi}{m_0 c^2} &= \gamma - 1. \end{aligned} \quad (6.21)$$

Then, we finally derive

$$\frac{1}{r} \frac{\partial}{\partial r} \left(r \frac{\partial\gamma}{\partial r} \right) = \frac{\gamma}{\gamma^2 - 1} \left(\frac{\partial\gamma}{\partial r} \right)^2. \quad (6.22)$$

Equation (6.22) is the fundamental differential equation for self-magnetic insulation, which has to be solved in agreement with the following boundary conditions and then combined with the solution for the vacuum region:

$$\gamma(r_c) = 1, \quad \gamma(r_m) = \gamma_m. \quad (6.23)$$

To obtain the solution, it is convenient to simplify (6.22) by changing the independent variable r to s , where

$$\frac{ds}{dr} = \frac{1}{r}. \quad (6.24)$$

Equation (6.22) becomes

$$\frac{d^2\gamma}{ds^2} = \frac{\gamma}{\gamma^2 - 1} \left(\frac{d\gamma}{ds} \right)^2, \quad (6.25)$$

which is equivalent to

$$\frac{d}{ds} \left(\frac{1}{\sqrt{\gamma^2 - 1}} \frac{d\gamma}{ds} \right) = 0. \quad (6.26)$$

Integrating (6.26) twice from $\gamma = 1$ at the cathode ($s = s_c$) to γ at s , we obtain

$$\ln \left(\gamma + \sqrt{\gamma^2 - 1} \right) = C_1 (s - s_c). \quad (6.27)$$

Generally, the electron sheath does not extend to the anode (see Fig. 6.10). Denoting the edge coordinate by s_m and the corresponding potential by γ_m , we can express C_1 using these quantities

$$C_1 = \frac{\ln\left(\gamma_m + \sqrt{\gamma_m^2 - 1}\right)}{s_m - s_c}. \quad (6.28)$$

In order to relate γ_m at s_m to the anode potential γ_0 at s_a , we must now find the solution for γ in the region between s_m and s_a and connect it to the solution (6.27) for the electron sheath region. Since there is no space charge in this region, this task reduces to solving Laplace's equation

$$\frac{d^2\gamma}{ds^2} = 0. \quad (6.29)$$

Integrating twice and taking into account the boundary conditions $\gamma(s_m) = \gamma_m$ and $\gamma(s_a) = \gamma_0$, we obtain

$$\gamma = \frac{\gamma_0(s - s_m) - \gamma_m(s - s_a)}{s_a - s_m}. \quad (6.30)$$

The radial electric field E_r is proportional to $d\gamma/ds$ and must have the same value at s_m if it is calculated from (6.27) or from (6.30). Making use of this, we obtain another expression for C_1 :

$$C_1 = \frac{\gamma_0 - \gamma_m}{(s_a - s_m)\sqrt{\gamma_m^2 - 1}}. \quad (6.31)$$

By equating (6.31) with (6.28), we can eliminate s_m and obtain

$$C_1 = \frac{\ln\left(\gamma_m + \sqrt{\gamma_m^2 - 1}\right) + \gamma_0 - \gamma_m/\sqrt{\gamma_m^2 - 1}}{s_a - s_c}. \quad (6.32)$$

Making use of (6.12) and taking into account the relationship between B_θ and E_r (6.18), we obtain the following for the current $I(r)$ flowing within a radius r :

$$I(r) = I_\alpha r \frac{\gamma}{\sqrt{\gamma^2 - 1}} \frac{\partial\gamma}{\partial r} = I_\alpha C_1 \gamma. \quad (6.33)$$

Equation (6.33) is valid for $r_c < r < r_m$, where r_m is the radius to which the electron cloud extends into the anode-cathode gap. For the total current I_0 flowing in the transmission line, we finally obtain the following by setting $\gamma = \gamma_m$:

$$I_0 = I_\alpha g \gamma_m \left(\ln\left(\gamma_m + \sqrt{\gamma_m^2 - 1}\right) + \frac{\gamma_0 - \gamma_m}{\sqrt{\gamma_m^2 - 1}} \right), \quad (6.34)$$

where g is the geometrical factor introduced in (6.17). Equation (6.34) can be transferred to other geometries if the corresponding value for g is used:

$$\begin{aligned} \text{Concentric cylinders:} \quad & g = \frac{1}{\ln r_a/r_c}, \\ \text{Parallel plates:} \quad & g = \frac{y_0}{2\pi x_0}. \end{aligned} \tag{6.35}$$

Here y_0 is the width of the plates and x_0 is the distance between the plates.

The current I_w flowing in the cathode wall or in a plasma sheath at the cathode is obtained by setting $\gamma = \gamma_c = 1$ in (6.33):

$$I_w = I_0/\gamma_m. \tag{6.36}$$

Here γ_m is still a free parameter, namely the relativistic factor (potential) at the upper boundary of the electron sheath, and another criterion is necessary to fix it. Figure 6.11 shows the total current I_0 and the wall current I_w as a function of the boundary layer potential $U_m(\gamma_m)$, for a pulse voltage of $U_0 = 1.8$ MV. The difference between these two currents is the electron sheath current. It is obvious that the total current has a minimum. It has been found from experimental observations on long transmission lines that the stationary operation point of the line is located close to this minimum. It can be shown within the framework of the laminar model that the current minimum coincides with an energy density minimum. Therefore we may use the minimum-current criterion to fix γ_m .

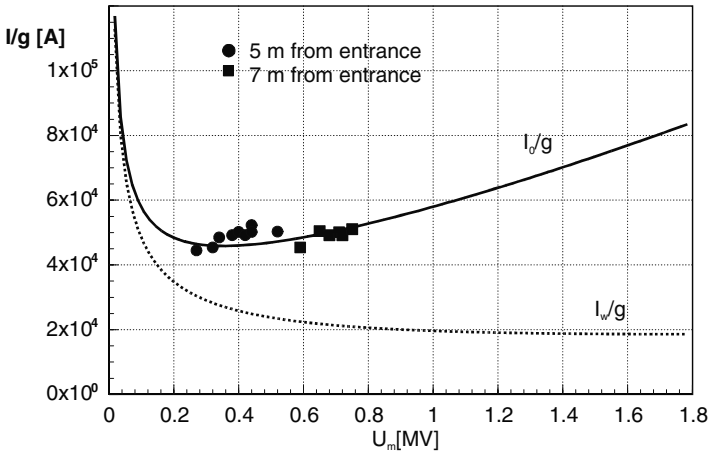


Fig. 6.11. Reduced wall current I_w and total current I_0 in a magnetically insulated vacuum line as a function of the sheath potential U_m for $U_0 = 1.8$ MV. The symbols represent experimental data obtained in a 7.5 m long parallel-plate line [Wang and DiCapua 1980]

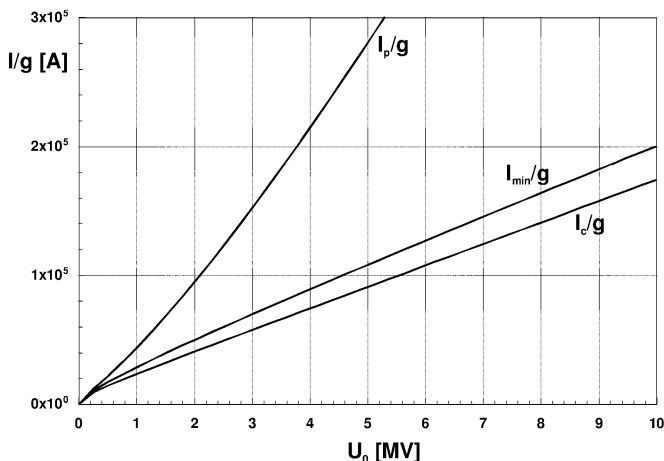


Fig. 6.12. Reduced minimum current I_{min}/g , critical current I_{cr}/g , and saturation current I_p/g in a self-magnetically insulated vacuum line as a function of the anode potential U_0

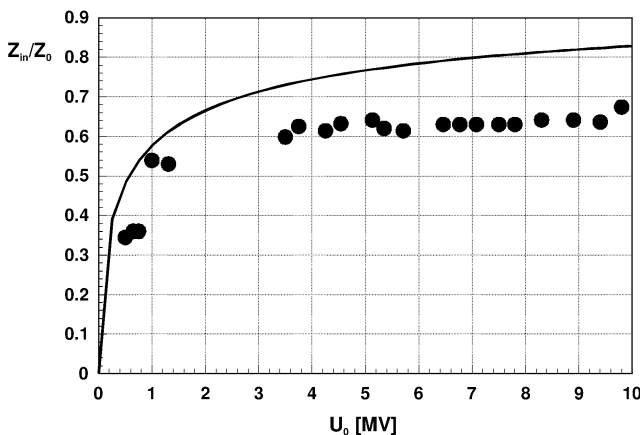


Fig. 6.13. Relative impedance Z_{in}/Z_0 of a vacuum line as a function of pulse amplitude

The minimum current I_{min} of a self-limited (infinitely long) transmission line can be determined by calculating the minimum of I_0 (6.34) for every γ_0 . This has been plotted in Fig. 6.12 as a function of the anode potential U_0 for values up to 10 MV. In addition, the critical current (6.16) and the saturation current I_p are shown. The latter is the line current if the electron sheath fills the entire anode–cathode gap and is obtained by setting $\gamma_m = \gamma_0$ in (6.34).

If the line is terminated with a load whose (matched) impedance corresponds to U_0/I_{min} , the energy transfer is maximum. If the load impedance

is larger, an electron loss current remains at the end of the line. If the load impedance is smaller, a reflected wave runs back into the line, reducing the electron sheath current and shifting the point of operation into the region to left of the minimum in Fig. 6.11.

For the design of a self-magnetically insulated transmission line, it is necessary to know the operating impedance relative to the vacuum impedance. The latter has been plotted in Fig. 6.13 for the minimum current as a function of the pulse voltage. The experimental results confirm the predictions of the model with satisfactory precision.

6.1.3.2 Simple Theory Based on Experimental Observations

A fundamental understanding of magnetically insulated transmission lines can also be derived from the following set of experimental observations [Mendel et al. 1983; Mendel and Rosenthal 1995, 1996]:

- the cathode is a space-charge-limited emitter of electrons;
- the ion emission from the anode is much less than the space charge-limited value.

Space-charge-limited emission occurs if the particle flux from the source is larger than the extracted flux. Under these conditions, the space charge of the accelerated particles limits the current density, and a stable condition is established in which the electric field at the emitting surface is zero. The second of the above observations is identical to stating that the magnetically insulated line is efficient. It can be shown that the assumption of space-charge-limited ion emission from the anode is not compatible with efficient line operation.

We consider a planar magnetically insulated transmission line of length ℓ , width b , and separation y_a , in which an electron cloud extends to a distance y_m from the cathode and moves parallel to the electrodes (see Fig. 6.10). In equilibrium, the cloud remains at the same distance from the electrodes. This is identical to stating that the sum of the electromagnetic and particle pressures is the same on both electrodes. Under the assumptions made above, we can neglect the particle pressures in comparison with the field pressures. Also, the electric-field pressure must be zero on the cathode. Therefore we have the following equation for the pressure balance:

$$\frac{B_a^2}{2\mu_0} - \frac{\varepsilon_0 E_a^2}{2} = \frac{B_c^2}{2\mu_0}. \quad (6.37)$$

Here B_a and E_a are the magnetic and the electric field, respectively, at the anode; B_c is the magnetic field at the cathode. Expressing the magnetic fields in terms of the corresponding currents I_a and I_c ($B_a = \mu_0 I_a/b$, $B_c = \mu_0 I_c/b$), we obtain the following for E_a :

$$E_a = \frac{c\mu_0}{b} \sqrt{I_a^2 - I_c^2}. \quad (6.38)$$

Introducing the vacuum impedance of the line $Z_0 = \sqrt{\mu_0/\varepsilon_0} y_a/b$, we can write this as

$$E_a y_a = Z_0 \sqrt{I_a^2 - I_c^2}. \quad (6.39)$$

This relation suggests that we should define a flow impedance Z_f through

$$Z_f = \frac{U}{\sqrt{I_a^2 - I_c^2}}. \quad (6.40)$$

Here U is the voltage across the line. This definition of Z_f does not relate to any specific distribution of space charge in the line. If the space charge distribution in the flow layer is uniform, we obtain the following for Z_f :

$$Z_f = Z_0 - \frac{mc^2}{2e} \frac{\sqrt{I_a^2 - I_c^2}}{I_c^2}. \quad (6.41)$$

By solving (6.40) and (6.41) for I_a , we can determine Z_f as a function of I_c for different values of U :

$$Z_f = \frac{Z_0 + (Z_0^2 - 2mc^2 U/eI_c^2)^{1/2}}{2}. \quad (6.42)$$

Once Z_f has been determined, I_a can be calculated from (6.40).

6.1.3.3 Non-Stationary Wave Propagation

As has been described previously, electron losses will occur at the head of a pulse of large amplitude entering the vacuum transmission line, which will affect its propagation. We are seeking a relation between the quantities at the wave front (propagation velocity, loss current, efficiency of energy transport, etc.) and the quantities far behind the wave front, which we have already described (following [Baranchikov et al. 1978, Wang and DiCapua 1980]). For this purpose we make the following simplifying assumptions:

1. The voltage pulse is rectangular.
2. The peak values of the voltage and current do not change during propagation.
3. The pulse front propagates undeformed with a uniform velocity u .
4. Ahead and behind the pulse front, the derivatives of all quantities with respect to z vanish.
5. The precursor pulse can be neglected.

Thus all quantities are functions of $\eta = z - ut$ and r only. Nevertheless, the pulse will erode during propagation. We have the following equations:

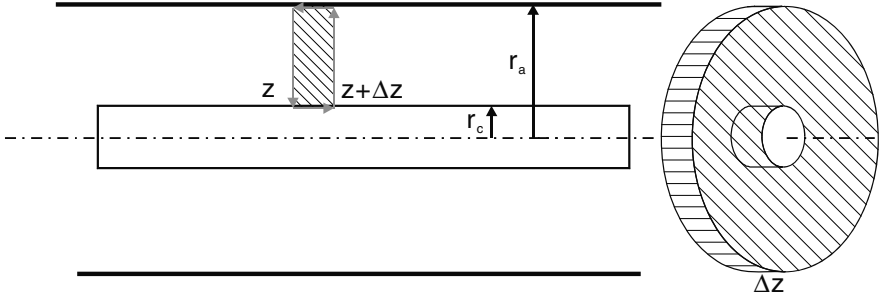


Fig. 6.14. Integration path for the derivation of (6.46)–(6.49)

$$f(r, z, t) = f(r, z - ut). \quad (6.43)$$

Faraday's law:

$$\int \nabla \times \vec{E} \, d\vec{A} = -\frac{\partial}{\partial t} \int \vec{B} \, d\vec{A},$$

$$\vec{B} = \nabla \times \vec{A}. \quad (6.44)$$

Transforming the surface integral into a line integral, we obtain

$$\oint \vec{E} \cdot d\vec{s} = -\frac{\partial}{\partial t} \oint \vec{A} \cdot d\vec{s}, \quad (6.45)$$

and, integrating (6.45) over the cross-section of the transmission line gap (see Fig. 6.14, left part), we obtain ($E_z = 0$, $A_r = 0$, $A_z(r_c) = 0$)

$$\int_{r_c}^{r_a} E_r(z + \Delta z) \, dr - \int_{r_c}^{r_a} E_r(z) \, dr = -\frac{\partial}{\partial t} \int_{z+\Delta z}^z A_z(r_a) \, dz,$$

$$U(z + \Delta z) - U(z) = -\frac{\partial}{\partial t} A_z(r_a) \Delta z. \quad (6.46)$$

Finally, we obtain

$$\frac{\partial U}{\partial z} = -\frac{\partial A_z}{\partial t}. \quad (6.47)$$

Using the continuity equation (6.48),

$$\frac{\partial}{\partial t} \int \rho \, dv = \int \nabla \cdot \vec{j} \, dv, \quad (6.48)$$

we obtain the following equation in a similar way, by integrating over a volume element determined by the cross-section of the line and a small extension Δz in the axial direction (Fig. 6.14, right part):

$$\frac{\partial I_z}{\partial z} = \frac{\partial Q}{\partial t} + \frac{\partial I_r}{\partial z}, \quad (6.49)$$

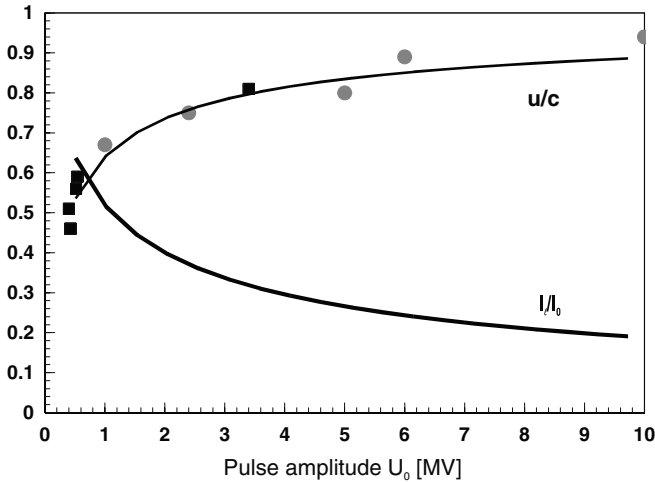


Fig. 6.15. Wave front propagation velocity and loss current in a self-magnetically insulated vacuum line as a function of pulse amplitude (*squares*, experimental results [Baranchikov et al. 1978]; *circles*, results from PIC-code simulations [Poukey and Bergeron 1978])

where Q is the electron charge per unit length in the line. With the help of the following coupling equations (6.50),

$$A_z = LI_z, \quad \frac{\partial I_r}{\partial z} = GU, \quad Q = CU, \quad (6.50)$$

one can derive a nonlinear telegrapher's differential equation. However, we shall not follow this approach here. Rather, we shall make use of our assumption that all quantities are functions of $\eta = z - ut$ only, to derive an expression for u . By integration over the pulse front, we obtain from (6.47)

$$\frac{\partial U}{\partial z} = -\frac{\partial A_z}{\partial t} = u \frac{\partial A_z}{\partial z}. \quad (6.51)$$

And, by using the stationary solution, we obtain

$$u = \frac{U_0}{A_z^a},$$

$$\frac{u}{c} = \frac{(\gamma_0 - 1)\sqrt{\gamma_m^2 - 1}}{\gamma_0\gamma_m - 1}. \quad (6.52)$$

Here we have made use of (6.13) and (6.33), observing that the integration between r_m and r_a has to be done with a constant current I_m . In a similar manner, we can obtain an expression for the loss current I_r by integration of (6.49) across the pulse front:

$$\begin{aligned}
I_0 &= uQ + I_r, \\
\frac{I_r}{I_0} &= \frac{\gamma_a - \gamma_m + \gamma_m^2 - 1}{\gamma_m(\gamma_a \gamma_m - 1)}. \tag{6.53}
\end{aligned}$$

Q can be derived from the expression for ρ given by (6.19). The diagram plotted in Fig. 6.15 shows the propagation velocity and the loss current as a function of the pulse amplitude. With increasing pulse voltage, the propagation velocity approaches the velocity of light. Simultaneously, the loss current decreases. Experimental results and numerical simulations confirm these findings.

6.1.3.4 Efficiency of Energy Transfer

Energy conservation for a system containing fields and particles is described by the following differential equation [Landau and Lifschitz 1981]:

$$\begin{aligned}
\frac{\partial}{\partial t} \int \left(\frac{1}{2} \mu_0 H^2 + \frac{1}{2} \varepsilon_0 E^2 + \frac{(\gamma - 1) mc^2 \rho}{e} \right) dV \\
= - \oint \left(\vec{E} \times \vec{H} + \frac{(\gamma - 1) mc^2}{e} \vec{j} \right) d\vec{A}. \tag{6.54}
\end{aligned}$$

On the left-hand side, we have the temporal change of the field and particle energy in the volume under consideration. The right-hand side describes the energy flow through the surface of that volume. Integrating this balance equation over the cross-section of the line leads to a differential equation for the total energy per unit length W and the energy flux P through the cross-section:

$$\frac{\partial W}{\partial t} + \frac{\partial P}{\partial z} - \frac{2\pi r_a (\gamma - 1) mc^2}{e} j_r(r_a) = 0. \tag{6.55}$$

As previously, we integrate (6.55) over the pulse front, assuming again that all quantities depend on $z - ut$:

$$-uW + P + \frac{(\gamma_a - 1) mc^2}{e} I_r = 0. \tag{6.56}$$

The flux of energy loss is $P_{\text{loss}} = P - uW$. W can be derived from the formulae of the laminar theory to determine the efficiency of energy transfer:

$$\eta = 1 - \frac{P_{\text{loss}} \ell / u}{P\tau} = 1 - \frac{\ell}{c\tau} \left(\frac{c}{u} - \frac{cW}{P} \right). \tag{6.57}$$

In Fig. 6.16, we present the energy transfer efficiency as a function of pulse amplitude.

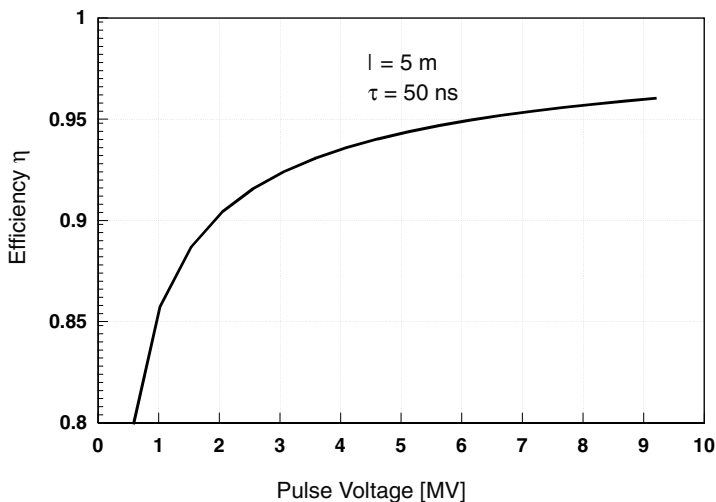


Fig. 6.16. Energy transfer efficiency as a function of pulse amplitude

6.1.3.5 Summary and Conclusions

We can summarise the results above as follows:

1. The condition for self-magnetic insulation in a long vacuum transmission line is

$$I > I_{\min}.$$

2. Division into a wall and a particle current occurs according to

$$\frac{I_0}{I_w} = \gamma_m.$$

3. Input impedance of a self-magnetically insulated line:

$$Z_{\text{in}} = (0.6-0.8)Z_0.$$

4. Propagation velocity:

$$\frac{u}{c} = 0.7-0.9.$$

5. Efficiency of energy transport:

$$\eta = 0.85-0.95.$$

At this point we must ask whether there is a limit on the power density that can be transported through a magnetically insulated transmission line. The largest experimentally achieved values are presently around 500 TW/m^2 . A fundamental limit cannot be derived from the models discussed previously. However, the electron loss current at the pulse front may create a very hot plasma on the anode surface, which can lead to an ion loss current and, through expansion into the line gap, to a short circuit.

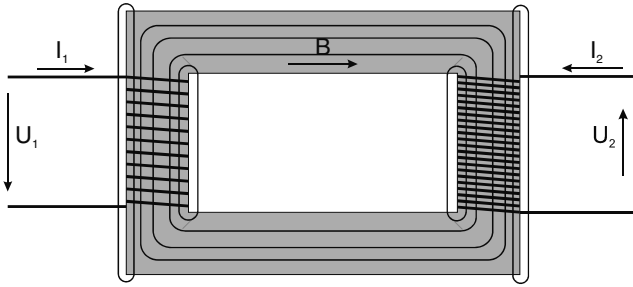


Fig. 6.17. Voltages, currents, fields, and flux in a transformer

6.2 Pulse Transformers

High-voltage transformers play an important role in pulsed-power techniques, both in high-voltage charging units and as pulse transformers. They are used for the transformation of current, voltage, and impedance, for polarity inversion, and for insulation and coupling between circuits at different potentials.

Transformers are based on magnetic coupling between two conducting circuits. In this process the output power is always smaller than the input power. A transformation of power wherein no energy is stored or lost in the transformer defines a perfect, or ideal, transformer. The ideal transformer has no ohmic losses, does not create any eddy currents, and is without hysteresis and stray field, i.e., the magnetic flux goes completely through both the primary and the secondary coil. The directions of the current and voltage are defined as shown in Fig. 6.17.

If a voltage U_1 is applied between the terminals of the primary, an induced equal voltage of opposite sign will compensate it, since the primary is inductive only. According to Faraday's law, this voltage is equal to the rate of change of the flux in all N_1 windings:

$$U_1 = N_1 \frac{d\Phi}{dt}. \quad (6.58)$$

The same rate of change of the flux $d\Phi/dt$ induces a voltage

$$U_2 = -N_2 \frac{d\Phi}{dt}. \quad (6.59)$$

The voltage ratio of the transformer is therefore

$$\frac{U_2}{U_1} = -\frac{N_2}{N_1}. \quad (6.60)$$

The minus sign results from the definition of the directionality of the voltage in Fig. 6.17 as parallel to that of the current. Relation (6.60) is independent of the load, i.e., of the magnitude of the current drawn from the secondary. It holds also for the ratio of the complex voltages u_2/u_1 .

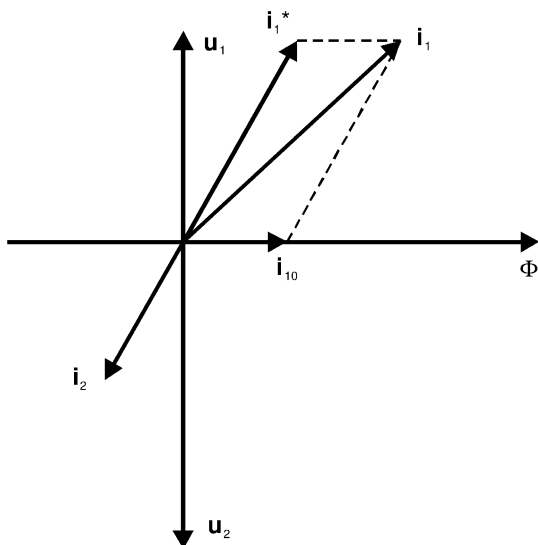


Fig. 6.18. Diagram in the complex plane showing the relationship between currents and voltages in the primary and secondary of a loss-free transformer

If the secondary is open, no current flows through it, i.e., the magnetic flux Φ in the transformer is caused only by the current I_1 in the primary. This open-circuit current I_{10} is associated with no power, and $\mathbf{i}_{10} = \mathbf{u}_1 / (i\omega L_1)$. If a load of complex impedance Z is connected to the secondary, a voltage $\mathbf{u}_2 = -(N_2/N_1) \cdot \mathbf{u}_1$ drives a current $\mathbf{i}_2 = \mathbf{u}_2/Z$ through it and contributes to the flux in the transformer. Nevertheless, the flux Φ must remain unchanged, since it is just sufficient to compensate for \mathbf{u}_1 . Therefore the additional flux $N_2 \mathbf{i}_2$ must be compensated by an additional current \mathbf{i}'_1 in the primary such that $N_1 \mathbf{i}'_1 = -N_2 \mathbf{i}_2$. Thus the primary current becomes

$$\mathbf{i}_1 = \mathbf{i}_{10} + \mathbf{i}'_1 = \mathbf{i}_{10} - \frac{N_2}{N_1} \mathbf{i}_2 = \mathbf{i}_{10} - \frac{N_2 \mathbf{u}_2}{N_1 Z}. \quad (6.61)$$

By complex addition, $|\mathbf{i}_1|$ becomes greater than $|\mathbf{i}_{10}|$, as shown in the diagram in Fig. 6.18. When the blind current \mathbf{i}_{10} is subtracted from the primary current, the primary and secondary powers become equal, as expected:

$$(\mathbf{i}_1 - \mathbf{i}_{10}) \mathbf{u}_1 = -\frac{N_2 \mathbf{u}_2}{N_1 Z} \mathbf{u}_1 = \mathbf{i}_2 \mathbf{u}_2. \quad (6.62)$$

If $I_{10} \ll N_2 I_2 / N_1$, we obtain an ideal transformer, for which

$$I_1 = \frac{-N_2 I_2}{N_1}. \quad (6.63)$$

If a resistor R_2 is connected to the terminals of the secondary, the current and the voltage at the primary are related by

$$U_1 = \frac{I_1 R_2}{n^2}, \quad (6.64)$$

where $n = N_2/N_1$. This is easily derived from the conservation of power, i.e., $I_1^2 R'_2 = I_2^2 R_2$. Similarly, we have

$$L'_2 = \frac{L_2}{n^2}, \quad (6.65)$$

and from $(1/2)C'_2 U_1^2 = (1/2)C_2 U_2$, we obtain

$$C'_2 = n^2 C_2. \quad (6.66)$$

Thus we can relate all circuit elements on the secondary side to the primary using the transformation rules (6.64)–(6.66). If we now take into account resistive, eddy current, and hysteresis losses and, in addition, consider the finite capacitance between the coil windings, we arrive at the equivalent-circuit model of a real transformer shown in Fig. 6.19.

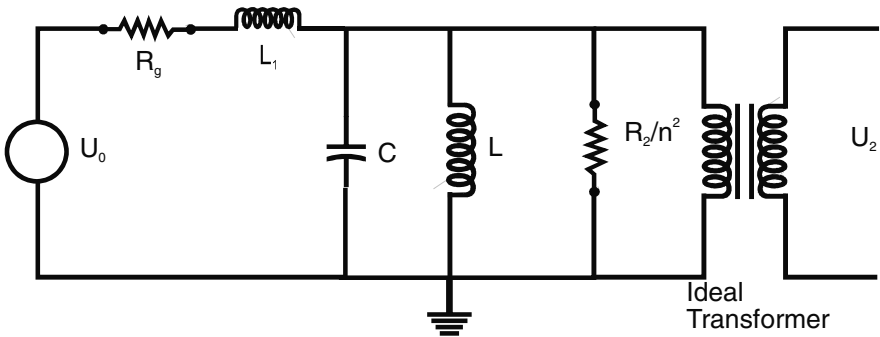


Fig. 6.19. Equivalent-circuit model of a real transformer

The current is divided into a leakage current and a load current. Therefore we must always have

$$I_1 \geq I_2 n. \quad (6.67)$$

In general, leakage currents are undesirable since they lead to energy losses.

In pulsed-power systems, transformers are very often used to transmit and transform (square) pulses to a larger voltage level. To calculate the rise time of the output pulse in such an application, it is generally possible to neglect the transformer inductance L in the equivalent-circuit model. The leakage inductance L_1 , however, is important since it determines the overshoot of the pulse. Deriving the solution for the circuit of Fig. 6.19 under these conditions, we obtain the following results for a voltage step:

$$\begin{aligned}
 U_2(t) = nU_0 \frac{R_2/n^2}{R_2/n^2 + R_g} \\
 \times \left\{ 1 - e^{-k\omega t} \left[\left(\frac{k}{2\sqrt{k^2-1}} + \frac{1}{2} \right) e^{\omega\sqrt{k^2-1}t} \right. \right. \\
 \left. \left. - \left(\frac{k}{2\sqrt{k^2-1}} - \frac{1}{2} \right) e^{-\omega\sqrt{k^2-1}t} \right] \right\}. \quad (6.68)
 \end{aligned}$$

Here, k and ω are given by

$$k = \frac{1}{2} \left[\frac{R_g}{L_1} + \frac{1}{(R_2/n^2)C} \right] \frac{1}{\omega}, \quad \omega^2 = \frac{R_g + R_2/n^2}{(R_2/n^2)L_1C}. \quad (6.69)$$

Equation (6.68) is valid for $k > 1$.

For the case of a critically damped circuit, where $k = 1$, we obtain

$$U_2(t) = nU_0 \frac{R_2/n^2}{R_2/n^2 + R_g} \{1 - (1 + \omega t) e^{-\omega t}\}. \quad (6.70)$$

Finally, for the underdamped case, where $k < 1$, we have

$$\begin{aligned}
 U_2(t) = nU_0 \frac{R_2/n^2}{R_2/n^2 + R_g} \\
 \times \left\{ 1 - e^{-k\omega t} \left[\frac{k}{\sqrt{1-k^2}} \sin(\sqrt{1-k^2}\omega t) + \cos(\sqrt{1-k^2}\omega t) \right] \right\}. \quad (6.71)
 \end{aligned}$$

Figure 6.20 shows the form of the output pulse for different degrees of damping.

For a critically damped circuit, the rise time of the output pulse (0.1–0.9 $U_{2\max}$) can be derived from (6.70):

$$t_r = 0.53T = 3.35 \left(\frac{L_1C(R_2/n^2)}{(R_2/n^2 + R_g)} \right)^{1/2}. \quad (6.72)$$

Here $T = 2\pi/\omega$. To achieve a fast rise time, L_1 and C have to be made as small as possible. Consequently, the transformer core must consist of a material with a large permeability at high frequencies (for good coupling). The circuit capacitance C is the sum of the stray capacitances in the primary and secondary circuits. The latter have to be multiplied by n^2 ($C = C_1 + n^2C_2$). Thus the rise time grows in proportion to n . Therefore, i.e., transformation factors that are too large should be avoided in this application.

For the droop of the transformed rectangular pulse, L_1 and C are of little importance. L determines mainly the time constant of the droop of the flat top:

$$t_d = \frac{L(R_g + R_2/n^2)}{R_g R_2/n^2}. \quad (6.73)$$

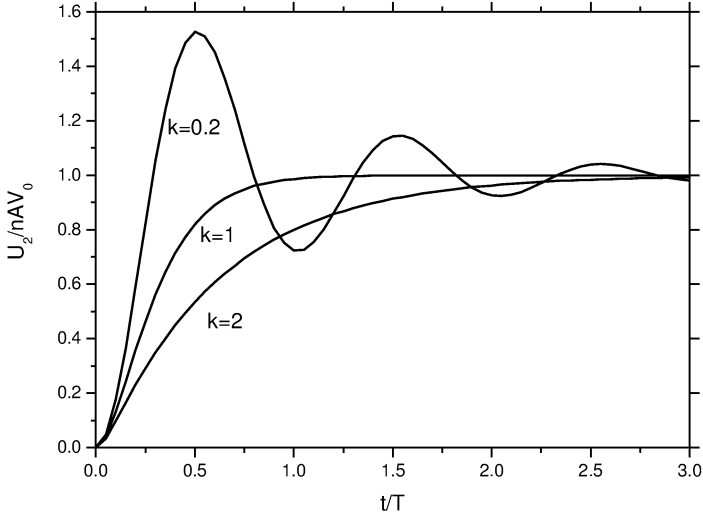


Fig. 6.20. Response of a pulse transformer to a voltage step for different degrees of damping ($A = (R_2/n^2)/(R_g + R_2/n^2)$, $n = N_2/N_1$, $k = [R_g/L_1 + 1/(R_2/n^2C)] T/4\pi$, $T = 2\pi(L_1(CA)^{1/2})$)

In this case also, L must be large to ensure that t_d is large compared with the pulse duration, i.e., that only a small droop occurs.

Power loss occurs in a real transformer because of eddy currents and hysteresis of the ferromagnetic core, as discussed in Sect. 4.1.3 for magnetic switches. A further problem is non-ideal coupling. There are always regions where the magnetic field is not completely compensated, an effect which leads to the appearance of L_1 in the equivalent circuit.

Besides this, limitations exist on the pulse shapes that can be transmitted undeformed by a transformer with ferromagnetic core. From the relation $N_1 d\Phi/dt = U$, it follows that

$$\begin{aligned}
 N_1 \frac{d\phi}{dt} &= N_1 \frac{d(A_1 B(t))}{dt} = V(t), \\
 [B(t) - B(0)] N_1 A_1 &= \int V(t) dt \leq 2B_s N_1 A_1. \tag{6.74}
 \end{aligned}$$

This limitation is already known to us from the discussion of the properties of a magnetic switch (Sect. 4.1.3). In general, transformers are operated far below this threshold to keep the hysteresis losses small.

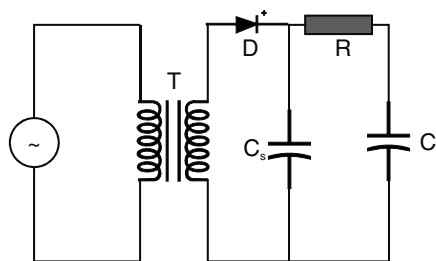


Fig. 6.21. Schematic of a resistive charging unit (D = rectifying diode, C_s = smoothing capacitor)

6.3 High-Voltage Power Supplies

6.3.1 Capacitor-Charging Techniques

There are three common techniques for charging a capacitor: linear charging, one-cycle command resonant charging, and high-frequency switch mode ('constant current') charging.

A simplified schematic of a linear charging supply is shown in Fig. 6.21. This consists of a transformer-rectifier set and some means of limiting the inrush current to the load capacitance. The limiting of the inrush current may be achieved by phase control of the AC input or by adding a series impedance to the input or output. This impedance is usually a resistor or an inductor (or both) in the DC output to isolate the power supply from the capacitor circuit. A filter capacitor is not normally included for a capacitive load. In Fig. 6.21, a single-phase rectifier circuit, a limiting resistor, and a smoothing capacitor are used.

This kind of charging supply is acceptable only for very low-average-power applications, where circuit simplicity is the dominating design factor and where size, regulation, and efficiency are not critical issues. A supply unit such as that shown in Fig. 6.21 has an efficiency η of less than 50%, where η is defined as the ratio of the energy in the capacitor C to the energy delivered by the source. The charging current drops exponentially: $I(t) = (U_0/R) e^{-t/RC}$:

$$\eta = \frac{q^2/2C}{U_0 \int_0^t I(t) dt} = \frac{1 - e^{-t/RC}}{2} \leq 0.5. \quad (6.75)$$

Before the development of high-voltage switching power supplies, command resonant charging was the most widely used technique for repetitive charging of capacitor banks [Glasoe and Lebacqz 1948]. One-cycle resonant charging also has a relatively simple circuit topology. In addition to the basic transformer-rectifier set, the system must have an additional storage capacitor, an inductor, and a switch. The achievable regulation is equal to the AC

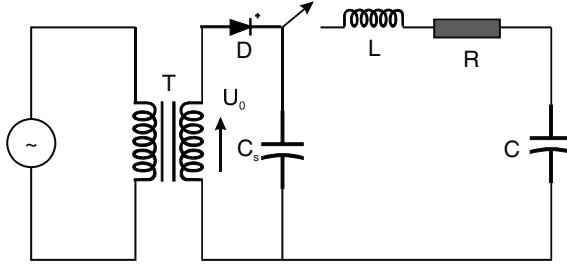


Fig. 6.22. One-cycle resonant charging system

line regulation, i.e., it depends on the capacitance of the smoothing capacitor. The basic circuit is shown in Fig. 6.22.

Solving the differential equation for the circuit of Fig. 6.22, we obtain the following for $U(t)$, the voltage on the capacitor C (see Sect. 3.3):

$$U(t) = U_0 \left(1 - e^{-at} \left[\cos(\omega t) - \left(\frac{a}{\omega} \right) \sin(\omega t) \right] \right). \quad (6.76)$$

This result has been derived assuming that the storage capacitor C_s is very large compared with C . Here $\omega^2 = \omega_0^2 - a^2$, $\omega_0^2 = 1/LC$, $a = R/2L$. The current is given by

$$I(t) = \frac{U_0}{L\omega} e^{-at} \sin(\omega t). \quad (6.77)$$

$Q = \omega L/R = \omega/(2a)$ is called the quality factor of the resonant circuit. The efficiency η is given by

$$\eta = \frac{(1/2)CU^2(t)}{U_0 \int_0^t I(t) dt} = \frac{(1/2) [1 - e^{-at} (\cos(\omega t) - a/\omega \sin(\omega t))]^2}{1 - e^{-at} [\cos(\omega t) + a/\omega \sin(\omega t)]}. \quad (6.78)$$

One-cycle resonant charging means that the charging time t_c is determined by $\omega t_c = \pi$. Therefore we obtain

$$\eta = \frac{1 + e^{-\pi a/\omega}}{2} = \frac{1 + e^{-\pi/2Q}}{2}. \quad (6.79)$$

Thus, if the circuit parameters are adjusted appropriately, the efficiency of the resonant charging circuit can approach 1. The disadvantages of command resonant charging are the size and weight of the circuit.

For medium- and high-power systems where minimum volume, high efficiency, and regulation are critical design criteria, high-frequency quasi-constant-current charging may be the most practical capacitor-charging system. Such power supplies rectify the incoming AC power, generate a high-frequency (~ 50 kHz) AC waveform through the operation of a series-resonant

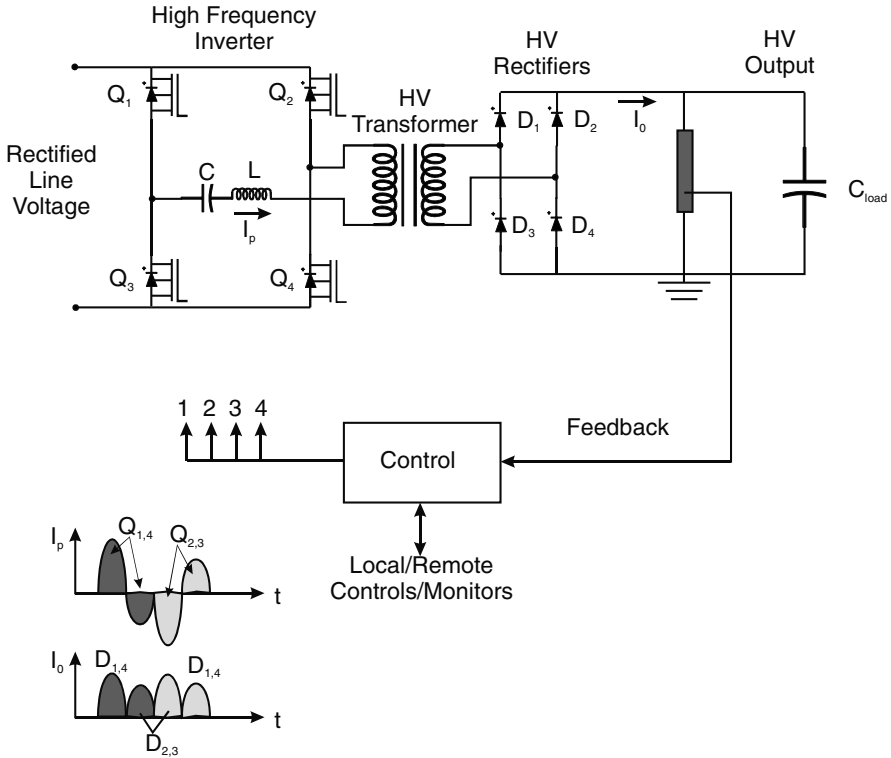


Fig. 6.23. Basic circuit diagram of a high-frequency switch mode power supply

H-bridge inverter, and finally transform and rectify the high-frequency AC waveform to the desired output. The highest-power-density, most reliable, and lowest cost H-bridge inverter uses insulated gate bipolar transistors (IGBTs) to generate the high frequency from a DC bus. The high-frequency waveform allows the use of smaller, lighter transformers to achieve the desired high-voltage output level, which is rectified using fast-recovery diodes. An H-bridge series-resonant inverter is shown in Fig. 6.23.

In the circuit diagram of Fig. 6.23, the switches have only conduction losses determined by the on-resistance of the switch, which is low. Owing to the sine wave character of the current in the LC circuit, the IGBTs can be made to switch at zero current. Careful analysis of the series-resonant equivalent circuit reveals that the current is a true sine wave only when the output voltage is zero, implying that the load is shorted. As the load capacitor begins to charge, the current in the forward direction of the bridge switches will increase, while the current in the reverse direction will decrease. This is due to the increasing voltage of the load capacitor, reflected into the primary circuit.

A desirable feature of a series-resonant converter is that the output appears as a constant-current source. Pulse rate modulation is typically used

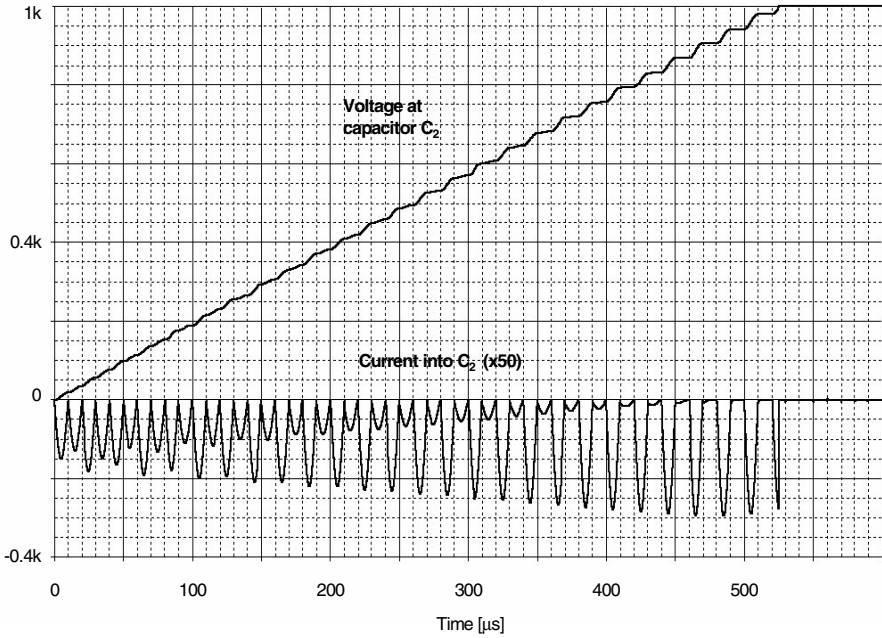


Fig. 6.24. Resonance-current pulses delivered to the load capacitor in Fig. 6.23 (*bottom part*), and voltage build-up (parameters: $U_{DC} = 100$ V, inverter frequency = 25 kHz, transformer step-up = 10)

to control the output current and hence the regulation in series-resonant capacitor-charging power supplies. Figure 6.24 shows the charge packages that are delivered per resonance cycle, together with the voltage build-up on the capacitor. It is obvious that this power supply circuit operates like a constant-current source. For units with an output voltage > 10 kV, the high-voltage power transformer and entire high-voltage output section are contained in a sealed, dielectric-oil-filled tank with oil-tight feedthroughs for all input/output lines.

Finally we derive the result that a constant-current source can charge a capacitor efficiently. The voltage on the load capacitor increases as $U = I_0 t / C$. For the efficiency, we have

$$\eta = \frac{(1/2)C (I_0 t / C)^2}{(1/2)C (I_0 t / C)^2 + RI_0^2 t} = \frac{t}{t + 2RC}. \quad (6.80)$$

Thus, for $t \gg RC$, η approaches 1, and for charging to a given voltage U_0 , we obtain

$$\eta = \frac{U_0 / I_0}{U_0 / I_0 + R}. \quad (6.81)$$

6.3.2 Cascade Circuits

At voltages above 100 kV, transformers become inconvenient because of the increasing core volume and increasing insulation requirements. With cascade circuits such as that shown in Fig. 6.25, supply voltages in the megavolt range can be achieved. The cascade consists of a pushing and a smoothing column. Charging occurs in steps. We can understand the operation of the circuit by considering the evolution of the voltage occurring at the positions 0, 1, 2, and 3 indicated in Fig. 6.25. We assume that the power of the AC voltage source is sufficiently large to charge C_1 within one quarter-cycle to the peak voltage of the source. During the first positive quarter-cycle, all points charge to U_0 . However, except for C_1 , no capacitor contains any charge.

When the source voltage begins to fall, the charge accumulated in C_1 commences flowing to C_2 . The charge transfer is complete at minimum source voltage. Relative to ground, positions 1 and 2 (and all other positions except for position 0) are now at zero potential (for $C_1 = C_2$). As the source voltage starts to rise from its minimum negative value, the potential at position 2 rises above zero and charge begins to flow from C_2 to C_3 and C_1 . When the source voltage at position 0 exceeds the potential at position 1 during the next positive quarter-cycle, C_1 is charged again to the level of the source amplitude and, after the peak source voltage has been exceeded, charge is again transferred from C_1 to C_2 , raising the potential at position 2 above that at position 1. At the same time, charge flows from C_3 to C_4 . Beginning in the last quarter of the second cycle, part of this charge flows back from C_2 to C_3 and C_1 , and from C_4 to C_5 .

This reasoning can be extended to subsequent cycles and subsequent points in the cascade. Net charge is delivered to the chain only through C_1 during the first quarter of the cycle. During the time in which the source voltage is falling (second and third quarters), charge is transferred from the lower to the upper chain, and during the time in which the source voltage is rising (fourth quarter and part of the first quarter of the following cycle), part of the charge is pushed back to the lower chain and smoothed out among the capacitors of this chain. Thus, on average, the voltage on each capacitor of the cascade is raised during every cycle. In the steady-state case, the voltage reaches U_0 on C_1 , while the voltage on all other capacitors approaches $2U_0$. A faster convergence to the equilibrium values can be achieved if the value of C_1 is made larger than that of the other capacitors. The main advantage of the cascade circuit is that it uses a smaller transformer core and is easier to insulate.

6.4 Transformation Lines

The impedance of a generator can also be matched to a load by a transformation line, instead of a pulse transformer.

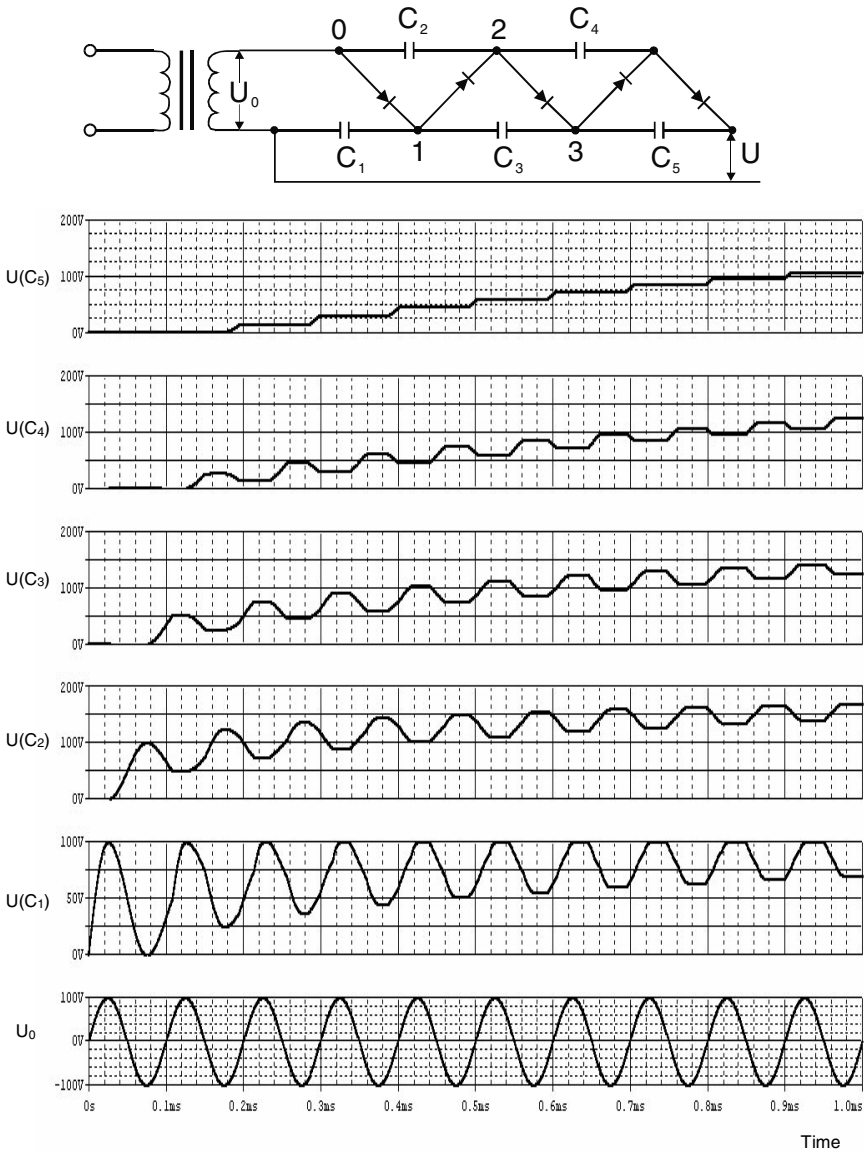


Fig. 6.25. Cascade circuit (*top*) and waveforms of the capacitor voltages. In this example, an AC source (U_0) of 100 V amplitude and 10 kHz frequency has been chosen. U is obtained by summation of all capacitor voltages in the lower chain

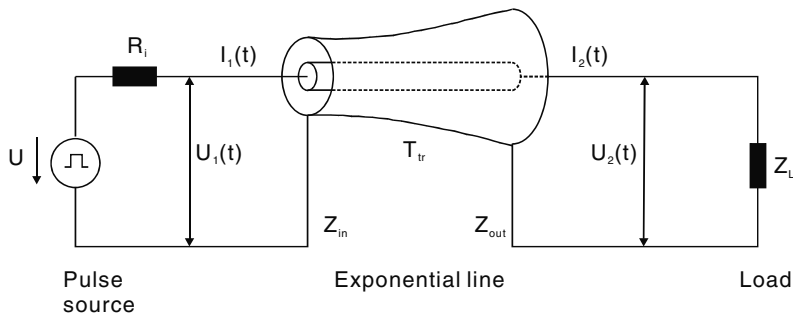


Fig. 6.26. Exponential line, including the source and the load circuit

One special case of a transformation line is the exponential line. Like a transformer, the exponential line is a power-conserving transmission system. In an exponential line, the inductance, capacitance, resistance, and conductance per unit length depend exponentially on the position x :

$$\begin{aligned} L'(x) &= L'_0 \times e^{Bx}, \\ C'(x) &= C'_0 \times e^{-Bx}, \\ R'(x) &= R'_0 \times e^{Bx}, \\ G'(x) &= G'_0 \times e^{-Bx}. \end{aligned} \quad (6.82)$$

The factor B can have both positive and negative values. An exponential line is drawn schematically in Fig. 6.26.

We consider a lossless line, i.e., $R'_0 = G'_0 = 0$. The Laplace transforms of the differential equations describing this line are

$$\begin{aligned} \frac{d^2 \mathbf{u}}{dx^2} - \frac{1}{L'} \frac{dL'}{dx} \frac{d\mathbf{u}}{dx} - \mathbf{p}^2 L' C' \mathbf{u} &= 0, \\ \frac{d^2 \mathbf{i}}{dx} - \frac{1}{C'} \frac{dC'}{dx} \frac{d\mathbf{i}}{dx} - \mathbf{p}^2 L' C' \mathbf{i} &= 0. \end{aligned} \quad (6.83)$$

It is convenient to define a spatially dependent impedance and delay per unit length:

$$\begin{aligned} Z_x &= \sqrt{\frac{L'_x}{C'_x}}, \\ T_x &= \sqrt{L'_x C'_x}. \end{aligned} \quad (6.84)$$

Using the spatial dependence of L' and C' given by (6.82), we obtain

$$\begin{aligned} \frac{d^2 \mathbf{u}}{dx^2} - B \frac{d\mathbf{u}}{dx} - \mathbf{p}^2 T_0^2 \mathbf{u} &= 0, \\ \frac{d^2 \mathbf{i}}{dx^2} + B \frac{d\mathbf{i}}{dx} - \mathbf{p}^2 T_0^2 \mathbf{i} &= 0, \end{aligned} \quad (6.85)$$

where $T_0 = \sqrt{L'_0 C'_0}$.

The solutions of the characteristic polynomial of the differential equation (6.85) are

$$r_1, r_2 = \frac{B}{2} \pm \frac{1}{2} \sqrt{B^2 + 4\mathbf{p}^2 T_0^2}. \quad (6.86)$$

Therefore, the general solution of the differential equation is

$$V = \vec{U}_0 e^{r_1 x} + \overleftarrow{U}_0 e^{r_2 x}. \quad (6.87)$$

If $B^2 \ll 4\mathbf{p}^2 T_0^2$, we obtain

$$U = \vec{U}_0 e^{B/2x} e^{-\mathbf{p}T_0 x} + \overleftarrow{U}_0 e^{B/2x} e^{\mathbf{p}T_0 x} \quad (6.88)$$

and we can immediately verify that in this case power is conserved during transmission. The assumption made above is identical to requiring that the relative impedance change $1/Z_x dZ_x/dx = B$ along the line is small compared with $4\pi/\lambda$, where λ is the wavelength of the transmitted signal. This equivalence can be derived if \mathbf{p} is replaced by $i\omega$, taking into account the fact that $\omega = 2\pi/\lambda T_0$. Of course, one must take the largest transmitted wavelength for λ .

7 Power and Voltage Adding

7.1 Adding of Power

Increasing the power and the pulse voltage requires an extended distance between the electrodes of a pulse-forming line to achieve the necessary breakdown strength. For example, a water-insulated coaxial transmission line for the production of a 15 MV, 100 TW pulse of 50 ns duration, charged from an intermediate storage within 300 ns to a voltage of 30 MV, would need to have a diameter of 16 m. It is evident that such a line would be inappropriate for the formation of a useful rectangular pulse, since charge balancing along the circumference of the conductor cannot occur within the available time. The power limit of a single-line element is reached when the transit time of an electromagnetic wave along the circumference becomes comparable to the discharge time of that element. In practice, this restricts the power that can be extracted from a single-line element to about 15 TW.

For pulsed-power levels above this value, the generator must be divided into separate units, which can be constructed much more compactly and thus use the available volume much more efficiently. The separate units are then switched synchronously to the load (Fig. 7.1). Synchronising independent lines requires special measures, for example, the use of laser-triggered switches with very low jitter. To match the generators to the load, the load impedance must equal the internal impedance of the generators divided by the number of generators, i.e., $R_L = R_g/n$.

7.2 Voltage Adding

7.2.1 Voltage Adding by Transit-Time Isolation

Some applications require accelerating voltages between 5 and 60 MV. Such high pulse amplitudes cannot be realised with single-line elements if, simultaneously, a large power is required. It is much more convenient to provide these pulse amplitudes by superposing pulses from separate units, using series connection. One special case of such a series connection is the Blumlein configuration (see below).

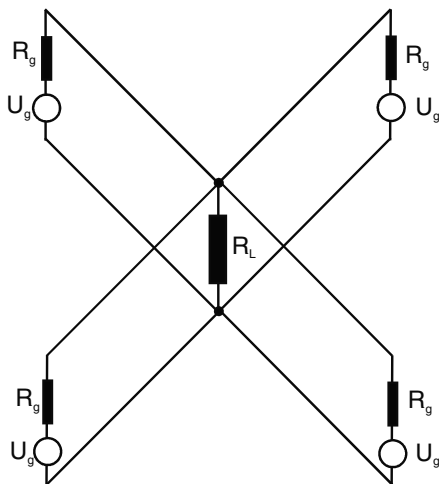


Fig. 7.1. Schematic representation of power addition by parallel switching of several generators to a common load ($R_L = R_g/n$; $n =$ number of units)

Similarly to the series connection of a number of batteries, we can combine individual pulse lines in a voltage adder configuration, by connecting the positive conductor of one line to the negative conductor of the next (Fig. 7.2). This can be done particularly easily with striplines. To prevent a short circuit from being created by this alternating connection, the junction points must be insulated, at least for the duration of the pulse. This can be achieved if the pulse lines are sufficiently long.

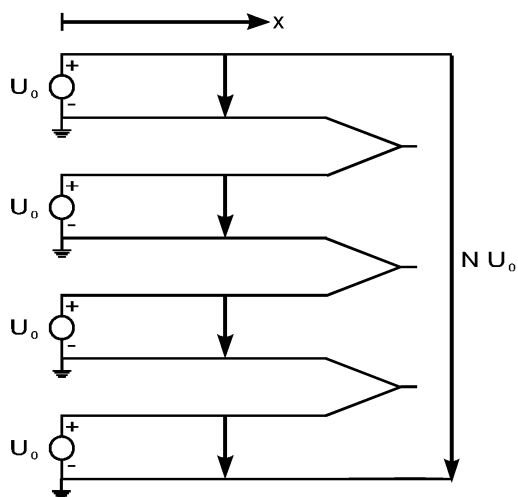


Fig. 7.2. Adding of voltage pulses by transit-time isolation

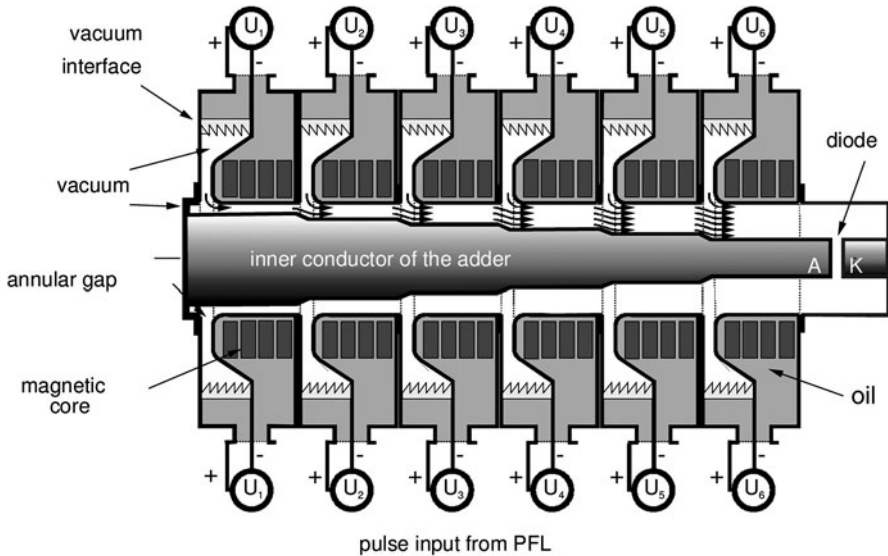


Fig. 7.3. Schematic illustration of a six-stage voltage adder based on inductive isolation

7.2.2 Voltage Adding by Inductive Isolation

A more compact accelerator set-up is possible if, instead of transit-time isolation, inductive isolation is used for adding the voltages of the pulses [Ramirez et al. 1985]. To explain the principles of voltage adding by inductive isolation, we shall consider the six-stage adder configuration of the KALIF-HELIA (High Energy Linear Induction Accelerator) generator shown in Fig. 7.3.

Each of the cylindrical cavities shown in Fig. 7.3 is fed radially by two conventional liquid-insulated-pulse forming networks. The feed points on the circumference are displaced relative to each other by 180° to homogenise the incoming waves. In addition, symmetry is improved by azimuthal distribution networks in the cavities. Each cavity can then deliver a 1 MV, 400 kA pulse of 50 ns duration into a matched, self-magnetically insulated vacuum transmission line. Voltage addition is achieved by connecting the positive side of one cavity to the negative side of the following cavity. Inevitably, the high-voltage conductor is thus joined to the grounded conductor. To make this junction a high-impedance connection, the relative permeability is strongly increased in this section. For that purpose, this part of the cavity is filled with strip-wound cores of ferromagnetic material. As long as the magnetic induction does not reach the saturation value of the material, the leakage current flowing through this ground connection remains small. Of crucial importance for the degree of magnetic insulation is the evolution in time of the ferromagnetic cores. Since the leakage current remains small only as long as the saturation value of the magnetic induction is not reached, the duration of

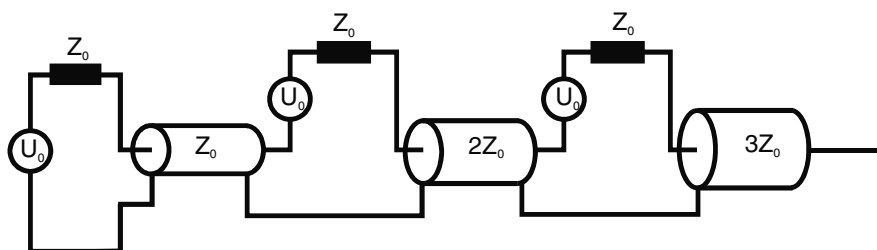


Fig. 7.4. Equivalent-circuit model of a voltage adder with self-magnetic insulation

the insulation is limited by the voltage–time integral according to Faraday’s law. The same considerations are valid as for the magnetic switch described in Chap. 4.

In the scheme shown in Fig. 7.3, voltage addition occurs on a coaxial self-magnetically insulated vacuum line. To prevent reflection of the pulses at the cavity feed points, the impedance of the vacuum line must grow in steps, i.e., increase like integer numbers.

Each of the coaxial-line sections drawn in Fig. 7.4 can be considered as a generator of impedance nZ_0 . This generator is in series with the generator $(n + 1)$ and drives, together with the latter generator, the line section $(n + 1)$, which therefore must have an impedance $(n + 1)Z_0$, so that the waves propagating to the right always see a matched load. Waves propagating to the left also see a matched load, and will be absorbed completely.

To simulate the configuration with a circuit program such as LEITER, we can use the diagram shown in Fig. 7.5. Here the lines driving the cavities have been condensed into voltage sources of internal impedance R_g . Between these voltage sources and the feed points, we have added delay lines to compensate for the different transit times to the junctions of the pulse propagating along the vacuum line. Maximum power transmission is achieved for $Z_1 = R_g$.

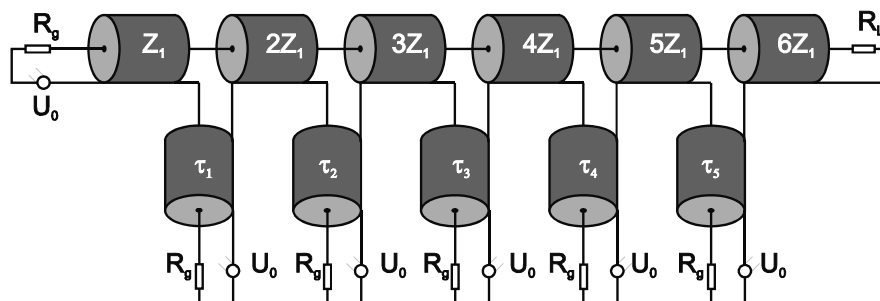


Fig. 7.5. Model for simulation of the voltage adder of Fig. 6.3 with the circuit program LEITER

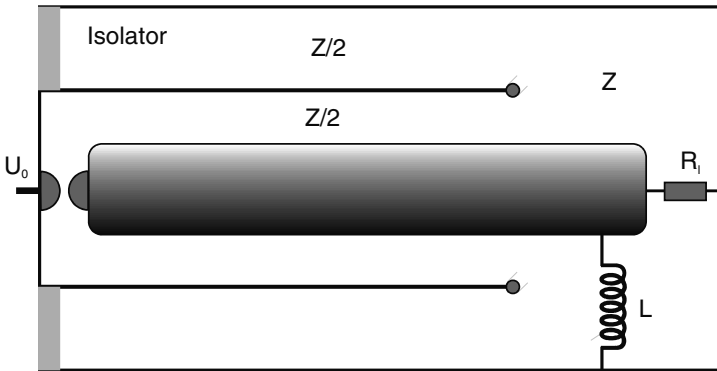


Fig. 7.6. Schematic representation of a classical Blumlein line

7.2.3 Blumlein Generators

A disadvantage of the common pulse-forming line is that the voltage amplitude into a matched load is just half of the charging voltage. In addition, the output switch is located before the load and therefore, if dynamically charged, can couple a prepulse to the load. These deficiencies are avoided by the Blumlein line shown in Fig. 7.6 [Blumlein 1941].

In its classic form, the Blumlein line consists of two interlaced lines, which, after closing of the switch, become connected in series. We can understand its operation if we consider the electrostatic voltages of both partial lines to be produced by two waves propagating in opposite directions. Before ignition, the field vectors of the waves propagating in the partial lines have opposite polarities at the line ends and compensate each other. Consequently, no current flows into the load.

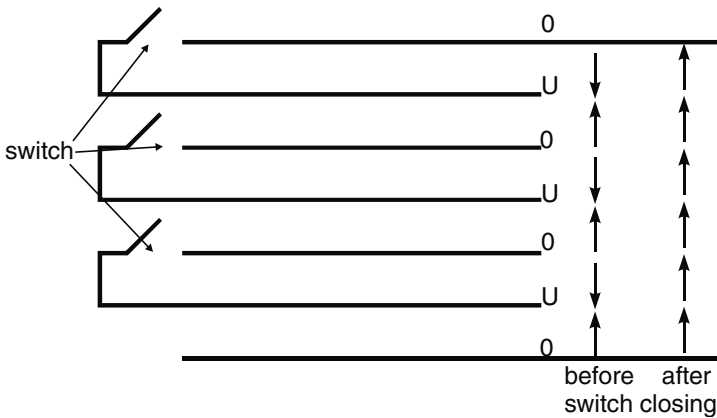


Fig. 7.7. Schematic representation of a generalised Blumlein line

After ignition of the switch, the polarity of the forward-going wave in the inner line is inverted. At the load end of the line, this wave therefore has the same polarity as the forward-propagating wave in the outer partial line. A voltage is thus created across the load and a current begins to flow. In a matched load, this voltage becomes U_0 . If the impedances of the individual lines are $Z/2$, the impedance of the Blumlein line becomes Z .

The Blumlein configuration can be generalised. Figure 7.7 represents a stack of striplines whose electrodes have been charged alternately. Alternate lines are synchronously short-circuited. At the open end, their field vectors are inverted and a voltage amplitude $2nU_0$ is created, where n is the number of switches. Naturally, the impedance of this configuration becomes $2nZ$.

7.2.4 Cumulative Pulse Lines

An interesting scheme for voltage multiplication is the cumulative pulse line shown in Fig. 7.8 [Smith 1980]. Similarly to the generalised Blumlein line, it can produce a multiplication of the initial charging voltage. An advantage compared with the latter is that it needs just one switch. A cumulative pulse line consists of n interconnected transmission line elements of equal transit time. Relative to the first line element, the impedance of the successive elements grows like the sums of the natural numbers: $1 + 2 = 3$, $1 + 2 + 3 = 6$, $1 + 2 + 3 + 4 = 10$, etc. The last (n th) section has an impedance $Z_n = n(n+1)Z_1/2$, where Z_1 is the impedance of the first element. After the switch S is closed, a discharge wave propagates to the load end of the line. If the line is open, this wave creates a voltage $-nU_0$ at the terminals. If the line is connected to a load of impedance Z_n at the time of arrival of the wave at the load end, the wave produces a pulse of amplitude $-nU_0/2$ for a duration of 2τ , where τ is the transit time for a line element.

In this case, the stored energy is completely transferred to the load. Why is the energy not reflected at the impedance jumps in the line? Indeed, we learned before that a pulse is reflected at an impedance mismatch and that the only situation in which reflections do not occur is when the interconnected lines have the same impedance. The difference here is that the lines

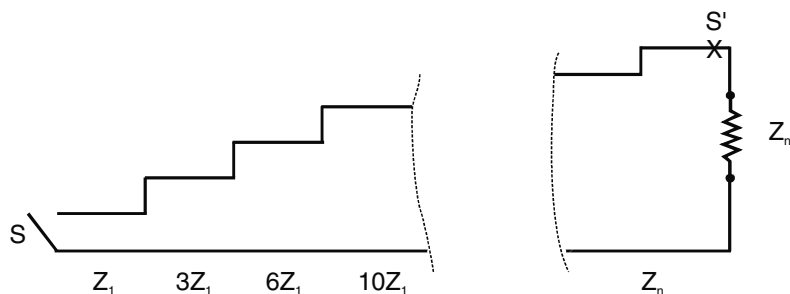


Fig. 7.8. Cumulative pulse line with stepwise-increasing impedance

are all charged. Before ignition of the switch, we can again consider the stationary charging voltage U_0 as a superposition of waves with amplitudes $U_0/2$ propagating in opposite directions. We can convince ourselves that the amplitudes of the transmitted and reflected waves cancel at the junctions. After closing of the switch, in line element 1 a negative wave of amplitude $-U_0/2$ runs towards Z_2 . At the junction, the wave is transmitted with amplitude $(-U_0/2)[2Z_2/(Z_1 + Z_2)]$. At this point, it is not necessary to take into account the forward-propagating wave of amplitude $U_0/2$ that exists in line element 2 because of the initial charge. However, this wave comes into play at the end of the line if a load is connected. As long as we have not reached the end, the amplitude of the forward-going wave increases at every junction by a factor

$$\frac{2Z_{n+1}}{Z_{n+1} + Z_n} = \frac{n+2}{n+1}. \quad (7.1)$$

Therefore the amplitude of the wave entering the n th section is

$$-\frac{U_0}{2} \frac{3}{2} \frac{4}{3} \frac{5}{4} \cdots \frac{n}{n-1} \frac{n+1}{n} = -\frac{U_0}{2} \frac{n+1}{2}. \quad (7.2)$$

This wave reaches the load together with the forward-propagating wave of amplitude $U_0/2$ in section n and creates a voltage

$$U_L = \left[-\frac{U_0}{2} \frac{n+1}{2} + \frac{U_0}{2} \right] \frac{2Z_L}{Z_L + Z_n} = -\frac{nU_0}{2} \frac{2Z_L}{Z_L + Z_n}. \quad (7.3)$$

Thus, for a matched load $Z_L = Z_n$, we obtain

$$U_L = -\frac{nU_0}{2}, \quad (7.4)$$

This pulse occurs for at least a time 2τ across the load, since, at the earliest, reflections cannot reach the load until after this time. Therefore the energy W_L that is transferred to the load is

$$W_L = \left(\frac{nU_0}{2} \right)^2 \frac{2\tau}{Z_n}, \quad (7.5)$$

or, since $Z_n = [n(n+1)/2] Z_1$,

$$W_L = \left(\frac{nU_0}{2} \right)^2 \frac{4}{n(n+1)} \frac{\tau}{Z_1}. \quad (7.6)$$

On the other hand, the transit time for a line section is $\tau = \ell\sqrt{L'C'}$ $Z = \sqrt{L'/C'}$. Here ℓ is the length of one section. Thus

$$\begin{aligned} \frac{\tau}{Z_1} &= \frac{\ell\sqrt{L'_1 C'_1}}{\sqrt{L'_1/C'_1}} = \ell C'_1 = C_1, \\ W_L &= \frac{nU_0^2}{n+1} C_1, \end{aligned} \quad (7.7)$$

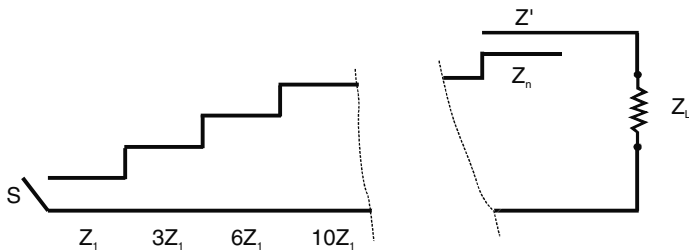


Fig. 7.9. Cumulative transmission line combined with Blumlein configuration

where C_1 is the capacitance of the first section. Comparing this with the energy initially stored in all line sections

$$\begin{aligned}
 W &= \frac{C_1}{2} U_0^2 + \frac{C_2}{2} U_0^2 + \dots + \frac{C_n}{2} U_0^2 \\
 &= \frac{1}{2} U_0^2 \sum_1^n C_i, \\
 \frac{C_i}{C_1} &= \frac{Z_1}{Z_i} = \frac{2}{i(i+1)}, \\
 W &= \frac{1}{2} U_0^2 2C_1 \sum_1^n \frac{1}{i(i+1)} = U_0^2 C_1 \sum_1^n \left(\frac{1}{i} - \frac{1}{i+1} \right) = U^2 C_1 \left(1 - \frac{1}{n+1} \right) \\
 &= \frac{nU_0^2}{n+1} C_1, \tag{7.8}
 \end{aligned}$$

we see that $W = W_L$, i.e., all energy has been transferred to the load. This also proves that the pulse reaches the load without any reflections. For a real line this is not completely true, since, as we know already, higher modes may be created at the junctions.

The output switch S' , which is necessary in the series configuration, and the difficult synchronisation between the switches S and S' can be avoided if the output line is combined with a Blumlein configuration as shown in Fig. 7.9. The last line section shares the high-voltage electrode with another transmission line of equal length. The grounded electrodes of both lines are connected to the load. The impedance of the additional line is chosen such that it delivers the same current into a matched load as does the cumulative line, i.e.,

$$\frac{U_0}{2Z'} = \frac{nU_0}{2} \frac{1}{Z_n} = \frac{nU_0}{2} \frac{1}{[n(n+1)/2] Z_1} = \frac{1}{n+1} \frac{U_0}{Z_1}, \tag{7.9}$$

and hence

$$Z' = \frac{n+1}{2} Z_1. \tag{7.10}$$

The load impedance must then be matched to the sum of Z_n and Z' :

$$\begin{aligned} Z_L &= \frac{n(n+1)}{2} Z_1 + \frac{n+1}{2} Z_1 \\ &= \frac{(n+1)^2}{2} Z_1. \end{aligned} \tag{7.11}$$

8 Examples of Pulsed-Power Generators

8.1 Single-Pulse Generators

Some scientific tasks do not need a repetition rate capability of the pulse generator. This is especially true if the experiment (the load) itself limits the pulse rate, for example, because the diagnostics are very complex, demanding time for preparation and evaluation after each shot, or because essential parts of the experimental set-up become destroyed and must be replaced after each pulse. Under these conditions, the set-up of the pulse generator can be simplified. Nevertheless, some single-pulse experiments require extremely high electrical power.

8.1.1 KALIF

KALIF, which stands for ‘Karlsruhe Light Ion Facility’ [Bluhm et al. 1985], is a typical representative of single-pulse terawatt machines (Fig. 8.1). Its primary energy store is a bipolar Marx generator consisting of 25 stages. Each stage is built from two $1\ \mu\text{F}$ capacitors that can be charged up to $\pm 100\ \text{kV}$. At maximum charge, the energy content is 250 kJ. After erection of the Marx generator, this energy is transferred within $1\ \mu\text{s}$ to a coaxial water-insulated intermediate storage capacitor with a capacitance equal to that of the erected Marx generator. The impedance of this line is $5\ \Omega$, and its outer diameter is 2.5 m. Owing to the large distance between the inner and the outer conductor, breakdown does not occur during charging. Through a self-breaking water switch, which is adjusted to ignite at maximum charge, the intermediately stored energy is transferred, within the double transit time of 300 ns of the electromagnetic wave, to a pulse-forming line. The latter has an impedance of $2.25\ \Omega$ and the same capacitance and outer diameter as the intermediate storage capacitor. Its electrical length is 25 ns. Because of the smaller impedance, the distance between the inner and the outer conductor is much less. This is possible because the charging time is much shorter.

At the exit of the pulse-forming line, a set of 14 self-breaking water switches is distributed over the outer radius of the inner conductor. These switches are largely decoupled through transit-time and inductive effects, but UV light can propagate from each switch to all others, and therefore

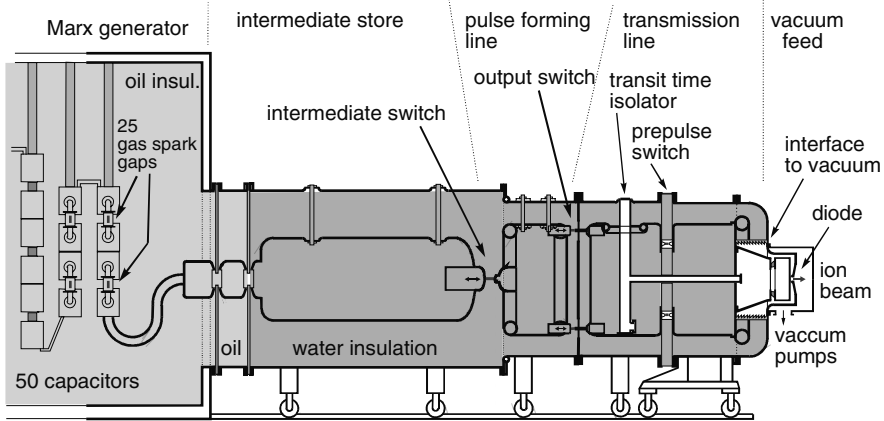


Fig. 8.1. Schematic illustration of the 1.5 TW pulse generator KALIF. The data for the pulse at the vacuum interface are: power = 1.5 TW, voltage = 1.7 MV, pulse duration = 50 ns, pulse energy = 75 kJ, electrical efficiency = 30%

synchronous ignition is achieved. Because of the large number of sparks, the inductance and resistance of the switch is small, and a fast-rising pulse enters the transmission line, which is of equal impedance. The pulse propagates through a dielectric prepulse slab, which divides the transmission line into two sections. This slab contains 11 gas switches to suppress the prepulse which is capacitively transmitted through the front face between the pulse-forming line and the transmission line during charge-up of the former, and which would propagate to the load. The gas pressure in the switches in the prepulse slab is adjusted such that they do not break through at the prepulse level, but ignite immediately on arrival of the main pulse. The pulse propagates along the second half of the transmission line, and enters the vacuum chamber containing the load through a stacked interface.

8.1.2 PBFA 2 and the Z-Machine

At present the world largest single-pulse generator is the Z-Machine [Spielman et al. 1997], located at Sandia National Laboratories in Albuquerque, USA. This facility was initially constructed as a particle beam fusion accelerator (PBFA 2) (Fig. 8.2) to produce intense light-ion beams [Turman et al. 1985]. PBFA 2 consisted of 36 generator modules, each having twice the power of KALIF. These generators were connected partly in series to increase the output pulse voltage and partly in parallel to increase the output power. Each of the 36 bipolar Marx generators contained 60 capacitors of capacitance $1.35 \mu\text{F}$, which could be charged to $\pm 100 \text{ kV}$. In total, the Marx generators stored an energy of 14.4 MJ. After erection of the Marx generators, the energy was again transferred to intermediate-storage water capacitors. These were

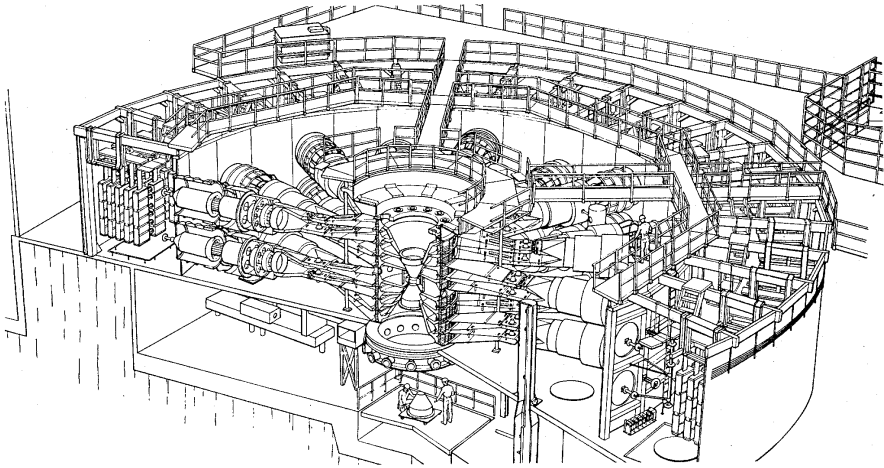


Fig. 8.2. Perspective drawing of the multimodular generator PBFA 2

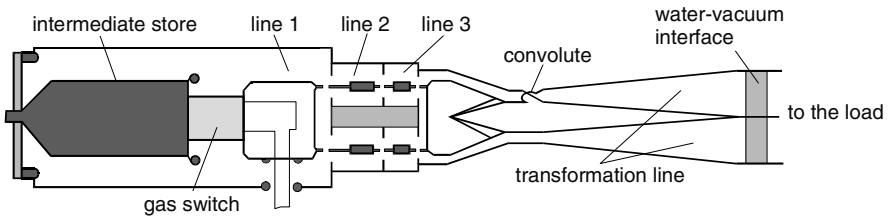


Fig. 8.3. Pulse-forming network of a single module of the PBFA 2 device

connected to the pulse-forming lines through laser-triggered gas switches. Since the jitter of these switches was less than 1 ns, a very precise synchronisation of all generator modules became possible. After ignition of the gas switches, the pulse was compressed with the help of three pulse-forming lines as shown in Fig. 8.3. The transmission line contained a transition from coaxial to plate geometry. At the same time, the $2.15\ \Omega$ coaxial line was split into two $4.3\ \Omega$ lines and in one of these lines, the positive and the negative conductor were interchanged with the help of a convolute. Simultaneously, the impedance grew along these lines, transforming the voltage amplitude by a factor of 2.8. Finally, at the insulator stack, nine modules were connected in parallel and the resulting four levels were connected in series. Thus, at the exit of the generator, a 14 MV pulse of 100 TW was developed for a duration of 30 ns. This pulse was used for the production of intense ion beams.

Around 1995, PBFA 2 was transformed into a Z-pinch driver. Similarly to PBFA 2, the Z-Machine (Fig. 8.4) stores 12 MJ of electrical energy in 36 Marx generators and delivers the energy to water-dielectric coaxial intermediate stores within $1\ \mu\text{s}$. The intermediate stores reach a peak voltage of 5 MV. A

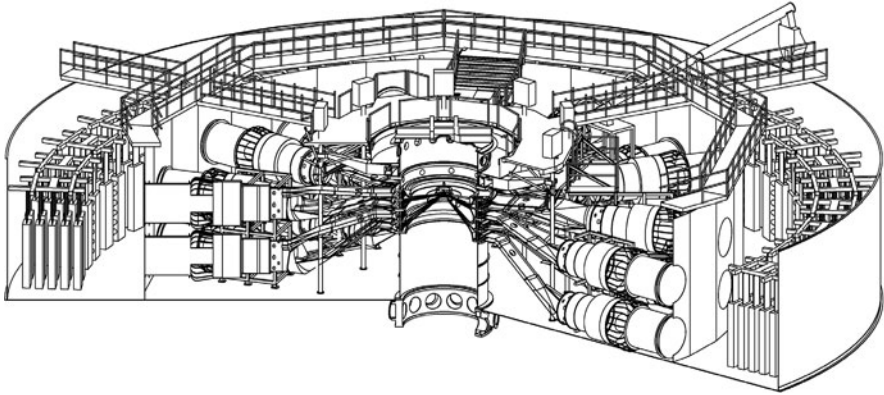


Fig. 8.4. Schematic illustration of the Z-Machine for driving Z-pinches, located at Sandia National Laboratory

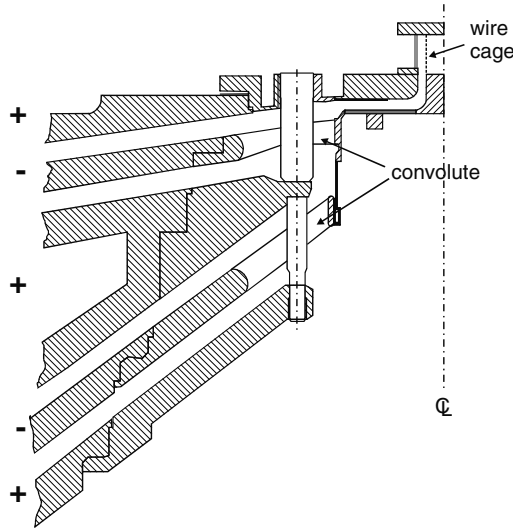


Fig. 8.5. Post-hole convolute in the Z-Machine

low-jitter laser-triggered gas switch is used to couple the energy into a second, lower-impedance coaxial water line in 200 ns. Self-breaking water switches are used to transfer the energy into a 4.32Ω constant-impedance water-dielectric parallel-plate line. The electrical pulse at this point has a voltage of 2.5 MV and a pulse width of 105 ns FWHM. The total power generated in the accelerator at this point is 60 TW. The electrical energy is delivered to an insulator stack, where it passes into the vacuum portion of the accelerator. There are four levels in the interface to which the lines are connected. The electrical energy is then transmitted through four conically converging, magnetically

insulated vacuum transmission lines towards the Z-pinch load. To combine the currents from all four levels, double-post-hole convolutes are used, as shown in Fig. 8.5.

The Z-pinchs driven by the Z-Machine consist of cylindrical wire cages, typically 20 mm in diameter and 20 mm in height. Each cage is built from a few hundred 5–10 μm thick wires. The azimuthal magnetic field created by the current pulse of 20 MA conducted through the wires transforms them into a plasma and accelerates the array radially inwards. At stagnation on the central axis, its kinetic energy is converted into a strong soft X-ray radiation pulse. Up to 2 MJ of soft X-ray radiation at power levels of a few hundred terawatts have been created with the Z-Machine. It is expected that the soft-X-ray yield will scale with the square of the current, and therefore an upgrade of the machine to 27 MA is planned. Soft X-rays smoothed out in a hohlraum to a very homogeneous distribution are considered to be ideal drivers for inertial-confinement fusion (see Chap. 11).

8.1.3 HERMES III

HERMES III is a 20 MV, 16 TW generator [Ramirez et al. 1988] that produces pulses of 40 ns duration (Fig. 8.6). It is based on the techniques of voltage adding by inductive isolation described in Chap. 7. Each of the ten Marx generators is used to charge two coaxial intermediate storage capacitors, which in turn each supply four pulse-forming lines. Each of the cavities, filled with ferromagnetic (Metglas) cores, is fed by four pulse lines delivering 1 MV pulses.

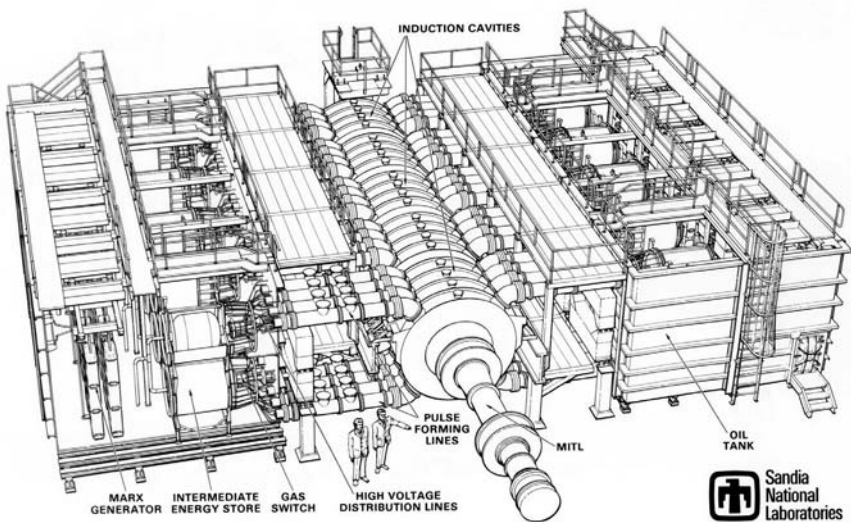


Fig. 8.6. Perspective drawing of the 20 MV pulse generator HERMES III

The cavities are connected in series to add the pulse amplitudes. The summed pulse propagates along a self-magnetically insulated vacuum line. At the end of this line, it can be applied to a load. The main purpose of this generator is to create intense X-ray pulses for simulations of the effects of weapons.

8.2 Repetitive Generators

Most industrial applications need generators that produce pulse rates of several hertz with component lifetimes of the order of 10^8 – 10^9 pulses. This requires either the elimination of spark gaps by use of non-wearing switches or a strong limitation on the switched power. In addition, storage capacitors must be used much below their rating and with little voltage reversal in those devices. Thus either magnetic or semiconductor switches are preferred for industrial applications.

8.2.1 RHEPP

In its final form RHEPP (Repetitive High Energy Pulsed Power) can operate with an average power of 350 kW at its output and produce 2.5 MV pulses of 60 ns duration with a pulse energy of 3 kJ at a repetition rate of up to 120 Hz [Harjes et al. 1991]. Only magnetic closing switches are used in this facility. Its first stages are based on magnetic pulse compression, and voltage adding occurs with the help of magnetic cavities.

The supply unit is a 600 kW, 120 Hz alternator, delivering an effective voltage of 3.2 kV and an effective current of 210 A. The pulse compression stage is represented schematically in Fig. 8.7.

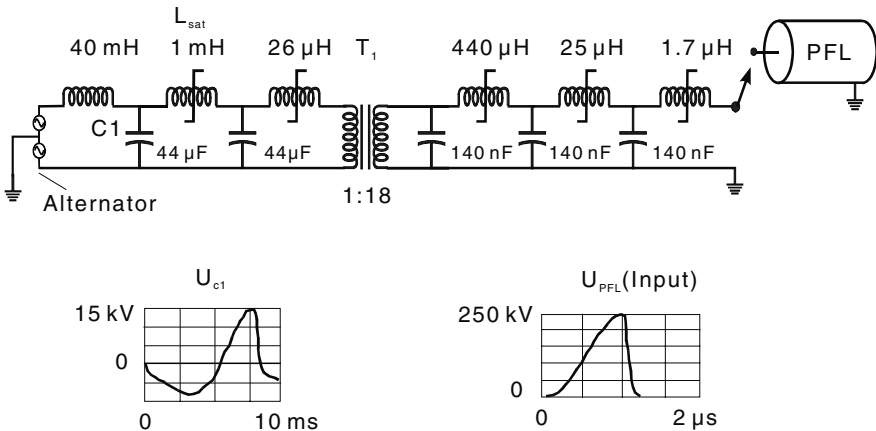


Fig. 8.7. Equivalent-circuit model of the RHEPP pulse generator

The frequency of the first LC circuit corresponds to the frequency of the generator, and the capacitor C_1 is resonantly charged to 15 kV. When the first switch has reached saturation, a 15 kV pulse is transferred to the subsequent compression stages. The transformer increases the pulse voltage to 270 kV. Finally, the fifth compression stage delivers a $[1 - \cos(\omega t)]$ pulse with a rise time of $1.2 \mu\text{s}$ and an amplitude of 250 kV to the pulse-forming network. Owing to the large mean power, the ferromagnetic cores must be cooled with water. The weight of these cores ranges from 750 kg for the first switch to 400 kg for the last. To increase the pulse voltage, the 250 kV pulses are distributed over ten inductively insulated cavities. In contrast to HERMES III, however, the pulses are added along an oil-insulated coaxial line. The facility could have been made much more compact using a self-magnetically insulated vacuum line, but at the expense of reliability, since plasma formation is difficult to avoid in stressed vacuum lines. At the end of the oil line, a 2.5 MV, 0.2 TW pulse is available.

8.2.2 Generators with Opening Switches

These generators use a relatively low voltage in most stages until the last stage, where a final voltage multiplication is achieved with the help of a semiconductor opening switch. Thus, although they are not generators that use only inductive storage, they can be made much more compact than conventional generators with closing switches. Such a generator using semiconductor switches of the SOS type is shown in Fig. 8.8 [Rukin et al. 1996]. It produces 1 MV pulses with a pulse power of 8 GW and a pulse duration of 50–60 ns at a repetition rate of 150 Hz. Its average power is 75 kW. The facility consists of a thyristor-controlled charging unit (TCU), an intermediate transformation and compression stage (IPC), and a high-voltage transformation and compression stage (HVT).

First the capacitor C_1 is charged to 900 V within 5 ms from the charging supply. After the thyristor switch is closed, the energy of C_1 is transferred through the transformer PT1 to the capacitors C_2 within about $100 \mu\text{s}$. Thus the capacitors C_2 are charged to 16 kV. The loading current of the upper capacitor C_2 reverses the magnetisation of MS1 and PT2. After saturation of PT1, the polarity of the lower capacitor C_2 is inverted. This leads to a voltage rise of 30 kV at MS1 within $25 \mu\text{s}$. Then the magnetic switch MS1 closes and the energy of C_2 is transferred to C_3 . Simultaneously, the voltage amplitude is transformed to 240 kV in $8 \mu\text{s}$ with the help of PT2. The load current of the right-hand capacitor C_3 flows through the windings of MS+ and MS-, inverting the magnetisation of their cores. After saturation of the core of transformer PT2, the voltage polarity of the left-hand capacitor C_3 is inverted, and the voltage across MS+ rises to 430 kV in $2.5 \mu\text{s}$. After the closing of the switch MS+, the SOS semiconductor switches are activated (current flow in the forward direction) and the capacitor C_4 becomes charged.

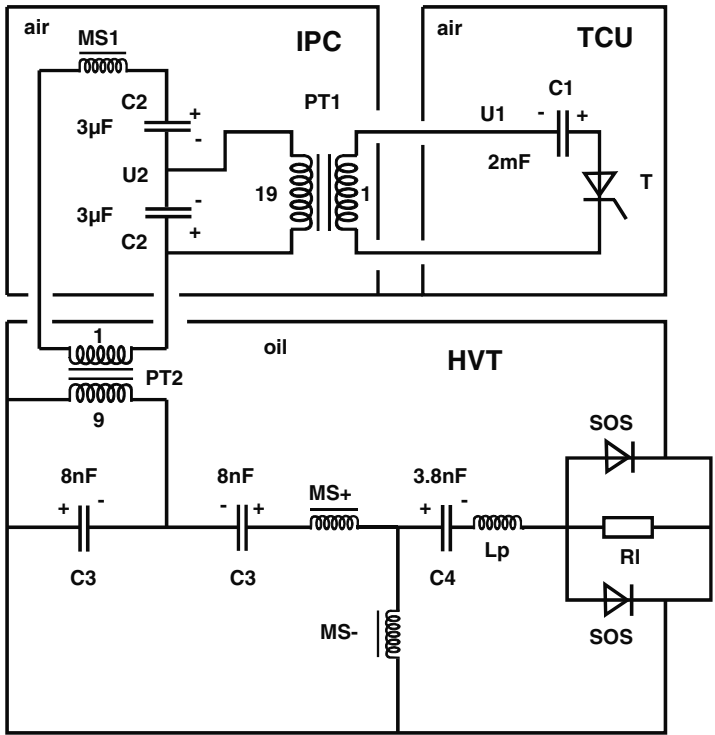


Fig. 8.8. A 1 MV generator with repetition rate capability based on semiconductor opening switches, consisting of a thyristor-controlled charging unit (TCU), an intermediate transformation and compression stage (IPC), and a high-voltage transformation and compression stage (HVT)

The amplitude of the forward current is 3 kA and the activation time 0.7 μs. When MS- saturates, the current reverses, and at the termination of the current conduction time of the SOS, a pulse voltage U is created at the load RL .

9 Diagnostics

The measurement of transient electromagnetic fields is of great importance, both for pulsed-power systems and for the testing of high-voltage equipment. The basic electrical quantities are always the electromagnetic fields \vec{E} and \vec{B} , from which pulse current and voltage must be derived.

A suitable sensor has to be constructed and positioned such that it does not perturb the fields to be measured. This property can be largely achieved with capacitive and inductive sensors. Similarly, electro-optical methods can satisfy this requirement. Conventional resistive voltage dividers, which frequently create weak points in the high-voltage insulation, are of more debatable value.

9.1 Electromagnetic-Field Sensors

Rapidly changing electromagnetic fields induce signal currents and voltages in the conductors of a sensor. Here we shall consider only electrically short sensors, whose dimensions are small compared with the distance over which the fields vary. For a pulse of rise time τ_r and propagation velocity c , this means $d \ll c\tau_r$, where d is the extension of the sensor in the direction of wave propagation. Generally, we can distinguish two basic types of sensors: the electric and the magnetic dipole (Fig. 9.1).

A rapidly changing electric field creates a displacement current density $\vec{j}_d = \partial\vec{D}/\partial t$ in addition to the conduction current density $j_c = \sigma\vec{E}$. The total current entering through an area A is given by the integral of the current density field over this area:

$$i(t) = \int_A \vec{j}_c(t) \cdot d\vec{A} + \int_A \frac{\partial\vec{D}(t)}{\partial t} \cdot d\vec{A}. \quad (9.1)$$

In the case of an ideal conducting sensor of area A placed in an insulated arrangement, (9.1) can be simplified:

$$\begin{aligned} i(t) &= \left[\vec{j}_c(t) + \dot{D}(t) \right] A, \\ i(t) &= \left[\sigma E(t) + \varepsilon\varepsilon_0 \dot{E}(t) \right] A. \end{aligned} \quad (9.2)$$

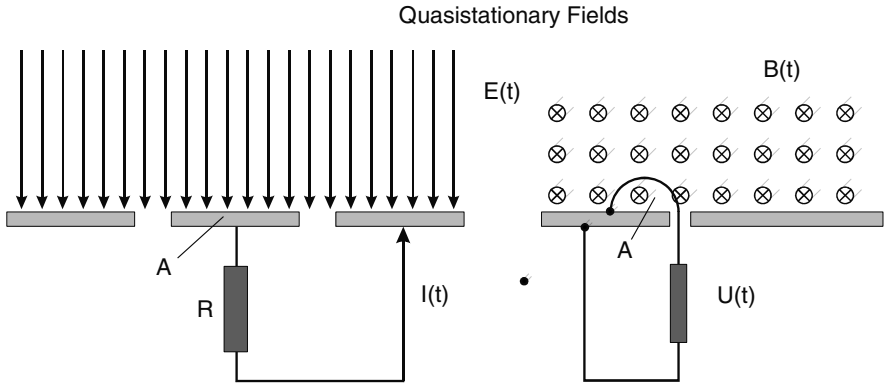


Fig. 9.1. Basic types of sensors: electric and magnetic dipoles

Thus the current flowing in the sensor circuit is determined by the electric field $E(t)$, the sensor area A , the conductivity in the field volume above the sensor σ , and the dielectric constant in this volume ϵ . The above equation describes the desired coupling of the signal to a capacitive sensor, but also the undesirable (capacitive) coupling into insufficiently shielded signal cables.

Alternating magnetic fields, which are also associated with an electromagnetic wave, induce currents in conducting loops. For a loop of area A penetrated by a magnetic field B , we obtain the following for the loop voltage:

$$u(t) = \oint \vec{B}(t) \cdot d\vec{A}. \tag{9.3}$$

If the field distribution is homogeneous, we obtain the following for the signal voltage in a loop with area A perpendicular to the field lines:

$$u(t) = \dot{B}(t)A. \tag{9.4}$$

This equation describes the desired coupling to a magnetic sensor and the undesirable coupling into parasitic loops in a measuring circuit. It is the sensor geometry that discriminates the useful signal from the interference.

9.1.1 Capacitive Sensors

For quasi-stationary fields, an electric field-sensor – also called a capacitive sensor – can be described by an equivalent circuit containing current or voltage sources and a load impedance. In most cases the load impedance of a capacitive sensor consists of a capacitance (either parasitic or a deliberate capacitance between the active sensor area and a reference area) and an ohmic load (signal cable, resistor, etc.), as shown in Fig.9.2.

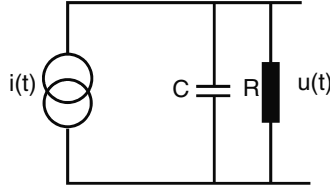


Fig. 9.2. Equivalent circuit of a loaded capacitive sensor

For most pulse-forming lines filled with dielectric, we can assume $\sigma = 0$. In this case the differential equation for the equivalent circuit and its solution are

$$\left(\frac{1}{R} + C \frac{\partial}{\partial t} \right) u(t) = i(t) = \left[\varepsilon \varepsilon_0 \dot{E}(t) \right] AR, \quad (9.5)$$

$$\dot{u}(t) + \frac{1}{RC} u(t) = \varepsilon \varepsilon_0 \frac{A}{C} \dot{E}(t),$$

$$u(t) = e^{-t/RC} \int_0^t \frac{\varepsilon \varepsilon_0 A}{C} \dot{E}(t') e^{t'/RC} dt',$$

$$u(t) = \frac{\varepsilon \varepsilon_0 A}{C} \left[E(t) - \int_0^t E(t') e^{-t-t'/RC} \frac{dt'}{RC} \right] = \frac{\varepsilon \varepsilon_0 A}{C} [E(t) - u_k(t)],$$

$$u_k(t) \leq E_m \left[e^{-t/RC} - 1 \right]; \quad (9.6)$$

$u_k(t)$ here is a correction term that becomes negligible if $RC \gg t$. E_m is the maximum electric field reached during the pulse. If we want to derive the pulse voltage from a measurement of the local electric field, we must know the relationship between $E(t)$ and $U(t)$. In a coaxial cylindrical line (outer radius r_a , inner radius r_i) for the case of a pure TEM_{00} wave, for example, we have

$$E(t) = \frac{U(t)}{r_a \ln r_a/r_i}. \quad (9.7)$$

Finally, we have

$$u(t) = \frac{\varepsilon \varepsilon_0 A}{C r_a \ln r_a/r_i} U(t). \quad (9.8)$$

The same result is obtained if we consider a capacitive sensor integrated into a transmission line as a capacitive voltage divider as shown in Fig. 9.3:

$$u(t) = \frac{C_H}{C_H + C_E} U(t). \quad (9.9)$$

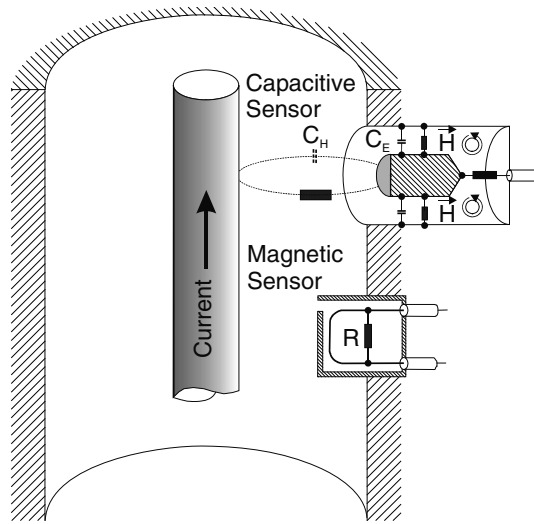


Fig. 9.3. Scheme of capacitive and magnetic sensors integrated into a coaxial line

Here C_H (given by (9.10) for cylindrical geometry) is the capacitance between the active sensor area and the opposite (high-voltage) electrode, and C_E is the capacitance between the sensor and ground:

$$C_H = \frac{\epsilon\epsilon_0 A}{r_a \ln r_a/r_i} . \tag{9.10}$$

In addition, $C_H \ll C_E$ has been assumed.

9.1.2 Inductive Sensors

In a B -field, or inductive, sensor loop, a voltage is induced according to Faraday’s law:

$$u(t) = \int \vec{B}(t) \cdot d\vec{A} = \frac{d\phi}{dt} . \tag{9.11}$$

To obtain the B -field, an integrating network is combined with the current loop. The equivalent circuit is shown in Fig. 9.4. Here a simple RC integrator has been applied.

In Fig. 9.4, L is the inductance of the loop, and R and C are the resistance and capacitance, respectively, of the integrator. The signal is given by

$$u(t) = \frac{d\phi}{dt} = L \frac{di}{dt} + Ri + \frac{1}{C} \int_0^t i dt' . \tag{9.12}$$

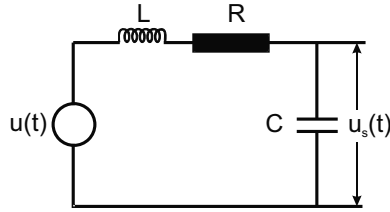


Fig. 9.4. Equivalent circuit of inductive sensor with RC integrator

For $R \gg L\omega$, where ω is the largest significant frequency in the Fourier spectrum of the pulse that is being measured, we obtain

$$u(t) = \frac{d\phi}{dt} = Ri + \frac{1}{C} \int_0^t i dt'. \quad (9.13)$$

Restricting the measurements to times $t \ll RC$, we finally have the following for the measured signal $u_s(t)$:

$$u(t) = Ri(t),$$

$$u_s(t) = \frac{1}{C} \int_0^t i dt = \frac{1}{RC} \int_0^t \frac{d\Phi}{dt} dt = \frac{1}{RC} \Phi(t) = \frac{1}{RC} B(t)A. \quad (9.14)$$

As in the case of an E -field measurement, the B -field can be related to the pulse current if the geometry of the system is known and if only a TEM_{00} wave is present. In this case we may write

$$\phi(t) = KNI(t), \quad (9.15)$$

where N is the number of windings of the inductive loop, sometimes called a ‘ B -dot loop’. In general, we can calculate the constant K with sufficient accuracy only if the current distribution and the corresponding direction of the magnetic field at the position of the loop are known. Consequently, a simple current loop must always be calibrated in situ.

If the current density distribution in the pulse line is not known and if an in situ calibration is not feasible, one must use a Rogowski coil instead of a simple current loop. A Rogowski coil [Rogowski and Steinhaus 1912] is a coil consisting of many windings lined up in a toroidal configuration encircling the current path, as shown in Fig. 9.5. Applying Ampère’s law, we have the following relationship between the current flowing through the Rogowski coil and the magnetic induction along the axis of the torus:

$$I(t) = \frac{1}{\mu_0} \oint \vec{B}(t) \cdot d\vec{s} = \frac{1}{\mu_0} \sum_{i=1}^N B_i(t) s_i \cos(\vec{n}_i, \vec{B}_i), \quad (9.16)$$

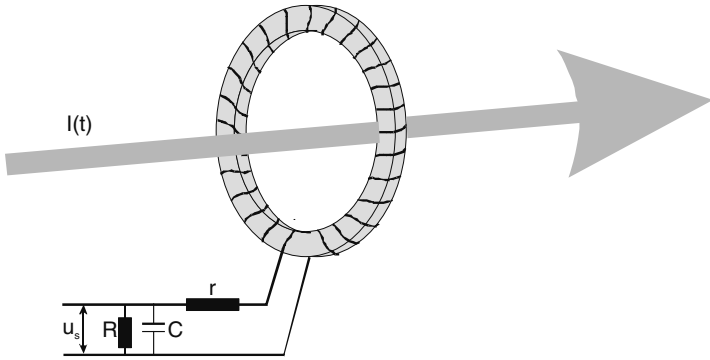


Fig. 9.5. Schematic representation of a Rogowski coil

where s_i is the mean distance between two windings and $\cos(\vec{n}_i, \vec{B}_i)$ is the cosine of the angle between the normal to the area of winding i and the field at this position.

On the other hand, neglecting the spatial dependence of the magnetic induction over the area A_i of a single winding of the toroidal coil, we obtain the following for the voltage induced at the terminals of the Rogowski coil:

$$u(t) = \int \vec{B}(t) \cdot d\vec{A} = \sum_{i=1}^N \dot{B}_i(t) A_i \cos(\vec{n}_i, \vec{B}_i). \quad (9.17)$$

Assuming (1) that the cross-section of the coil is everywhere the same, i.e., $A_i = A$, and (2) that the number of turns per unit length is constant, i.e., $s_i = s$, we can derive a unique relationship between the induced signal voltage $u(t)$ and the current $I(t)$ penetrating the Rogowski coil, irrespective of its distribution:

$$u(t) = \frac{A}{s} \mu_0 \dot{I}(t). \quad (9.18)$$

As with a simple loop, we can use an integrating RC network to obtain the current (Fig. 9.4). In this case also we must realise the condition $L\omega \ll R$, which, because of the larger L , is more difficult to achieve for high frequencies. Therefore, in general, one tries to satisfy the opposite condition with Rogowski coils. If the sum of the internal resistance r and the external resistance R is small compared with $L\omega$, and if $R \ll 1/\omega C$, we obtain the following from (9.12) for the sensor circuit:

$$\frac{d\phi}{dt} \approx L \frac{di}{dt}, \quad (9.19)$$

$$i = \frac{\phi}{L} = \frac{\mu_0 N A I / s}{\mu_0 N^2 A / s} = \frac{I}{N}, \quad (9.20)$$

$$u_s(t) = iR = \frac{R}{N} I. \quad (9.21)$$

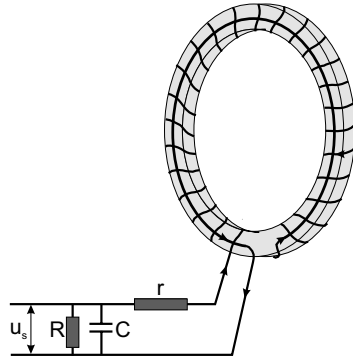


Fig. 9.6. Compensated Rogowski coil to eliminate the portion of the signal created by the flux penetrating the main opening of the coil

Thus, within the limitations stated, the output signal of the Rogowski coil is proportional to the main current I , i.e., the Rogowski coil can be considered as a transformer. Evidently, the lowest measurable frequency is determined by the condition $r + R \ll L\omega$. The upper frequency boundary is established by the LC resonance frequency of the Rogowski coil. The wavelength of the lower frequency boundary corresponds to the length of the wire of the coil. An extension to lower frequency can be achieved by placing a ferromagnetic material in the torus. Naturally, the upper frequency boundary will be affected by this arrangement. Although a high-permeability core will decrease the lowest measurable frequency, there is always the risk of saturation for a coil with such a core.

In many applications, it becomes necessary to eliminate the spurious signal due to capacitive coupling by surrounding the Rogowski coil with a slotted metallic case.

Another problem can result from a large flux penetrating the main opening of the torus. It is possible to compensate for this signal by feeding one end of the wire back through the windings, as shown in Fig. 9.6. Alternatively, the Rogowski coil can be built into a metallic housing which short-circuits the main opening. Naturally, the housing must be slotted at the inner side to allow the flux to penetrate. However, at the large electrical stresses associated with high-power fast-rising pulses, flashover can occur at the shielding groove or along the surface of the sensor itself, resulting in false signals.

Also, the lumped-circuit description of the Rogowski coil must be replaced by a transmission line model if the rise time of the current pulse is shorter than the transit time in the sensor [Küchler and Schwab 1987]. In this case the voltages induced in different locations along the torus reach the metering resistor with different delays distorting the pulse shape. Although it is still possible to reproduce the rise time of a step pulse if the Rogowski coil is terminated with an impedance $Z \gg Z_0$, where $Z_0 = \{L/C\}^{1/2}$ is the impedance of the Ro-

gowski coil, it is no longer possible to measure current pulses with durations $t < T$, where T is the wave transit time along the coil. However, the most severe limitation of the self-integrating Rogowski coil is non-uniform excitation in the windings of the coil. This can lead to strong oscillations in the sensor signal. Therefore it is not completely true that the signal response of a Rogowski coil is independent of the current density distribution inside the torus.

9.2 Current-Viewing Resistors (CVRs)

The problems associated with flux-coupled sensors when used with high-power fast-rising pulses can be avoided with current-viewing resistors, also called shunts. The use of a shunt is based on measurement of the voltage drop across a resistor of known value, incorporated into the circuit. In general, the current path and the measuring circuit are coupled not only through the ohmic resistor but also magnetically. In this case the measured voltage signal cannot be proportional to the current. Therefore it is preferable to place the metering contact in a field-free space or to make the coupling coefficient negligible. A cylindrically symmetric shunt geometry providing zero magnetic coupling at the metering contacts is shown in Fig. 9.7 [Schwab 1981].

Diffusion of the magnetic field through the material is the most important limitation on the frequency response of a CVR. The general solution for magnetic diffusion into a hollow cylinder is very clumsy (see, e.g., [Knoepfel 1970]). However, assuming that the thickness d of the cylinder is small compared with its outer radius r_a , the signal response to a current step function of magnitude I_0 can be approximated by [Malewski 1968]

$$\frac{U(t)}{U^*} = 2\sqrt{\frac{t^*}{\pi t}} \exp\left(-\frac{t^*}{4t}\right). \quad (9.22)$$

Here $U(t)$ is the voltage drop measured between the metering contacts, and U^* is the maximum voltage drop

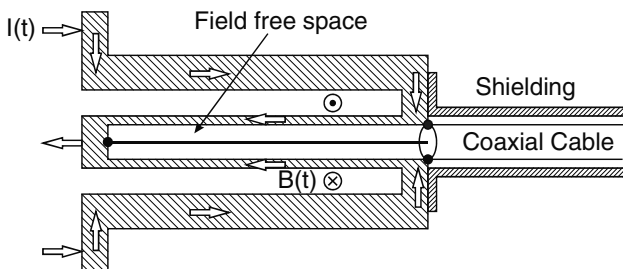


Fig. 9.7. Cylindrically symmetric shunt providing a field-free space at the position of the metering contacts

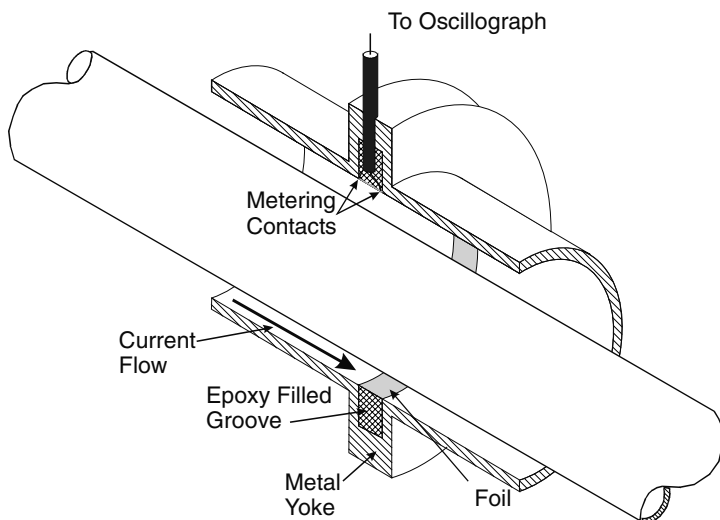


Fig. 9.8. Cross-section of a CVR integrated into the outer conductor of a coaxial transmission line

$$U^* = \frac{I_0 \rho \ell}{2\pi r_a d}, \quad (9.23)$$

where ℓ is the distance between the contact points and ρ is the material resistivity. t^* is a characteristic time for the diffusion process, given by

$$t^* = \frac{\mu \mu_0 d^2}{\rho}; \quad (9.24)$$

t^* is related to the 10–90% rise time τ of the signal by $\tau = 0.25t^*$.

For current measurements in a coaxial transmission line, the shunt geometry shown in Fig. 9.8 has been adopted. This type of current monitor is especially useful in vacuum transmission lines, where charged-particle emission with plasma formation is common and where a Rogowski coil positioned in a slotted groove can lead to erroneous signals. The shunt consists of a deep groove cut into the wall of the outer conductor of the line which is filled with a dielectric (epoxy) and covered with a thin metallic foil that is welded to the inner surface of the outer conductor. Two metering contacts are tightly fixed to the back surface of the foil to measure the voltage drop between them.

The shunt geometry shown in Fig. 9.8 can be considered as a parallel connection of a resistor R_f (the foil) and an inductance L_g , whose magnitude is determined by the depth of the groove. A signal proportional to the current $I(t)$ is obtained only for times short compared with $\tau_d = L_g/R_f$ and long compared with $\tau = 0.25t^*$. τ_d can easily reach a few microseconds since foil resistances are typically about $10^{-3} \Omega$, and inductances of greater than 10^{-9} H result from grooves with reasonable depth. A further source of

error can result from the time-varying flux coupled to the area subtended between the metering connections and the foil. Therefore the CVR must be constructed to minimise this area. Joule heating can change the resistance of the foil and thus lead to another source of error.

9.3 Current Measurements Based on the Faraday Effect

The Faraday effect consists of a rotation of the plane of polarisation of light propagating in a medium in the presence of a magnetic field parallel to the direction of propagation. Right and left circularly polarised waves with different refractive indices are created by the magnetic field. Thus the plane of polarisation rotates by an angle that is proportional to the line integral of the magnetic field H along the length of the light path ℓ . Naturally, this can lead to results that depend on the current distribution relative to the position of the light path. The dilemma is similar to that with a magnetic probe. Hence it can also be eliminated in the same way, using a scheme equivalent to that of a Rogowski coil, i.e., letting the optical path in the medium encircle the current makes the rotation angle independent of the current distribution. For a closed light path, we can write

$$\theta = V \oint \vec{H} \cdot d\vec{\ell} . \quad (9.25)$$

Using Ampère's law, we can replace the loop integral by I , where I is the total current enclosed by the path of integration. V is a factor of proportionality known as the Verdet constant. For any particular medium, the Verdet constant depends on the wavelength and on the temperature. For fused quartz glass (silica) at 633 nm, this constant is 4.1 rad/MA. Thus the rotation angle can be expressed by

$$\theta = VI . \quad (9.26)$$

The simplest way to construct a current probe based on the Faraday effect is with the help of an optical fibre. Since the state of polarisation must be preserved, only single-mode, polarisation-maintaining fibre can be used. To increase the sensitivity of the probe, the fibre can encircle the current several times. The most suitable light source for this scheme is a plane-polarised laser beam.

A major problem results from birefringence effects in the fibre, especially when they occur during the current pulse, for example if the fibre is shocked in its sensing region. Linear birefringence is also produced if the fiber is bent. The effect is proportional to $(r/R)^2$, where r is the fibre radius and R the radius of curvature. Twisting the fibre in the sensing region in the direction of the Faraday rotation has been used by some experimentalists to greatly reduce the effects of linear birefringence [Stokes et al. 1995].

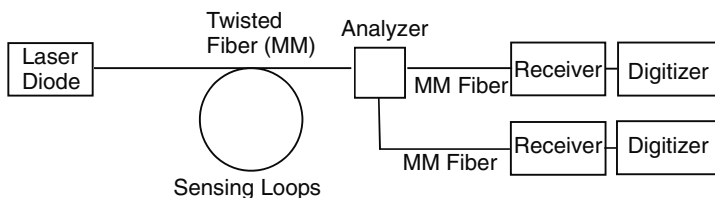


Fig. 9.9. Schematic of a Faraday rotation diagnostic system

A schematic illustration of a typical Faraday rotation diagnostic system is shown in Fig. 9.9. In this system an 830 nm laser diode with 12 mW power is used. The laser diode is coupled to a single-mode, polarisation-maintaining fibre. The fibre is twisted in the sensing region, with about 40 turns/m in the direction of the Faraday rotation. This measure greatly reduces the effects of linear birefringence in the bent fibre. The analyser consists of a lens, a half-wave plate, a non-polarising beam splitter, glass polarisers on both output legs, and output lenses. The polarisers are set orthogonal to each other to give quadrature signals in the two outputs. A plastic tube surrounds the fibre to protect it against squeezing and shocks.

Two different methods can be used to evaluate the signals from the two legs depending upon whether the value of θ at peak current is much greater or very much less than π . If θ_{\max} is small, we take the sum and the difference of the signals from the two legs:

$$\begin{aligned} S_1 &= S_0 \cos^2\left(\theta - \frac{\pi}{4}\right), \\ S_2 &= S_0 \cos^2\left(\theta + \frac{\pi}{4}\right), \\ s &= \frac{S_1 - S_2}{S_1 + S_2} = \sin(2\theta), \end{aligned} \quad (9.27)$$

or, for $\theta \ll \pi$, using (9.26),

$$s = kI, \quad (9.28)$$

where k is a proportionality constant. Of course, the accuracy of this computation depends on the signal-to-noise ratio of the system and the maximum value of θ .

If θ_{\max} is large compared with π , it suffices to evaluate one signal. If the analyser is set perpendicular to the initial direction of polarisation, the signal becomes

$$S(t) = S_0 \sin^2(\theta(t)) = \frac{S_0[1 - \cos(2\theta(t))]}{2} = \frac{S_0[1 - \cos(2VI(t))]}{2}. \quad (9.29)$$

To obtain $I(t)$, this signal must be inverted numerically.

The main advantage of a Faraday current monitor is that it is relatively immune against electronic noise.

9.4 Electric-Field Measurements Based on Electro-Optic Effects

Electric-field measurements can be based on electric-field-induced birefringence in crystals or liquids or on changes in the refractive indices of crystals where birefringence already exists at zero electric field. The phase shift between the ordinary and the extraordinary beam propagating in the field probe is given by

$$\theta = \frac{2\pi\ell}{\lambda} (n_o(E) - n_{eo}(E)) . \quad (9.30)$$

Here, a homogeneous field distribution has been assumed along a probe of length ℓ . As discussed in Sect. 9.3, this phase shift leads to a rotation of the polarisation and therefore the same signal analysis as in Sect. 9.3 can be used [Duvillaret et al. 2002, Santos et al. 2000].

$\Delta n = n_o - n_{eo}$ can depend either linearly or quadratically on the electric field. The first case is known as the Pockels effect, while the second case is called the Kerr effect, and is often referred to as the quadratic electro-optic effect.

The Pockels effect occurs only in certain crystals which lack a centre of symmetry. Of these, ADP (ammonium dihydrogen phosphate) and KD*P (potassium dideuterium phosphate) are the most commonly used. A Pockels cell sensor generally consists of an appropriate single crystal, whose optic axis is parallel to the probe beam and the electric-field direction (Fig. 9.10). A polarised laser beam passes through the crystal and exits through an analyzer, whose transmission axis is parallel to the polarisation vector of the light wave at zero electric field. A useful quantity is the half-wave voltage $V_{\lambda/2} = E_{\lambda/2}\ell$,

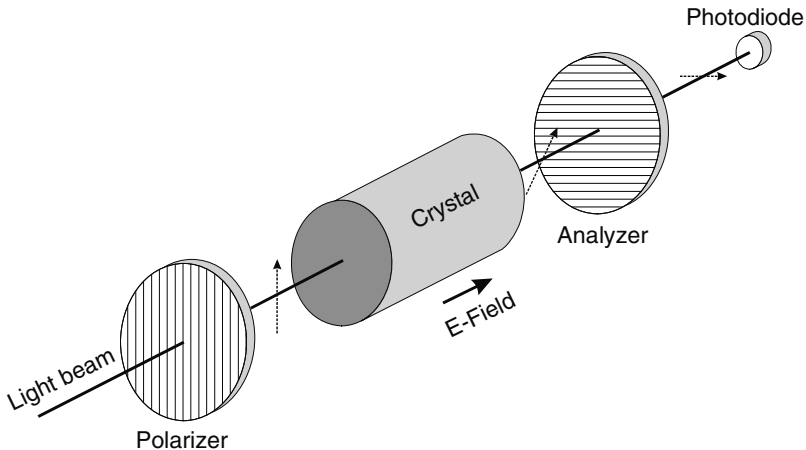


Fig. 9.10. Electro-optic sensor for electric-field measurement

corresponding to a phase shift of π ; ℓ is the length of the crystal. With this definition, the phase shift can be written as

$$\theta = \pi \frac{E\ell}{V_{\lambda/2}}. \quad (9.31)$$

Typical values for $V_{\lambda/2}$ at $\lambda = 546.1$ nm are 9.2 kV for ADP and 3.4 kV for KD*P.

The response time of the crystals is quite short, allowing measurements with nanosecond resolution.

While the Pockels effect occurs only in solid crystals, the Kerr effect can occur in both liquids and crystals. The phenomenon in liquids results from a partial alignment of anisotropic molecules by the electric field. Thus it is possible to install the sensor in a high-voltage system using a liquid as a dielectric insulating medium without introducing much distortion of the electric-field distribution. This is especially useful in pulsed-power systems using water as the dielectric. A disadvantage, however is, that the Kerr effect depends quadratically on the electric field. The phase shift thus becomes

$$\theta = 2\pi K\ell E^2, \quad (9.32)$$

where K is the Kerr constant, which, for water, is 5.1×10^{-14} m/V² at $\lambda = 589$ nm. Because of the quadratic dependence of θ on E it is especially advantageous in the case of small signals to exploit the difference signal as described in Sect. 9.3 and explicitly presented in (9.27). Using such a scheme for signal processing, the signal is proportional to E^2 .

9.5 Magnetic Ion Energy Analysers

Voltage measurements in vacuum can also be obtained from a determination of the energy of charged particles that have been fallen through the potential drop. The principal features of a magnetic energy analyser are shown in Fig. 9.11. The analyser consists of a collimator, a circular permanent magnet, and a set of particle detectors. The charged particles enter the magnet region as a well-collimated beam and are deflected in the magnetic field. After leaving the magnet, they propagate ballistically towards the detector array. The energy resolution of the instrument is determined by the degree of collimation, the size of the magnet and its strength, the geometrical position of the detectors with respect to the magnet, and their sensitive area. A suitable detector array that can be used in such an instrument may consist of an array of small-area pin diodes, each detector matching a small energy interval. For a single particle species, the deflection angle β is related to the kinetic energy W_k of the particles and therefore to the accelerating voltage by the following equation:

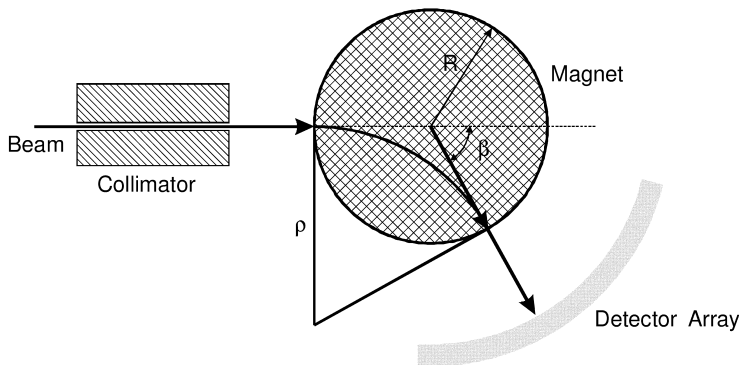


Fig. 9.11. Set-up of a magnetic energy analyser for pulsed-voltage measurements

$$\beta = 2 \operatorname{arctg} \frac{R}{\rho} = 2 \operatorname{arctg} \frac{ZeRB}{\sqrt{2mW_k}}. \quad (9.33)$$

Here ρ is the radius of curvature of the particles, with charge Ze and mass m , in a magnetic field of strength B . R is the radius of the circular magnet.

Time-resolved measurements of the voltage pulse shape are possible with this set-up if enough particles enter the detector.

9.6 Vacuum Voltage Monitors

Another instrument suitable for local pulsed-high-voltage measurements in a vacuum environment is a special resistive voltage divider. Since at very high voltage amplitudes free electrons will always be present in the system, the monitor design must make sure that the formation of electron avalanches does not occur on its surface. A cross-section of such a monitor is shown in Fig. 9.12. This was constructed for measurements of pulse voltages of up to 2.5 MV with a rise time of less than 2.5 ns. Its overall length is 54 cm, and the outer diameter is 15 cm. It is a two-stage divider. The primary stage consists of a column filled with a solution of sodium thiosulphate, leading to a resistance of 200 Ω . A division ratio of 88 : 1 is obtained by placing an aluminium tap ring a few millimetres above the ground plate. To achieve an overall divider ratio of 8800 : 1 the secondary divider has a resistance of 5000 Ω .

When this monitor is connected to the 50 Ω input of an oscilloscope, an additional 100 : 1 division ratio is obtained. The insulator/gradient-ring stack is held in place on the base plate by a compressive load applied by a preloaded nylon drawbar. The stack is designed to eliminate flashovers initiated by electron avalanches. It consists of truncated cones of acrylic insulator separated by aluminium field-grading rings. In addition to this set-up, a metallic conical shield might be used to absorb electrons emitted from the walls of the apparatus.

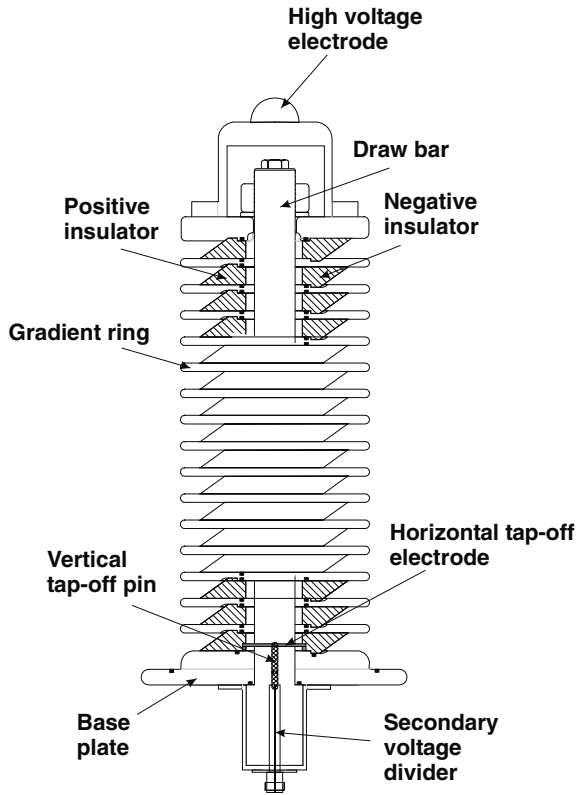


Fig. 9.12. Schematic illustration of a resistive divider for operation at megavolt voltage levels in a vacuum environment. It consists of a primary and a secondary divider. The primary divider is built from an electrolytic column surrounding the drawbar. The secondary divider consists of a solid resistive network. Two different set-ups, for operation with negative (*right*) and positive (*left*) polarity, are shown

10 Applications of Pulsed Electromagnetic Fields

In this chapter we shall present applications where pulsed electric or magnetic fields are the central tools. Of course, in general, all pulsed-power applications are driven or accompanied by electromagnetic fields, but in many applications these fields are just the instrument to transform electrical energy into other forms of energy such as particle energy or radiation.

10.1 Pulsed Electric Fields

Strong electric fields have been used in atomic physics to study the Stark effect under very extreme conditions; in chemical-structure analysis to induce the alignment of dipolar interactions of molecules, which can provide information in the context of the determination of molecular structures and in solid-state physics, where phase transitions have been induced that change, for example, the resistivity of a material. However, these applications are often individual special cases. We shall restrict the discussion, therefore, to the effects of pulsed electric fields on biological systems, an area that has recently regained much interest and where attractive large-scale industrial applications seem possible.

10.1.1 Introduction

Electric fields play an important role in biological systems, where they control transport processes across membranes and the transfer of information along neurons. Biological cells are closed systems, whose internal structures (cell nucleus, organelles, and cytoplasm) are partitioned from the exterior by a dielectric membrane [Campbell 2000]. However, this membrane is a leaky dielectric, with protein channels and pores that can be activated to enable the metabolism of the cell. The basic structure of this membrane is a 5 nm thick insulating phospholipid double layer of rather high breakdown strength. Electrical breakdown, i.e., irreversible destruction, occurs if the membrane potential exceeds 1 V, corresponding to a field strength of 2×10^6 V/cm. When the voltage across the membrane exceeds the natural gating voltage of about 0.2 V, its permeability increases. In contrast to the cell membrane, the cytoplasm is an electrolytic conductor. If an electric field is applied to a cell

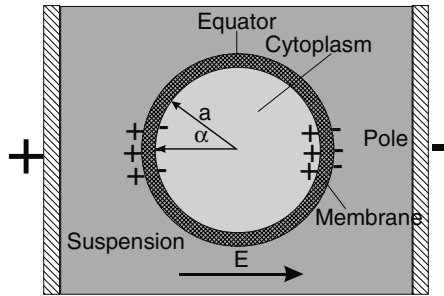


Fig. 10.1. Spherical cell in an external electrical field E

surrounded by an electrolytic suspension, ions move to the membrane and it becomes polarised. Because of this polarisation, the cell interior becomes screened after a short transition period, and the potential initially occurring across the entire cell now appears across the cell membrane. Thus the electric field at the membrane becomes enhanced compared with the external applied field by a factor given by the ratio of the extension of the cell in the direction of the field (a few micrometres) to the membrane thickness (5 nm). The situation for a spherical cell is depicted in Fig. 10.1. The field enhancement factor ε_ν can attain quite large values (100–1000) and makes it possible for membrane breakdown to be obtained with external fields below the dynamic breakdown strength of water, which generally is the main component of the suspension.

Obviously, the field enhancement depends on the shape of the cell. For the spherical cell shown in Fig. 10.1, it depends on the azimuth too:

$$\varepsilon_\nu = \frac{E_{\text{mem}}}{E_{\text{ext}}} = \frac{1.5 a \cos(\alpha)}{h}. \tag{10.1}$$

Here a is the cell radius, α is the azimuthal angle, and h is the membrane thickness.

The relaxation time for complete polarisation depends on the cell dimensions, the specific membrane capacitance, and the conductivities of the cytoplasm and the suspension:

$$\begin{aligned} \Delta U_{\text{membrane}} &= 1.5 a E_{\text{ext}} \cos(\alpha) \left[1 - e^{-t/\tau} \right], \\ \tau &= aC \left[\rho_i + \frac{\rho_e}{2} \left\{ \frac{1 + 2f}{1 - f} \right\} \right]. \end{aligned} \tag{10.2}$$

In (10.2), $\Delta U_{\text{membrane}}$ is the potential drop across the membrane, τ is the relaxation time constant, C the capacitance per unit area, ρ_i is the resistivity of the cytoplasm, ρ_e is the resistivity of the suspension, and f is the volume fraction of the suspension occupied by cells. For bacterial cells in municipal water with a conductivity of 0.1 S/m, the time for polarisation lies between 80 and 500 ns for small (*Listeria monocytogenes*) and large (*Saccharomyces cerevisiae*) cells, respectively. To describe the process for arbitrary pulse shapes,

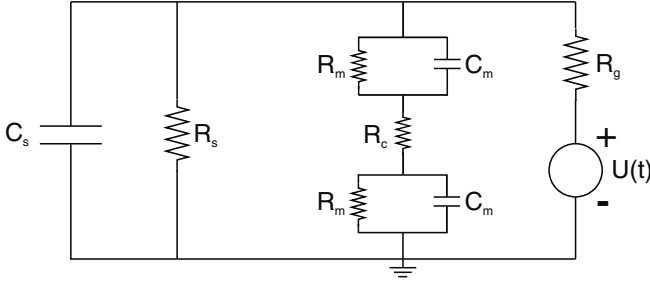


Fig. 10.2. Equivalent circuit of a biological cell. R_m = membrane resistance, C_m = membrane capacitance, R_s = resistance of suspension, C_s = stray capacitance bypassing the cell, R_g = generator impedance, $U(t)$ = time-dependent voltage pulse

the equivalent circuit presented in Fig. 10.2 is useful. If the potential drop $\Delta U_{\text{membrane}}$ across the membrane exceeds a critical value of about 0.5 V, openings created by thermal fluctuations begin to grow. Although the exact mechanism of pore formation is still not completely understood, many researchers in that field accept that it is a two-stage process [Weaver 1994, Weaver and Chizmadzhev 1996, Neu and Krassowska 1999, Teissie and Rols 1994]. At first, pores appear in a ‘hydrophobic’ form at a rate that depends on the temperature and on the local electric field. When the pore radius exceeds a certain value, they turn into a ‘hydrophilic’ form suitable for the exchange of water-soluble substances between the cell and its surroundings. The driving force for the increase of the pore radius is the free energy of pore formation. This has different forms for hydrophobic and hydrophilic pores and consists of a sum of various energy terms. For the hydrophobic form, it is given by (10.3),

$$F(r, t) = 2\pi hr\zeta(\infty) \frac{I_1(r/r_0)}{I_0(r/r_0)} - \pi a_p U^2 r^2, \quad (10.3)$$

and for the hydrophilic form it is given by (10.4),

$$F(r, t) = 2\pi\xi r - \pi\zeta r^2 + \frac{c}{r^4} - \pi a_p U^2 r^2. \quad (10.4)$$

In these equations, I_0 and I_1 are the modified Bessel functions of zero and first order, with r_0 representing a scale length of the Helmholtz layers in which the transition from the boundary to the bulk properties of water occurs (see Sect. 2.3.1); it is typically of the order of 1 nm. $\zeta(\infty)$ is a surface energy, equal to 0.05 J/m^2 ; $U(t)$ is the time-dependent membrane potential, to be calculated with the help of the equivalent circuit presented in Fig. 10.2; c is a constant; $a_p = (\varepsilon_W - \varepsilon_M)/(2h)$, where h is the membrane thickness and r the pore radius; ε_W and ε_M are the permittivities of water and of the membrane, respectively; and ξ is the energy per unit length of the pore perimeter. The last terms in (10.3) and (10.4) stand for the capacitive energy

with and without the membrane as a dielectric. This energy is responsible for the quadratic dependence of the free energy on the electric field. The first term in (10.4) describes the rim stress in the pore, the second term is the surface energy, and the third term represents the steric repulsion between the polar lipid heads in the pore. A table with numerical values for all constants in (10.3) and (10.4) can be found in [Joshi and Schoenbach 2000].

The shape of F as a function of the pore radius has been plotted in Fig. 10.3 for potentials of 0 V and 0.2 V. Under the action of an external field, the potential hump is strongly reduced. At an even higher potential, it disappears and the pore starts to grow. If the pore radius exceeds the value corresponding to the maximum in the zero-volt potential well during the pulse duration the pore becomes irreversible, the cytoplasm flows out, and the cell dies. If this critical radius is not reached during the pulse, the pore can heal and the effect is reversible. The temporal evolution of the

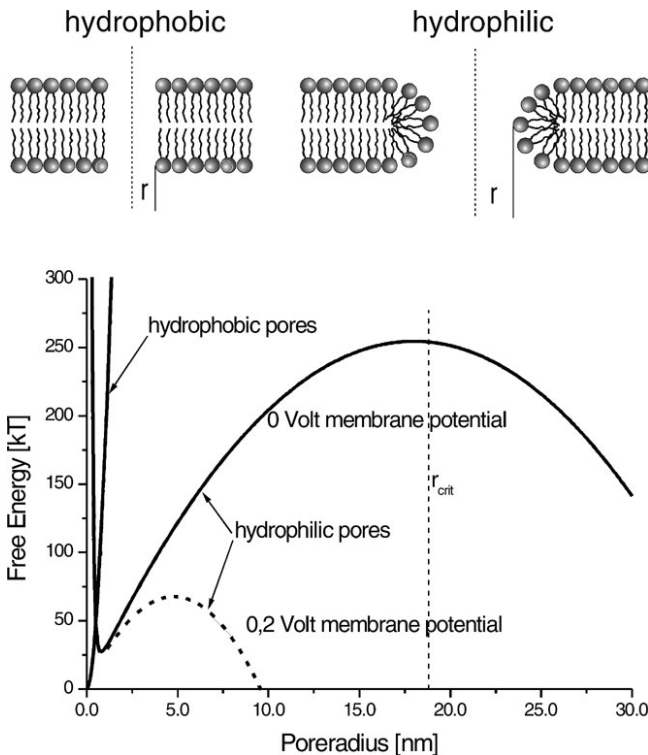


Fig. 10.3. Free energy F of pore formation as a function of pore radius for hydrophobic and hydrophilic pores. For hydrophilic pores, F is shown for two membrane potentials (0 and 0.2 V). During the pulse, the pore radius must grow above r_{crit} if a permanent irreversible opening is to be obtained. Otherwise, the pore is reversible, i.e., the cell can heal it after disappearance of the membrane potential

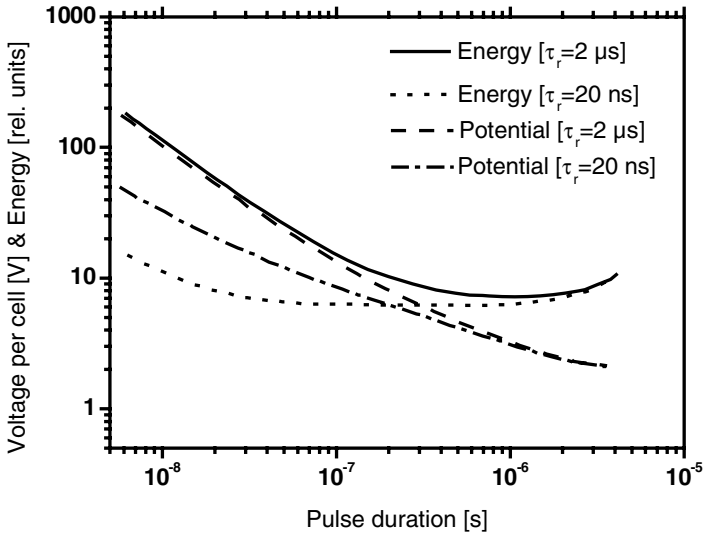


Fig. 10.4. Pulse voltage and energy for irreversible breakdown as a function of the minimum pulse width for two different internal time constants $R_c C_m$

distribution of pore radii in an ensemble of pores can be described by a diffusion-type equation, first used by Smoluchowsky and Einstein for the treatment of Brownian molecular motion [Joshi and Schoenbach 2000]. It is obvious from the model described above that the amplitude of the pulse, its shape, and its duration above a certain threshold have a crucial influence on pore formation.

If a permanent opening in the cell is to be obtained, it is necessary that the duration of the electrical pulse is larger than the sum of the time constants for the creation of membrane polarisation and for the attainment of the critical pore radius. If only organelles, structures, or molecules in the cell interior are to be affected, without destroying the membrane, the pulse length must be short compared with the time period required to reach complete polarisation, i.e., typically less than 100 ns.

Joshi and Schoenbach [Joshi and Schoenbach 2000] have numerically solved the diffusion equation and determined the pore density distribution function for various internal-circuit time constants $R_c C_m$ (see Fig. 10.2), and calculated from this distribution the voltage and energy as a function of the minimum pulse width for irreversible breakdown. Their result is reproduced in Fig. 10.4.

Reversible electroporation has been used in fundamental biological research for many years for the delivery of genetic material, drugs, and molecules into the cell interior. Irreversible electroporation, which can be used for the extraction of plasma material from biological cells or for the killing of micro-organisms, has also been described in the literature since the

late 1960s. However, industrial applications are still rare and are restricted to a very few special areas. The main reason for this is the lack of suitable high-voltage pulse generators able to produce the necessary electric fields of up to 10 MV/m reliably and repetitively in large volumes.

Compared with the common cell extraction and sterilization methods, electroporation has a large potential for energy saving for the avoidance of critical chemical substances, and for the production of purer food products.

10.1.2 Pulse Generation

Pulse generators suitable for industrial applications must provide electric fields of 0.1–10 MV/m for pulse durations of 10 ns–10 μ s in large volumes determined by the required throughput. In addition, each cell needs to be exposed to a certain number of pulses to induce the desired effect. Given a certain product flow rate and the length of the field zone this determines the required repetition rate of the pulse generator. For economic reasons many applications need large throughputs ($> 100 \text{ m}^3/\text{h}$) and therefore large electrode areas ($> 1000 \text{ cm}^2$) and large interelectrode gaps. Typically, the electrolytic conductivity of a cell suspension is around 0.1 S/m. For an electric field strength of 1 MV/m, the generator must therefore supply a pulse current of greater than 10 kA. This means that only low-impedance generators are appropriate. Depending on the interelectrode distance, pulse amplitudes of up to 1 MV may be required. Therefore the suitable pulse generators are Marx generators, *LC*-chain and transmission line generators, and combinations of these types (see Sect. 3.2 and Chap. 5).

10.1.3 Treatment of Plant Cells

To extract foodstuffs such as sugar, starch, and oil from plant cells, the outer membrane and, in many cases, also the membranes of organelles which serve as storage compartments in the cell interior must be opened. This can be achieved thermally, mechanically, chemically, or enzymatically or just by electroporation. Plant cells that have larger dimensions than bacterial cells require much lower fields to open their membranes. Here we shall discuss the advantages of electroporation compared with conventional methods for the example of the extraction of sugar from sugar beet, probably the first large-scale application of irreversible electroporation [Schultheiss et al. 2002, Bluhm et al. 2004].

The standard procedure for the production of sugar from beet consists of carving the fruits into cossettes and subsequently extracting the juice from these cossettes at elevated temperatures with as little water as possible [Schweck and Clarke 2001]. The sugar dissolved in the cell juice can leave the beet cossettes only if the cell and vacuole membranes have been destroyed. In modern sugar plants, this is achieved by thermal denaturation at temperatures above 70°C. The transport of sugar and other water-soluble substances from

the inside of the cossettes to the extraction water occurs by diffusion. Since the diffusion coefficient is temperature-dependent, the extraction temperature should be as high as possible. However, at excessively high temperatures considerable amounts of structural substances from the cell walls are also denatured and become water-soluble. Thus impure raw juices are obtained, which need extensive processing. Therefore a temperature programme is applied which represents a compromise: denaturation is achieved by heating the cossettes to 70–78°C for a short time, and extraction is carried out at 69–73°C.

The temperature programme also influences the survival of micro-organisms introduced into the process by soil on the beets. Metabolism by these bacteria can lead to sugar losses. Some organisms are not inhibited at all at the temperatures used, and therefore disinfectants (e.g., hydrogen peroxide and formalin) are generally introduced into the extraction system.

Appreciable energy savings and less expensive purification procedures are conceivable if the juice extraction could be carried out at a much reduced temperature. The use of pulsed electric fields as a non-thermal method for the breakage of cell membranes in vegetables was first described by Doevenspeck in 1962 [Doevenspeck 1962]. Later, this method was also linked to the non-thermal killing of micro-organisms. Recently, Bouzrara and Vorobiev [Bouzrara and Vorobiev 2000, 2001] have proposed the use of a combination of pressing and pulsed-electric-field treatment for the extraction of juice from sugar beet. Although this process can lead to a much reduced energy consumption, it represents a completely new technology and requires a redesign of the entire sugar plant.

The potential advantages of electroporation for the extraction of juice from sugar beet cells were first demonstrated with a mobile test device called KEA (Karlsruher Elektroporations Anlage). A general view of this facility is shown in Fig. 10.5. The treatment chamber, shown in the right part of Fig. 10.5, was built from a polypropylene tube of inner diameter 18 cm. It contained four electrode pairs, constructed from stainless steel. Each pair consisted of two disc-shaped electrodes of diameter 4 cm, displaced axially and azimuthally by 16 cm and 90°, respectively. The twisted electrode pairs guaranteed that each cell of an entire sugar beet passing through the tube had seen at least the minimum field at the centre between two electrodes. At the nominal pulse voltage, this field reached a value of 12 kV/cm. The treated beets leaving the reaction tube were transported to a tub with the help of a screw conveyor, visible on the left side in Fig. 10.5. A maximum throughput of 300 kg/h could be handled with this set-up.

High-voltage pulses with amplitudes of up to 300 kV were created with the help of a six stage low-impedance Marx generator. By discharging the Marx generator into the reaction chamber, a unipolar critically damped pulse of duration about 1 μ s (FWHM) was achieved. Each pulse represented an electrical energy of 0.75 kJ. The Marx generator was capable of running at repetition rates of up to 10 Hz. Both the Marx generator and the reaction tube were



Fig. 10.5. View of the KEA mobile electroporation device. *Left photograph:* Faraday cage housing the Marx generator and the process chamber (*right*); power supply and screw conveyor (*middle*); and tub for collection of treated beets (*left*). *Right photograph:* process chamber, consisting of a polypropylene tube with four pairs of distributed electrodes

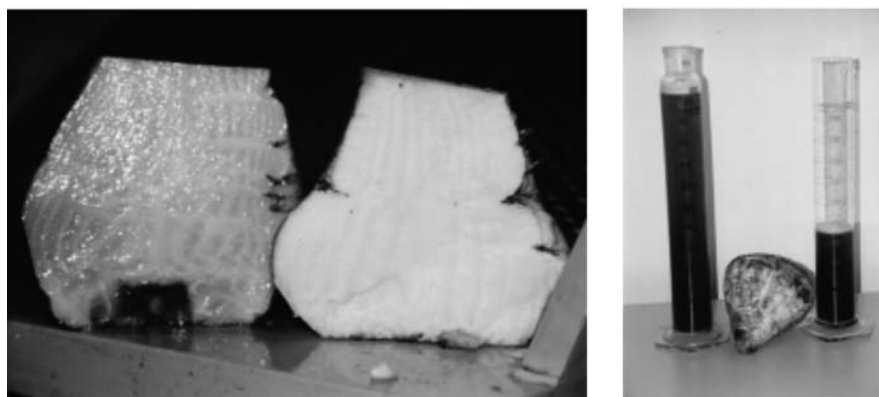


Fig. 10.6. *Left photograph:* Sugar beets before (*right*) and after (*left*) treatment with pulsed electric fields. *Right photograph:* corresponding yields of juice obtained by cold pressing at 32 bar

housed in a Faraday cage to eliminate the emission of electromagnetic noise. The high-voltage supply was a 10 kW commercially available charging unit.

The treated sugar beets were cut into pieces and either cold-pressed or extracted in water at various temperature levels. Figure 10.6 shows a sugar beet before and after treatment in the reaction chamber, together with the corresponding yield of juice obtained by cold pressing with a pressure of 32 bar for 15 minutes. The juice droplets appearing on the cut surface of the treated beet are indicative that the cell membranes have been destroyed by

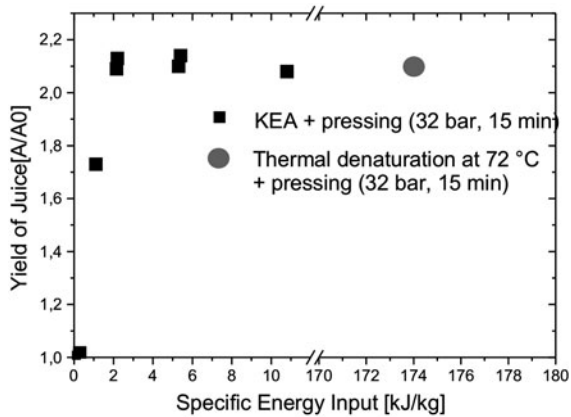


Fig. 10.7. Yield of juice versus specific energy input for thermal denaturation and for pulsed-electric-field treatment (A0, untreated; A, treated)

the pulsed electric field. In Fig. 10.7, the specific yield is plotted as a function of the number of pulses or the equivalent of the specific energy input. For comparison, the yield for thermal denaturation at 72°C has been plotted too. In this case, the necessary specific energy input for heating the beet from 20°C to 72°C is 174 kJ/kg.

It is evident that electric-pulse treatment has a large potential for energy saving. There are two major areas in which energy saving may be achieved in a sugar factory by adding an electroporation step to the process line: extraction can be carried out at lower temperatures and with lower raw juice draft, i.e., a lower amount of water is required to extract the sugar juice. It seems feasible to integrate the electroporation step into the process line without requiring major changes in the other components of the sugar plant.

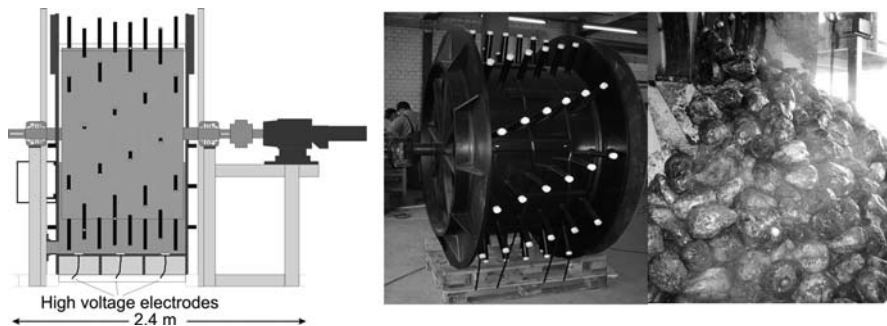


Fig. 10.8. Schematic illustration of the KEA-ZAR reaction chamber (*left*). The photographs to the *right* show the transport drum before installation into the reaction chamber, and sugar beets leaving the reaction chamber after treatment

To demonstrate that this technology was economic and scalable to the large throughputs necessary for a large sugar factory, the facility KEA-ZAR (Zellaufschlussreaktor) was built by the Karlsruhe group. In this device, the reaction chamber consisted of a large drum with spokes to transport the beets (Fig. 10.8). Stainless steel electrodes were integrated into the bottom of the reaction chamber and connected to two Marx generators. The counter-electrodes were stainless steel ribbon bands bent onto the drum case. The transport capacity of this drum was up to 800 t/d. Two Marx generators, each delivering voltage pulses of up to 350 kV at a repetition rate of up to 20 Hz, were connected to the electrodes.

10.1.4 Bacterial Decontamination

Killing of bacteria such as *Escherichia coli*, *Bacillus cereus*, and *Staphylococcus aureus* with strong pulsed electric fields (PEFs) has been described in the literature since the middle of the 1960s. In their pioneering work of 1967, Sale and Hamilton concluded that the observed killing of bacteria was due to destruction of the cell membrane, leading to cell lysis [Sale and Hamilton 1967]. By applying electric fields of greater than 10 kV/cm for a duration of 20 μ s, they found that the killing rate depended strongly on the bacterial species. Gram-positive bacteria showed a higher threshold for lethal electric fields than Gram-negative bacteria [Hülsheger et al. 1983]. In addition, it was observed that spores were insensitive to pulsed electric fields. Despite the early success, sterilisation with pulsed electric fields never left the laboratory stage. Again, to a large extent this was due to the lack of pulse generators adequate for industrial applications. Also, many of the results published are contradictory. In addition, it was found that the lethality rate saturates with increasing number of pulses. Thus pulsed electric fields can probably only be used effectively to reduce the number of germs by up to four logarithmic steps. The reason for this limit is not completely understood but many researchers believe that it is due to individual properties that make some bacteria of the same species more resistant to PEF treatment than others. This raises the question of whether bacteria can develop an ‘electroresistance’. However, when bacteria which had survived PEF treatment over more than 12 generations were recultivated, no evidence for ‘electroresistance’ was found [Bluhm et al. 2004].

Nevertheless, it seems improbable that PEF treatment alone can be used for sterilisation. Consequently, further developments of PEF treatment for industrial applications should focus on three areas:

1. Reduction of germs to prolong the shelf life of food products.
2. Dilution of bacterial contamination in purified water from sewage plants before release to the environment.
3. Combining PEF treatment with other biological, chemical or physical techniques to obtain a more efficient and ecologically and economically more attractive system.

Increasing the shelf life of food products with pulsed electric fields is quite attractive since it is non-toxic and does not destroy any vitamins, flavours, etc. Clarified water from sewage plants still contains large concentrations of bacteria, and increasingly, antibiotic-resistant species, with unpredictable consequences for the ecosystem. Diminishing their amount by an innocuous method before delivery to the surface water system would be of great benefit to the environment.

An obvious extension of bacterial decontamination with pulsed electric fields is the use of underwater corona discharges. Corona discharges are low-current partial discharges. They occur at metallic tips, as described in Sect. 2.3.2. Extremely high electric fields appear at the ends of a corona tree. In addition, strong oxidants such as OH radicals, ozone, and H₂O₂, as well as UV radiation, are created. The oxidant yield can probably be increased further by the injection of gas microbubbles. It is expected that a combination of these effects will lead to a more efficient method for the destruction of micro-organisms in water and probably also to the extermination of spores. Corona discharges have been created in large volumes from thin wire anodes [Akiyama 2000, Akiyama et al. 2001] and on the surface of metallic cylinders covered with a thin, porous ceramic layer [Sunka et al. 1999, Sunka 2001]. The latter geometry seems especially to be scalable to the large volumes and long lifetimes required for industrial applications.

Recently it has been found that very short pulses (< 10 ns) with field amplitudes of more than 10 MV/m can induce apoptosis and fragment DNA in mammalian cells without disrupting the cell membrane [Schoenbach et al. 2001, Beebe et al. 2002, Buescher and Schoenbach 2003]. Besides offering new methods for cancer treatment and basic biological research, these pulses also provide the possibility for a new approach to bacterial decontamination.

10.1.5 Further Applications of PEF Treatment

A task similar to that described in the previous subsection is the suppression of biofouling in the aquatic systems that exist in industrial waters and processes. By the term 'biofouling', we mean any attachment of biological material to wet surfaces. A large number of very different organisms such as bacteria, protozoa, fungi, mussels, and algae, can participate in the formation of such deposits on surfaces. The occurrence of biofouling can be an annoying and costly problem in many industrial processes and in the surroundings of the plant. Any untreated water that is used in an industrial process carries micro-organisms, which can lead to the formation of biofilms in pipes, cooling towers, heat exchangers, etc. [Walker et al. 1998].

The attachment of marine organisms such as mussels on surfaces below the waterline causes billions of dollars' worth of damage to shipping and other marine industries. Some anaerobic bacteria use carbon dissolved in steel for their metabolism and thus accelerate the corrosion of steel in water. Inhibiting the growth of biofilms with biocides is often difficult or is unacceptable

because of the environmental burdens connected with it or because of incompatibility with an industrial process.

Pulsed-electric-field treatment is therefore a very attractive method for eliminating biofouling. It has already been applied successfully to prevent the attachment of mussels in the pipes of power stations using seawater for cooling [Schoenbach et al. 1997] and to eliminate the growth of algae in drinking-water reservoirs [Akiyama 2000].

Another unexploited area of applications for electroporation is its use for the production of valuable substances from micro-organisms such as microalgae and bacteria. Microalgae are of growing interest as a sustainable supplier of raw materials for the food industry, as well as for the pharmaceutical and cosmetic industries. Biopolyester from bacterial cells (*Ralstonia eutrophia*), for example, is of great interest as a regenerative, biologically digestible material. Its mechanical and chemical properties are similar to those of polyethylene and it is therefore a valuable material for medical implants. At present it is obtained from bacteria grown in fermentation vessels with the help of a chemical-enzymatic process [Schumann and Müller 2001]. Combining this process with electroporation could lead to a more effective use of the chemical and enzymatic agents used to dissolve the cell membranes of the bacteria. As a result of the formation of irreversible pores, the cell-lytic agents could diffuse more rapidly into the cell and dissolve the cell walls, thus liberating the polymer granules from the bacteria.

Finally, electroporation has a large potential for applications in therapy. A faster and larger delivery of pharmaceuticals seems possible through the creation of reversible pores in the membranes of mammalian cells. Thus a stronger effect in chemotherapy of cancer cells can be achieved with concurrently reduced stress for the patient [Dev and Hoffmann 1994, Rabussay et al. 2003].

10.2 Pulsed Magnetic Fields

10.2.1 Introduction

Pulsed magnetic fields in the range of up to a few hundred tesla are of great interest for applications in both basic and applied sciences. Especially in the region above 100 T, new physical phenomena are to be expected. At these fields, the Lorentz force becomes comparable to the Coulomb force that keeps an electron in its atomic orbital. For example, in a hydrogen atom the two forces become equal at a value of B given by the following expression:

$$B = \left(\frac{13.3}{n} \right)^3 \times 100 \text{ (tesla)}, \quad (10.5)$$

where n is the main quantum number. In solids, the specific magnetic-field energy at these intensities becomes comparable to fundamental interaction energies, the electron orbits shrink to molecular dimensions, and the spacing of

Landau levels $(h/2\pi)\omega_c$ becomes larger than kT at room temperature. From these simple considerations, it becomes obvious that the electronic properties of solids and the kinetics of physical and chemical processes will change significantly at fields above 100 T. Many effects become nonlinear at these fields, and stringent experimental tests of theory can be carried out. For this reason, several high-magnetic-field laboratories have been built in the last decade in Europe, the United States, and Japan (in Berlin, Talahassee, and Tokyo, respectively), and research at high fields is considered to be of high priority. Today, high magnetic fields play a crucial role in materials science. Investigations of magnetoresistance have led to the discovery of the quantum and fractional quantum Hall effects, which have been recognized by two Nobel Prizes. Some other areas of contemporary research where high magnetic fields are fundamental are investigations of high-temperature superconductors, molecular conductors, magnetic phenomena in solids, heavy fermions, and order-disorder transitions in monolayers. For more information, we refer to the proceedings of a recent conference on physical phenomena in high magnetic fields [Boebinger et al. 2002].

In addition to applications in solid-state physics, pulsed magnetic fields can be used to produce strong shock waves in conductors to determine their thermodynamic, electrical, and optical properties at high energy densities. Moreover, the confinement of plasmas and the development of hydrodynamic instabilities can be studied under these conditions. In addition, pulsed magnetic fields can be used to accelerate projectiles to high velocities and to produce intense electromagnetic pulses. Only a few investigations have been carried out to determine the effect of strong magnetic fields on living organisms. It is expected that biochemical and biophysical processes will be altered in the presence of strong magnetic fields [Maret and Dransfeld 1985].

Owing to limitations on the strength of materials, magnetic fields of the order of 100 T can be produced only in short pulses or through the superposition of stationary and pulsed fields. Stationary fields are limited to values below 50 T. The world's largest facility, which is presently located in Talahassee, Florida, USA, can provide a field of 45 T in a cylindrical volume 32 mm in diameter. The highest pulsed fields that can be produced with non-destructive coils are around 70 T, while up to 300 T has been created with destructive coils. Concepts for the generation of fields around 500 T have been developed, although for very short times ($\sim 3 \mu\text{s}$) and in small volumes (9 mm diameter) only.

To attain higher fields, a scheme of magnetic flux compression must be applied. In flux compression, systems, a conductor enclosing a preformed magnetic flux is compressed by external forces, thereby converting mechanical into magnetic energy. We shall first discuss the limitations on the field strength achievable with coil systems and then describe flux compression schemes in more detail.

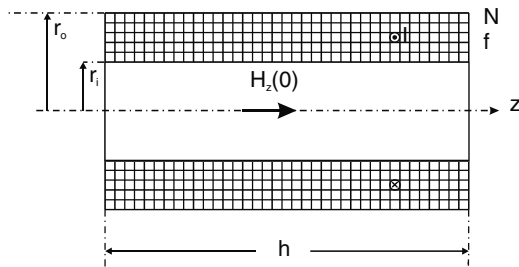


Fig. 10.9. Multiturn solenoid

10.2.2 Field Limitations for Non-Destructive Coil Operation

10.2.2.1 Coil and Circuit Parameters

Before we begin to discuss the limitations of the field for the non-destructive operation of multiturn solenoidal coils, we shall derive some basic relations between the discharge circuit parameters and the properties of the field coil. The coil to be considered is sketched in Fig. 10.9. We assume that it has N turns with a filling factor f . The filling factor describes the ratio of the conductor cross-section of all turns to the total cross-section of the coil:

$$f = \frac{NA}{h(r_o - r_i)}, \tag{10.6}$$

where N is the total number of turns and A is the conductor cross-section of a single turn. The relation between the field on the coil axis at position z and the current flowing through the turns is given by [Knoepfel 1970]

$$H_z = \frac{1}{2} H_0 \left[\frac{h-z}{r_o - r_i} \ln \frac{r_o + \sqrt{r_o^2 + (h-z)^2}}{r_i + \sqrt{r_i^2 + (h-z)^2}} + \frac{z}{r_o - r_i} \ln \frac{r_o + \sqrt{r_o^2 + z^2}}{r_i + \sqrt{r_i^2 + z^2}} \right]. \tag{10.7}$$

Here $H_0 = NI/h$, and the expression is valid if the diameter of the wire is much smaller than the skin depth. Naturally, the inductance of such a coil is quite large, and if it is driven by a discharge from a capacitor bank, the period will be long. Also, the resistance of the coil can be an important part of the discharge circuit. The inductance and resistance are given by

$$L_c = \mu_0 N^2 \frac{\pi r_i^2}{h} K_c, \quad R_c = \frac{\pi}{\sigma} \frac{N^2}{fh} \frac{r_o + r_i}{r_o - r_i}. \tag{10.8}$$

Here K_c is a correction factor that takes into account the edge fields in a coil of finite size [Knoepfel 1970].

For the discharge circuit shown in Fig. 10.10, we find the following solutions for the undercritically and overcritically damped cases:

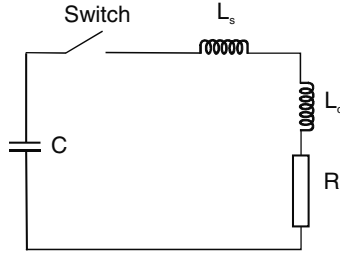


Fig. 10.10. Equivalent circuit of a multiturn solenoid charged from a capacitor discharge

$$I = \frac{U_0}{\omega L} \exp\left(-\frac{R}{2L} t\right) \sin(\omega t), \quad (10.9)$$

$$I = \frac{U_0}{\omega^* L} \exp\left(-\frac{R}{2L} t\right) \frac{e^{\omega^* t} - e^{-\omega^* t}}{2}, \quad (10.10)$$

where $\omega = \omega_0 \{1 - \gamma^2\}^{1/2}$, $\omega^* = \omega_0 \{\gamma^2 - 1\}^{1/2}$, and

$$\gamma = \frac{1}{2} R \sqrt{\frac{C}{L}}, \quad (10.11)$$

$$\omega_0 = \frac{1}{\sqrt{LC}}. \quad (10.12)$$

γ is called the circuit parameter. It determines the maximum current I_m through the coil and the time t_m at which it is reached. L is the sum of the coil inductance L_c and the stray inductance L_s of the circuit. From the expressions given above, we obtain the following for $0 < \gamma < 1$:

$$\begin{aligned} \frac{I_m}{I_0} &= \exp\left\{-\frac{\gamma}{\sqrt{1-\gamma^2}} \arcsin \sqrt{1-\gamma^2}\right\}, \\ \frac{t_m}{T/4} &= \frac{2}{\pi} \frac{1}{\sqrt{1-\gamma^2}} \arcsin \sqrt{1-\gamma^2}. \end{aligned} \quad (10.13)$$

For $1 < \gamma < \infty$, we have

$$\begin{aligned} \frac{I_m}{I_0} &= \left[\gamma + \sqrt{\gamma^2 - 1}\right]^{-\gamma/\sqrt{\gamma^2 - 1}}, \\ \frac{t_m}{T/4} &= \frac{2}{\pi} \frac{\ln\left(\gamma + \sqrt{\gamma^2 - 1}\right)}{\sqrt{\gamma^2 - 1}}. \end{aligned} \quad (10.14)$$

Here $T = 2\pi/\omega_0$, and $I_0 = \{2W_0/L\}^{1/2}$ is the maximum current achievable in a circuit without resistance.

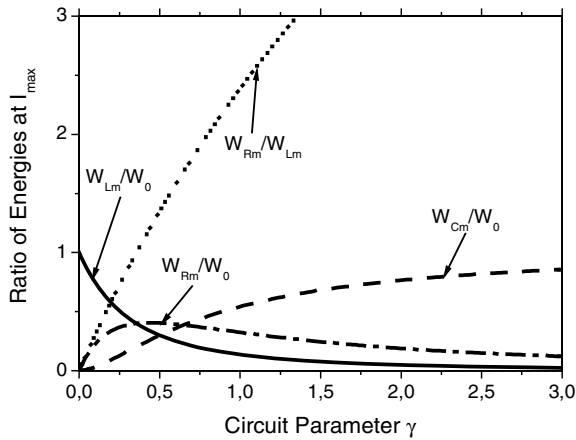


Fig. 10.11. Partition between inductive energy, dissipative energy and the remaining energy in the capacitor at the time of maximum current. In addition, the ratio between the dissipative and the inductive energy is shown

At the time t_m when the maximum current is reached, the energy initially stored in the capacitor, W_0 , is divided between a term W_{Rm} representing the energy dissipated in the circuit resistance, a term W_{Lm} representing the magnetic energy in the circuit, and a term W_{Cm} representing the remaining energy in the capacitor. These terms can be described by functions of the circuit parameter γ only:

$$\begin{aligned} \frac{W_{Lm}}{W_0} &= \left(\frac{I_m}{I_0}\right)^2, \\ \frac{W_{Rm}}{W_0} &= 1 - \left(\frac{I_m}{I_0}\right)^2 (1 + 4\gamma^2), \\ \frac{W_{Cm}}{W_0} &= 4\gamma^2 \left(\frac{I_m}{I_0}\right)^2. \end{aligned} \tag{10.15}$$

These quantities are plotted in Fig. 10.11.

If we now assume that the coil inductance is much larger than the stray inductance and that, in addition, the circuit resistance is dominated by the coil resistance, we derive the following for the circuit parameter γ :

$$\gamma = \frac{1}{2} R \sqrt{\frac{C}{L}} = \frac{N}{2\sigma f} \frac{r_o + r_i}{r_o - r_i} \left(\frac{\pi C}{\mu_0 K_L h r_i^2}\right)^{1/2}. \tag{10.16}$$

From Fig. 10.11 it is evident that circuit parameters greater than 1 lead to inefficient transformation of capacitive into inductive energy. This sets limits on N and C , i.e., low capacitance and high voltage are to be preferred over high capacitance and low voltage.

10.2.2.2 Quasi-Static Containment of Magnetic-Field Pressure

In Chap. 1, we quoted some expressions describing thermal and mechanical restrictions on the containment of a magnetic field ((1.1) and (1.2)), which we shall now consider in more detail. The expression for the mechanical containment of the magnetic pressure is valid for static conditions under the assumption that a magnetic surface pressure is acting on a cylindrical metallic wall. These assumptions are contradictory, since under static conditions the magnetic pressure would not be restricted to the surface of the conductor. Nevertheless, they may lead to a good approximation for the case of a thin conducting cylinder contained in a currentless, thicker, cylindrical pressure-taking vessel. Needless to say, all considerations in this subsection are valid for slow pulses whose duration is much longer than the characteristic oscillation period $T_o = 2\pi r_o(\rho/Y)^{1/2}$ of the cylinder. Here r_o is the radius of the cylinder, ρ is the material density, and Y is Young's modulus.

The magnetic stress can be described by Maxwell's stress tensor, which, in its simplest one-dimensional form, is given by

$$\begin{aligned} p(r, t) &= \int_{r_i}^r j_\theta B_z \, dr = - \int_{r_i}^r \frac{\partial H_z}{\partial r} B_z \, dr, \\ &= \frac{1}{2} \mu_0 H_z^2(r_i, t) - \frac{1}{2} \mu_0 H_z^2(r, t). \end{aligned} \quad (10.17)$$

For the case considered here, this leads to a surface pressure $p = \mu_0 H^2/2$. (We always assume materials with a relative permeability of 1 in this subsection.) For a cylindrical wall with radii r_i and r_o , the maximum tangential stress occurs at the inner surface, where it has a value of [Ebert 1976]

$$\Sigma_\theta = p \frac{r_o^2 + r_i^2}{r_o^2 - r_i^2}. \quad (10.18)$$

Therefore an approximate criterion for the static containment of the magnetic pressure is

$$\frac{1}{2} \mu_0 H^2 < \Sigma_Y \frac{r_o^2 - r_i^2}{r_o^2 + r_i^2}. \quad (10.19)$$

Here Σ_Y is the maximum yield strength of the material under consideration.

A similar criterion has been derived for a long multilayer coil assuming constant current density and no radial transmission of stress between turns. Here the relation between the field at the centre and the maximum stress, which occurs at $r = r_o/2$ (for $r_i < r_o/2$), is [Herlach and Ortenberg 1996, Herlach et al. 1996]

$$B(0) = \mu_0 H(0) < \sqrt{2\mu_0 \Sigma_Y} \sqrt{2} \left(1 - \frac{r_i}{r_o}\right). \quad (10.20)$$

Table 10.1. Yield strength and maximum induction for various materials

Material	Soft Cu	Hardened Cu	CuBe	Maraging steel
Yield strength (GPa)	0.2	0.45	1	2
B_{\max} (T)	22	33	50	70

In a multiturn, multilayer coil with radial transmission of stress, the radial stress can become negative ($\Sigma_r < 0$) for $r < 1.8r_i$ and the layers can be pulled apart. The part of the coil in which this happens then behaves like a coil with free turns.

Because of the large variety of different failure mechanisms in high-field coils, detailed simulations are often of little value and a reasonable estimate of the maximum achievable field with a non-destructive coil can be obtained from the first factor in (10.20). Table 10.1 lists the yield strength and the corresponding estimated maximum field for various materials.

10.2.2.3 Dynamic Containment of Magnetic-Field Pressure

Under dynamic (pulsed) loading, we must take into account the inertia of the container. We begin our discussion by considering a thin superconducting cylinder of thickness d , radius r_0 , and height h . If the magnetic-pressure pulse $p(t)$ is short compared with the oscillation period $T_0 = 2\pi r_0[\rho/Y]^{1/2}$, the momentum transferred to the wall is

$$P = 2\pi r_0 h \int_0^t p(t) dt. \quad (10.21)$$

The resulting strain can be obtained by equating the kinetic energy imparted to the cylinder to the deformation energy:

$$\frac{P^2}{2M} = \int_0^{2\pi \Delta r} \Sigma dh dx, \quad \Sigma = Y \frac{x}{2\pi r_0}. \quad (10.22)$$

Here Σ is the stress, and M is the mass of the cylinder, equal to $2\pi r_0 dh\rho$. Finally, when we equate the momentum expressed by (10.21) with that derived from (10.22), the criterion for dynamic containment becomes

$$\frac{1}{2} \mu_0 \int_0^t H^2 dt < \sqrt{\frac{\rho}{Y}} \Sigma_Y d, \quad (10.23)$$

where Σ_Y is again the yield strength of the container material. For a rectangular pulse of duration T , we therefore obtain

$$\frac{1}{2} \mu_0 H^2 < \frac{T_0}{T} \Sigma_Y \frac{d}{2\pi r_0}. \quad (10.24)$$

Comparing (10.24) with (1.2) shows that the dynamic containment is increased by a factor T_0/T , which has been assumed to be large. We can transfer these results to calculate the containment of a multiturn solenoid.

If we restrict our discussion to a single-layer solenoid of thickness d and assume that the field outside the coil is negligible, we can make use of (10.22). However, we have to consider the fact that the pressure acts only on the windings, i.e., p increases owing to the filling factor. Thus, with

$$p \approx \frac{1}{2} \frac{\mu_0 H_0^2}{f}, \quad (10.25)$$

(10.23) becomes

$$\int_0^t \frac{1}{2} \mu_0 H_0^2 dt < \sqrt{\frac{\rho}{Y}} \Sigma_Y df. \quad (10.26)$$

In this derivation, it has been assumed that the cylinder serves both as the inertial mass and as the elastic containment. In general, however, these functions are separated and the containment is further improved.

10.2.2.4 Thermal Limitations

Although mechanical effects cause the most serious problems, thermal effects cannot be neglected. The energy balance in a volume element of the wire can be described by the following balance equation:

$$\frac{\partial (c_V T)}{\partial t} = \frac{j^2}{\sigma} + \lambda \Delta T, \quad (10.27)$$

where c_V is the specific heat capacity, and λ and σ are the thermal and electrical conductivities, respectively. Since the coil wires are generally embedded in an electrically insulating and also thermally insulating matrix, we can in many cases neglect the second term on the right-hand side of (10.27). This is also true for magnetic diffusion problems (e.g., when the magnetic field diffuses into a thick conductor), since the thermal skin depth is always much smaller than the electrical skin depth. Here, however, we are considering the case where the magnetic-diffusion skin depth is much larger than the wire diameter. Since, in general, we cannot neglect the temperature dependence of the electrical conductivity, it is convenient to formulate a criterion for the maximum allowable current density integral before the wire begins to melt:

$$J = \int_0^t j^2 dt = \int_{Q_0}^{Q_f} \sigma dQ. \quad (10.28)$$

Here Q_0 and Q_f are the initial and final specific energy densities, $c_V T_0$ and $c_V T_f$, respectively. Equation (10.28) shows that the current integral J depends only on Q_0 and Q_f . It is obvious that J has to remain below the value corresponding to the melting point of the metal. This value depends on the initial temperature of the coil. For Cu and Al heated from room temperature to the melting temperature of the solid, the values of J are $0.89 \times 10^{17} \text{ A}^2 \text{ s m}^{-4}$ and $0.32 \times 10^{17} \text{ A}^2 \text{ s m}^{-4}$, respectively. J can be increased if the conductor is pre-cooled. Applying these results to a multiturn solenoid, we obtain the following condition:

$$\frac{1}{A^2} \int_0^t I^2 dt \leq J_{\text{sm}}. \quad (10.29)$$

If the dependence of H on I is known [e.g., (10.7)], we can use (10.29) to formulate a criterion for the maximum achievable magnetic field before the coil melts. However, it is the current integral taken over the entire pulse duration (not only over $T/4$) that must remain below J_{sm} if the coil is to survive a series of discharges. To limit the current integral through the coil, it is therefore customary to activate a crowbar switch in the circuit after the maximum field has been reached.

10.2.3 Field Limitations for Destructive (Coil) Operation: Single-Turn Solenoid

Magnetic fields above 100 T can be only produced by destructive systems. Ultimately, the destruction is a consequence of the high energy density. A field of 500 T corresponds to an energy density of 100 kJ/cm^3 and can exert a pressure of 100 GPa. This is higher than the energy density of any storage system, including TNT, and requires some kind of energy concentration, for example, a low-inductance converging transmission line.

The most widely used system for the production of magnetic fields above 100 T is the single-turn coil (Fig. 10.12). This is a simple, inexpensive, and mechanically rugged system and therefore allows a reasonably short turnaround time between successive experiments. An advantage compared with flux compression systems (see next subsection) is that the coil disintegrates radially outwards. Thus even delicate samples survive the experiment and can be reused.

Naturally, a single-turn coil whose radial and axial dimensions are of the order of centimetres has a low inductance and a short field lifetime of the order of a few μs , and therefore requires a low-inductance capacitor bank with a low resistance, and a very high current and stored energy. To generate a field of 100 T, a current of 0.8 MA per cm axial length is required. Owing to the limited current (and energy) available from a fast capacitor bank the dimensions of the coil are small. At Humboldt University, Berlin, 300 T has

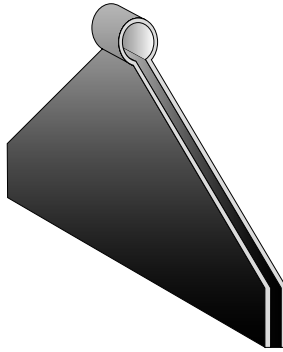


Fig. 10.12. Single-turn coil with converging low-impedance stripline

been created in a coil of 5 mm inner diameter, 5 mm axial length, and 2 mm wall thickness using a 60 kV, 225 kJ capacitor bank [Herlach and Ortenberg 1996].

The relation between the centre field $H_z(0)$ and the current in a single-turn solenoid of length h , inner radius r_i , and outer radius r_o is given by the following expression:

$$H_z(0) = (I/h)K_H. \quad (10.30)$$

K_H is a function of $h/2r_i$ and r_o/r_i and is plotted in Fig. 10.13.

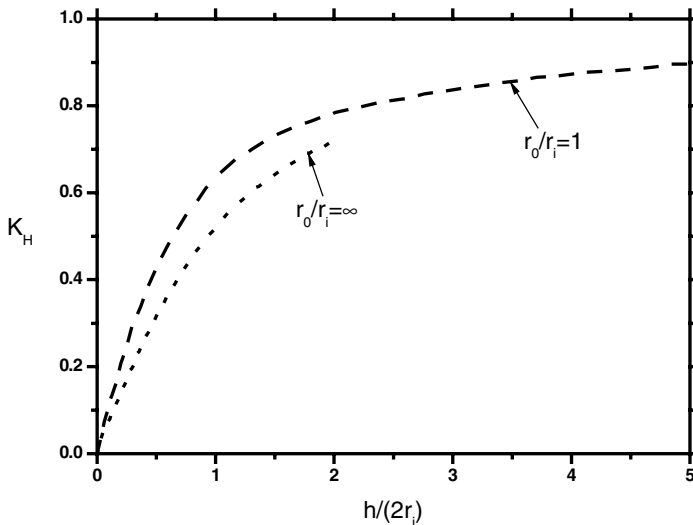


Fig. 10.13. Field factor K_H as a function of $h/2r_i$ for $r_o/r_i = 1$ [Bardotti et al. 1964] and $r_o/r_i = \infty$

We can conclude from this plot that the field strength in a sufficiently long coil should not affect the field-to-current ratio. However, a coil that expands because the yield point of the metal is exceeded creates a variable inductance dL_c/dt which increases the effective resistance of the system. At expansion velocities of around 2 km/s, this contribution to the circuit impedance can become of the same order as the internal resistance of the capacitor bank and may reduce the maximum current I_m . A delayed expansion has been observed in some single-turn coils with a small inner diameter ($r_i \sim 1$ mm, $h \sim 2$ mm, wall thickness ~ 2 mm) [Miura and Herlach 1985]. It has been speculated that axial compression causes a tendency to squeeze the inner wall towards the centre.

At very high fields, the magnetic pressure pulse drives shock waves into the metal. These shock waves also lead to a radial surface expansion. From the Hugoniot relations, we have the following relation between the pressure and the shock and particle velocities v_s and u :

$$p = \rho_0 v_s u. \quad (10.31)$$

Here ρ_0 is the mass density. For many metals, a linear relationship between v_s and u holds for a large range of velocities if the pressure is not too high:

$$v_s = c_0 + Su. \quad (10.32)$$

Using this relationship, we obtain the following for the functional dependence between the magnetic-field pressure and the particle velocity:

$$\frac{B^2}{2\mu_0} = u(c_0 + Su)\rho_0. \quad (10.33)$$

This can be considered as a fundamental limitation on the production of very high magnetic fields. It occurs even in the absence of other mechanisms that lead to an expansion of the coil radius. To give an example, for copper $c_0 = 3.94$ km/s, $S = 1.49$, and $\rho_0 = 8930$ kg/m³. Thus, for $B = 300$ T, we obtain $u = 784$ m/s, i.e., the volume to be filled with flux increases by a factor of 2 every microsecond for a coil with an initial inner radius of 2 mm. These considerations also suggest that heavy metals such as Ta, which result in a small particle velocity, are to be preferred. In addition, Ta has a relatively large resistivity, leading to a large skin depth even for the short pulses used with single-turn coils, which is favourable for the generation of low particle velocities (i.e., lower speed of the receding wall).

10.2.4 Flux Compression

10.2.4.1 Principles of Flux Compression

Magnetic fields greater than 500 T can be created only by flux compression schemes in volumes sufficiently large to accommodate physical samples. In a

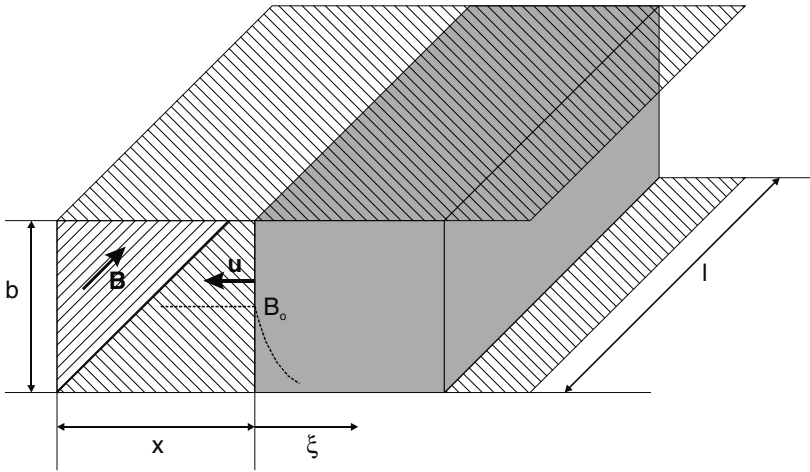


Fig. 10.14. Superconducting box in which a seeded magnetic flux is compressed by a plane piston with finite conductivity. A gedankenexperiment to derive some basic relations for flux compression schemes

flux compression system, a closed conductor surrounding a seeded magnetic flux is compressed by external forces, thereby converting mechanical into magnetic energy. The efficiency of this transformation can be rather high. To understand the principles of flux compression, we consider first a thick, incompressible metallic wall of constant resistivity that moves into a box with superconducting walls at velocity u , as shown in Fig. 10.14.

We assume further that a magnetic field has been pre-established inside the box, filling it with a flux Φ . Owing to the finite resistance of the metal sheet, the flux will diffuse into it and decay inside the box. Starting from an energy balance for this system, we can derive some fundamental relations:

$$\frac{d[(1/2)LI^2]}{dt} + RI^2 = -\frac{d[(1/2)mu^2]}{dt} = -Ku. \quad (10.34)$$

Here I is the current induced in the metal sheet, and K is the force with which the sheet has to be pushed against the magnetic field if its velocity is u . R is the resistance of the skin layer in which the current has penetrated into the sheet. All quantities are to be considered as functions of time. Thus the first term on the left-hand side of (10.34) represents the change of magnetic energy in the system both in the box and in the metal sheet. The second term corresponds to the ohmic energy dissipation, and the term on the right-hand side describes the work done against the magnetic force per unit time. We can express the mechanical energy in terms of electrical quantities:

$$\vec{K} = \int_V \vec{j} \times \vec{B} dV. \quad (10.35)$$

For the one-dimensional geometry of Fig. 10.14, this becomes

$$K_x = \ell b \int_0^\infty \frac{1}{\mu_0} \frac{\partial B}{\partial \xi} B \, d\xi = \frac{\ell b}{\mu_0} \int_{B_0}^0 B \, dB = -\frac{\ell b}{2\mu_0} B_0^2, \quad (10.36)$$

where $B_0^2/2\mu_0$ is the magnetic pressure at the surface of the metallic sheet. This result could have been derived in a quite general form using the formalism of Maxwell's stress tensor (see, e.g., [Becker and Sauter 1964]). The magnetic force acting on any incompressible body can be expressed in terms of the surface field alone. Multiplying (10.36) by $-dx$, we obtain the change of magnetic energy due to this displacement and we can therefore set the right-hand side of (10.34) equal to a change dL of the inductance of the system multiplied by $1/2 I^2$. Thus (10.34) becomes

$$\frac{d[(1/2)LI^2]}{dt} + RI^2 = -\frac{1}{2} I^2 \frac{dL}{dt}. \quad (10.37)$$

The efficiency of conversion of mechanical into magnetic energy depends therefore on the resistivity of the piston. Equation (10.37) can be rearranged by combining the first term on the left side with the term on the right and dividing by I :

$$\frac{d\Phi}{dt} + \frac{R}{L} \Phi = 0, \quad (10.38)$$

where the flux $\Phi = LI$ has been introduced. Integrating (10.38), we obtain

$$\Phi(t) = \Phi(0) \exp \left\{ -\int_0^t \frac{R}{L} dt \right\}. \quad (10.39)$$

R and L are both time-dependent and are related to the diffusion of flux into the metallic piston. A lucid term often used in the discussion of the limitations of flux compression is the flux diffusion speed u_f . We can define it as the ratio of the induced electric field E to the magnetic induction B in the piston:

$$u_f = \frac{E}{B}. \quad (10.40)$$

The meaning of u_f becomes apparent if we consider the situation where the magnetic field in the cavity remains constant. In this case all the magnetic flux encountered by the piston, moving with velocity u , must penetrate into the piston, i.e., the speed of movement and the flux diffusion speed are equal. Therefore we have

$$u_f = \frac{E}{B} = \frac{U}{Bb} = -\frac{d\Phi/dt}{Bb} = -\frac{Bb \, d\xi/dt}{Bb} = u. \quad (10.41)$$

Replacing E in (10.41) using ρj , we also obtain

$$u_f = \frac{\rho j}{B} = -\frac{\rho}{\mu_0} \frac{1}{B} \frac{\partial B}{\partial x}. \quad (10.42)$$

Thus, to calculate the flux diffusion speed, we must know B and its spatial derivative, i.e., solve the magnetic diffusion equation

$$\Delta \vec{B} - \frac{\mu_0}{\rho} \frac{\partial \vec{B}}{\partial t} = 0. \quad (10.43)$$

Here we have assumed a spatially independent resistivity. Also, displacement currents have been neglected, which is always justified in a conductor, where they are small in comparison with conduction currents. In addition, we have assumed that the relative permeability is 1. For our one-dimensional problem, (10.43) reduces to

$$\frac{\partial B}{\partial t} = \frac{\rho}{\mu_0} \frac{\partial^2 B}{\partial x^2}. \quad (10.44)$$

To solve this equation, it is often assumed that the magnetic field inside the liner rises exponentially:

$$B(0, t) = B_0 e^{t/\tau}. \quad (10.45)$$

This can only occur as long as $u_f \ll u$. For the field distribution in the (very thick) piston, we finally obtain

$$B(\xi, t) = B_0 \exp \left\{ \frac{t}{\tau} - \frac{\xi}{\sqrt{\rho\tau/\mu_0}} \right\}. \quad (10.46)$$

For our further considerations, it is convenient to define a magnetic-flux skin depth δ_Φ such that the total diffused flux can be expressed as the surface inductance $B(0, t)$ multiplied by δ_Φ :

$$B(0, t) \delta_\Phi = \Phi(t) = \int_0^\infty B(x, t) dx. \quad (10.47)$$

Integrating (10.46), we finally obtain

$$\delta_\Phi = \sqrt{\frac{\rho\tau}{\mu_0}}. \quad (10.48)$$

Under the same conditions, the flux diffusion speed is

$$u_f = \sqrt{\frac{\rho}{\mu_0\tau}}. \quad (10.49)$$

10.2.4.2 Cylindrical Shells

Among the most effective flux compression systems are imploding cylinders converging towards the axis. Considering a highly conductive incompressible cylinder enclosing a seeded flux $\Phi = B_0\pi(r_{i0})^2$, we obtain the following for the field amplification after compression to a radius r_{i1} , neglecting any flux losses:

$$\frac{B}{B_0} = \left\{ \frac{r_{i0}}{r_{i1}} \right\}^2. \quad (10.50)$$

The magnetic energy density increases with the fourth power of the compression ratio. The implosion stops when all of the kinetic energy of the cylinder has been transformed into magnetic energy.

When one is dealing with real metals, one has to take into account their compressibility and their finite conductivity. As has been discussed before, the finite conductivity leads to flux diffusion into the cylindrical shell, which can be described by a flux diffusion speed u_f . The compressibility of the material induces shock waves that penetrate into the shell, and the inner wall recedes with a corresponding particle velocity u_p . For a large part of the implosion, the shell can be considered as freely moving. It is only at the end of the implosion process, that the field begins to rise rapidly and the inner surface is suddenly decelerated by the shock wave. In this case the peak field is reached when the sum of u_f and u_p equals the speed of the inner wall before the final deceleration, u_{it} :

$$u_{it} = u_f + u_p \quad (10.51)$$

Equation (10.51) is sometimes called the ‘turnaround’ condition in the literature [Miura and Herlach 1985]. This is misleading, however, since the inner wall may still move with a speed corresponding to u_f towards the axis and destroy the sample.

A realistic calculation of the cylindrical flux compression problem can only be carried out numerically. A suitable code must simultaneously solve the MHD equations, with the appropriate equation of state, and the magnetic diffusion equation, with a suitable temperature- and field-dependent conductivity. In addition, the metal–field interface can become unstable, and to study the effect of such instabilities the fully three-dimensional geometry has to be treated.

Experimentally, the implosion can be driven either by high explosives or electromagnetically. The peak field achievable depends on the speed of the inner wall, on the initial flux, and on the occurrence of instabilities.

An example of an explosively driven flux compression scheme is shown in Fig. 10.15 [Herlach and Kennedy 1973]. Here the seed field has been produced by a field coil. A representative field waveform obtainable with this arrangement is plotted in Fig. 10.16. It is obvious that during a large part of the implosion, the liner can be considered as a freely imploding shell, while during the final phase of the implosion, the field rises exponentially.

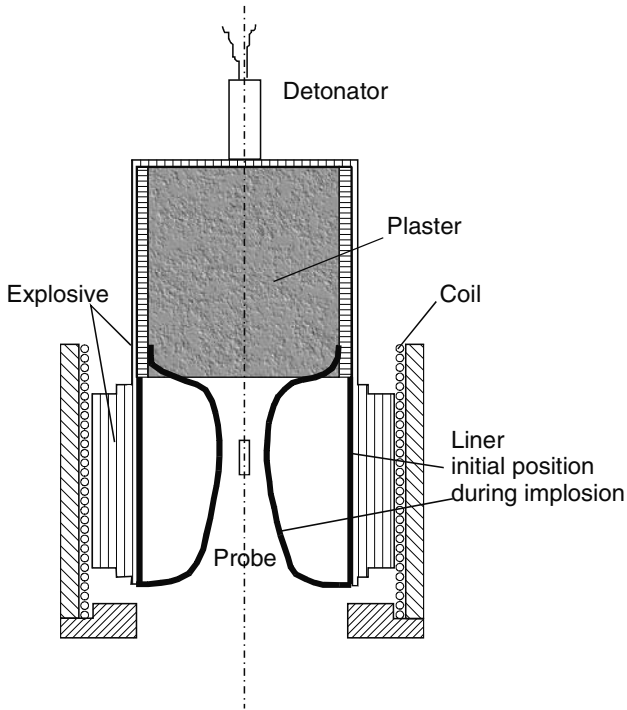


Fig. 10.15. Cylindrical flux compression device. The plaster serves to contain the implosion within the volume of the magnetic coil. Typically, the liner has an inner diameter of 8 cm

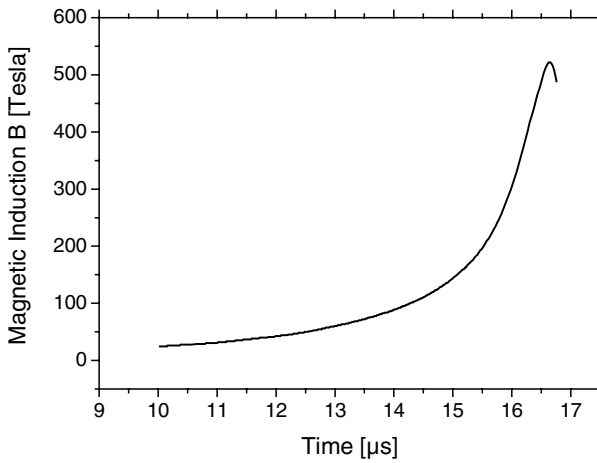


Fig. 10.16. Representative waveform from a cylindrical implosion experiment of the kind shown in Fig. 10.15

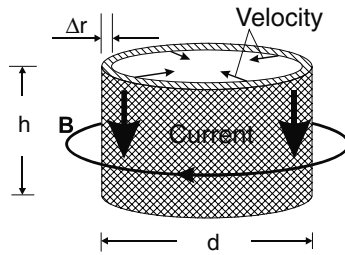


Fig. 10.17. Liner geometry for implosion by electromagnetic forces. Typical dimensions for a liner driven by a very high-energy capacitor bank (ATLAS): $d = 8.5$ cm, $h = 4$ cm, $\Delta r = 1.6$ mm

10.2.4.3 Electromagnetically Imploded Liners

The liner can also be imploded electromagnetically by a strong pulsed current flowing in its surface (Fig. 10.17). The $j \times B$ force associated with this current flow accelerates the cylindrical sheet to a high velocity. Kinetic energy is taken up gradually over a large surface and delivered to a small volume in a short time. The efficiency for converting electrical into kinetic energy with this scheme is typically of the order of 10%. Thus a very large energy is needed to drive an electromagnetic implosion to a very high field. Although its main purpose is to perform materials science experiments, the ATLAS facility [Keinigs et al. 2001] has the potential to produce very high magnetic fields with such a scheme. The facility consists of a 23 MJ capacitor bank arranged in 12 separate Marx generator tanks and can deliver a pulse current of 32 MA in a quarter-cycle time of approximately $5 \mu\text{s}$, and impart a kinetic energy of 1.5 to 2 MJ to a relatively massive Al cylinder ($d = 5$ cm, $h = 4$ cm, $\Delta r = 1.6$ mm; see Fig. 10.17) and accelerate it to a velocity of 14 km/s, which is much higher than the velocities achievable with explosives.

10.2.4.4 Pulsed Power from Flux Compression Devices

Flux compression devices can also be used as pulsed-power generators to produce high-power electromagnetic pulses from a very compact package. Owing to the large value of dB/dt , the device can be used either to compress energy into smaller volumes or to produce strong pulses of microwave radiation. Magnetoexplosive generators have been discussed since the 1970s.

Besides the imploding-cylindrical-shell configuration, exploding cylinders have been investigated. Such a configuration is shown in Fig. 10.18. Here, the high explosive located in the inner cylinder is ignited from one end and a flux compression wave propagates along the axis towards the load. The exploding inner tube makes a progressing contact with the outer coil, which has established the seed flux beforehand. To produce multimegajoule pulses with this configuration, the seed flux generator must provide a significant

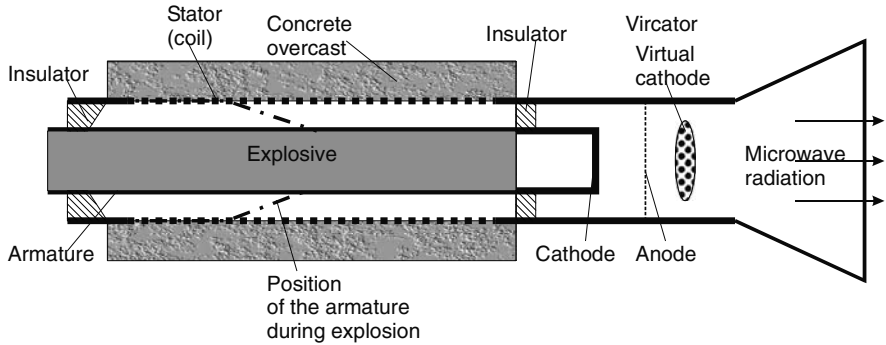


Fig. 10.18. Exploding flux compression generator driving a vircator for the production of intense pulsed microwave radiation

fraction of a megajoule. If a capacitor bank is used for this purpose, it will dominate the size of the configuration. Therefore, for mobile compact systems it might be advantageous to cascade explosive generators, i.e., to use one generator to supply the seed flux for the second stage. Such a configuration is reproduced in Fig. 10.19 [Reinovsky et al. 1985]. To match the inductance of the second stage to the relatively low inductance which takes best advantage of the first stage, a transformer coupling has been used here between the two stages. A low-inductance single-turn coil surrounds the coil of the second stage. The seed flux necessary for the first stage can be supplied from a much smaller capacitor bank.

The recent appearance of generators with pulse energies in the multi-megajoule range, such as ATLAS, Z, and Shiva Star (see papers presented at the IEEE International Pulsed Power Conferences 1997–2001) enable realisa-

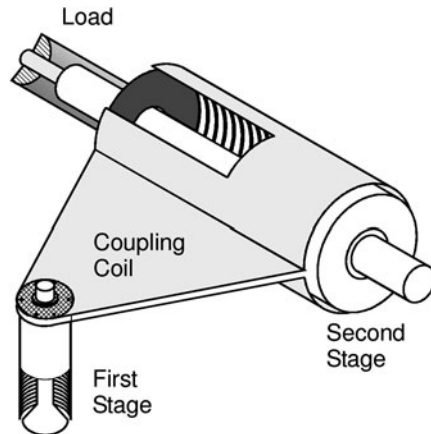


Fig. 10.19. Two-stage cascade system, inductively coupled

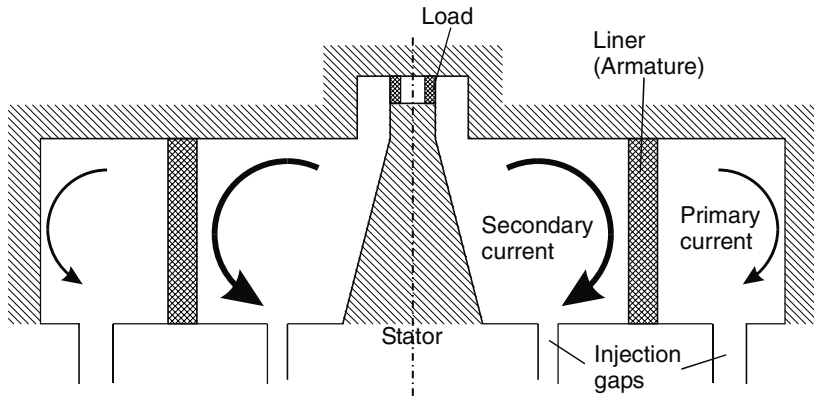


Fig. 10.20. Schematic illustration of power amplifier based on magnetic-flux compression in cylindrical geometry. The primary current drives the liner (armature) towards the axis, and the secondary current establishes a magnetic field, which becomes amplified in the stator-load loop [L'Eplattenier et al. 2001]

tion of this flux compression scheme with high-current drivers also. In such a scheme, the current is split into two parts (Fig. 10.20). One part is needed to establish the seed flux. The second part drives the flux compression. Power amplification is achieved again by accumulating kinetic energy in the liner, which can be considered as the armature, through integration over a large area and over a relatively long time and then by delivering this energy to the load, which can be regarded as the stator, within a much shorter time. As in all flux compression schemes, energy losses occur owing to magnetic flux trapped in the skin depth of the liner and to the kinetic energy dissipated as heat as the liner impacts with the stator.

11 Intense Radiation Sources

11.1 High-Power Pulsed Electron Beams

When intense particle beams became a research subject for a broader scientific community in the mid 1970s, that community was in search of an effective, very high-power driver for inertial-confinement fusion (ICF) [Beams 1975, 1977; Yonas 1978], focusable to extreme power densities of more than 100 TW/cm^2 . In the ICF approach to the utilisation of nuclear fusion energy, a small pellet containing a solid mixture of deuterium and tritium is compressed to 1000 times solid density by the ablation pressure caused by an intense radiation beam interacting with the outer shells of the pellet. Ultimately, the compressed fuel is ignited in some spot and a nuclear burn wave spreads over the entire volume of fuel. The confinement time and therefore the burning time are determined by the inertia of the pellet. A large burn fraction can only be achieved if the fuel is compressed to a high density.

After a short while, it became evident that intense pulsed electron beams would be the wrong choice for this purpose, mainly because of their long range in matter and because the bremsstrahlung created during interaction with the target material preheats the fuel inside the fusion pellet and thus prevents compression to high density.

Although an electron beam accelerator for ICF did not evolve, research in this field has created much progress in collective-beam physics, and this has promoted the application of intense beams in other areas. At present, intense pulsed electron beams are being developed mainly for the surface modification of materials [Müller et al. 2002], as pumping sources for high-power excimer lasers [Sethian et al. 2001], as high-power radiation sources for flash X-ray radiography [Cooperstein 2002], and for the production of intense pulsed microwaves [Granatstein and Alexeff 1987]. In this section, we shall give a brief overview of progress in the first three areas.

11.1.1 Beam-Generated Forces and Transport Limits

In an intense beam, the particle trajectories are strongly influenced by self-generated electric and magnetic fields. These fields must be calculated self-consistently from the distributions of charge and current density in the beam

and combined with the externally applied fields. In general, the resulting set of coupled differential equations can only be solved numerically. The method of treating this problem is the particle-in-cell (PIC) method described in Sect. 6.1.

Analytic solutions for the dynamics of collective charged particles are possible only for simple geometries that approximate real beams. In particular, the transverse components of particle velocity must be small compared with the axial velocity. For an azimuthally symmetric cylindrical beam whose length is very large compared with its diameter, we have the following for the ratio of the magnetic and electric forces:

$$\frac{F_\gamma(\text{magnetic})}{F_\gamma(\text{electric})} = \frac{v_z^2(1 - f_m)}{c^2(1 - f_i)} = \frac{\beta^2(1 - f_m)}{1 - f_i}. \quad (11.1)$$

Here f_i is the fractional charge neutralisation, f_m is the fractional current neutralisation, and β is the ratio of the axial particle velocity v_z to the velocity of light c . This means that in an unneutralized beam ($f_i = f_m = 0$), the inward-directed magnetic force is always smaller than the outward directed electrostatic repulsion force.

When the beam is injected into a vacuum region, the space charge of the beam can strongly limit its propagation. Treating this problem in a fully three-dimensional way can become quite complex. An analytic solution can be derived for a cylindrical beam of radius r_0 injected into a metallic drift tube of radius R at anode potential filled with an axial magnetic field satisfying the condition $B_0^2/8\pi \gg n_e mc^2 \gamma$, where n_e is the density of the electrons in the beam, B_0 is the magnetic field intensity, and $\gamma = (1 - v^2/c^2)^{-1/2}$ is the relativistic factor.

Requiring that the relative reduction of particle energy on the beam axis $\xi = (W_R - W_0)/W_R$ is small, where W_R is the initial kinetic energy of the electrons and W_0 is their final energy on the beam axis, we obtain the following for the maximum transportable current:

$$I = \frac{4\pi}{\mu_0} \frac{mc}{e} \xi \beta (\gamma - 1) \frac{1}{1 + 2 \ln R/r_0}. \quad (11.2)$$

Considering a beam of 100 keV electrons ($\gamma = 1.195$, $\beta = 0.547$) and requiring $\xi \leq 0.1$ and $R/r_0 = 2$, we obtain $I \leq 77$ A. The beam power must therefore be below 7.7 MW. Much higher electron beam power is possible if the beam is injected into a neutralising background such as a plasma.

For other current limitations resulting from magnetic forces and plasma instabilities, we must refer to the literature [Bogdankevich and Rukhadze 1971, Bogdankevich et al. 1970].

11.1.2 High-Current Electron Sources

Large electron currents can be produced by either large-area or high-current-density sources. We are interested here in both high current densities

($\approx 10^4$ A/m²) and large areas (several hundred square centimetres). There are two main categories of electron sources: thermionic and plasma cathodes. Thermionic sources emit large current densities only if they are heated to a high temperature (see Sect. 4.1).

A much easier way to produce a large-area, high-current density source is to generate a plasma covering the cathode surface. This plasma can, for example, be created through electron field emission from a set of microscopic fibres homogeneously distributed over the cathode surface. A very effective material for this purpose is graphite. If the electric field at the tips of the carbon fibres exceeds several times 100 kV/cm the field emission current heats the fibres, evaporates material, and desorbs gas, and finally leads to breakdown of this gas layer and subsequently to the formation of a plasma which spreads axially and radially. Detailed investigations have shown that the main source of the plasma is a flashover process occurring along the fibre surface [Krasik et al. 2001]. Although plasma expansion is necessary to form a large-area, continuous source, it can become a problem too if it leads to plasma closure and shorting of the acceleration gap.

One simple and very efficient cathode is based on large arrays of carbon fibre bundles [Vasilevskii et al. 1980, 1981, 1986, 1988]. Connecting each bundle to a high-voltage generator through a resistor not only enables turn-on of all bundles in the array but also suppresses fluctuations in the electron current and thus improves the operating stability of the cathode. In addition, this source provides a low rate of plasma generation, allowing operation for tens of microseconds without plasma closure. Uniform turn-on of all emission sites is possible if the rate of rise of the voltage pulse is greater than 10^{12} V/s.

Besides fibre arrays, ferroelectric cathodes have been used as electron sources [Krasik et al. 2001]. In this case also, the electron emission occurs from a surface flashover plasma, initiated at the triple point where the dielectric, the metal, and the vacuum come together.

11.1.3 Pulsed Electron Diodes

In analogy to a vacuum electron tube, we call a device for the acceleration of charged particles in a configuration consisting of two electrodes in vacuum a diode. In an electron diode, the cathode incorporates the electron source. When a high electric field is applied to the diode gap, electrons are extracted from the cathode and accelerated towards the anode.

If the anode is transparent, a beam can propagate towards a target. In most high-current diodes, the electrons are accelerated in a space-charge-limited mode, where the electric field vanishes at the cathode surface. At relativistic electron energies, we obtain the following for the space-charge-limited current density [Humphries 1990]:

$$j_e = \frac{\varepsilon_0 m_0 c^3}{ed^2} \frac{[G(\gamma_0)]^2}{2},$$

$$\gamma_0 = 1 + \frac{eU_0}{m_0c^2}. \quad (11.3)$$

At non-relativistic energies, this leads to the well-known one-dimensional Child–Langmuir law,

$$j_e = \frac{4\epsilon_0}{9} \sqrt{\frac{2e}{m_0}} \frac{U_0^{3/2}}{d^2}. \quad (11.4)$$

Here U_0 is the acceleration voltage applied to the diode, and d is the gap width. j_e is the maximum current density that can be created in a diode of gap width d and voltage U_0 . At high current the electrons can pinch, i.e., be compressed to a tight focus on the anode. Pinching results from the strong azimuthal magnetic field generated by the high-current electron beam. Current densities exceeding 1 MA/cm^2 can be achieved by this effect at currents greater than 100 kA and voltages of about 1 MV .

Although these pinches are of interest for the formation of high-intensity, point-like bremsstrahlung sources for flash X-ray radiography of fast-moving objects, they can become a nuisance when large-area beams of uniform current density are required. Such applications will be discussed below. We can, however, counteract pinching by a strong axial magnetic field in the extractor.

11.1.4 Surface Modification of Materials

High-energy electrons can penetrate deeply into materials of solid density and efficiently transform their kinetic energy into heat. Therefore a high-power pulsed electron beam can rapidly heat a surface layer of up to $100 \mu\text{m}$ thickness to temperatures above the melting point (Fig. 11.1). The actual melting depth depends on the material, the particle energy, the power density, and the pulse duration. Typically, a specific energy deposition of $3\text{--}15 \text{ kJ/cm}^3$ is required to heat a material from room temperature to above the melting point. Thus, for the achievable electron beam power densities of a few MW/cm^2 and for the penetration depth of $100\text{--}400 \text{ keV}$ electrons ($\sim 20\text{--}100 \mu\text{m}$), pulse durations of a few tens of microseconds are required. This is still short enough for us to neglect heat losses from the deposition zone. Using a high-current electron pulse, heating rates of up to 10^9 K/s can be obtained, and melting of large surface areas (up to several hundreds of square centimetres) to a depth of tens of micrometres, corresponding to the electron particle range, becomes possible. Subsequent to the pulse, rapid quenching due to heat conduction into the unaffected bulk material occurs. At the resulting high cooling rates of up to 10^7 K/s , amorphous glass-like structures or new nanocrystalline structures are created, which can improve the corrosion and wear resistance and increase the hardness of the treated surface layer. In addition, alloys can be formed by co-melting a thin surface coating together with a thin layer of the base material.

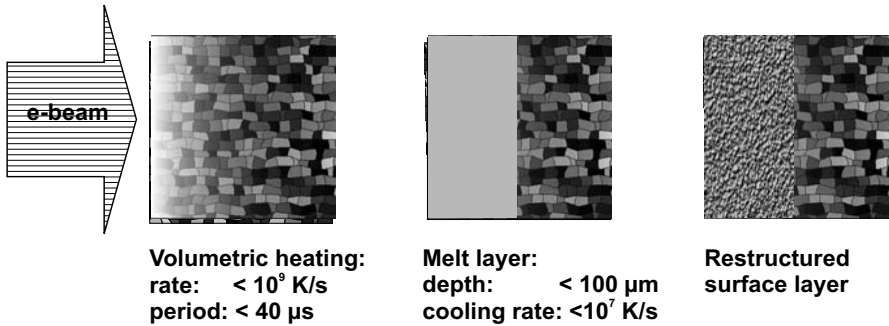


Fig. 11.1. Schematic illustration of e-beam surface modification. Owing to the high cooling rate caused by heat conduction into the cold bulk material, structural and phase changes can occur, changing the hardness, the wear resistance, and the corrosion and oxidation resistance

A schematic illustration of the pulsed-electron-beam facility GESA, which has been used for such treatments at Forschungszentrum Karlsruhe, is shown in Fig. 11.2. To create a rectangular pulse, the high-voltage pulse generator consists of four *LC* chains charged in parallel and discharged in series in a Marx-like configuration. Each stage consists of eight *LC* elements and one

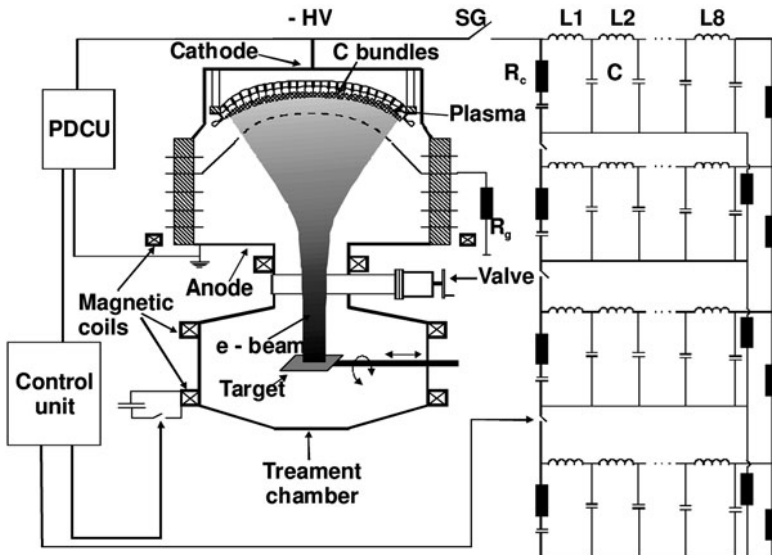


Fig. 11.2. Schematic illustration of the pulsed-electron-beam facility GESA (electron energy 50–150 keV, electron current ≤ 700 A, energy flux on target $\leq 50 \text{ J/cm}^2$). ‘PDCU’ stands for ‘pulse duration control unit’, which serves to control the pulse duration

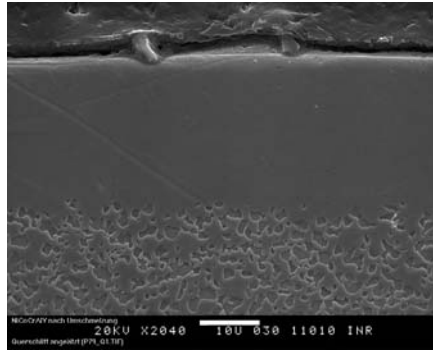


Fig. 11.3. MCrAlY oxidation protection layer after pulsed-electron-beam treatment. The *upper part* of the electron micrograph shows the restructured surface layer. *Lower part*: original MCrAlY two-phase structure

RC element that amends the pulse shape. The electron source is a multipoint explosive-emission cathode constructed from 700 graphite fibre bundles as described before, each connected through a resistor to the high-voltage generator [Engelko et al. 2001a, 2001b]. Its emissive area is 700 cm^2 .

Initially, the entire voltage pulse appears across the cathode–grid gap. This ensures a homogeneous and rapid turn-on of all bundles. After turn-on, the voltage pulse is divided between the cathode–grid and the grid–anode gap.

A magnetic focusing system consisting of six coils guides the electron beam through a 50 cm long transport section to the target and allows variation of the beam diameter in the range 6–10 cm.

The electron energy can be varied between 50 and 150 keV. Electron beam currents of up to 700 A are possible because a plasma spreads from the target into the beam at the beginning of the pulse, leading to partial beam charge neutralization. A pulse duration control unit allows the pulse duration to be adjusted between 5 and 40 μs . At the target, current densities between 1 and 20 A/cm^2 and energy flux densities of up to 50 J/cm^2 can be achieved. This is sufficient to melt any metallic material adiabatically.

Pulsed-electron-beam treatment has been applied very successfully to MCrAlY superalloy coatings, which are widely used for oxidation protection on gas turbine blades at high temperatures above 900°C. Here M stands for Ni and/or Co. Without a protective coating, the turbine blade base material would burn in an oxygen-containing atmosphere at these high temperatures. The thickness of the coating is typically 200 μm which is about a factor of ten thicker than the range of the electrons used for the treatment. Therefore, the turbine blade base material is not affected by the pulsed heat treatment.

After treatment with a 30 μs , 120 keV electron beam, maximum cooling rates of $2.5 \times 10^6\text{ K/s}$ were achieved, leading to a glassy surface layer of 20 μm

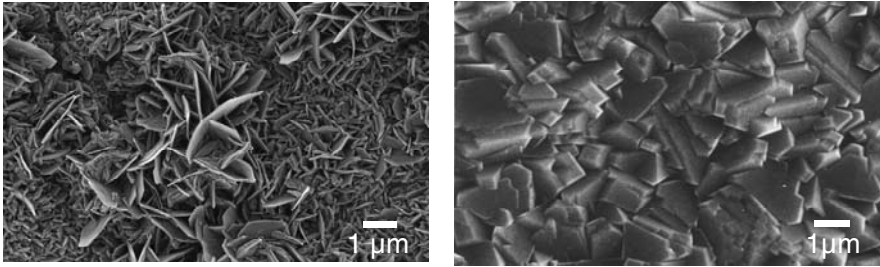


Fig. 11.4. Surface morphology of the oxide scale grown on the surface of a NiCrAlY oxidation protection layer after 200 h at 950°C. *Left*, with conventional polishing of the plasma-sprayed layer; *right*, with GESA electron beam treatment

thickness. As shown in Fig. 11.3, the original two-phase structure was changed into a single-phase structure in the melted zone. When the usual etching techniques were applied to visualise the phase structure of the material, it became obvious that the original two-phase structure had disappeared in the treated zone. Also, the surface roughness was reduced significantly and the hardness had increased from 440 HV to 1200 HV [Strauss et al. 2001].

When the MCrAlY layer is exposed to air at 1000°C Al migrates to the surface and a thermally grown Al_2O_3 oxide scale develops, which protects the underlying material against further oxidation. The stability of this layer is responsible for the lifetime of the oxidation protection layer.

Increased efficiency in the utilisation of energy can make an important contribution to more sustainable energy production. Gas-fired power plants are among those with the highest thermodynamic efficiencies. A further increase could be achieved if a higher gas temperature could be realised in the gas turbine. This requires thermal insulation of the turbine blade surface to keep the temperature of the base material and of the oxidation protection layers within acceptable limits.

The thermally grown oxide (TGO) scale not only protects the underlying material against further oxidation but also serves as a bonding layer for a thermal-barrier coating (TBC), consisting of yttria-stabilised zirconia (YSZO). The lifetime of such systems is limited by failure of the TGO, leading to spallation of the TBC. This failure mode depends on the morphology of the TGO. Since the plasma-sprayed MCrAlY layer is generally very rough, the coating is mechanically polished. Surface treatment with pulsed electron beams also leads to surface smoothing but, as described above, it creates an amorphous or nanocrystalline layer structure. As shown in Fig. 11.4, the two treatments lead to very different types of oxide scale growth. $\theta\text{-Al}_2\text{O}_3$ blades appear on the mechanically polished surface, while pure $\alpha\text{-Al}_2\text{O}_3$ grows on the electron-beam-treated surface. Depositing the TBC onto this surface results in regularly grown YSZO columns with minimal transverse tension. Therefore a longer lifetime of these coatings can be expected.

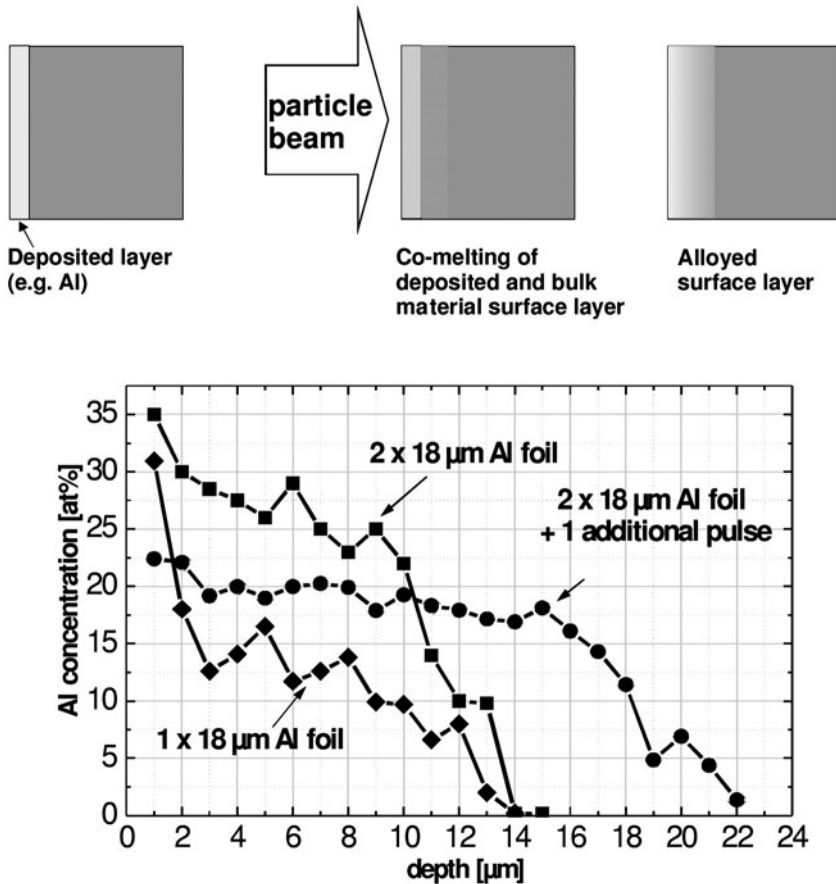


Fig. 11.5. Formation of an AlFe alloy on a steel surface. Al foils and thin surface layer are co-melted by the pulsed electron beam, leading to turbulent mixing of Fe and Al

Another very attractive application of pulsed-electron-beam treatment is surface alloying. As an example, the formation of an AlFe alloy on a steel surface is demonstrated in Fig. 11.5. For that purpose, Al-foils of thickness $18\mu\text{m}$ were deposited on the steel surface. Figure 11.5 shows the Al concentration in the surface layer after 1–3 pulses using either one or two Al foils. A rather homogeneous distribution up to a depth of $20\mu\text{m}$ can be achieved with a sequence of three pulses that co-melt two foils and a surface layer of the bulk material sequentially [Müller et al. 2005].

Alloying has also been used to reduce the corrosion of steel in Pb- and Pb/Bi-cooled accelerator-driven nuclear reactor systems (ADS) [Müller et al. 2000, 2003]. These systems are being developed to transform long-lived fission products, plutonium, and higher actinides from nuclear power reactors into

products with a shorter half-life or less radiotoxicity. Because of their hard neutron energy spectra and their inherent safety features, accelerator-driven subcritical nuclear reactors with Pb or Pb/Bi cooling are currently being developed for this task. A key problem in the development of such systems is corrosion of steel in the liquid metal. In particular, Ni is easily dissolved in liquid Pb or Pb/Bi at temperatures around 600°C or above. A protective oxide scale can form on the steel surface if a controlled oxygen concentration of around 10^{-5} at.% is maintained in the liquid heavy metal. However, this layer, consisting of magnetite and FeCr spinels, grows rather fast, and thus can lead to progressive steel oxidation and long-term instability. This can be avoided by alloying Al into the steel surface with the help of the pulsed electron beam from GESA. For that purpose, a thin Al layer is deposited onto the steel surface and co-melted with an underlying steel layer of several tens of micrometres thick. The Al becomes mixed into the molten steel owing to convection, and, owing to the rapid quenching, remains frozen in the steel matrix. When oxygen is dissolved in the liquid Pb/Bi, the alloyed Al leads to the formation of a thin protective alumina layer that grows very slowly and covers the underlying steel surface against corrosive attack. Corrosion experiments in the Pb/Bi test loops at IPPE, Obninsk, and Prometheus, St Petersburg, at flow velocities around 1 m/s have shown that only those steels where a layer containing 10% of Al had been alloyed into the surface survived the test without damage after 4000 h.

Some applications – especially the treatment of machine parts – require spatially and temporally homogeneous, stable beams. It is well known [Pareira 1983; Engelko et al. 2000, 2001] that the interaction between the beam and the target results in reflected electrons and ions, both of which move backward into the triode and change the beam profile from a more rectangular current density distribution to a Gaussian one. Moreover, it has been discovered that beam oscillations with a frequency of a few megahertz occur, whose structure and amplitude depend on the mirror ratio, i.e., the ratio of the magnetic field at the target to that at the anode. Investigations to control these instabilities are currently being undertaken [Müller et al. 2002a, 2002b].

11.1.5 High-Power KrF Lasers

Because of their high efficiency, their short wavelength (248 nm), and their high beam uniformity, KrF lasers are presently considered to be one of the most attractive drivers for inertial-fusion energy (IFE) [Bodner et al. 2000]. To explore whether the necessary laser beam power of several hundred terawatts and beam energy of several megajoules can be generated with the required efficiency of better than 5% at affordable cost, programmes have been started in several laboratories to develop the basic technologies [Sethian et al. 2001].

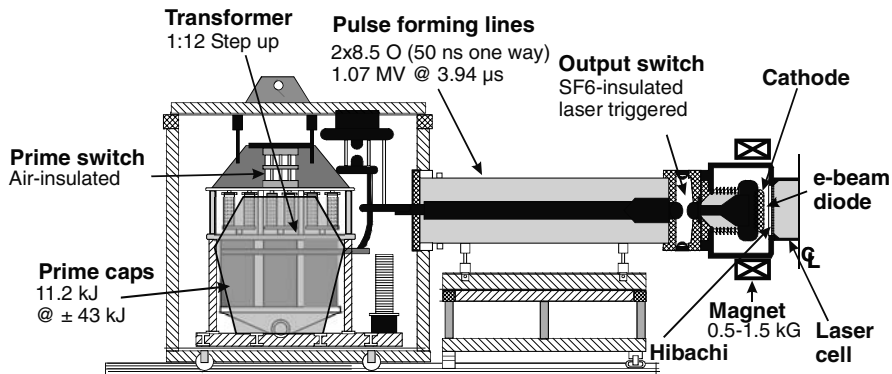


Fig. 11.6. One half of the ELECTRA pulsed-power system: 500 kV, 100 kA, 100 ns flat-top electron beam, 5 Hz repetition capability

High-power KrF lasers are pumped by large-area, high-current pulsed electron beams. Because of their modularity, the electron beam generators presently under development are considered to be scalable to the parameters required for a real IFE driver. The main challenges are to develop a durable, efficient, and cost-effective pulsed-power system; a durable electron beam emitter; a long-life, transparent pressure foil structure (which isolates the laser cell from the electron beam diode; this foil is called a ‘hibachi’); a recirculator to cool and damp out turbulence in the laser gas between shots; and long-life optical windows.

Typically, a single electron beam module must deliver 100 kA of electron beam current with a particle energy around 500 keV to the laser cell for a duration of several hundred nanoseconds. Figure 11.6 shows a schematic illustration of one half of the ELECTRA system currently being constructed at NRL Washington [Hegeler et al. 2002].

This system uses a capacitor/step-up transformer primary power system that pulse-charges a pair of coaxial, water-dielectric pulse-forming lines. The energy in the lines is then switched into the electron beam diode load using laser-triggered spark gaps. A strong axial magnetic field is used to prevent pinching of the beam in the gas cell.

A general schematic illustration of the diode, hibachi, and gas cell is presented in Fig. 11.7. In addition to the cathode, the hibachi foil support structure is the key element for a long-lived KrF laser system. It must enable efficient and reliable electron beam injection into the gas. Plasma sources based on carbon fibres or metal-dielectric structures look most promising as durable electron sources. To provide the high efficiencies required, the cathode emission must be restricted to areas between the ribs of the hibachi structure. In addition, the cathode emitter must be counter-rotated by a fixed amount to compensate for the rotation of the beam in the axial magnetic guiding field.

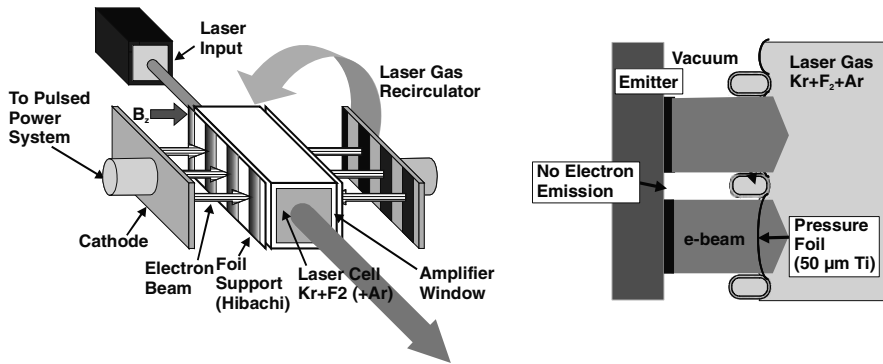


Fig. 11.7. Principal features of an electron-beam-pumped KrF laser

Experiments have also shown that large-area electron beams are subject to instabilities which can lead to energy spread and large divergence of the accelerated electrons [Friedman et al. 2000]. To damp the RF oscillations, the cathode was built as a slow-wave structure by loading the gaps between the segmented cathode areas with resistive elements.

Long lifetimes (more than 10^8 pulses) of the hibachi foil are possible only if it is cooled efficiently. The recirculator used for this purpose not only has to cool the foil and the laser gas but also has to remove turbulence from the gas before the next shot. A system based on louvres has been designed at NRL [Hegeler 2003] to solve this task. This system guides the gas stream towards the hibachi between shots and rapidly transforms the turbulent flow into a laminar flow during the pulse by opening the louvres.

11.1.6 Flash X-Ray Radiography

Pulsed X-ray radiography of explosively driven hydrodynamic experiments ('hydrotests') continues to be one of the main motivations for research on intense electron beams and related developments in pulsed power. Some of the largest hydrodynamic experiments study the implosion of mock-ups of nuclear weapons in which the actinides have been replaced by non-fissile metals. In contrast to industrial radiographic sources, where electrons are spread across the anode surface to limit the power density and to minimise anode damage, thereby allowing multiple-shot operation, high-brightness X-ray sources for 'hydrotests' are single-shot devices.

The radiographic source must be matched to the needs of the test. The main requirements are high spatial resolution, sufficient penetration power and contrast, and adequate intensity at the detector position. In addition, it is desirable to have multiple pulses to follow the evolution of the object.

Point-projection radiography as shown in Fig. 11.8 is the most common technique used to image these dynamic experiments. A pulsed 'point' source

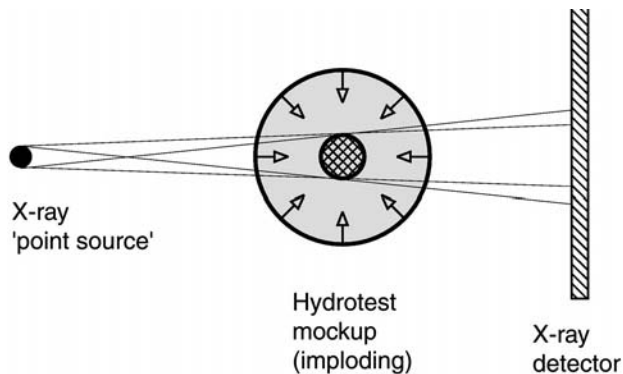


Fig. 11.8. Schematic illustration of point-projection radiography of fast-moving objects

of penetrating bremsstrahlung photons illuminates the object from behind, projecting a ‘snapshot’ of the hydrodynamic effects onto a large-area film or a camera-based imaging system.

The resolution is ultimately limited by the spot size of the radiation source, which is affected significantly by the source design. The goal is to achieve sub-millimetre spot sizes. At present, four different diode sources [Maenchen et al. 2002] are being studied (Fig. 11.9). The pinched-beam X-ray source operates above the critical current

$$I_{\text{crit}}(\text{kA}) = 8.5 (\gamma^2 - 1)^{1/2} (R_c/d), \quad (11.5)$$

where R_c is the cathode radius and d is the axial vacuum gap spacing. This current produces a strong azimuthal magnetic field, which leads to beam-pinching at the planar anode. This effect is enhanced by counter-streaming ions extracted from the anode plasma created by interaction with the electron beam. Thus a small electron beam focus is formed. A disadvantage of this source is the anode plasma, which expands into the vacuum gap and ultimately leads to an impedance collapse. Also, the sweeping electron beam during the pinch phase produces a radiographic halo. Typically, 2 mm spot sizes and electron beam power densities of around 1 TW/cm² have been reached with these diodes.

A more stable impedance and a more robust spot size are achieved with the paraxial diode shown in Fig. 11.9b. This diode produces a large-area electron beam, which enters a gas-filled drift cell and ionises the gas within a few nanoseconds. The electron beam space charge becomes compensated by the drift cell plasma, and the remaining magnetic field gradually compresses the beam to a small focus at the position of the converter target. Because of the larger diode gap and the lower beam current density, the expansion of the plasma from the drift cell has a smaller effect, and therefore a more

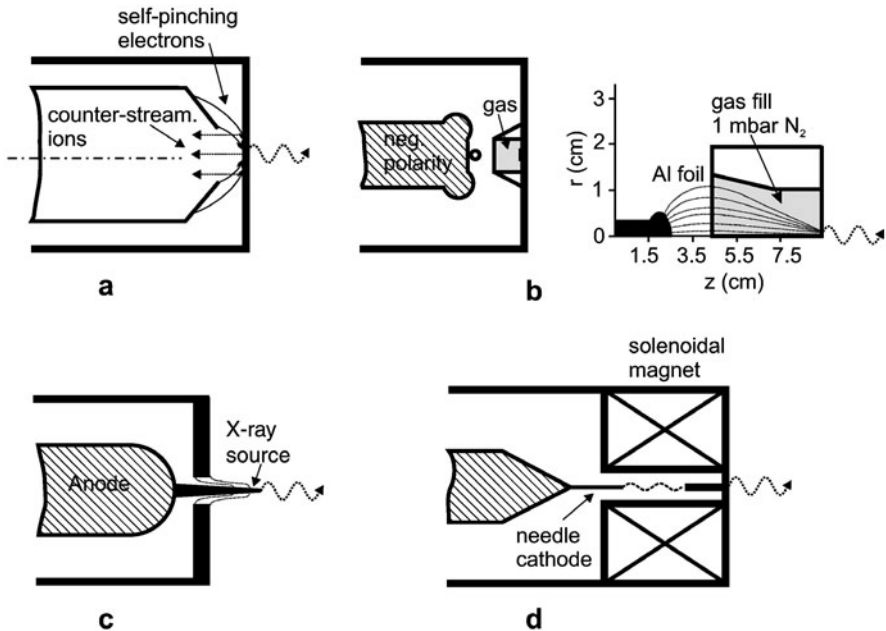


Fig. 11.9. Diode sources for the production of intense pulsed X-ray radiation. (a) Pinched-beam source; (b) paraxial diode: electron trajectories self-pinching in the gas cell are shown to the right of the geometric scheme; (c) rod pinch diode; (d) magnetically immersed diode

stable impedance history is obtained. Consequently, the paraxial diode has been the workhorse for hydrotests for several decades.

More recently, the rod pinch source has attracted much interest [Cooperstein et al. 2001]. Its geometry is shown in Fig. 11.9c. It consists of a small-diameter rod that extends through a hollow cathode. The electron beam launched from the hollow cathode self-pinches onto the anode rod. The diameter of the converter rod may be comparable to or smaller than the electron range. Electrons passing through the rod are reflected and re-enter it. The X-ray source spot size is thus solely determined by the rod diameter, which, however, owing to plasma expansion from its surface, increases with time. Spot size diameters below 1 mm have been achieved. Most beam electrons enter the rod radially, producing less dose in the desired forward cone. Nevertheless, the rod pinch diode has become a reliable high-intensity radiographic source at accelerating voltages up to 6 MV.

In contrast to the rod pinch diode, the magnetically immersed diode shown in Fig. 11.9d [Maenchen et al. 2002] operates with negative polarity. The cathode emitter is a very small needle that extends into a strong solenoidal applied magnetic field, which contains the electron orbits within a small cylinder. The diameter of this cylinder determines the spot size on the

anode. However, the very high intensity on the anode produces a hot plasma, from which ions are accelerated that interact with the electron beam and create a hose instability. Thus rotation of beam enlarges the effective spot diameter.

In a high-atomic-number bremsstrahlung converter, the dose at 1 m distance that is produced per coulomb is given by

$$\frac{\text{Gy at 1 m}}{\text{C}} = 12.9 U^{2.8} \exp \left\{ -\frac{(U + 0.5)\beta_{\perp}}{0.67\pi} \right\}. \quad (11.6)$$

where U is the voltage in megavolts, and β_{\perp} is the relativistic electron beam velocity component transverse to the radiographic axis. Thus, to achieve a high dose, it is advantageous to use a large accelerating voltage. Radiation scattered by the object causes a noise background in the image, and scattering increases rapidly with the number of mean free paths through the object. For high-atomic-number objects, the X-ray attenuation coefficient has a minimum between 3 and 4 MeV and increases at higher X-ray energies. Obviously, the minimum in the attenuation coefficient corresponds to a maximum of the mean free path. Thus an upper limit is set on the energy of the accelerator, and the accelerator design cannot take full advantage of the strong scaling of dose with beam energy. Moreover, the useful dose for imaging is a complex function of the bremsstrahlung spectrum, the attenuation coefficients of the object materials, and the spectral sensitivity of the imaging detector. Planning of hydrotests therefore requires detailed experimental, analytical, and numerical (Monte Carlo) analyses [Ekdahl 2001].

The image resolution is also determined by the movement of the object. The shock pressures in high-explosive-driven hydrodynamic experiments are multi-megabar, and the corresponding shock velocities exceed 1 cm/ μ s. To maintain a resolution of 1 mm, the pulse width of the accelerated electron beam and thus of the bremsstrahlung radiation must be 100 ns or less.

11.2 High-Power Ion Beams

Intense light ion beams are promising tools in matter research [Kanel et al. 1998], inertial-fusion energy [VanDevender and Bluhm 1993], and radiation (boron neutron capture) therapy [Bluhm and Hoppé 1999]. They can provide a technically simple, cost-effective path to delivering high specific power densities (several times 100 TW/g) to condensed matter. The key element of this approach is an accelerator, consisting of two stages, the injector diode and the post-accelerator diode, both operating at power densities of several times 10 GW/cm² and at electric fields of several MV/cm, both values being two orders of magnitude higher than in conventional accelerators. In this concept, the accelerator is powered from a repetitive multiterawatt, multi-megavolt pulse generator. The approach of the high-energy linear-induction

accelerator (HELIA) [Ramirez et al. 1985] is considered to be the most attractive concept [Moses et al. 1989] for this generator (see Chap. 8).

The most extreme requirements result from the development of drivers for IFE. Ultimately, each light-ion driver module should be able to deliver an ion beam with atomic masses greater than 4, particle energies greater than 30 MeV, and pulse energies of more than 500 kJ at power levels greater than 10 TW. Consequently, a beam with a 1000 cm² cross-section must be extracted from the accelerator if the power density in the accelerating gap is limited to less than 10 GW/cm². To focus the beam to power densities of more than 10 TW/cm² needs a spatial convergence of more than 1000. In addition, depending on the beam transport scheme, only a small divergence is tolerable.

Here we shall discuss the recent progress that has been achieved in the understanding of diode accelerator gaps, in the development of suitable ion sources, and in beam transport.

11.2.1 Accelerator Physics

To a certain extent, it seems possible to break up the development of light-ion accelerators into three parts: the development of the ion source, of the injector gap, and of the post-accelerator gap. Although there is an interaction between the gap physics and the physics of the ion and electron source plasmas, much of the accelerator gap physics is determined by the high power densities in the gap.

11.2.1.1 Injector Gap

So far, most investigations have concentrated on the injector diode gap, and here we shall summarise the results [Bailey et al. 1995; Mehlhorn et al. 1994; Hanson et al. 1992; Greenly et al. 1994, 1996; Bluhm et al. 1992; Licht et al. 1998]. The injector (Fig. 11.10) consists of a massive anode and a hollow cathode separated by a few millimetres. A high-power multimegavolt pulse is applied to the diode gap for a duration of up to several tens of nanoseconds. Prior to the application of the voltage pulse, an ion source must have been prepared on the anode surface. In most concepts, this is a pulsed plasma layer produced simultaneously with the accelerating pulse. Owing to the large electric field in the diode gap, electron field emission with plasma formation also occurs instantaneously on the cathode.

Therefore, in general, we have both an electron and an ion current in the diode. For space-charge-limited current flow from both electrodes, we obtain the following for the ratio of the ion to the electron current density:

$$\frac{j_i}{j_e} = \sqrt{\frac{Zm_e}{m_i}}. \quad (11.7)$$

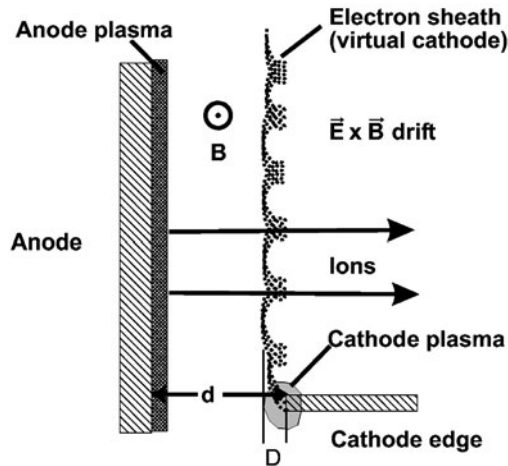


Fig. 11.10. Schematic illustration of injector diode with hollow cathode. Strong electric fields lead to explosive electron emission, with plasma formation at the cathode edge. A magnetic field is required to prevent electrons from reaching the anode. Electrons drift in the $\vec{E} \times \vec{B}$ -direction and form an electron sheath with virtual cathode

We can interpret this relation in another way:

$$\frac{j_i}{j_e} = \frac{\tau_e}{\tau_i}, \tag{11.8}$$

i.e., the current densities are inversely proportional to their residence times in the gap. Here, the residence times τ_e and τ_i for the electrons and ions, respectively, are given by

$$\begin{aligned} \tau_e &= \int_0^d \frac{dx}{v_e}, \\ \tau_i &= \int_d^0 \frac{dx}{v_i}. \end{aligned} \tag{11.9}$$

Thus the ion current portion in the diode can be increased by prolonging the electron trajectories in the diode gap. This can be achieved by deflecting the electrons with the help of self-generated or externally generated magnetic fields perpendicular to the electric field. Relying on the self-magnetic field alone, ion production efficiencies of around 50% have been achieved [Goldstein and Lee 1975, Humphries 1980], while an ion current fraction of more than 90% can be obtained with strong externally applied magnetic fields [Johnson et al. 1979].

Many aspects of the physics of the accelerating gap can be studied independently of the specific ion source if this source is homogeneous and does not expand too fast across the magnetic-field lines. Much of the gap physics, however, is dominated by electrons streaming into the diode along the magnetic field lines and forming an electron sheath and a virtual cathode. Initially, this electron sheath is quite thin and drifts in the $\vec{E} \times \vec{B}$ direction (Fig. 11.10). A fluid instability, known as the ‘diocotron’ [Buneman 1966], spreads the electrons across the diode gap within a few nanoseconds. If the sheath comes close to the anode, the high-frequency diocotron instability, whose effect on beam divergence is small, is replaced by a lower-frequency ion-mode instability, whose frequency is roughly equal to the inverse of the ion transit time in the gap [Lemke and Sultz 1995], and which therefore has a drastic effect on beam divergence.

The occurrence of instabilities and the spreading of the electron sheath over the entire gap have a strong impact on diode operation. Since the ion current density in high-power diodes in general is space charge limited, the space charge compensation that comes along with the distributed electron sheath leads to an enhancement of the ion current much above the Child–Langmuir value given by (11.5). This in turn creates a stronger diamagnetic effect of the electrons drifting in the $\vec{E} \times \vec{B}$ direction and results in a movement of the virtual cathode towards the anode. Since the magnetic flux is conserved, the rising magnetic pressure will finally stop this process, and a new equilibrium is achieved [Desjarlais 1989]. However, if the increasing diamagnetic field can penetrate into the electrode plasmas, the strength of the magnetic insulation in the diode gap is reduced and a further degradation of the diode impedance occurs. All of these conclusions were first drawn from analytic modelling and three-dimensional fully relativistic, electromagnetic, particle-in-cell code simulations [Desjarlais 1989, Quintenz et al. 1994] for rather simplified geometries. To check these predictions experimentally, new, sophisticated diagnostics had to be developed [Bailey et al. 1990, Bluhm et al. 1994, Maron et al. 1989, Yoo 1997]. Measurements with these tools have clearly confirmed the theoretical findings. Using a very sensitive and robust dispersion interferometer, even the electron density distribution in the diode gap could be measured with high space and time resolution (0.5 mm and 1 ns) [Licht and Bluhm 2000].

Figure 11.11 demonstrates the excellent agreement between the measured electron density and that predicted by an analytic diode model [Desjarlais 1989].

By means of these investigations, a rather consistent understanding of the physics of the accelerating gap has been achieved, which confirms the description of the operation of diodes outlined above.

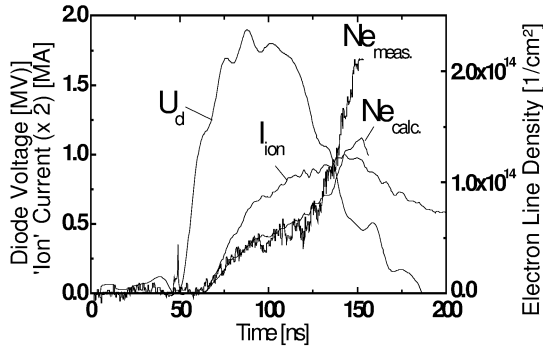


Fig. 11.11. Diode voltage U_d , ion current I_{ion} , and electron density Ne at a position 3 mm from the anode surface. Also shown is the electron density Ne_{calc} derived from U_d and I_{ion} using an analytic model for the saturated (constant-density) electron distribution

11.2.1.2 Post-Accelerator Gap

The present experience with magnetically insulated single-stage ion diodes suggests that the operational stability necessary and the low beam divergence required can be achieved only with multistage acceleration. Also, the goal of accelerating light ions to 30 MV can be reached only in a multistage configuration, since very large insulating magnetic fields would be required for single-stage acceleration. However, owing to the rapidly increasing complexity, it seems unlikely that more than two stages can be realised (Fig. 11.12). Because of the strong beam self-fields, space charge neutralisation is necessary between stages. For that purpose, the interstage drift section must be

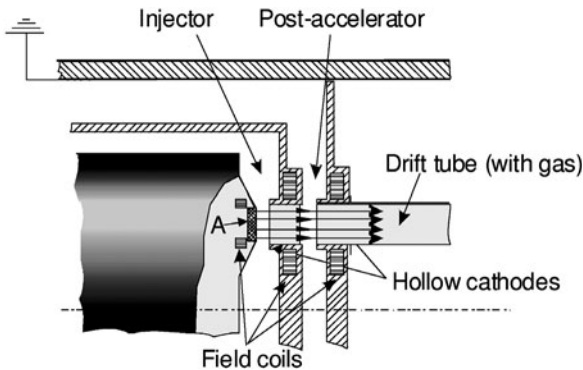


Fig. 11.12. Schematic illustration of a two-stage ion diode. The insulating magnetic field in the accelerating gaps is established by six field coils supplied by capacitor banks. The beam transport sections are filled with gas

filled with a gas or plasma and separated from the high vacuum required in the accelerating gaps.

The expectation of reduced beam divergence is based on the observation that the frequency of the ion mode depends on the ion transit time, which is different for each gap. Thus the effects of instability do not add coherently from stage to stage, and the ion divergence should decrease. Simulations with the PIC code Quicksilver [Quintenz et al. 1994] have confirmed that for sufficiently low beam current densities, ion divergence can be reduced significantly by post-acceleration [Slutz et al. 1994].

Only very few preliminary two-stage experiments have been carried out [Lockner et al. 1993, Miyamoto et al. 1992, Lockner et al. 1994], most of them at very low power and low voltage. Nevertheless, these experiments showed a strong reduction of beam divergence.

Some of the results that have been obtained for the injector gap can certainly be extended to the post-accelerating gap. Since the electric fields in this gap will be of similar magnitude, a virtual cathode will be formed too, and it is very likely that the post-accelerating gap will also be filled entirely with electron space charge. Nevertheless, there are certain differences between the post-accelerator and the injector that need additional consideration. It has been found [Slutz and Desjarlais 1990] that, as in the single-stage case, a limiting voltage U_{2^*} exists, depending on the injected ion energy W and the strength of the magnetic insulation B , above which an unlimited current density can penetrate the stage without the formation of a virtual anode. A virtual anode can be useful, however, to suppress the acceleration of ions from plasmas that form at the injection side of the stage. It is well known from the fixed-gap monopolar problem of beam injection that, above a maximum current density $j_2(U_2)$ penetrating the gap, instabilities occur, which prevent further transfer of current through the gap [Birdsall and Bridges 1961].

Such a limiting current also exists for the bipolar case with movable virtual cathodes. However, this limitation appears only below a second limiting voltage $U_{2^{**}}$, which is unique to the theory of multistage acceleration and depends on W and B . If the electron sheath fills the entire post-acceleration gap, $U_{2^{**}} = 0$. As can be seen from Fig. 11.13, if suppression of unwanted ions from the injection side of the second stage were required, the saturated behaviour would limit the final beam energy to only slightly higher than the critical insulating voltage U_c determined by the magnetic-insulation strength. On the other hand, if a virtual anode cannot be established, we must tolerate a certain fraction of unwanted ions, extracted from the anode side of the post-accelerator. Fortunately, steady-state calculations of the ion current extracted from the injection side of the second stage show that even a small fraction leads to a significant increase in U_{2^*} [Slutz 1993].

From this discussion of the peculiarities of post-acceleration, it is obvious that detailed experimental investigations of the second stage are necessary. In particular, time- and space-resolved measurements of electric and magnetic

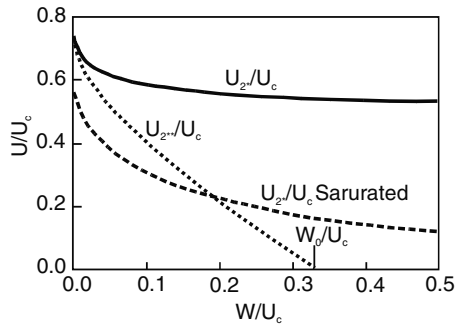


Fig. 11.13. Critical voltages U_{2^*} and $U_{2^{**}}$ in the post-acceleration gap as a function of the injected ion energy W , normalized to the critical voltage U_c for magnetic insulation (from [Slutz and Desjarlais 1990])

fields are needed to identify the mode of operation and to probe the existence of a virtual anode. Of course, the degree of divergence reduction and the operational stability that can be attained by post-acceleration are of greatest interest. These measurements are still awaited.

11.2.1.3 Ion Source

The lack of an adequate preformed ion source has greatly hampered progress in the development of a light-ion beam driver during the last decade. Although the preformed proton source [Laqua et al. 1995] used in experiments at the KALIF facility is acceptable for studying the physical phenomena of accelerating gaps, it is inappropriate for accelerating voltages of 30 MV. The pitfalls of ion source development can be attributed to the following circumstances:

- The ion source must emit homogeneously a current density of around 1 kA/cm^2 for a duration of 50 ns, i.e., supply $\sim 10^{15}$ ions/cm² over an area of several hundred square centimetres on the anode surface; 10^{15} ions/cm² are equivalent to a few atomic monolayers.
- The source should conform smoothly to the desired anode shape. This may need a conducting surface in the vicinity if the source is a plasma.
- The source must not expand into the accelerating gap by more than a small fraction of the dynamic gap (5–10 mm).
- It must be ready to emit when the voltage pulse appears in the diode.
- It should emit a single ion species.
- It should scale to repetition rates of a few hertz and to lifetimes of 10^8 pulses. For development in the intermediate term, a single-shot source meeting the above requirements would be adequate for assessing the properties of diode operation and beam transport.

All electrode surfaces, including the active source area, will be covered with a few monolayers of contaminants [Cuneo et al. 1997, Cuneo 1999 and references therein]. The main adsorbates are H_2 , H_2O , CO , CO_2 , and various species with compositions C_nH_m , with binding energies on the relevant electrode surfaces in the range 0.4–1.8 eV [Cuneo 1999]. In addition, more tightly bound oxides (1.7–3.5 eV) may exist on the surface. Various cleaning techniques (heating and RF glow discharge) have been applied to remove the contaminants. However, at the typical base pressure conditions of 10^{-3} – 10^{-2} Pa in large-scale pulsed-power systems, the recontamination rate can be as high as a few monolayers per second. Cleaning can therefore only be successful if the base pressure in the vacuum chamber is reduced below 10^{-3} Pa.

If adsorbates are present on electrode surfaces in the vicinity of a high-power diode, they will eventually be released owing to electrons diffusing to the anode side or owing to stray ions hitting the cathode surface [Vesey et al. 1999]. It has been pointed out [Cuneo et al. 1997] that, in the environment of a high-power diode, thermal desorption becomes much more important than stimulated desorption.

Two types of ion sources must be distinguished at this point: field emission and space-charge-limited emission sources. Field emission threshold sources such as the LiF source investigated at Sandia [Cuneo et al. 1997] are inherently more susceptible to the release of gaseous adsorbates from the surface. If the desorbed gas layers develop into a plasma, a zero-work-function emitter begins to compete with the field emitter and rapidly dominates the beam composition. This behaviour has been observed on PBFA II and SABRE and was termed the parasitic-load problem. While initially Li ions are the most abundant species, later in the pulse C, O, and H prevail.

In the case of a space charge limited active (plasma) source, such as the TiH source used on KALIF [Laqua et al. 1995], surface contaminants are mixed into the source plasma at its creation. Since hydrogen has the largest mobility, it tends to dominate at the plasma edge. Therefore, very little C, O, Ti, etc. were observed in the extracted beam. A possible way to prevent contamination is the cryogenic source [Kasuya et al. 1991], where a gas is sprayed onto a cooled anode and frozen out in a thin layer immediately before the pulse, such that recontamination is avoided.

11.2.2 Beam Transport

Efficient transport of intense ion beams (light and heavy) is necessary for ion-driven inertial-fusion energy (Fig. 11.14). It has been stated earlier that the most preferable transport mode would be self-pinch transport (SPT). In SPT, the space charge of the beam becomes compensated, while the net self-magnetic field is sufficiently large to confine the beam particles. To realise SPT, the net beam current required is given by

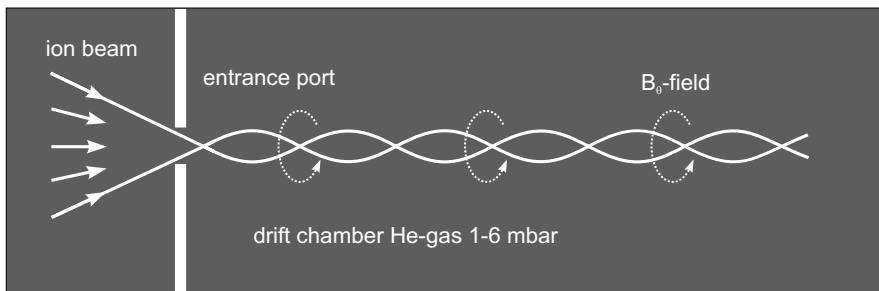


Fig. 11.14. Schematic illustration of self-pinch ion beam transport

$$I_{\text{net}} > \left(\frac{u_{\perp}}{u_b} \right)^2 I_{\alpha}, \quad (11.10)$$

where u_b and u_{\perp} are the total particle velocity in the beam and the velocity perpendicular to the transport axis, respectively. I_{α} is the Alfvén current, given by

$$I_{\alpha} = 31 \times 10^6 \left(\frac{A}{Z} \right) \beta_0 \gamma_0, \quad (11.11)$$

where A is the atomic number of the ions and Z is their charge state. For a long time, ion beam SPT was considered to be impossible because of the rapid ion-beam-induced gas ionisation, which would prevent the establishing of sufficiently high net currents. However, recent numerical simulations [Welch et al. 1996, Welch and Olson 1996, Rose et al. 1999] and a pioneering experiment at the Naval Research Laboratory [Ottinger et al. 2000] suggest that ion beam SPT should be possible in a certain window of gas pressure. Theory predicts that there is a pressure window for SPT around $n_g \sim Z n_b$, where n_g and n_b are the gas and beam particle densities, respectively.

12 Pulsed Discharges Through Solid and Liquid Dielectrics

12.1 Extracorporeal Shock Wave Lithotripsy

In addition to pulsed laser systems, lithotripsy was one of the first successful civil applications of pulsed-power techniques. Since its introduction in 1980, extracorporeal shock wave lithotripsy (ESWL) has become the most effective tool for the treatment of diseases caused by stones, such as urinary and biliary stones [Coleman and Saunders 1993]. The technique is based on the focusing of shock waves generated outside the body onto stones located inside the human body. Although the detailed mechanism of stone fragmentation is still not completely understood, it seems most likely that it is a combination of direct and indirect effects. The direct effects are related to tensile stresses resulting from internal reflection of the shock wave, mainly at the stone boundary or at internal fissures. The indirect effects are due to phenomena in the liquid medium surrounding the stones, including cavitation and pitting [Lokhandwalla and Sturtevant 2000]. Today, several million patients have been treated worldwide successfully, with very few side effects.

The first lithotripters were based on pulsed underwater electrical discharges between spark gap electrodes located at the focal point of an ellipsoidal reflector. Consequently, the object to be destroyed was placed at the second focus of the ellipsoid. As discussed in Chap. 2, the impedance of a spark is mainly resistive, with an additional series inductance. As the spark channel becomes heated during the electrical discharge, it expands and drives a shock wave into the surrounding water. Today, three different types of shock wave generators are in use (Fig. 12.1). Besides the underwater electrohydraulic (EH) discharge generator, electromagnetic (EM) and piezoelectric (PE) shock wave generators are on the market. All generators use a high-voltage capacitor discharge to induce a physical effect that results in the formation of an underwater shockwave. The electromagnetic generator is based on a flat coil and a metal membrane in front of it. It resembles a powerful underwater loudspeaker. The pulsed discharge current through the primary coil induces eddy currents in the metallic membrane, accelerates it into the adjoining water and launches a planar pressure pulse. An acoustic lens is used to focus the wave at the object. The piezoelectric generator utilises the property of certain anisotropic crystals of expanding if they are

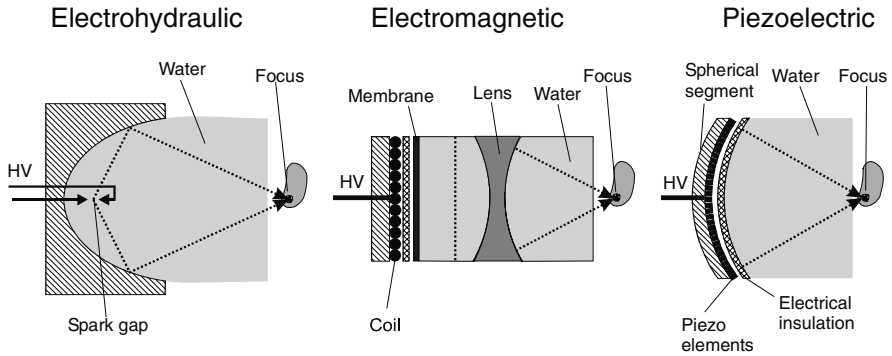


Fig. 12.1. Schemes for shock wave generation for lithotripsy, based on electrohydraulic, electromagnetic, and piezoelectric discharges

exposed to an electric field. A self-focusing system is obtained by placing several thousand crystals on a spherical surface.

Typical values of the parameters of the discharge circuit are presented in Table 12.1 [Coleman and Saunders 1993]. Generally, the electro-acoustical efficiency, i.e., the ratio of the acoustical energy to the electrical energy available to the transducer, is of the order of 0.1%. The pressure waveform resulting from an electrohydraulic discharge consists, at the intracorporeal focus, of a fast-rising positive (compressive) pulse with a peak amplitude of less than 50 MPa and a negative (decompressive) wave of amplitude less than 10 MPa (Fig. 12.2). The positive peak lasts for about 1 μ s, and the negative wave has

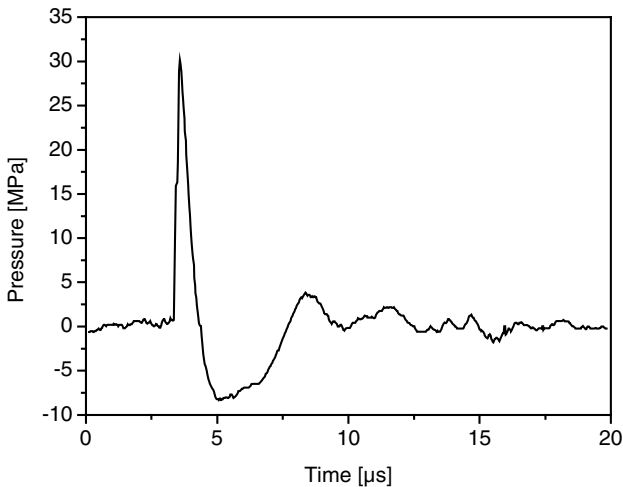


Fig. 12.2. Typical pressure pulse waveform of an electrohydraulic lithotripter at the focus

Table 12.1. Typical values of parameters for lithotripters

Source type	Load type	V (kV)	C (nF)	L (nH)	R (Ω)	I_0 (kA)	E_0 (J)	η_{ea} %
EH	Resistive	10–30	40–200	50–200	$\ll 1$	10–30	15	0.5
PE	Capacitive	2–6	300–800	1000	< 1	1–3	5	0.05
EM	Inductive	5–20	1000–1500	> 1000	< 1	4–10	50	0.03

a duration of 3–5 μ s. Several hundred to a thousand pulses are required to fragment the stones to pieces of sufficiently small size (< 1 mm) that can be discharged naturally. It has been found that many small pulses are more effective in reaching this goal than a few strong pulses.

Recently, extracorporeal shock waves have also been considered to be an efficient therapy in orthopedics and traumatology [Haupt 1997].

12.2 Electroimpulse Destruction of Solid Dielectric Materials

12.2.1 General Phenomena and Energy Balance

A ‘buried’ pulsed electric discharge in a solid dielectric, depositing an energy of 10–100 J/cm within a few microseconds, heats the spark channel to temperatures above 10^4 K and creates a pressure of 10^9 – 10^{10} Pa. The spark channel, initially only a few tens of micrometres wide, expands and launches a pressure wave into the surrounding solid material, which can lead to its disintegration. The energy balance equation for the spark channel can be written as

$$p dV + dW = dQ, \quad (12.1)$$

where p is the pressure in the channel, and W is the sum of the internal energy W_{int} of the channel products and the losses W_{loss} due to leakage at the channel ends, to radiation, and to heat conduction. Q is the energy provided by the discharge.

To determine the channel expansion and the pressure field around the spark, one has to add the momentum equation and the equation of mass conservation and solve the system with the appropriate equation of state, both for the channel products and for the solid. A complete numerical simulation is very difficult, and for heterogeneous composite materials is probably impossible. However, to give an orientation, a rather simple hydrodynamic model using boundary conditions for the radius of the expanding spark channel derived from experimental observations, has been adopted in the literature [Burkin et al. 1975]. Also, losses from the channel are neglected, and an equation of state of the form

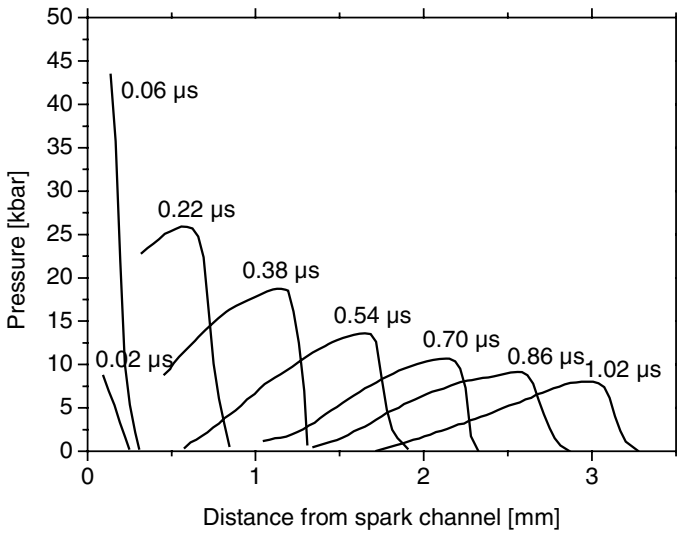


Fig. 12.3. Time-dependent calculated pressure wave profiles originating from a discharge channel in a plexiglas body [Zinov'ev and Semkin 1978]

$$W_{\text{int}} = \frac{pV}{\chi - 1} \quad (12.2)$$

is used [Zinov'ev and Semkin 1978], where χ is the effective ratio of specific heat capacities. Results from this kind of analysis for spark channels in plexiglas samples are shown in Fig. 12.3 [Burkin et al. 1975, Zinov'ev and Semkin 1978]. As the pressure pulse propagates into the solid material, its amplitude decreases and its profile becomes triangularly shaped, which is important for the destruction of composite materials.

To initiate the discharge, the arrangement drawn schematically in Fig. 12.4 is used. A capacitive energy storage device delivers a fast-rising voltage pulse of a few hundred kilovolts to a rod electrode touching the solid, which rests on a grounded plate electrode. A discharge through the solid will occur if its breakdown voltage is smaller than the applied voltage and if the breakdown strength of any other path outside the solid is larger. A necessary condition for this is that the local electric field inside the solid body exceeds the breakdown field, while it does not in the dielectric surrounding it. This can always be accomplished if the solid body is embedded in a dielectric liquid whose breakdown strength is larger. A further possibility is to concentrate the electric field in the solid and to lower it outside. This requires a liquid with much larger dielectric constant than that of the solid. Finally, the path length between the electrodes through the liquid could be made much larger than the path length in the body. For example, if the solid body is spherically shaped, the shortest path-length outside the body is $\pi/2$ times larger.

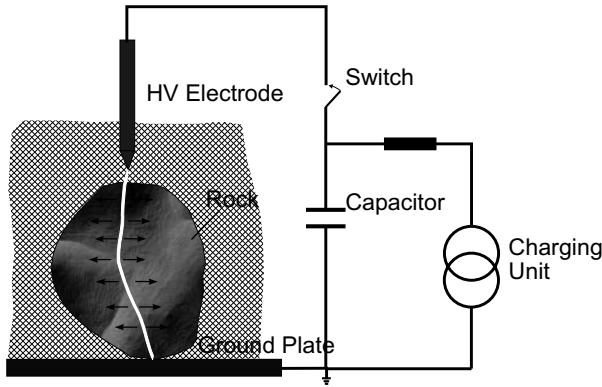


Fig. 12.4. Schematic illustration of a set-up to induce an electric discharge through a solid dielectric material

A suitable dielectric liquid is water, whose breakdown strength increases strongly if the rise time of the voltage pulse is reduced. This is shown schematically in Fig. 12.5, where the breakdown field strength of water is compared with that of a solid rock material, of transformer oil, and of air. It can be seen that at short voltage ramp rise times, the breakdown strength of water becomes greater than that of the solid material (see also Sect. 2.3.3). This effect was first discovered in the late 1950s both at Tomsk Polytechnical University [Sjomkin et al. 1995] and at Aldermaston, where it was utilised for the design of low-impedance, high-power pulse-forming lines with a water

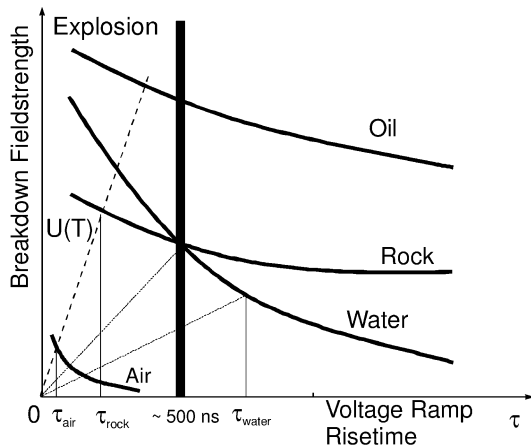


Fig. 12.5. Dynamic breakdown strength of liquid, solid and gaseous dielectrics as a function of the voltage ramp rise time. Below a critical value of the voltage ramp time, the breakdown strength of water becomes larger than that of most solid dielectrics

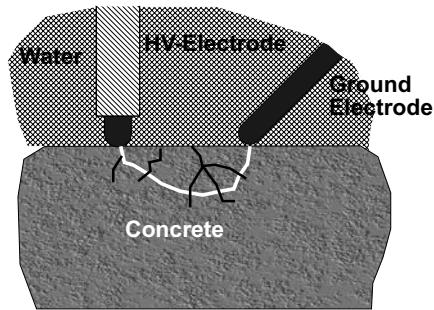


Fig. 12.6. Electrode arrangement to achieve scrape-off from a surface. This requires that the high-voltage breakdown strength between the electrodes is larger outside the body than inside

dielectric [Martin et al. 1996]. This can be understood by considering the streamer mechanism of electric breakdown in liquids, where the streamer velocity depends only weakly on the macroscopic electric field strength. Rather, the velocity is determined by the field at the tip of the gaseous filaments (see Sect. 2.3.2). Nevertheless, it is difficult to understand why the breakdown strength of a liquid can become larger than that of a solid material, since it is well known that the ‘intrinsic’ breakdown field strength (for thin samples and short periods of stress) of solid dielectrics is higher. Recently, it has been suggested and experimentally demonstrated that the breakdown of gas-filled pores inside the solid may play an important role in this process [Lisitsyn et al. 1999].

Although transformer oil has a higher breakdown strength than water, it is obviously not appropriate for many technological applications, especially for recycling. Water not only has a good insulation strength if it is stressed for a short period of time, but also has a very high dielectric constant and thus pushes the electric-field lines into the solid material, which, in general, has a much lower dielectric constant. Of course, this effect occurs only if we have a layered distribution of liquid and solid materials between the electrodes. However, this is the most frequent situation in an operating discharge vessel filled with pieces of material to be fragmented.

Water also allows one to realise a configuration where both the high-voltage electrode and the grounded electrode contact the solid at the same side (Fig. 12.6). In this case the discharge can be carried through the solid and blow off pieces from its surface. By scanning across the surface with this pair of electrodes, one can remove material layers from large areas.

To assess the efficiency of the destruction of a material by pulsed electric discharges, one has to consider the following steps. Charging of the capacitive energy storage device can certainly be carried out with efficiencies $\eta_1 > 0.95$. For most industrial applications, tap water, with a conductivity around 0.6 mS/cm, is chosen as the dielectric liquid. In many cases, the con-

ductivity rises during the process because of salt release from the fragments. Therefore electrolytic current losses occur before breakdown. To minimise these losses, most of the electrode rod needs to be covered by a solid insulating material. If the electrode tip does not contact the material the discharge may be delayed and the electrolytic losses can become quite large before breakdown, depending on the water quality and on the material filling factor in the interelectrode gap. Values as low as 0.2–0.4 have been measured for the pulse-coupling efficiency η_2 on FRANKA-Stein, a semi-industrial prototype for concrete fragmentation (see below) in positive polarity. In negative polarity, η_2 fell below 0.1. However, by controlling the water quality and the filling fraction, the losses can be reduced to 10% and η_2 approaches 0.9. It has been found that a conductivity of up to 2 mS/cm can be tolerated in the process water.

Since breakdown is a stochastic process, not every pulse will lead to a discharge in the solid. The probability can vary over a wide range, depending on the geometry, the dielectric properties of the material, the electrolytic conductivity of the water in the process chamber, etc. However, in an optimised configuration, this probability η_3 can be as large as 0.8–0.9. Only a fraction η_4 of the available electric energy is deposited in the discharge channel. The rest is wasted in the generator, i.e., appears as ohmic and dielectric losses. However, experience has shown that $\eta_4 = 0.65$ –0.7 can be achieved. Since the electrodes do not always touch the solid, part of the arc channel can arise in the surrounding liquid, where it is less effective. Therefore, another efficiency coefficient η_5 must be introduced to account for this effect ($\eta_5 \sim 0.9$).

The product of all these efficiencies leads to the estimate that a fraction $\eta \sim 0.4$ of the stored electric energy can be released in the useful part of the arc channel. This energy Q splits into various forms:

$$Q = W_{\text{mech}} + W_{\text{int}} + W_{\text{loss}} , \quad (12.3)$$

where $W_{\text{mech}} = \int p \, dV$ is the mechanical work performed by the expanding channel in the surrounding solid. If losses due to the fast, pulsed character of the process are neglected, one can estimate a thermodynamic efficiency $\eta_6 = W_{\text{mech}}/Q = 1 - W_{\text{int}}/Q$. Q is obtained from current and voltage measurements. Using (12.2) for W_{int} with $\chi = 1.1$ –1.2 and deriving V from experimental observations of the channel radius and p from the simplified hydrodynamic simulations mentioned above [Sjomkin et al. 1995, Burkin et al. 1975], one can estimate $\eta_6 = 0.1$ –0.2. This relatively small value results from the large part of the internal energy that is expended on dissociation and ionisation. Losses start to become important if the ratio of the channel radius r_c to the channel length ℓ_c exceeds 0.1. Taking all efficiencies into account leads to the conclusion that $\eta_{\text{tot}} = 4$ –8% of the electrical energy is available for the destruction of the solid material.

Part of this energy is expended in deforming the solid. If the main application is fragmentation, one may consider that only that fraction of energy

which is used to create new surfaces is beneficial. In this case the efficiency becomes

$$\eta_{\text{frag}} = \frac{\sigma A}{W_{\text{mech}}} \eta_{\text{tot}}, \quad (12.4)$$

where σ is the specific free surface energy, and A is the area of the newly created surface. Using the assumption that most of the energy W_{mech} is expended on plastic deformation of the solid, represented by W_{pl} , and applying the approximate relation [Sjomkin et al. 1995]

$$W_{\text{pl}} = 9\sigma A \ln \left(\frac{G}{\pi \Sigma_y} \right) \quad (12.5)$$

where Σ_y is the yield strength ($3\text{--}300 \times 10^6 \text{ N/m}^2$) and G is the shear modulus ($1\text{--}4 \times 10^{10} \text{ N/m}^2$), one obtains $\sigma A \approx (0.013\text{--}0.047) \times W_{\text{mech}}$; i.e., $\eta_{\text{frag}} \approx 0.04\text{--}0.32 \%$.

This value has to be compared with the corresponding value for mechanical fragmentation devices, which is of the order of 0.002–1%, depending on the degree of fragmentation. We can therefore conclude that electric-impulse fragmentation is energetically comparable but not superior to mechanical fragmentation methods. Consequently, one should use the electric method particularly for those applications where its technological benefits are obvious. Among these benefits are the smaller width of the grain size distribution curve, the relatively small amount of contamination introduced by the process, and the low amount of heat transferred to the milled material on average. However, its main advantage is the capability for selective destruction. Consequently, electrodynamic fragmentation can be used to destroy or scrape off material, to mill material to a given small grain size, and to separate composite materials at boundaries or interfaces, maintaining the integrity of certain components.

12.2.2 Selectivity of Destruction

Recycling of composite materials (such as concrete and fibre-glass-reinforced plastics) or material composites (such as electrical apparatus and circuit boards) and recovery of minerals from a rock matrix requires separation of components. Electric-impulse destruction can produce separation at material or grain boundaries by three effects:

1. At inclusions whose dielectric properties are very different from those of the matrix, the electric field intensity can be magnified and attract the discharge track to the inclusion, where it can continue to develop along the boundary. This is schematically shown in Fig. 12.7a, where a conducting sphere has been embedded in an insulating matrix. In this case separation of the inclusion from the matrix is caused directly by the discharge channel.

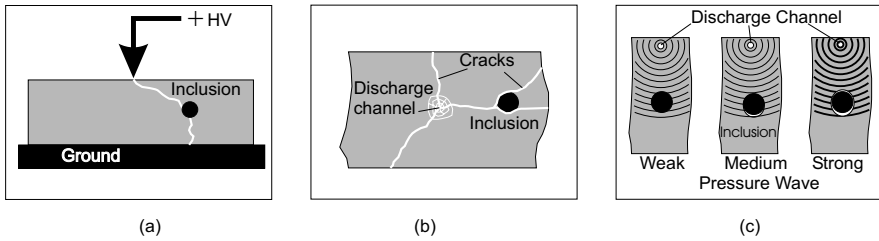


Fig. 12.7. Mechanisms by which components in a composite material can be separated. (a) Metallic inclusions or inclusions with a high dielectric constant can attract the discharge track. (b) A crack propagating from the discharge channel into the solid can branch around an inclusion if the mechanical properties of the inclusion are different from those of the matrix. (c) A compression wave can be transformed into a tensile and a shear wave by reflection and refraction at an inclusion and separate it from the matrix

2. A second, more important effect starts from cracks created in the immediate surroundings of the channel. As can be concluded from Fig. 12.3, the pressure exerted by the expanding channel almost always exceeds the tensile strengths of materials and leads to the formation of cracks. If cracks have been formed in contact with the spark channel, channel products can penetrate into them and exert a force on the crack walls. The character, the dynamics, and the intensity of crack formation are determined by the rate of energy deposition in the channel and by the properties of the material. Brittle materials show a large number of cracks in a radial zone a few millimetres in size around the discharge channel, created early in the discharge. In a later phase, a number of radially propagating cracks start to grow from this zone. The extension and the density of cracks around the channel correlate with the rate of energy release [Sjomkin et al. 1995]. However, the number of cracks reaching the surface of the sample depends more on the total energy released in the spark channel. Consequently, one can conclude that to achieve comminution, a high power of the pulse is required, while the detachment of large fragments is most effectively achieved with high pulse energies deposited over a longer time interval. For the selectivity of fragmentation, it is important to realise that material inhomogeneities in general and acoustic inhomogeneities in particular influence the propagation of cracks in a composite material. The reason for this is the existence of increased mechanical stress at the boundary of an inclusion. Stress waves reflected from inhomogeneities or inclusions can interact with the growing crack before the inclusion is reached [Guz 1974, Sher 1974, Martynyuk and Sher 1974, Volodarskaya et al. 1975]. If cracks hit the inclusion they can branch, depending on the angle of incidence, as schematically indicated in Fig. 12.7b, and separate the inclusion from the matrix.

3. A third effect leading to separation at the interface between an inclusion and the surrounding medium is connected with the action of an incident compressive wave launched from the discharge channel [Achenbach et al. 1970, Baron and Matthews 1961, Pao and Mow 1963, Kanel et al. 1996]. This is schematically shown in Fig. 12.7c. Initially, in the immediate surroundings of the spark channel, the wave has the character of a shock wave; later, it develops into a compression wave. It has been shown [Achenbach et al. 1970] that a compressive stress wave is converted into a tensile wave after refraction and reflection inside an inclusion. At small amplitudes separation occurs first at the shadow side if the inclusion has a higher acoustic impedance. Complete separation over the entire interface between the inclusion and the matrix was observed at sufficiently high wave pressures.

An important question is whether inclusions can be separated unbroken from the matrix. It is well known that a shock wave arriving at a free surface or at a material interface with a strong jump in acoustic impedance can lead to spallation [Kanel et al. 1996]. A big advantage of electric-impulse destruction is that the energetic parameters of the pulsed-power generator can be varied over a wide range and adapted to the physico-mechanical and acoustic properties of the composite. Because of the complexity of composite materials, these parameters have to be determined experimentally for each material.

12.2.3 The Fragmentation Device

Since gas bubbles created during the high-voltage discharge must disappear from the discharge vessel before the next pulse can be applied, the pulse frequency cannot be extended much above 10 Hz. Therefore a material throughput per discharge section of a few hundred kilograms per hour, which is necessary for many industrial processes to become economic, requires an interelectrode distance of a few centimetres. To break down a material bed of this size electrically, a voltage pulse of a few hundred kilovolts is required. A fast-rising voltage pulse of this amplitude can be generated with the help of a Marx generator ([Marx 1924]; see Sect. 3.2). The Marx generator should be able to produce pulses with an energy content of a few kilojoules and deliver a large fraction of this energy to the discharge channel. This requires a low internal resistance of the Marx generator, which is also necessary to obtain a fast-rising voltage ramp. High power, typically a few gigawatts, is needed if a large degree of fragmentation is desired. Therefore, the Marx generator and its connections to the discharge vessel should have a low inductance too. In cases where big material lumps are acceptable and where the main goal is to separate components without destroying them, it may, however, become necessary to increase the inductance.

The baseline design of a Marx generator where milling is the main application is shown in Fig. 12.8. This generator, which has been built for recycling



Fig. 12.8. Photograph of a 400 kV, 1.8 kJ Marx generator designed to operate at 10 Hz with a component lifetime of 10^8 pulses. The generator discharge period is $2.5 \mu\text{s}$

of metals from dross and for milling of special glasses, consists of seven stages with two capacitors of capacitance 72 nF per stage. Its inductance, including the contributions from the lead and the high-voltage electrode, has been measured to be $7.7 \mu\text{H}$. The internal resistance of the erected Marx generator is largely determined by the resistance of the spark gaps used as closing switches in the configuration, and has been measured to be around 0.5Ω for the present design. With this small resistance, about 80% of the available energy can be deposited in the reaction chamber. Each capacitor is charged up to 60 kV. Thus a 1.8 kJ oscillating pulse train with a maximum amplitude of more than 400 kV and a period of $2.5 \mu\text{s}$ is achieved. Despite the large voltage reversal and high ringing frequency, a lifetime of more than 10^8 pulses has been rated by the capacitor vendor.¹ The switch electrodes are copper-tungsten spheres with a Borda profile [Borda 1766] to assure a homogeneous burn of the electrode material. Polyethylene is used as the switch housing material.

The Marx generator itself is housed in a thick-walled metallic tank, visible behind the generator in Fig. 12.8. Transformer oil is used in the tank for high-voltage insulation and as a cooling medium. The pulse from the generator

¹ Atesys.

is transmitted through a plexiglas interface to the reaction chamber using a large-diameter flexible metallic tube.

Some important aspects of operation in an industrial environment are high-voltage safety, electromagnetic interference, and noise protection. High-voltage safety can be ensured by standard regulations and will not be discussed here. However, to operate electronic devices safely in the environment of the Marx generator careful shielding is required. It turns out that shielding of the magnetic stray field is difficult to achieve with non-ferromagnetic materials. On the other hand, Mumetal may be too expensive for some applications. However, by wiring the Marx generator such that closed loops are avoided and internal currents compensate each other, one can drastically reduce the external magnetic field. Another source of electromagnetic interference and noise is the spark in the discharge vessel. Therefore, either the discharge vessel itself needs to be built as a Faraday cage or it needs to be installed in a screening box, which, at the same time can serve as sound insulation.

In many cases the discharge vessel is built from polyethylene except for the bottom part, to reduce electrolytic current losses. Since the process water can become increasingly conductive during operation, the high-voltage electrode must be insulated anyway, except for a small tip. In this case it is acceptable to use a metallic vessel, which then itself can shield the electromagnetic noise. To relieve the electric-field stress at the insulator–metal–water triple point, the tip at the end of the electrode is shaped like a mushroom. Depending on the process, the bottom part of the vessel is built as a mesh, a grid, or a closed half-sphere.

In Fig. 12.9, the voltage and current wave shapes and the derived spark channel resistance are presented for various conditions in the discharge vessel. For this series of measurements, an interelectrode distance of 30 mm was chosen. The voltage signal shown in Fig. 12.9, which was measured with a fast resistive voltage divider, includes the inductive voltage drop at the electrode and spark inductances. To calculate the spark resistance R_s , it must therefore be corrected:

$$R_s = \frac{U(t) - LdI/dt}{I(t)} \quad (12.6)$$

where $U(t)$ and $I(t)$ are the measured pulse voltage and current, respectively, and L is the inductance between the tap-off of the voltage monitor and ground.

If the material (concrete) fills the entire gap, a rapid breakthrough is achieved during the initial rise of the voltage pulse and the mean value of the spark resistance remains above 2Ω . It is observed that the spark resistance rises periodically around the zero-crossing of the current. This has been attributed to an inflow of cold material from the channel wall and to heat losses dominating over heat production at this time, both leading to cooling of the channel plasma. If a large fraction of the discharge runs through water,

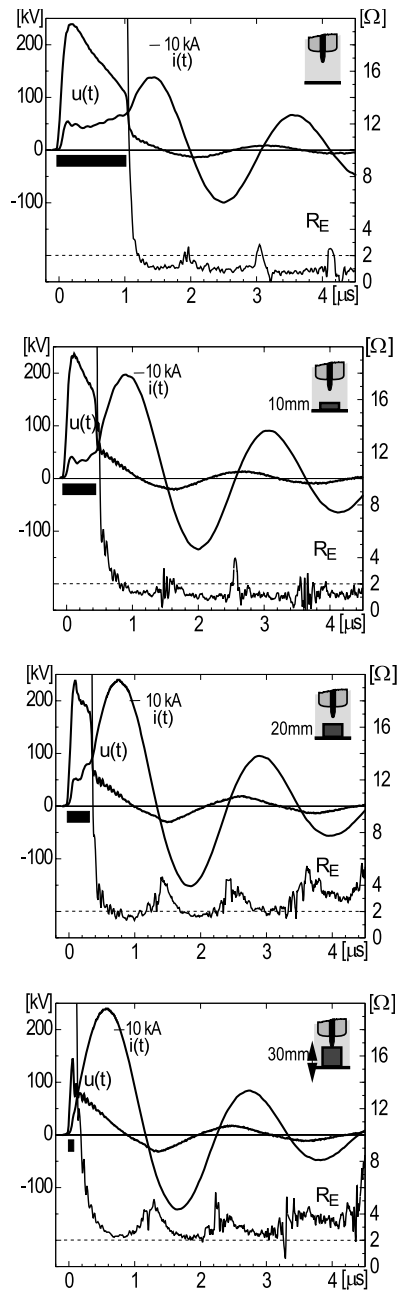


Fig. 12.9. Voltage and current wave shapes $U(t)$ and $I(t)$ and the derived spark channel resistance R_s for various conditions in the interelectrode gap. For this series of measurements, an interelectrode distance of 30 mm was chosen. The voltage traces shown have not been corrected for the inductive voltage drop

an ignition delay occurs and the voltage begins to drop owing to electrolytic current losses. Correspondingly, the maximum attainable spark current and the energy deposited in the spark drop too.

The spark resistance R_s , ignition delay, and energy efficiency can be used to control the operation, and determine the filling level and the interelectrode distance.

12.3 Industrial Applications

12.3.1 Recycling of Building Materials

About 1 m^3 of concrete per inhabitant per year is used for building purposes in Germany. Similar quantities are consumed in other industrialised countries. The raw materials gravel, sand, and cement are taken completely from natural resources. On the other hand 30 million tons of concrete, mortar, and brick waste is created per year in Germany. The rate of reutilisation of these building materials is quite low and is restricted to secondary constructional measures such as backfilling and noise protection dams. Reutilisation without degradation requires an improved separation into sand, gravel, and cement. Crushing the material with multistage jaw breakers or impact mills cannot separate the constituents and produces a large fraction of dust and small particles.

Concrete is a composite, heterogeneous material and is therefore well suited for separation into its original components by electrodynamic fragmentation. Microcracks between the aggregate and the cement matrix already exist in the unstressed concrete. Alternation of the load expedites the detachment of aggregate particles from the cement matrix. Since the acoustic inhomogeneities are rather large in concrete, ideal conditions exist for separation by pressure waves. Also, the pressure impulse in the discharge channel creates mainly tensile and shear forces, conditions under which the strength of concrete is low. Therefore cracks will originate and spread from the channel.

Figure 12.10 demonstrates that prebroken concrete can indeed be separated completely into its components. The grading curve of the recycled aggregate approaches the initial grading curve of the natural aggregate for the specific type of concrete (according to DIN) [Schultheiss et al. 1998]. It is striking that no coarse fragments appear in the grading curve of the separated concrete aggregate. Nearly all particles are monomineral. Under a light microscope, the gravel fraction ($> 2 \text{ mm}$) is apparently free from contaminants and baked particles. Spherical particles are dominant in the sand fraction ($< 2 \text{ mm}$, $> 0.5 \text{ mm}$) and seldom have cement adhesions. The total fraction of cement in the aggregate part (gravel and sand) is about 1%.

The recycled aggregate is not mechanically predamaged, and fulfils the increased demands for frost and dew resistance according to DIN 52104.

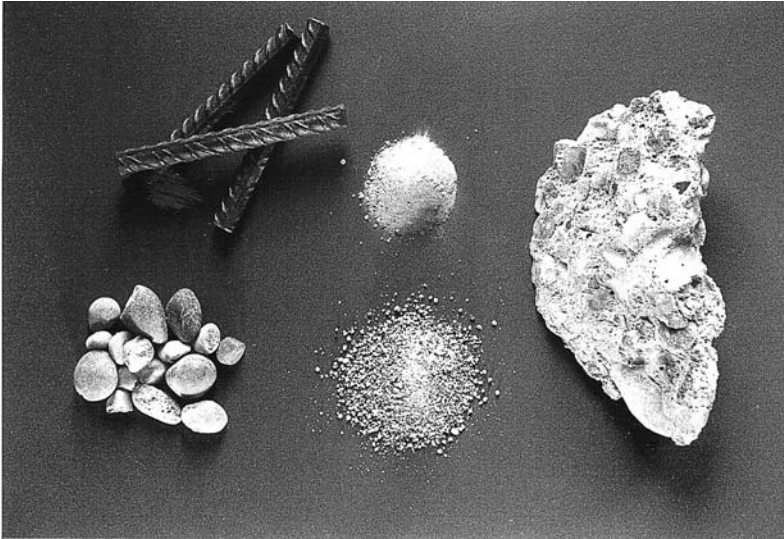


Fig. 12.10. Prebroken concrete piece before (*right*) and after (*left and centre*) treatment in the discharge vessel of FRANKA 0. Sand and gravel are recovered without degradation. The cement fraction (to the side of the steel pieces) can be baked to produce cement clinker

Concrete made from this recycled aggregate has the same material strength as that made from natural aggregates.

Radiography of the silt fraction (< 0.063 mm) shows that it is free of quartz. It consists of calcium silicate hydrate, ettringite, calcium aluminium carbonate hydrate, and calcite.

From a chemical point of view, the cement fraction is very similar to newly made cement. On a laboratory scale, cement clinker has been produced by baking it at high temperature. Recycling the cement fraction has the following attractive advantages:

1. It saves raw materials (clay and lime).
2. Milling of raw materials is unnecessary.
3. No decarbonisation of the milled raw material is required. (The baking process consumes 80% of the energy investment.)
4. Reduction of the CO_2 emission is possible. (7% of the worldwide anthropogenic CO_2 release is due to cement production.)
5. No waste disposal of the cement fraction is required.

Of course, energy is necessary to dehydrate the cement fraction. If 50% of the raw materials used for cement production are replaced by the recycled cement fraction, a 10% saving in the energy cost of the firing process can be expected.

Table 12.2. Productivity of concrete fragmentation at FRANKA-0

Productivity (kg/h)	160
Average electric power (kW)	3
Specific energy consumption (kWh/t)	19

In Table 12.2, the specific productivity of concrete fragmentation is listed. These data were obtained at the FRANKA-0 laboratory facility. This generator is able to produce pulses with an amplitude of 250 kV, rising in 200 ns and with an energy content of 750 J. Operating at 4–5 Hz, its power consumption is around 3–4 kW. In these experiments, 2 kg of concrete was destroyed within 45 s of operation at a repetition rate of 4–5 Hz.

To demonstrate a larger throughput of up to 1 t/h, the semi-industrial prototype facility FRANKA-2, alias FRANKA-Stein, shown in Fig. 12.11,



Fig. 12.11. View of FRANKA-Stein, a semi-industrial prototype to demonstrate concrete recycling with complete separation of the aggregate at a throughput of up to 1 t/h. The Marx generator is housed in the top cylindrical case

was built. The concrete lumps are transported to the processing chamber with the help of a vibrating conveyor. The treated material is extracted from the reaction chamber through a cylindrical shaft at the bottom of the chamber. The material treatment time is controlled by the speed of rotation of a disc that transports the fragments away from the duct. The Marx generator consists of six stages powered from a 10 kW charging unit. At 60 kV charging voltage, the output of the Marx generator rises to a 350 kV pulse amplitude within 0.2–0.4 μs , depending on the water quality. Although throughputs approaching 1 t/h have been demonstrated with this facility, a compromise between throughput and the quality of the secondary aggregate has to be found. Generally speaking, fast energy deposition (i.e., high power) in the discharge channel leads to a large peak pressure in the channel, resulting in many short cracks and a high degree of fragmentation in the immediate neighbourhood of the discharge channel. Slower energy deposition creates fewer but longer cracks and blows off bigger lumps from a concrete block.

During concrete recycling, salts are continuously released into the process water, increasing its conductivity. To keep electrodynamic fragmentation efficient, the conductivity of the water must remain low. Therefore either fresh water must be added or the water must be reprocessed in a closed water circuit. Because of ecological reasons only the latter is acceptable. Fortunately, most of the salts can be neutralised by just blowing CO_2 into the water.

12.3.2 Treatment of Incineration Ash

Thermal treatment of municipal solid waste is an effective method of waste disposal, which is becoming increasingly important. It not only reduces the volume to be dumped but also is a valuable source of energy and a resource for metals and mineral building materials. The utilisation of ash as an aggregate for the production of concrete requires the separation of metals and the immobilisation of heavy metals. Heavy metals can be eluted from fresh ash in contact with water. An unavoidable content of anhydrous lime is responsible for the high pH value of more than 12 in ash. Thus the elution of lead ions in water, for example, is increased by a factor of 1000 over that in a pH-neutral solution. Therefore, fresh ash must be stored for a period of at least three months before utilisation as a building material. During this time, absorption of CO_2 from the atmosphere reduces the pH value.

It has been found that underwater electrodynamic fragmentation (UWEDF) to separate the metal from the ash also reduces the pH value. This is attributed to the production of oxidants, created in the discharge channel and by the shock waves launched from it. Subsequent measurements of heavy-metal elution show spectacular reductions, so that, in principle, storage can be replaced by an on-line treatment with UWEDF directly after the furnace.

To demonstrate this process in an industrial environment, the facility FRANKA-1 was built and installed at a municipal incineration plant.



Fig. 12.12. FRANKA-1 before shipment to an incineration plant. FRANKA-1 is used to separate metallic components from the ash and to immobilise heavy metals in the ash

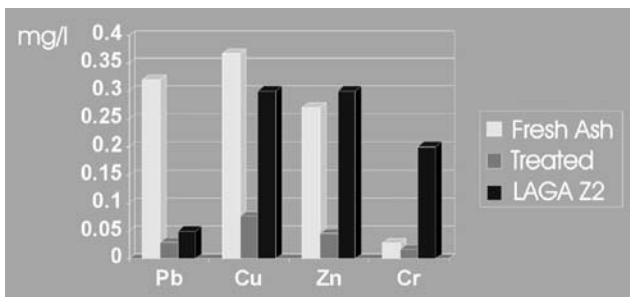


Fig. 12.13. Comparison of heavy-metal elution from treated and untreated fresh ash. Also shown are the values for the German LAGA Z2 regulations

FRANKA-1, which is shown in Fig. 12.12 before shipment to the incineration plant, can treat up to 2 tons of ash per hour. FRANKA-1 operates at 7 Hz and a mean power of 10 kW and produces voltage pulses of 350 kV amplitude. Figure 12.13 depicts the values of heavy-metal elution from the ash before and after treatment with the FRANKA-1 facility. For comparison, the threshold values specified by the German LAGA Z2 regulations for reutilisation as a building material are shown too.

A problem with this process is the strong enrichment of salts in the process water, leading to increasing electrolytic losses. An important part of the process is therefore the desalting of the process water.

12.3.3 Removal of Surface Layers and Drilling

The configuration shown in Fig. 12.6 can be used to remove surface layers contaminated by hazardous chemicals or radionuclides. Laboratory experiments have been carried out at Textron [Goldfarb et al. 1997], Tomsk [Sjomkin et al. 1995], and the Karlsruhe Research Centre, where a device was built that can be moved in all three dimensions above a $2\text{ m} \times 3\text{ m}$ water-filled basin [Schultheiss et al. 1998].

To find the optimum set of machine parameters for a certain material we can proceed in the following way. Keeping the discharge characteristics L , C , and U of the pulse generator constant, we can determine the material volume V removed per shot as a function of the gap distance s . At a certain interelectrode distance, this curve will have a maximum. By repeating this experiment at other pulse amplitudes U , we obtain a set of functions similar to that schematically shown in Fig. 12.14a. Instead of V , we can plot the specific energy $W_{\text{spec}} = (1/2)CU^2/V$. For each voltage U , there will be

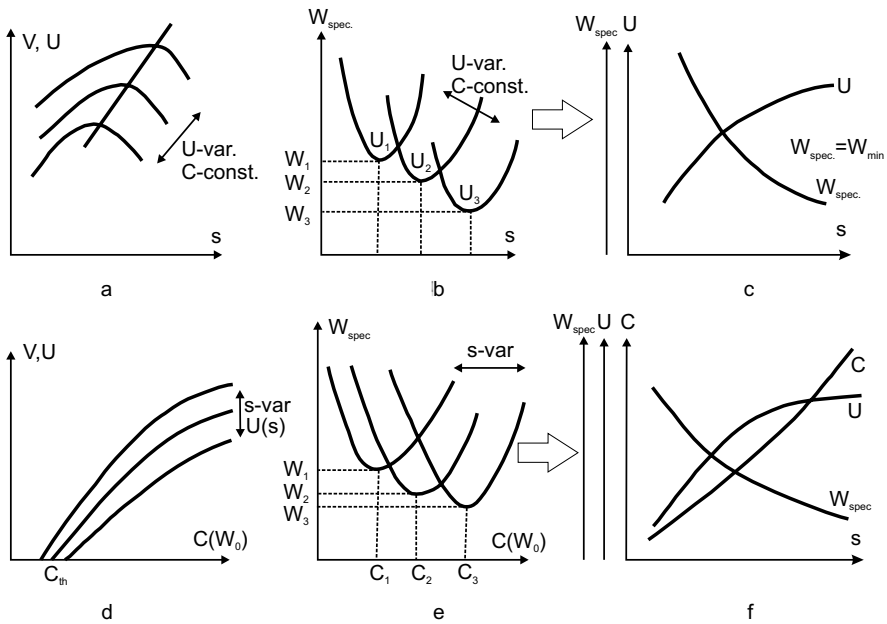


Fig. 12.14. Schematic representation of a procedure to determine the optimum voltage amplitude and generator capacitance as a function of interelectrode distance s for the minimum energy consumption W_{spec} (after [Sjomkin et al. 1995])

a minimum energy and a corresponding optimum interelectrode distance, as shown in Fig. 12.14b. The function $W_{\text{spec}}(s)$ plotted in Fig. 12.14c is the curve interconnecting the minima in Fig. 12.14b, and $U(s)$ corresponds to the voltage belonging to each minimum. Physically, this means that we can reduce the specific energy required if we increase the interelectrode distance and simultaneously increase the voltage amplitude. The value of U necessary to achieve a minimum specific energy can also be read from Fig. 12.14c.

However, this set of curves alone is still not sufficient to determine all parameters so as to optimise the process. In particular, the stored electric energy W_0 is still a free parameter. We must therefore optimise the stored energy in a second step. Instead of W_0 , we can use $C = 2W_0/U^2$ as the independent variable. From Fig. 12.14c, we take for each value of s the corresponding optimum value of U . Subsequently, we determine the removed volume V as a function of $C(W_0)$ and obtain a set of curves similar to that shown in Fig. 12.14d, for different values of s . We can assume that there will be a threshold energy W_{th} (or capacitance C_{th}) below which the removed volume becomes zero. Therefore we can expect a minimum for the specific energy W_{spec} , as shown in Fig. 12.14e. Each curve corresponds to certain values of s and $U(s)$, and therefore also each minimum, relating to a certain value of C , can be plotted as a function of s . This has been done in Fig. 12.14f, where all related parameters C , U , and W_{spec} are presented as a function of s . Obviously, such an optimisation procedure can become quite tedious and probably has never been carried out systematically. It should also be noted that it does not necessarily provide the most economic technical solution. Low specific energy consumption is only one economic factor; productivity and machine costs are others.

While at Karlsruhe only single pairs of electrodes have been tried so far, long parallel strips of electrodes have been used at Textron [Goldfarb et al. 1997]. It was expected that in this configuration, breakdowns would travel randomly along the electrode gap and that removal of concrete at one location would increase the breakdown strength there and enable a discharge at another, weaker position. Because of this kind of self-regulation, a uniform depth across the scabbling path was predicted. The prototype system consisted of a 120 kV Marx generator delivering a 0.8–2 kJ pulse at a repetition rate of 5–40 Hz. The average scabbling speed was around 5–20 cm per minute and thus up to a factor of 10 larger than that of a low-voltage (20–30 kV) electrohydraulic scabbling system based on water breakdown, although the energy consumption of the latter was up to a factor of 4 larger. The specific energy consumption of the high-voltage system was 500–1000 J/cm³. Trials were also conducted at a DOE test site, where a uranium-contaminated concrete layer was removed from the plant floor. On the basis of the experience gained in these experiments, these techniques can be used to decontaminate large floor areas. The radioactive products released during the process are contained either in the concrete rubble or in the water as fine, suspended



Fig. 12.15. View of a block of reinforced concrete with the surface layer removed. Here the two-electrode system shown in the upper left corner of the photograph was used

particles. These components must be removed from the water by filtering or be separated by evaporation of the water. Recontamination of the concrete surface laid open cannot be avoided completely but can be kept small by fast recycling of the water.

As in the case of separation of concrete into its components, the conductivity of the process water rises with time and needs to be controlled. This is especially important for the parallel-strip electrodes used in the experiments at Textron. It seems preferable, therefore, to use rod electrodes that can be entirely enveloped by an insulator except for a small section at the tip. Also, the pulse amplitude should be raised to more than 400 kV. At 350 kV, the specific energy consumption was as low as 70 J/cm^3 in the experiments conducted at Karlsruhe. A result from these trials is shown in Fig. 12.15, where the concrete has been removed up to the first grid of reinforcement steel. Even lower specific energy consumption has been found by [Sjomkin et al. 1995]. Sjomkin et al. used a powerful 420 kV, 19 kJ per pulse Marx generator and a comb-like electrode system to destroy reinforced concrete plates. The electrodes were sequentially connected to the generator. With this system, values between 7 and 30 J/cm^3 were found, depending on the number of reinforcement grids.

12.3.4 Recycling of Other Products

In addition to building materials, numerous other composite materials have been treated. We can divide these into two groups:

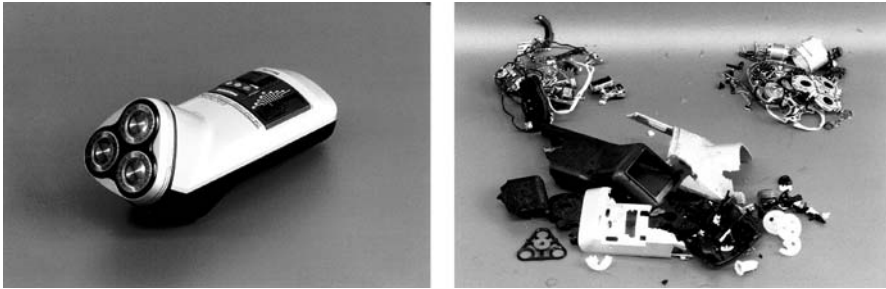


Fig. 12.16. Pulsed electric discharges can be used to separate metallic and dielectric components of electrical appliances. The *right* photograph shows the result of treatment of an electric razor with a few pulses

- Material composites containing metallic and dielectric components, such as electrical appliances, spark plugs, and circuit boards.
- Brittle, homogeneous materials such as glass, silicon, colouring pigments, and minerals.

Easy separation of metallic and non-metallic components can be achieved directly for small electrical appliances, as shown in Fig.12.16. Large electrical appliances need coarse crushing before processing. Unlike the case in conventional recycling facilities, the metallic components can be retrieved as complete parts, enabling much easier recovery of precious metals. It is supposed that the discharge occurs at material interfaces and thus detaches the bonding between components.

The interest in using electrodynamic fragmentation to mill or destroy homogeneous materials is based on the observation that relatively small amounts of contamination are introduced by the process and that more favourable grain size distributions, without a large fraction of fines, can be achieved. For example, low-contamination milling of borosilicate glass for biotechnological applications to grain sizes of less than $100\mu\text{m}$ has been demonstrated. The glass particles suspended in the process water were continuously removed by a filter of suitable pore size. Iron contamination from electrode burn was reduced further by magnetic separators at the entrance to the sedimentation pit. Compared with the conventional milling process, not only was the amount of contamination reduced but also the grain size distribution was much smaller, and thus the useful yield was increased too. Another advantage is that a relatively small fraction of the material came into contact with the hot channel products and became molten. Thus the porous structure on the surface of the borosilicate grains – an important feature for the biological application – was preserved for a larger fraction of particles than with conventional milling.

12.3.5 Recycling of Elastoplastic Materials

Electrodynamic fragmentation has turned out to be less successful for elastic or impact-resistant materials. In an attempt to improve the performance of the method in this field of application, investigations were launched at Tomsk Polytechnical University [Kurets et al. 1995], in which elastic materials (in particular rubber) were immersed in liquid nitrogen (LN_2) to increase their brittleness.

However, the success of this approach depends not only on the increased brittleness of the material but also on the dielectric properties of LN_2 . A real drawback of LN_2 as a dielectric liquid is its small dielectric constant $\varepsilon = 1.454$. Thus field intensification inside a solid material immersed in the liquid cannot be expected. On the contrary, since many solid materials have higher dielectric constants, a weak field enhancement in the liquid may occur.

Although a considerable amount of information can be found in the literature on the breakdown characteristics of LN_2 , very little is of relevance for the dynamic stress situation typical of electrodynamic fragmentation. A summary of results obtained from experiments conducted at Tomsk is shown in Fig. 12.17 [Kurets et al. 1995]. Here the breakdown voltage is depicted as a function of the sample thickness for LN_2 and three different pulse rise times, 200 ns, 1 μs , and a 5 ms sine wave, and for two different rubber samples, car tyre rubber and vacuum seal rubber. The rise times always refer here to a pulse amplitude of 250 kV and can thus be expressed as ramp rates of

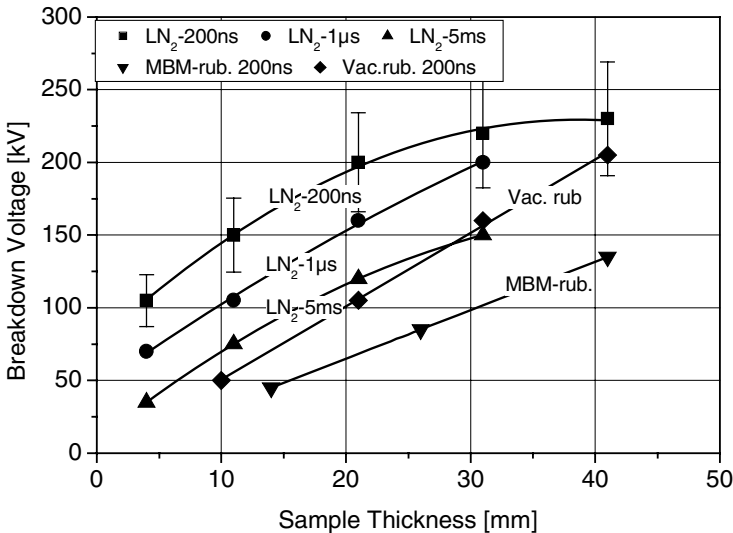


Fig. 12.17. Dependence of the breakdown voltage of LN_2 on sample thickness for various ramp rates. Also shown is the breakdown voltage of rubber at cryogenic temperatures (from [Kurets et al. 1995])

1.25 MV/ μs , 250 kV/ μs and 50 V/ μs . It was observed that the breakdown behaviour of LN₂ differs significantly from that of other dielectric liquids, such as transformer oil, glycerine, alcohol, and water (under normal conditions).

Only for LN₂ layer thicknesses (gap widths) below 20 mm does the breakdown voltage rise linearly. Above 20 mm, the increase becomes much slower. This behaviour is probably connected with a change in the breakdown mechanism from an area to a volume effect. The probability of the appearance of bubbles grows if the stressed volume increases. Such bubbles promote the formation of streamers inside the volume and reduce the macroscopic breakdown field strength. The formation of bubbles in an LN₂ bath is of particular relevance, since the temperature of a liquefied gas under atmospheric pressure stabilises close to the boiling point. In such liquids, even the minute heat production induced by prebreakdown currents can lead to the appearance of bubble chains, along which premature breakdown can occur, before a discharge path through the solid material has been established.

It can also be concluded from Fig. 12.17 that the variation of the breakdown strength with the pulse rise time is much less pronounced than for water: while in the case of water, the breakdown strength increases by a factor of 10 when one passes from a pulse rise time of 1 μs to 200 ns, the corresponding increase in LN₂ is merely 25%. On the other hand, the rubber materials investigated showed a linear increase of breakdown voltage with sample thickness.

From these results, Kurets et al. concluded that to induce a discharge in a solid material such as rubber with a greater probability than in LN₂, one must apply pulses with a rise time of $(0.2\text{--}0.5) \times 10^{-6}$ s and an amplitude of 200 kV for samples up to 30 mm thick.

Another reason for the weakening of the electric breakdown strength in LN₂ may be an accumulation of ice crystals within the liquid, originating from frozen-out air humidity, if the surface is exposed to normal atmospheric air. Of course, these problems could be reduced significantly by pressurising the LN₂ and by minimising the contact of its surface with atmospheric air.

The removal of bubbles from the LN₂ bath can also severely limit the achievable repetition rate. If, typically 125 J of energy is deposited in the discharge channel and converted into heat, about 0.5 L of N₂ gas must be removed from the bath between shots. Although the viscosity of LN₂ is relatively small (2.1 mp² at 77 K, as opposed to 1 cp³ for water at 20°C), which facilitates bubble movement to the surface under buoyancy forces, corresponding experiments [Takahashi and Ohtsuka 1975, Takahashi 1977] have shown that N₂ gas bubbles in LN₂ subject to buoyancy forces move upwards with a speed of only 0.2 m/s. Given a depth of the LN₂ bath of 20 cm, the pulse rate will be limited to less than 1 Hz if complete removal of bubbles be-

² mp = millipoise = 10^{-4} N m⁻² s.

³ cp = centipoise = 10^{-3} N m⁻² s.



Fig. 12.18. FRANKA-3, built to explore the applicability of electrodynamic fragmentation under liquid nitrogen. The Marx generator is located in the barrel hanging from the roof

tween shots is required. Only practical experience will show, however, what the real repetition rate limitations are.

To explore the applicability of electrodynamic fragmentation under LN_2 for industrial processes, the FRANKA-3 facility, shown in Fig. 12.18, was built in Karlsruhe. A Marx generator of design similar to that for the other FRANKA facilities allowed us to produce pulses of up to 300 kV with a ramp rate of $2 \text{ MV}/\mu\text{s}$ and an energy content of 440 J. It was contained in a barrel hanging from the roof above the LN_2 process vessel and was insulated with SF_6 . The electrode gap was adjusted to 30–40 mm. The stainless steel LN_2 process vessel visible in the lower part of Fig. 12.18 was placed on a scissor-type elevating platform below the Marx generator.

Using this facility, a large number of components were treated:

- components from motor vehicles containing rubber or other plastic parts;
- optical-fibre wave-guides;
- printed circuit boards;
- laminated plastics;
- pressure tubing, vacuum seals, etc.

Gross separation of metal–rubber and metal–plastic composites was easily achieved. However, small traces of rubber remained on the metallic surfaces that could not be removed even by prolonged treatment. Also, small craters appeared on the metallic surface at arc footpoints.

The separation of components from thin sheets of material, such as printed circuit boards, could not be achieved efficiently. In this configuration, the channel products can escape rapidly from the channel and prevent the build-up of any significant pressure. Also, it was found that many organic materials were decomposed at the high temperatures in the discharge channel and, during cooling, led to new, uncontrollable substances. Although the quantities were small and may be tolerable in some processes, they would certainly be unacceptable in the treatment of pharmaceutical and food products.

Therefore, and because of the appreciable cost of liquid nitrogen, it has not been possible so far to identify any industrial application that justifies electrodynamic fragmentation or milling under LN₂.

12.3.6 Scaling and Economic Considerations in Relation to Recycling

The economics of any recycling technique are determined by the machine price, the specific energy consumption, the operating and maintenance costs, and the number and quality of personnel required to run the facility. Most industrial applications need large throughputs to become economic, and therefore considerable extrapolations from the present laboratory-type electrodynamic fragmentation devices to industrial-size facilities are necessary, leading to large uncertainties in cost estimates.

It is obvious that the quantity of material that can be treated per arc channel is limited and cannot be increased much above that of an optimised laboratory device. The repetition rate must stay below about 15 Hz to allow gas bubbles to decay between pulses. Also, it does not seem reasonable to raise the pulse amplitude appreciably above 500 kV, since the expenditure on insulation may become prohibitive. The pulse amplitude determines the possible length of the discharge channel and thus the accessible volume in the treated material. Some other parameters that have an influence on productivity are the power of the pulse and its energy. Augmenting the energy per pulse is, however, counteracted by a reduction of the resistance of the discharge channel, leading to smaller efficiencies. Nevertheless, raising the power may lead to a certain gain in productivity, especially if milling is the main task of the device. The achievable increment in productivity will of course depend on the specific product. A systematic study of the disintegration of granite samples has been carried out by Andres [Andres 1989], where an optimum set of parameters in an energy–field plane was derived. However, the term ‘disintegration’ was not defined, and therefore it is difficult to relate these data to the specific productivity. Considering concrete fragmentation for complete separation of the aggregate, we expect that an increase in throughput by a

factor of 3–5 over that obtained with the FRANKA facilities described above can be achieved with an optimised discharge channel. That is, a throughput of about 1–3 t/h of completely separated concrete may be produced per channel with an average power of 30 kW and a pulse energy of 2 kJ, operating at 15 Hz. Thus, to realise an industrial facility with a throughput of 100 t/h, up to 100 arcs operating simultaneously are required. Every arc needs a certain process space that does not interfere with its neighbours. Either parallel or serial arrangements of the active arc zones are conceivable.

To produce 100 arcs simultaneously does not necessarily mean that all components need to be multiplied by this number. For example, the Marx generator can run at a higher frequency and distribute its pulses alternately to different discharge sections. Also, a capacitor-charging unit of sufficient power can supply several units in parallel. Since the price of a power supply does not increase in proportion to the power, there is a large potential for savings in the scale-up of a facility.

Component wear and lifetime are further important economic factors. The components with the largest wear are the high-voltage electrodes in contact with the material to be fragmented, and the switch electrodes. We have found that the material loss from the steel electrode used for concrete fragmentation amounted to 10 μg per shot. Consequently, an electrode with a 1 cm^2 cross-section consumes approximately 1 cm of its length per week of full operation (for an 8 hour working day). Therefore, provision must be made to continuously adjust the electrode, and replacement is necessary from time to time. However, the wear is sufficiently small to be economically irrelevant. Concerning the lifetime of the insulator enveloping the steel rod, insufficient experience exists for operation under industrial conditions. Damage to the insulator can occur through impact of material fragments on its surface. Laboratory experience shows that it is most important to reduce electric stress at the triple point of the electrode tip.

Of bigger concern than the erosion of the operating electrode is the wear of the switch electrodes. A loss of 3 g has been measured after 10^6 pulses from spherical steel electrodes. Using CuW with a Borda profile and a sufficiently large diameter should lead to acceptably small wear at the power densities involved. Nevertheless, adjustment of the gas pressure in the switches will be routinely necessary, and the electrode gap distances will probably need to be readjusted at maintenance intervals of the order of a few weeks.

The capacitor lifetime has been guaranteed to be more than 10^8 pulses even for the conditions of large voltage reversal occurring in the electric discharges here, and is presently not considered to be an economic limitation.

Depending on the process, strong liberation of salts can occur and increase the conductivity of the process water. At a conductivity above 1500 $\mu\text{S}/\text{cm}$, efficient operation becomes impossible and the water must be either replaced or conditioned, which can become an important factor for cost-effectiveness.

References

- ABB (2001) Catalogue: *Special Components for Pulsed Power Applications*. ABB Semiconductors AG, Lenzburg, Switzerland
- Achenbach J, Hemann J, Ziegler F (1970) Separation at the interface of a circular inclusion and the surrounding medium under an incident compression wave. *Trans. ASME, J. Appl. Mech. E* 37: 298–304
- Akiyama H. (2000) Streamer discharges in liquids and their applications. *IEEE Trans. Dielectr. Electr. Insulat.* 7(5): 646–653
- Akiyama H, Katsuki S, Namihira T, Ishibashi K, Kiyosaki N (2001) Production of large volume discharges in water and their industrial applications. In: Reinovsky R, Newton M (eds.) *Proc. 28th IEEE Int. Conf. on Plasma Science and 13th IEEE Int. Pulsed Power Conf.*, 17–22 June 2001, Las Vegas, pp. 150–153
- Andres U (1989) Parameters of disintegration of rock by electrical pulses. *Powder Technol.* 58: 265–269
- Arad R, Tsigitkin K, Maron Y, Fruchtman A, Huba JD (2003) Observation of faster-than-diffusion magnetic field penetration into a plasma. *Phys. of Plasmas* 10(1): 112–125
- Artsimowitsch LA, Sagdejew RS (1983) *Plasmaphysik für Physiker*. Teubner, Stuttgart
- Badent R (1996) *Modell der elektronendominanten Streamerentladung in Isolieröl*. PhD thesis, University of Karlsruhe
- Bailey J, Carlson A, Morrison R (1990) Visible spectroscopy measurements in the PBFA II ion diode. *Rev. Sci. Instrum.* 61(10): 3075–3080
- Bailey JE, Filuk AB, Carson AL, Johnson DJ, Lake P, McGuire EJ, Mehlhorn TA, Pointon TA, Renk TJ, Stygar WA, Maron Y (1995) Measurements of acceleration gap dynamics in a 20-TW applied-magnetic-field ion diode. *Phys. Rev. Lett.* 74: 1771–1774
- Baranchikov EI, Gordeev AV, Korolev VD, Smirnov VP (1978) Magnetic self-insulation of electron beams in vacuum lines. *Sov. Phys. JETP* 48(6): 1058–1068
- Bardotti G, Bertotti B, Gianolio L (1964) Magnetic configuration of a cylinder with infinite conductivity. *J. Math. Phys.* 5: 1387–1390
- Barlow RE, Proscan F (1975) *Statistical Theory of Reliability and Life Testing*. Holt, Rinehart and Winston, New York
- Baron M, Matthews A (1961) Diffraction of a pressure wave by a cylindrical cavity in an elastic medium. *Trans. ASME, J. Appl. Mech. E* 28: 347–354

- Beams (1975) *Proc. Int. Topical Conf. on Electron Beam Research and Technology*, Albuquerque, NM, 3–6 November 1975, SAND76-5122
- Beams (1977) *Proc. 2nd Int. Topical Conf. on High Power Electron and Ion Beam Research and Technology*, Cornell University, Ithaca, NY, 3–5 October 1977
- Becker R, Sauter F (1964) *Theorie der Elektrizität*. Teubner, Stuttgart
- Beebe SJ, Fox PM, Rec LJ, Somers K, Stark RH, Schoenbach KH (2002) Nanosecond pulsed electric (nsPEF) effects on cells and tissues: apoptosis induction and tumor growth inhibition. *IEEE Trans. Plasma Sci.* 30: 286–292
- Benda H, Spenke E (1967) Reverse recovery processes in silicon power rectifiers. *Proc. IEEE* 55(8): 1331–1354
- Beroual A (1993) Electronic and gaseous processes in the prebreakdown phenomena of dielectric liquids. *J. Appl. Phys.* 73(9): 4528–4533
- Birdsall CK, Bridges WB (1961) Space-charge instabilities in electron diodes and plasma converters. *J. Appl. Phys.* 32 (12): 2611
- Birdsall CK, Langdon AB (1991) *Plasma Physics via Computer Simulation*. Hilger, Bristol
- Bluhm H (2004) Aufschluss und Abtötung biologischer Zellen mit Hilfe starker gepulster elektrischer Felder. Frühjahrstagung der Deutschen Physikalischen Gesellschaft, Kiel, 08-11. März 2004
- Bluhm H, Hoppé P (1999) Perspectives of high power pulse generators for the boron neutron capture therapy (BNCT) of tumors. In: Stalling C, Kirbie H (eds.) *Proc. 12th IEEE Int. Pulsed Power Conf.*, Monterey, CA, Vol. 1, pp. 502–505
- Bluhm H, Böhnel K, Buth L, Hoppé P, Karow HU, Klumpp A, Rusch D, Scherer T, Schülken H, Singer J (1985) Experiments on KFK's light-ion accelerator KALIF. In: Turchi PJ, Rose MF (eds.) *Proc. 5th IEEE Int. Pulsed Power Conf.*, Arlington, VA, pp. 114–117
- Bluhm H, Hoppé P, Laqua H, Rusch D (1992) Production and investigation of TW proton beams from an annular diode using strong radial magnetic insulation fields and a preformed anode plasma source. *Proc. IEEE* 80: 995–1009
- Bluhm H, Hoppé P, Bachmann H, Bauer W, Baumung K, Buth L, Laqua H, Ludmirski A, Rusch D, Stoltz O, Yoo S (1994) Stability and operating characteristics of the applied B proton extraction diode on KALIF. In: Rix W, White R (eds.) *10th Int. Conf. on High Power Particle Beams*, San Diego. NTIS, Springfield, VA, pp. 77–82
- Bluhm H, Schultheiß C, Frey W, Gusbeth C, Sack M, Strässner R (2004) Industrial scale treatment of biological cells with pulsed electric fields. In: Kirkici H (ed.) *Conf. Record of the 26th Int. Power Modulator Conf. and 2004 High-Voltage Workshop*, San Francisco, pp. 8–14
- Blumlein AD (1941) Improvements in or relating to apparatus for generating electrical impulses. UK Patent 589127
- Bodner SE, Colombant DG, Schmitt AJ, Klapisch M (2000) High gain direct drive target design for laser fusion. *Phys. Plasmas* 7: 2298–2301

- Boebinger G, Lacerda A, Fisk Z, Gor'kov LP, Schrieffer JR (eds.) (2002) *Physical Phenomena at High Magnetic Fields IV. Proc. 4th Conf.*, 19–25 October 2002, Santa Fe, NM. World Scientific, Singapore
- Bogdankevich L, Rukhadze A (1971) Stability of relativistic electron beams in a plasma and the problem of critical currents. *Sov. Phys. Uspekhi* 14(2): 163–179
- Bogdankevich L, Zhelyazkov I, Rukhadze A (1970) Limiting currents in relativistic electron beams. *Sov. Phys. JETP* 30(1): 174–176
- Borda JC (1766) Sur l'écoulement des fluids par les orifices des vases. *Mém. Acad. Roy. Sciences, Année 1766*: 579–607
- Bouattou B, Lowell J (1988) Contact charging and small-scale charge migration in polymers. *J. Phys. D: Appl. Phys.* 21: 1787–1795
- Bouzzara H, Vorobiev E (2000) Beet juice extraction by pressing and pulsed electric fields. *Int. Sugar J.* 102(1216): 194–200
- Bouzzara H, Vorobiev E (2001) Nicht-thermisches Pressen und Auswaschen von frischen Zuckerrübenschnitzeln kombiniert mit der Anwendung eines pulsierenden elektrischen Feldes. *Zuckerindustrie* 126: 463–466
- Braginskii SI (1958) Theory of the development of a spark channel. *Sov. Phys. JETP* 34(7): 1068–1074
- Buescher ES, Schoenbach KH (2003) Effects of submicrosecond, high intensity pulsed electric fields on living cells – intracellular electromanipulation. *IEEE Trans. Dielectr. Electr. Insulat.* 10(5): 788–794
- Buneman O, Levy RH, Linson LM (1966) Stability of crossed-field electron beams. *J. Appl. Phys.* 37: 3203–3222
- Burkin V, Makarov P, Semkin B, Shubin B (1975) Pressure field around a spark in a solid dielectric. *Sov. Phys. Techn. Phys.* 20(11): 1490–1492
- Campbell NA (2000) *Biologie*. Spektrum Akademischer Verlag, Heidelberg
- Christiansen J, Hartmann W (1990) The pseudospark. In: Schaefer G, Kristiansen M, Guenther A (eds.) *Gas Discharge Closing Switches*. Plenum, New York, pp. 509–520
- Coleman AJ, Saunders JE (1993) A review of the physical properties and biological effects of the high amplitude acoustic fields used in extracorporeal lithotripsy. *Ultrasonics* 31(2):75–89
- Cooke CM (1998) Personal communication
- Cooperstein G (2002) Status of particle beam and pulsed power research in US. In: Mehlhorn TA, Sweeney MA (eds.) *Proc. 14th Int. Conf. on High-Power Particle Beams*, 23–28 June 2002, Albuquerque, NM, pp. 3–8
- Cooperstein G, Boller JR, Commisso RJ, Hinshelwood D, Mosher D, Ottinger PF, Schumer JW, Stephanakis SJ, Swanekamp SB, Weber BV, Young F (2001) Theoretical modeling and experimental characterization of a rod-pinch diode. *Phys. Plasmas* 8: 4618–4636
- Creedon JM (1975) Relativistic Brillouin flow in the high n/g diode. *J. Appl. Phys.* 46(7): 2946–2955

- Cuneo ME (1999) The effect of electrode contamination, cleaning and conditioning on high-energy pulsed-power device performance. *IEEE Trans. Dielectr. Electr. Insulat.* 6(4): 469–485
- Cuneo ME, Menge PR, Hanson DL, Fowler WE, Bernard ME, Ziska GR, Filuk AB, Pointon TD, Vesey RA, Welch DR, Bailey JE, Desjarlais MP, Lockner TR, Mehlhorn TA, Slutz SA, Stark MA (1997) Results of vacuum cleaning techniques on the performance of LiF field-threshold ion sources on extraction applied-B ion diodes at 1–10 TW. *IEEE Trans. Plasma Sci.* 25(2): 229–251
- Dekker AJ (1964) *Solid State Physics*. Macmillan, London
- Desjarlais M (1989) Theory of applied-B ion diodes. *Phys. Fluids B* 1(8): 1709–1720
- Dev SB, Hofmann GA (1994) Electrochemotherapy – a novel method of cancer treatment. *Cancer Treat. Rev.* 20(1): 105–115
- Devins JC, Rząd SJ, Schwabe RJ (1981) Breakdown and prebreakdown phenomena in liquids. *J. Appl. Phys.* 52(7): 4531–4545
- DiCapua MS (1980) Magnetic insulation. *IEEE Trans. Plasma Sci.* 11(3): 205–215
- Doevenspeck H (1962) Über die Beeinflussung von Zellen und Zellverbänden durch elektrostatische Impulse. *Arch. Lebensmittelhygiene* 13(3): 68–69
- Doran AA (1968) The development of a Townsend discharge in N₂ up to breakdown investigated by image converter, intensifier, and photomultiplier techniques. *Z. Phys.* 208: 427–440
- Driga MD, Pratap SB, Walls AW, Kitzmiller JR (2001) The self-excitation process in electrical rotating machines operating in pulsed power regime. *IEEE Trans. Magn.* 37(1): 295–300
- DuVillaret L, Riolland S, Coutaz JL (2002) Electro-optic sensors for electric field measurements. I. Theoretical comparison among different modulation techniques. *J. Opt. Soc. Am. B* 19(11): 2692–2703
- Ebert H (ed.) (1976) *Physikalisches Taschenbuch*. Vieweg, Braunschweig
- Ekdahl C (2001) Modern accelerators for radiography. In: Reinovsky R, Newton M (eds.) *Proc. 28th IEEE Int. Conf. on Plasma Science and 13th IEEE Int. Pulsed Power Conf.*, 17–22 June 2001, Las Vegas, pp. 29–34
- Engelko A, Bluhm H (2004) Optimal design of semiconductor opening switches for use in the inductive stage of high power pulse generators. *J. Appl. Phys.* 95(10): 5828–5836
- Engelko V, Kusnetsov V, Viazmenova G, Müller G, Bluhm H (2000) Influence of electrons reflected from a target on the operation of triode-type electron sources. *J. Appl. Phys.* 88(7): 3879–3888
- Engelko V, Müller G, Bluhm H (2001a) Influence of particle fluxes from target on characteristics of intense electron beams. *Vacuum* 62: 97–103
- Engelko V, Yatsenko B, Müller G, Bluhm H (2001b) Pulsed electron beam facility (GESA) for surface treatment of materials. *Vacuum* 62: 211–216
- Fitch RA (1964) Novel principle of transient high-voltage generation. *Proc. IEE* 111(4): 849–854
- Fowler RH, Nordheim L (1928) Electron emission in intense electric fields. *Proc. Roy. Soc. (London)* 119A(781): 173–181

- Frank K, Rath W (1990) The triggered pseudospark discharge. In: Schaefer G, Kristiansen M, Guenther A (eds.) *Gas Discharge Closing Switches*. Plenum, New York, pp. 521–530
- Frank K, Christiansen J, Hartmann W (1991) Triggerbare Hochleistungsschalter. *Physik in unserer Zeit* 22(4): 156–164
- Friedman M, Swanekamp S, Obenschain S, Chan Y, Ludeking L, Smithe D (2000) Stability of large area electron beam diodes. *Appl. Phys. Lett.* 77: 1053–1055
- Fueki K, Feng DF, Kevan L (1972) A semiempirical estimate of the scattering cross-section and mobility of excess electrons in liquid hydrocarbons. *Chem. Phys. Lett.* 13: 616–618
- Gerlach W (1979) *Thyristoren*. Springer, Berlin, Heidelberg
- Glasoe GN, Lebacqz JV (1948) *Pulse Generators*. MIT Radiation Laboratory Series Vol. 5, McGraw-Hill, New York
- Goldfarb V, Budny R, Dunton A, Shneerson G, Krivosheev S, Adamian Y (1997) Removal of surface layer of concrete by a pulse-periodical discharge. In: Cooperstein C, Vitkovitsky I (eds.) *Proc. 11th IEEE Int. Pulsed Power Conf.*, 29 June–2 July 1997, Baltimore, pp. 1078–1084
- Goldstein SA, Lee R (1975) The ion induced pinch and enhancement of ion current by pinched electron and ion flow in relativistic diodes. *Phys. Rev. Lett.* 35: 1079–1082
- Granatstein VL, Alexeff I (1987) *High Power Microwave Sources*. Artech House, Boston
- Greenly JB, Appartaim RK, Olson JC, Brisette L (1994) Extraction ion diode studies for optimised performance: divergence, ion species and parasitic load. In: Rix W, White R (eds.) *10th Int. Conf. on High Power Particle Beams*, San Diego. NTIS, Springfield, VA, pp. 398–401
- Greenly JB, Appartaim RK, Olson JC (1996) Anode plasma dynamics in an extraction applied-*B* ion diode: effects on divergence, ion species and parasitic load. In: Jungwirth K, Ullschmied J (eds.) *11th Int. Conf. on High Power Particle Beams*, Prague, Tiskárna ‘K’ Ltd, Prague, pp. 111–114
- Grekhov I, Mesyats G (1999). Physical basis for high power semiconductor nanosecond opening switches. In: Stalling C, Kirbie H (eds.) *12th IEEE Int. Pulsed Power Conf.*, Monterey, CA, pp. 1158–1161
- Guenther AH (ed.) (1987) *Opening Switches. Advances in Pulsed Power Technology*. Plenum, New York
- Guillemin EA (1944) *A Historical Account of the Development and a Design Procedure for Pulse Forming Networks*. Radiation Laboratory Report No. 43, Massachusetts Institute of Technology, Cambridge, USA
- Guz IS (1974) Interaction between stress waves and a growing crack. *J. Appl. Mech. Tech. Phys.* 15: 726–730
- Halbritter J (1985) On contamination on electrode surfaces and electric field limitations. *IEEE Trans. Electr. Insulat.* 20: 671
- Halbritter J (1986) Dynamical enhanced electron emission and discharges at contaminated surfaces. *Appl. Phys. A (Solids Surf.)* 39: 49–57

- Hanson DL, Cuneo ME, McKay PF, Maenchen JE, Coats RS, Poukey JW, Rosenthal SE, Fowler WE, Wenger DF, Bernard MA, Chavez JR, Stearns WF (1992) Operation of a high impedance applied-*B* extraction ion diode on the SABRE positive polarity linear induction accelerator. In: Mosher D, Cooperstein G (eds.) *9th Int. Conf. on High Power Particle Beams*, Washington, DC. NTIS, Springfield, VA, pp. 781–787
- Harjes HC, Penn KJ, Reed KW, McClenahan CR, Laderach GE, Wavrik RW, Adcock J, Butler M, Mann GA, Martinez L, Morgan FA, Weber GJ, Neau EL (1991) Status of the repetitive high energy pulsed power project. In: Prestwich K, White R (eds.) *Proc. 8th IEEE Int. Pulsed Power Conf.*, San Diego, pp. 543–548
- Hegeler F (2003) Personal communication
- Hegeler F, Myers MC, Friedman M, Sethian JD, Swanekamp SB, Rose DV, Welch DR (2002) Efficient electron beam deposition for repetitively pulsed krypton fluoride lasers. In: Mehlhorn TA, Sweeney MA (eds.) *Proc. 14th Int. Conf. on High-Power Particle Beams*, 23–28 June 2002, Albuquerque, NM, pp. 357–360
- Herlach F, Kennedy JE (1973) The dynamics of imploding liners in magnetic flux compression experiments. *J. Phys. D: Appl. Phys.* 6: 661–676
- Herlach F, Ortenberg M (1996) Pulsed magnets for strong and ultrastrong fields. *IEEE Trans. Magn.* 32(4): 2438–2443
- Herlach F, Li L, Harrison N, Bockstal L (1996) Approaching 100 T with wire wound coils. *IEEE Trans. Magn.* 32(4): 2507–2510
- Hilmert H, Schmidt WF (1991) Electron detachment from negative ions of sulfur hexafluoride – swarm experiments. *J. Phys. D: Appl. Phys.* 24: 915–921
- Hülsheger H, Poter J, Niemann E (1983) Electric field effects on bacteria and yeast cells. *Radiat. Environ. Biophys.* 22: 149–162
- Humphreys D, Penn K, Cap J, Adams R, Seamen J, Turman B (1985). Rimfire: a six megavolt laser-triggered gas-filled switch for PBFA II. In: Rose MF, Turchi PJ (eds.) *5th IEEE Int. Pulsed Power Conf.*, Arlington, VA, pp. 262–265
- Humphries S (1990) *Charged Particle Beams*. Wiley, New York
- Humphries S (1980) Intense pulsed ion beams for fusion applications. *Nucl. Fusion* 20: 1549–1612
- Ieda M (1984) Electrical conduction and carrier traps in polymeric materials. *IEEE Trans. Electr. Insulat.* EI-19(3): 162–178
- Illy S, Kuntz M, Westermann T (1994) Investigations on the vacuum current in the magnetic insulated Karlsruhe light ion facility high-energy linear induction accelerator (KALIF-HELIA). *Phys. Plasmas* 1(8):2748–2761
- Johnson D, Kuswa G, Farnsworth A, Quintenz J, Leeper R, Burns E, Humphries S (1979) Production of 0.5-TW proton pulses with a spherical focusing magnetically insulated diode. *Phys. Rev. Lett.* 42(9): 610–613
- Jones HM, Kunhardt EE (1994) Pulsed dielectric breakdown of pressurized water and salt solutions. *J. Appl. Phys.* 77(2): 795–805
- Jones HM, Kunhardt EE (1995a). Ionic sheath formation in water and aqueous solutions and its influence on pulsed dielectric breakdown. In: Baker W, Cooperstein G (eds.) *10th IEEE Int. Pulsed Power Conf.*, 3–6 July 1995, Albuquerque, NM, pp. 580–585

- Jones HM, Kunhardt EE (1995b) Pre-breakdown currents in water and aqueous solutions and their influence on pulsed dielectric breakdown. *J. Appl. Phys.* 78(5): 3308–3314
- Jonscher AK, Lacoste R (1984) On a cumulative model of dielectric breakdown in solids. *IEEE Trans. Electr. Insulat.* EI-19(6): 567–577
- Joshi R, Schoenbach K (2000) Electroporation dynamics in biological cells subjected to ultrafast electrical pulses: a numerical simulation study. *Phys. Rev. E* 62(1): 1025–1033
- Kanel GI, Razorenov SV, Utkin AV (1996) Spallation of solids under shock wave loading. In: Davison L, Grady DE, Shahinpoor M (eds.) *High Pressure Shock Compression of Solids II*, Springer, Berlin, Heidelberg, pp. 1–24
- Kanel GI, Baumung K, Bluhm H, Fortov VE (1998) Possible applications of the ion beams technique for investigations in the field of equation of state. *Nucl. Instrum. Methods A* 415: 509–516
- Kasuya K, Kishi Y, Kamiya T, Funatsu M (1991) Low microdivergence medium-mass ion beam produced from a N₂O cryogenic diode. *Laser Part. Beams* 19: 309–316
- Katschinski U (1994) *Optisch aktivierte Galliumarsenidschalter für die Erzeugung von Hochleistungsimpulsen*. PhD thesis, University of Braunschweig, VDI, Düsseldorf
- Keinigs RK, Atchison WL, Anderson WE, Barlsch RR, Faehl RJ, Flower-Maudlin EC, Hammersberg JE, Holtkamp DB, Jones ME, Kyrala G, Lindemuth JR, Oro DM, Parker JV, Preston DL, Reinovsky RE, Rodriguez G, Scudder DW, Shehey PT, Shlachter JS, Stokes J, Taylor AJ, Tonks DL, Turchi PJ, Chandler E (2001) Material science experiments on the Atlas facility. In: Reinovsky R, Newton M (eds.) *Proc. 28th IEEE Int. Conf. on Plasma Science and 13th IEEE Int. Pulsed Power Conf.*, 17–22 June 2001, Las Vegas, pp. 356–360
- Kind D (1958) Die Aufbaufläche bei Stoßspannungsbeanspruchung technischer Elektrodenanordnungen in Luft. *Elektrotech. Z.* 79(3): 65–69
- Kindersberger J (1986) *The Statistical Time-Lag to Discharge Inception in SF₆*. PhD thesis, Technical University of Munich
- Kingsep AS, Chukbar KV, Yankov VV (1990) Electron magnetohydrodynamics. In: Kadomtsev BB (ed.) *Rev. Plasma Phys.* 16: 243–288, Consultants Bureau, New York
- Knoepfel H (1970) *Pulsed High Magnetic Fields*. North-Holland, Amsterdam
- Kolb AC, Strickland BE (1995) Dual use power supply development. *AIP Conf. Proc.* 25(1): 91–101
- Korolev YD, Mesyats GA (1998) *Physics of Pulsed Breakdown in Gases*. URO-Press, Yekaterinburg
- Krasik YE, Dunaevsky A, Felsteiner J (2001) Intense electron emission from carbon fiber cathodes. *Eur. Phys. J. D* 15(3): 345–348
- Küchler A (1996) *Hochspannungstechnik*. VDI, Düsseldorf
- Küchler A, Schwab A (1987) Räumlich ausgedehnte Sensoren für transiente elektromagnetische Felder. *Arch. Elektrotechnik* 70: 341–347

- Kunhardt EE, Tzeng Y (1988) Development of an electron avalanche and its transition into streamers. *Phys. Rev. A* 38: 1410–1421
- Küpfmüller K, Kohn G (2000) *Theoretische Elektrotechnik und Elektronik: Eine Einführung*. Springer, Berlin, Heidelberg
- Kurets VI, Tarakanovskii EN, Filatov GP (1995) Electric pulse resistance of liquid nitrogen and rubber. *Russ. Phys. J.* 38: 455–457
- Lafferty JM (1980) *Vacuum Arcs, Theory and Application*. Wiley, New York
- Landau LD, Lifschitz EM (1981) *Klassische Feldtheorie*. Akademie-Verlag, Berlin
- Laqua H, Bluhm H, Buth L, Hoppé P (1995) Properties of the non-equilibrium plasma from a pulsed sliding discharge in a hydrogen gas layer desorbed from a metal hydride film. *J. Appl. Phys.* 77(11): 5545–5552
- Latham RV (1981) *High Voltage Vacuum Insulation: The Physical Basis*. Academic Press, London
- Legler W (1955) Zur Statistik der Elektronenlawinen. *Z. Phys.* 140(1): 221–240
- Legler W (1961) Die Statistik der Elektronenlawinen in elektronegativen Gasen bei hohen Feldstärken und bei großer Gasverstärkung. *Z. Naturforsch.* 16a: 253–261
- Lemke RW, Slutz SA (1995) A full mode set electromagnetic stability analysis of magnetically insulated ion diodes. *Phys. Plasmas* 2(2): 549–556
- L'Epplattenier P, Bavay M, Lalle B (2001) On numerical modelization and optimization of flux compression experiments. In: Reinovsky R, Newton M (eds.) *Proc. 28th IEEE Int. Conf. on Plasma Science and 13th IEEE Int. Pulsed Power Conf.*, 17–22 June 2001, Las Vegas, pp. 665–668
- Lewis TJ (1984) The role of electrodes in conduction and breakdown phenomena in solid dielectrics. *IEEE Trans. Electr. Insulat.* EI-19(3): 210–216
- Lewis TJ (1985) Electronic processes in dielectric liquids under incipient breakdown stress. *IEEE Trans. Electr. Insulat.* EI-20(2): 123–132
- Lewis TJ (1987) An overview of electronic processes leading to dielectric breakdown of liquids. In: Kunhardt EE, Christophoru LG, Luessen LH (eds.) *The Liquid State and Its Electrical Properties*. Plenum, New York, pp. 431–453
- Lewis TJ (1989) A simple general model for charge transfer in polymers. *Faraday Discuss. Chem. Soc.* 88: 189–201
- Lewis TJ (1990) Charge transport, charge injection and breakdown in polymeric insulators. *J. Phys. D: Appl. Phys.* 23: 1469–1478
- Lewis TJ (1993). The basic processes of conduction in dielectric liquids. 11th Int. Conf. on Conduction and Breakdown in Dielectric Liquids, Baden-Dattwil, Switzerland, pp. 32–41
- Lewis TJ (1994a) Basic electrical processes in dielectric liquids. *IEEE Trans. Dielectr. Electr. Insulat.* 1(4): 630–643
- Lewis TJ (1994b) Nanometric dielectrics. *IEEE Trans. Dielectr. Electr. Insulat.* 1(4): 812–825
- Lewis TJ (1994c) Liquid motion induced by electrocapillary action at solid metal-liquid interfaces. *J. Colloid Interface Sci.* 162: 381–389

- Lewis TJ (1996). New electro-mechanical concepts of the primary mechanism of electrical breakdown in liquids. *12th Int. Conf. on Conduction and Breakdown in Dielectric Liquids*, Rome, pp. 273–278
- Lewis TJ (1998) A new model for the primary process of electrical breakdown in liquids. *IEEE Trans. Dielectr. Electr. Insulat.* 5(3): 306–315
- Lewis TJ (2002) Polyethylene under electrical stress. *IEEE Trans. Dielectr. Electr. Insulat.* 9(5): 717–729
- Lewis TJ, Bowen PJ (1984) Electronic processes in biopolymer systems. *IEEE Trans. Electr. Insulat.* EI-19(3): 254–256
- Lewis IA, Wells FH (1959) *Millimicrosecond Pulse Techniques*. Pergamon, London
- Licht V, Bluhm H (2000) A sensitive dispersion interferometer with high temporal resolution for electron density measurements. *Rev. Sci. Instrum.* 71: 2710–2715
- Licht V, Bluhm H, Hoppé P, Yoo SJ (1998) Time dependent field and particle density measurements in the acceleration gap of a high power ion diode. In: Markovits M, Shiloh J (eds.) *12th Int. Conf. on High Power Particle Beams*. Haifa, Israel, pp. 203–207
- Lisitsyn I, Inoue H, Katsuki S, Akiyama H, Nishizawa I (1999) Drilling and demolition of rocks by pulsed power. In: Stalling C, Kirbie H (eds.) *Proc. 12th IEEE Int. Pulsed Power Conf.*, Monterey, CA, 27–30 June 1999, pp. 169–172
- Llewellyn-Jones F (1957) *Ionisation and Breakdown in Gases*. Methuen, London
- Lockner TR, Slutz S, Poukey JW, Stygar WA (1993) Theoretical and experimental studies of the 2-stage ion diode. In: Prestwich K, Baker W (eds.) *9th IEEE Int. Pulsed Power Conf.*, Albuquerque, NM, pp. 714–717
- Lockner T, Slutz S, Johnson DJ, Desjarlais M, Poukey J (1994) Results of the first 2-stage diode experiments on PBFALL. In: Rix W, White R (eds.) *10th Int. Conf. on High-Power Particle Beams*, San Diego. NTIS, Springfield, VA, pp. 61–64
- Lokhandwalla M, Bradford S (2000) Fracture mechanics model of stone comminution in ESWL and implications for tissue damage. *Phys. Med. Biol.* 45:1923–1940
- Loubriel GM, Zutavern FJ, Baca AG, Hjalmarson HP, Helgeson WD, O'Malley MW (1995) Photoconductive semiconductor switches for firing sets and electro-optic modulators. In: Baker W, Cooperstein G (eds.) *Proc. 10th IEEE Int. Pulsed Power Conf.*, Albuquerque, NM, pp. 354–359
- Loubriel GM, Zutavern FJ, Baca AG, Hjalmarson HP, Plut TA, Helgeson WD, O'Malley MW, Ruebush MH, Brown DJ (1997) Photoconductive semiconductor switches. *IEEE Trans. Plasma Sci.* 25(2): 124–130
- Lupton WH, Ford RD, Jenkins D, Vitkovitsky IM (1981) Homopolar generator concept for versatile pulsed output. In: Martin TH, Guenther AH (eds.) *3rd IEEE Int. Pulsed Power Conf.*, Albuquerque, NM, pp. 122–125
- Lyubutin SK, Mesyats GA, Rukin SN, Slovikovskii BG, Turov AM (1996) New solid state opening switches for repetitive pulsed power technology. In: Ullschmied J, Jungwirth K (eds.) *11th Int. Conf. on High-Power Particle Beams*, Prague, pp. 135–138

- Maenchen JE, Hahn K, Kincy M, Kitterman D, Lucero R, Menge PR, Molina J, Olson C, Rovang DC, Fulton RD, Carlson R, Smith J, Martinson D, Droemer D, Gignac R, Helvin T, Ormand E, Wilkins F, Welch DR, Oliver BV, Rose DV, Bailey V, Corcoran P, Johnson DL, Smith JD, Wiedenheimer D, Cooperstein G, Commisso R, Mosher D, Stephanakis S, Schumer J, Swanekamp S, Young F, Goldsack TJ, Cooper GM, Pearce AG, Phillips MA, Sinclair MA, Thomas KJ, Williamson M, Cordova S, Woodring R, Schamiloglu E (2002) Intense electron sources for flash radiography. In: Mehlhorn TA, Sweeney MA (eds.) *Proc. 14th Int. Conf. on High-Power Particle Beams*, 23–28 June 2002, Albuquerque, NM, pp. 117–122
- Malewski R (1968) New device for current measurement in exploding wire circuits. *Rev. Sci. Instrum.* 39: 90–94
- Maret G, Dransfeld K (1985) Biomolecules and polymers in high steady magnetic fields. In: Herlach F, Dransfeld K (eds.) *Strong and Ultrastrong Magnetic Fields and Their Applications*. Topics in Applied Physics, Vol. 57, Springer, Berlin, Heidelberg, pp. 143–204
- Maron Y, Sarid E, Nahshoni E, Zahavi O (1989) Time-dependent spectroscopic observation of the magnetic field in a high-power-diode plasma. *Phys. Rev. A* 39(11): 5856–5862
- Maron Y, Arad R, Weingarten A, Tsigitkin K, Ralchenko YV, Osin D, Chakrabarti N, Commisso RJ, Weber BV (2002) Interaction of rapid magnetic fields with plasmas and implications to pulsed-power systems. In: Kirbie H, Goebel D (eds.) *25th Int. Power Modulator Symp. and 2002 High-Voltage Workshop*, Hollywood, pp. 17–22
- Martin TH, Guenther AH, Kristiansen M (1996) *J.C. Martin, on Pulsed Power*. Plenum, New York
- Martynyuk P, Sher E (1974) Elastic-wave diffraction by a finite crack under antiplane strain conditions. *J. Appl. Mech. Techn. Phys.* 13: 406–410
- Marx E (1923) Verfahren zur Schlagprüfung von Isolatoren und anderen elektrischen Vorrichtungen. German Patent 455933
- Marx E (1924) Versuche über die Prüfung von Isolatoren mit Spannungsstößen. *Elektrotech. Z.* 25: 652–654
- Meek JM, Craggs JD (1978) *Electrical Breakdown of Gases*. Wiley, New York
- Mehlhorn TA, Bailey JE, Chandler GA, Coats RS, Cuneo ME, Derzon MS, Desjarlais MP, Dukart RJ, Filuk AB, Hail TA, Ives HC, Johnson DJ, Leeper RJ, Lockner TR, Mendel CW, Menge PR, Mix LP, Moats AR, Moore WB, Pointon TD, Poukey JW, Quintenz JP, Rosenthal SE, Rovang D, Ruiz CL, Slutz SA, Stygar WA, Wenger DF (1994) Progress in lithium beam power, divergence, and intensity at Sandia National Laboratories. In: Rix W, White R (eds.) *10th Int. Conf. on High-Power Particle Beams*, San Diego. NTIS, Springfield, VA, pp. 53–60
- Mendel CW, Rosenthal SE (1995) Modelling magnetically insulated devices using flow impedance. *Phys. Plasmas* 2: 1332–1342
- Mendel CW, Rosenthal SE (1996) Dynamic modelling of magnetically insulated transmission line systems. *Phys. Plasmas* 3: 4207–4219

- Mendel CW, Seidel DB, Rosenthal SE (1983) A simple theory of magnetic insulation from basic physical considerations. *Laser Part. Beams* 1(3): 311–320
- Mesyats GA (1998) *Explosive Electron Emission*. URO-Press, Ekaterinburg
- Milton O (1972) Pulsed flashover of insulators in vacuum. *IEEE Trans. Electr. Insul.* 7:9–15
- Miura N, Herlach F (1985). Strong and ultrastrong magnetic fields. In: Herlach F, Dransfeld K (eds.) *Strong and Ultrastrong Magnetic Fields and Their Applications*. Topics in Applied Physics, Vol. 57, Springer, Berlin, Heidelberg, pp. 278–297
- Miyamoto S, Yasuike K, Imasaki K, Yamanaka C, Nakai S (1992) Intense light ion beam divergence in single and two-stage diode. In: König D (ed.) *15th Int. Symp. on Discharges and Electrical Insulation in Vacuum*, Darmstadt, Germany. VDE-Verlag, Berlin, pp. 711–715
- Moses GA, Kulcinski GL, Bruggink D, Engelstad R, Lovell E, McFarlane J, Musicki Z, Petersen R, Stanislavsky I, Wittenberg L, Kessler G, Von Möllendorff U, Stein E, Smith I, Corcoran P, Nichimoto H, Fockler J, Cook D, Olson R (1989). Overview of the LIBRA light ion beam fusion conceptual design. *Fusion Technol.* 15: 756–765
- Müller G, Schumacher G, Zimmermann F (2000) Investigation on oxygen controlled liquid lead corrosion of surface treated steels. *J. Nucl. Mater.* 278:85–95
- Müller G, Engelko V, Bluhm H, An V, Kuznetsov V, Viazmenova G (2002a) Precision of intense electron beams transported in vacuum by applied magnetic field. In: Mehlhorn TA, Sweeney MA (eds.) *Proc. 14th Int. Conf. on High-Power Particle Beams*, Albuquerque, NM, 23–28 June 2002, pp. 337–340
- Müller G, Engelko V, Bluhm H, Heinzel A, Schumacher G, Strauss D, Weisenburger A, Zimmermann F, Shulov V, Notchovnaia N (2002b) Application of pulsed electron beams for improvement of material surface properties. In: Mehlhorn TA, Sweeney MA (eds.) *Proc. 14th Int. Conf. on High-Power Particle Beams*, Albuquerque, NM, 23–28 June 2002, pp. 325–328
- Müller G, Heinzel A, Schumacher G, Weisenburger A (2003) Control of oxygen concentration in liquid lead and lead–bismuth. *J. Nucl. Mater.* 321: 256–262
- Müller G, Engelko V, Weisenburger A, Heinzel A (2005) Surface alloying by pulsed intense electron beams. *Vacuum* 77:469–474
- Nation J (1979) High-power electron and ion beam generation. *Part. Accel.* 10: 1–30
- Neu J, Krassowska W (1999) Asymptotic model of electroporation. *Phys. Rev. E* 59(3): 3471–3482
- Ottinger PF, Young FC, Stephanakis SJ, Rose DV, Neri JM, Weber BV, Myers MC, Hinshelwood D, Mosher D, Olson CL, Welch DR (2000) Self-pinch transport of an intense proton beam. *Phys. Plasmas* 7(1): 346–358
- Pao YH, Mow C (1963) Scattering of plane compressional waves by a spherical obstacle. *J. Appl. Phys.* 34(3): 493–499
- Papoulis A (1968) *Systems and Transforms with Applications in Optics*. McGraw-Hill, New York

- Pareira NR (1983) Electron backscatter and impedance in one-dimensional space-charge limited diodes. *J. Appl. Phys.* 54(11): 6307–6310
- Paschen F (1889) Über die zum Funkenübergang in Luft, Wasserstoff und Kohlen-säure bei verschiedenen Drucken erforderliche Potentialdifferenz. *Ann. Phys. Chem.* 37: 69–96
- Pfeiffer W (1971) Der Spannungszusammenbruch an Funkenstrecken in komprimierten Gasen. *Z. Angew. Phys.* 32(4): 265–273
- Poukey JW, Bergeron KD (1978) Space-charge effects in long coaxial vacuum transmission lines. *Phys. Lett.* 32(1): 8–10
- Quintenz J, Seidel D, Kiefer M, Pointon T, Coats R, Rosenthal S, Mehlhorn T, Desjarlais M, Krall N (1994) Simulation codes for light-ion diode modelling. *Laser Part. Beams* 12(2): 283–324
- Rabussay D, Dev NB, Fewell J, Smith LC, Widera G, Zhang L (2003) Enhancement of therapeutic drug and DNA delivery into cells by electroporation. *J. Phys. D: Appl. Phys.* 36: 348–363
- Raether H (1964) *Electron Avalanches and Breakdown in Gases*. Butterworths, London
- Ramirez JJ, Hasti DE, Corley JP, Poukey JW, Prestwich KR, Genuario RD, Nishimoto HN, Fockler JJ, Smith ID, Champney PD, Nielsen KE, Schlitt LG, Spence PW (1985) The four stage HELIA experiment. In: Rose MF, Turchi PJ (eds.) *Proc. 5th IEEE Int. Pulsed Power Conf.*, 10–12 June 1985, Arlington, VA, pp. 143–146
- Ramirez JJ, Prestwich KR, Alexander JA, Corley JP, Denison GJ, Huddle CW, Johnson DL, Pate RC, Weber GJ, Bugess EL, Hamil RA, Poukey JW, Sanford TW, Seamons LO, Zawadzka GA, Smith ID, Spence PW, Schlitt LG (1988) Hermes III – A 16 TW short pulse gamma ray simulator. In: Bauer W, Schmidt W (eds.) *Proc. 7th Int. Conf. on High-Power Particle Beams*, Karlsruhe, Germany, 4–8 July 1988, pp. 148–157
- Redi M, Hopfield JJ (1980) Theory of thermal and photo-assisted electron tunnelling. *J. Chem. Phys.* 72(12): 6651–6660
- Reinovsky RE, Smith DL, Baker WL, Degnan JH, Henderson RP, Kohn RJ, Kloc DA, Foderick NF (1982) Inductive store pulse compression system for driving high speed plasma implosions. *IEEE Trans. Plasma Sci.* 10: 73–81
- Reinovsky RE, Levi PS, Welby JM (1985) An economical, 2 stage flux compression generator system. In: Rose MF, Turchi PJ (eds.) *Proc. 5th IEEE Int. Pulsed Power Conf.*, 10–12 June 1985, Arlington, VA, pp. 216–219
- Rogowski W, Steinhaus W (1912) Die Messung der magnetischen Spannung. (Messung des Linieneintegrals der magnetischen Feldstärke). *Arch. Elektrotechnik* 1(4): 141–150
- Rompe R, Weizel W (1944) Über das Toeplersche Funkengesetz. *Z. Phys.* 122: 9–12
- Rose DV, Ottinger PF, Welch DR, Oliver BV, Olson CL (1999) Numerical simulations of self-pinch transport of intense ion beams in low-pressure gases. *Phys. Plasmas* 6(10): 4094–4103

- Rukin SN, Kotov YA, Mesyats GA, Filatov AL, Lyubutin SK, Alichkin YA, Darznez SA, Telnov VA, Slovikovskii BG, Timoshenkov SP, Bushlyakov AI, Turov AM (1996) Pulsed power accelerator technology based on solid-state semiconductor opening switches. In: Jungwirth K, Ullschmied J (eds.) *Proc. 11th Int. Conf. on High Power Particle Beams*, Prague, 10-14 June 1996, pp. 33-36
- Rusch D (1991) Handbuch zum Programm LEITER. Numerische Simulation pulstechnischer Netzwerke, Forschungszentrum Karlsruhe, unpublished
- Sale A, Hamilton W (1967) Effects of high electric fields on microorganisms – I. Killing of bacteria and yeasts. *Biochem. Biophys. Acta* 148: 781-788
- Santos JC, Taplamacioglu CM, Hidaka K (2000) Pockels high-voltage measurement system. *IEEE Trans. Power Delivery* 15(1): 8-13
- Sarjeant WJ, MacDougall FW (1997) Capacitors for high power electronics. In: Cooperstein G, Vitkovitsky I (eds.) *Proc. 11th IEEE Int. Pulsed Power Conf.*, Baltimore, MD, pp. 603-609
- Schiweck H, Clarke M (2001) In: *Ullmann's Encyclopedia of Industrial Chemistry*, 6th edn, 2001 Electronic Release. Wiley-VCH, Weinheim
- Schoenbach K, Kristiansen M, Schaefer G (1984) A review of opening switch technology for inductive energy storage. *Proc. IEEE* 72(8): 1019-1040
- Schoenbach KH, Peterkin FE, Alden RW, Beebe SJ (1997) The effect of pulsed electric fields on biological cells: experiments and applications. *IEEE Trans. Plasma Sci.* 25(2): 284-292
- Schoenbach KH, Beebe SJ, Buescher ES (2001) Intracellular effect of ultrashort pulses. *Bioelectromagnetics* 22: 440-448
- Schultheiss C, Sträßner R, Bluhm H, Stemmermann P (1998) Concrete recycling and scraping by electrodynamic fragmentation. In: Bluhm H (ed.) *Physics of Intense Light Ion Beams. Production of High Energy Density in Matter, and Pulsed Power Applications*, Annual Report 1996/97, Karlsruhe, FZKA-Report 6205
- Schultheiss C, Bluhm H, Mayer H, Kern M, Michelberger T, Witte G (2002) Processing of sugar beets with pulsed electric fields. *IEEE Trans. Plasma Sci.* 30(4): 1547-1551
- Schumann D, Müller RA (2001) Verfahren zur Gewinnung von Polyhydroxyalkanoaten (PHA) oder deren Copolymeren. German Patent DE 100 13514 C2
- Schwab AJ (1981) *Hochspannungsmesstechnik*. Springer, Berlin, Heidelberg
- Sethian JD, Hegeler F, Myers M, Friedman M, Obenschain S, Lehmborg R, Guilian J, Kepple P, Swanekamp S, Smith I, Weidenheimer D, Morton D, Schlitt L, Smilgys R, Searles S (2001) The Electra KrF laser program. In: Reinovsky R, Newton M (eds.) *Proc. 28th IEEE Int. Conf. on Plasma Science and 13th IEEE Int. Pulsed Power Conf.*, 17-22 June 2001, Las Vegas, pp. 232-236
- Sher E (1974) Investigation of the dynamics of the development of cracks by the method of photoelasticity. *J. Appl. Mech. Techn. Phys.* 16(6): 858-864
- Shpitalnik R, Weingarten A, Gomberoff K, Krasik Y, Maron Y (1998) Observations of two-dimensional magnetic field evolution in a plasma opening switch. *Phys. Plasmas* 5(3): 792-798

- Sjomkin BW, Ussow AF, Kurets VI (1995) *The Principles of Electric Impulse Destruction of Materials*. Russian Academy of Sciences, Kola Science Centre (in Russian)
- Skotheim TA (1986) *Handbook of Conducting Polymers*. Dekker, New York
- Slenes KM, Winsor P, Scholz T, Hudis M (2001) Pulse power capability of high energy density capacitors based on a new dielectric material. *IEEE Trans. Magn.* 37(1): 324–327
- Slutz SA (1993) Ion emission from anode foils during multistage acceleration of intense ion beams. *Phys. Fluids B* 5(1): 209–215
- Slutz SA, Desjarlais MP (1990) Theory of multistage intense ion beam acceleration. *J. Appl. Phys.* 67(11): 6705–6717
- Slutz SA, Poukey JW, Pointon TD (1994) Simulations of magnetically insulated multistage ion diodes. *Phys. Plasmas* 1(6): 2072–2081
- Smith ID (1980) A novel voltage multiplication scheme using transmission lines. Report, AWRE Aldermaston, unpublished
- Sommerfeld A (1950) *Vorlesungen über Theoretische Physik*. Akademische Verlagsgesellschaft, Leipzig
- Spielman RB, Stygar WA, Seamen JF, Long F, Ives H, Garcia R, Wagoner T, Struve KW, Mostrom M, Smith I, Spence P, Corcoran P (1997) Pulsed power performance of PBFA Z. In: Cooperstein C, Vitkovitsky I (eds.) *Proc. 11th IEEE Int. Pulsed Power Conf.*, 29 June–2 July 1997, Baltimore, pp. 709–714
- Stokes JL, Bartsch RR, Cochrane JC, Chrien RE, Forman PJ, Looney LD, Tabaka LJ, Veaser LR, Marshall BR, Broste WB, Warthen BJ (1995) Precision current measurements on Pegasus II using Faraday rotation. In: Baker W, Cooperstein G (eds.) *Proc. 10th IEEE Int. Pulsed Power Conf.*, Albuquerque, NM, pp. 378–385
- Strauss D, Müller G, Schuhmacher G, Engelko V, Stamm W, Clemens D, Quadakkers WJ (2001) Oxide scale growth on MCrAlY bond coatings after pulsed electron beam treatment. *Surf. Coat. Technol.* 135: 196–201
- Sunka P (2001) Pulse electrical discharges in water and their applications. *Phys. Plasmas* 8(5): 2587–2594
- Sunka P, Babicky V, Clupek M (1999) Generation of chemically active species by electrical discharges in water. *Plasma Sources Sci. Technol.* 8: 258–265
- Takahashi Y (1977) Koronaentladungen in flüssigem Stickstoff. *Bull. Facul. Sci. Eng., Chuo Univ.* 20: 247–255
- Takahashi Y, Ohtsuka K (1975) Corona discharges and bubbling in liquid nitrogen. *J. Phys. D* 8: 165–169
- Teissier J, Rols M (1994) Manipulation of cell cytoskeleton affects the lifetime of cell membrane electropermeabilization. *Ann. N.Y. Acad. Sci.* 720: 98–110
- Toepler M (1924) Stoßspannung, Übersschlag und Durchschlag bei Isolatoren. *Elektrotechn. Z.* 45: 1045–1050
- Toepler M (1927) Zur Bestimmung der Funkenkonstante. *Arch. Elektrotechn.* 18: 549–562

- Toney MF, Howard JN, Richer J, Borges GL, Gordon JG, Melroy OR, Wiesler DG, Yee D, Sorensen LB (1994) Voltage-dependent ordering of water molecules at an electrode–electrolyte interface. *Nature* 368: 444–446
- Turman BN, Martin TH, Neau EL, Humphreys DR, Bloomquist DD, Cook DL, Goldstein SA, Schneider LX, McDaniel DH, Wilson JM, Hamil RA, Barr GW, VanDevender JP (1985) PBFA II, A 100 TW pulsed power driver for the inertial confinement fusion program. In: Turchi PJ, Rose MF (eds.) *Proc. 5th IEEE Int. Pulsed Power Conf.*, Arlington, VA, pp. 155–161
- Urban J (2002) *Spektroskopische und elektrische Charakterisierung des Entladeverhaltens von Pseudofunken-Schaltssystemen*. PhD thesis, University of Erlangen
- VanDevender JP (1976) Short pulse electrical breakdown strength of H₂O. In: Burkes TR, Kristiansen M (eds.) *1st IEEE Int. Pulsed Power Conf.*, Lubbock, TX, pp. IIIE3.1–IIIE3.5
- VanDevender JP, Bluhm H (1993) Light ion accelerators for ICF. In: Velarde G, Ronen Y, Martinez-Val JM (eds.) *Nuclear Fusion by Inertial Confinement*, CRC Press, Boca Raton, pp. 455–484
- Vasilevskii MA, Roife IM, Engelko VI (1980) Impedance of a diode with a multispikes explosive-emission cathode. *Sov. Phys. Tech. Phys.* 25(11): 1380–1382
- Vasilevskii MA, Roife IM, Engelko VI (1981) Operating characteristics of explosive-emission multipoint cathodes with microsecond pulse length. *Sov. Phys. Tech. Phys.* 26(6): 671–678
- Vasilevskii MA, Roife IM, Engelko VI, Yankin EG (1986) Dynamics of plasma generated by a multitip explosive-emission cathode. *Sov. Phys. Tech. Phys.* 31(3): 284–287
- Vasilevskii MA, Engelko VI, Yankin EG (1988) The influence of emitter density and anode process on the time of operation of a diode with multitip explosive emission cathodes. *Sov. Phys. Tech. Phys.* 33(9): 1060–1066
- Vesey RA, Pointon TD, Cuneo ME, Mehlhorn TA, Bailey JE, Johnson DJ, Stygar WA (1999) Electron–anode interactions in particle-in-cell simulations of applied-*B* ion diodes. *Phys. Plasmas* 6(8): 3369–3387
- Volodarskaya SG, Guz' IS, Kumkin IA, Finkel VM (1975) An investigation into the interaction of a stress wave with a stationary macrocrack in elastic–plastic and quasibrittle materials. *J. Appl. Mech. Tech. Phys.* 13: 432–437
- Walker J, Surman S, Jass J (2000) *Industrial Biofouling – Detection, Prevention and Control*. Wiley, Chichester
- Wang MY, DiCapua MS (1980) Operating point of long magnetically insulated vacuum transmission lines. *J. Appl. Phys.* 51(11): 5610–5614
- Weaver J (1994) Molecular basis for cell membrane electroporation. *Ann. N.Y. Acad. Sci.* 720: 141–152
- Weaver J, Chizmadzhev Y (1996) Theory of electroporation: a review. *Bioelectrochem. Bioenerget.* 41: 135–160
- Weizel W, Rompe R (1947) Theorie des elektrischen Funkens. *Ann. Physik* 6(1): 285–300

- Welch DR, Olson CL (1996) Self-pinched transport for ion-driven inertial confinement fusion. *Fusion Eng. Design* 32–33: 477–483
- Welch DR, Cuneo ME, Olson CL, Mehlhorn TA (1996) Gas breakdown effects in the generation and transport of light ion beams for fusion. *Phys. Plasmas* 3: 2113–2121
- Yoo S (1997) *Spektroskopische Messungen im Anodenplasma einer fremdmagnetisch isolierten Hochleistungs-Ionendiode*. PhD thesis, University of Karlsruhe, FZKA-Report 5976
- Yoxas G (1978) Fusion power with particle beams. *Sci. Am.* 239: 50–61
- Zeller HR, Pfluger P, Bernasconi J (1984) High-mobility states and dielectric breakdown in polymeric dielectrics. *IEEE Trans. Electr. Insulat.* EI-19(3): 200–204
- Zinov'ev N, Semkin B (1978) Energy balance for a spark in a solid dielectric. *Sov. Phys. Tech. Phys.* 23(3): 369–370

Index

- adding of
 - power 193
 - voltage
 - inductive isolation 195
 - transit time-isolation 193
- ADS 264
- ATLAS 254
- avalanche initiation, probability 21

- B*-dot loop 215
- bacterial decontamination 236
- beam current, maximum transportable 258
- beam divergence 273
- beam transport, self-pinchd 277
- biofouling 237
- biological cell, equivalent circuit 229
- Blumlein line 197
- breakdown
 - in liquids
 - electronic energy states 28
 - resonance tunnelling 29
 - in solids 41
 - cumulative model 49
 - experimental 44
 - intrinsic breakdown strength 44
 - metal contact 47
 - polymers 45
- breakdown strength
 - dynamic 283
 - inhomogeneous field 15
 - liquid nitrogen 301
 - SF₆ 13

- capacitive sensor 212
- capacitive voltage divider 213
- capacitor
 - complex impedance 59
 - lumped circuit 55
 - metallized film 62
- capacitor lifetime 61
 - voltage rating 62
 - voltage reversal 61
- cascade circuit 188
- cell lysis 236
- cells, short pulse effects 237
- charging unit 184
 - resistor limited 184
 - resonant 184
 - series-resonant converter 186
 - switch mode 185
- Child–Langmuir law 260
- circuit simulation, LEITER 152
- closing switches 83
- composite material, mechanisms of separation 287
- concrete reutilisation 292
- concrete separation into components, process water conductivity 299
- conversion efficiency, mechanical to magnetic energy 250
- corrosion in liquid Pb/Bi 265
- cross-section for reaction 8
- crowbar switch 69
- cumulative pulse line 198
- current shunt 218
- current-viewing resistors 218

- destruction selectivity 286
- diagnostics, electrical 211
- dielectric polarisation 59
- distribution function, velocity 9
- double layer 32

- efficiency of fragmentation 285
- ELECTRA 266

- electric breakdown, statistics 50
- electric field sensor 211
- electric strength, general 7
- electro-optic sensor 222
 - Kerr effect 222
 - Pockels effect 222
- electrodynamic fragmentation
 - economic considerations 304
 - elastoplastic materials 301
 - generator parameters 288
 - milling of materials 300
 - productivity 294
 - removal of surface layers 297
 - spark channel resistance 290
- electrodynamic treatment
 - incineration ash 295
- electron diode 259
 - current limitation 259
- electron field emission 159
 - dielectric inclusions 160
 - metallic surfaces 159
- electron sources 258
 - carbon fibre 259
 - plasma 259
- electronegative gas 13
- electroporation 231
 - plant cells 232
 - raw-material production 238
- emission centres 19
- energy dissipation 58
- energy storage
 - capacitive 3, 55
 - inductive 3
 - mechanical 2, 76
- energy transfer stage 70
- exponential line 190

- Faraday effect monitor 220
- field enhancement factor 15
- field sensors 211
- flux compression 248
 - by high current 256
 - cylindrical scheme 252
 - cylindrical shells 252
 - explosive cascade system 255
 - turnaround condition 252
- flux diffusion speed 250
- flywheel 76
- Fowler–Nordheim equation 18, 159

- FRANKA 294

- gas switches 83
- generator scheme 2
- GESA 261
- Gouy–Chapman layer 31
- Guillemin network 149

- HELIA 195, 271
- Helmholtz layer 31
- HERMES III 207
- hibachi 266
- high magnetic fields 239
 - effects 239
- hollow cathode 98
- homopolar generator 76
- Hugoniot relations 248

- IGBT 112
- ignitor 100
- ignitron 100
- imploding liner 254
- inductive energy storage 73
- inductive loop 214
- inductive pulse compression 74
 - power multiplication 76
 - voltage multiplication 76
- inertial-confinement fusion 257
- inertial-fusion energy 265, 270
- insulating interface 157
- intense beams, self-fields 257
- interface, breakdown strength 158
- ionisation coefficient 9

- KALIF 203
- KEA 233
- KrF laser 265
 - electron-beam-pumped 266
- krytron 102

- ladder networks 145
 - LC* chain 146
- laminar electron flow 167
- LC* Marx generator 69
- light-ion accelerator
 - injector diode 271
 - multistage 274
 - post-accelerating gap 275
- light-ion diode

- current enhancement 273
- diocotron instability 273
- magnetic insulation 272
- light-ion driver for IFE 271
- light-ion source 276
- liquids
 - effective electron mobility 30
 - hole transport 31
 - region of low density 30
- lithotripsy
 - pressure waveform 280
 - shock wave 279
- loss angle 58

- magnetic energy analyser 223
- magnetic-field limitations 240
- magnetic-field pressure, dynamic
 - containment 244
- magnetic-field sensor 211
- magnetic field strength
 - destructive systems 246
 - mechanical limitations 243
 - thermal limitations 245
- magnetic-flux skin depth 251
- magnetic insulation 161
- magnetic pulse compression 208
- magnetic stress 243
- magnetic switch 116
 - hysteresis loop 116
- magnetoexplosive generators 254
- magneto-optic sensor 220
- magneto-resistance 239
- Marx generator 63
 - bipolar 64
 - capacitive coupling 67
 - self-discharge 65
 - stray capacitance 66
 - triggering 66
 - unipolar 63
- material destruction by electric
 - discharges 284
- material surface modification
 - cooling rates 260
 - electron beam 260
 - oxidation protection 263
- mean free path, definition 9
- membrane
 - charging time 228
 - field enhancement 228
- membrane polarisation 228
- Metglass 117
- multichannel spark gaps 95

- neutralisation
 - charge 258
 - current 258

- opening switches 119
 - counter-pulse 122
 - fuse 120
 - mechanical interrupter 121
 - plasma 123
 - plasma flow 127
 - semiconductor 127
 - DSDR 131
 - SOS 133
 - superconducting 123
- optical absorption depth in semiconductors 114

- particle beams 257
- Paschen law 11
- PBFA 2 204
- peaking circuit 69
- PIC code 163
- polyethylene 46
- pore formation 229
 - free energy 229
- prepulse suppression 204
- production of sugar 232
- pseudospark switch 98
 - virtual anode 98
- pulsed breakdown
 - area-time relationship 22
 - avalanche build-up time 21
 - liquids 27
 - liquids, bulk processes 27
 - liquids, electrocapillarity 35
 - liquids, electrode processes 31
 - liquids, empirical formulae 39
 - liquids, practical considerations 38
 - statistical delay time 18
 - water 38
- pulsed electric discharge, in solids 281
- pulsed magnetic fields 238
- pulsed-power applications, categories

- radiation therapy, BNC 270
- radiographic source 267
- radiography, point-projection 267
- Raether 16
- RHEPP 208
- rise time 94
- Rogowski coil 215
 - compensated 217
- self-magnetic insulation 161
 - analytic models 165
 - critical current 167
 - energy transfer 177
 - minimum current 172
 - non-stationary 174
 - sheath current 171
 - total current 170
 - wall current 171
 - wave propagation velocity 178
- semiconductor closing switches 104
 - optically activated 113
- shockwave generation 280
- shunt, coaxial 219
- single-turn coil 246
- solenoidal coil 240
- SOS-based generators 209
- spallation 288
- spark formation
 - Braginskii model 24
 - current-time relationship 26
 - Rompe-Weizel model 24
 - Toepler model 23
- spark gap 85
 - laser-triggered 92
 - multistage 94
 - overvoltage triggering 85
 - plasma triggering 87
- streamer breakdown
 - in gases 17
 - in liquids 34
 - anode initiation 37
 - cathode initiation 35
- superalloy coatings 262
- surface alloying 264
- thermal-barrier coating 263
- thyatron 96
 - thermionic cathode 97
- thyristor 104
 - conducting state 106
 - doping profile 104
 - forward blocking 105
 - GTO 109
 - photon triggering 109
 - reverse blocking 104
 - spiral gate 110
- time jitter 95
- Townsend condition 11
- transformation lines 188
- transformers 179
 - droop 182
 - equivalent-circuit model 181
 - step pulse response 182
- transmission line 135
 - circuit element 142
 - losses 140
 - pulse formation 144
 - terminations and junctions 138
- trigatron switch 87
- triggered vacuum gap 103
- turbine blades 262
- Verdet constant 220
- Vitrovac 117
- voltage monitor
 - capacitive 212
 - vacuum 224
- water switch 203
- Weibull statistics 51
- X-ray dose 270
- X-ray radiography 267
- X-ray sources
 - magnetically immersed diode 269
 - paraxial diode 268
 - pinched-beam 268
 - rod pinch 269
- Z-Machine 205
- Z-pinch 207